Université catholique de Louvain
Faculté des Sciences
Ecole de Chimie

Development of Photocleavable Block Copolymers as Precursors for Functional Nanomaterials

Jean-Marc Schumers

Promoteur: Professeur J.-F. Gohy
Co-promoteur: Professeur C.-A. Fustin

Dissertation présentée en vue de l'obtention
du grade de Docteur en Sciences

2010

Université catholique de Louvain
Faculté des Sciences
Ecole de Chimie

Development of Photocleavable Block Copolymers as Precursors for Functional Nanomaterials

Jean-Marc Schumers

Membres du jury:

Prof. J.-F. Gohy (UCL), promoteur
Prof. C.-A. Fustin (UCL), co-promoteur
Prof. J. Marchand-Brynaert (UCL)
Prof. B. Elias (UCL)
Prof. P. Dubois (UMH)
Prof. F. Duprez (UGent)
Prof. S. Demoustier-Champagne (UCL), présidente

Dissertation présentée en vue de l'obtention
du grade de Docteur en Sciences

2010

"*The pessimist complains about the wind; the optimist expects it to change; the realist adjusts the sails.*"

"*Le pessimiste se plaint du vent, l'optimiste espère qu'il va changer, le réaliste ajuste ses voiles.*"

William Arthur Ward

ACKNOWLEGDMENTS

Fier tel un matelot du haut de son trois-mâts, je m'embarquais voici quatre ans pour un long voyage nommé *Thèse de doctorat*. Longue fût l'hésitation avant de me jeter à l'eau car je savais que cette dernière s'apparanterait plutôt à une traversée de l'océan qu'à celle d'un long fleuve tranquille. Pourtant, l'appel du large et la soif d'aventure prirent le dessus et c'est ainsi que je levai l'ancre en septembre 2006. A l'instar de la mer, la thèse peut être calme, houleuse, agitée voire même tempétueuse à certains moments! Heureusement pour moi, le voyage ne fût pas une traversée en solitaire et c'est pourquoi, j'aimerais dédier ces quelques lignes à tous les membres d'équipage qui m'ont aidé à arriver à bon port.

En premier lieu, je remercie de tout coeur le Professeur Jean-François Gohy, capitaine du *laboratoire de chimie macromoléculaire* à bord duquel j'ai navigué pendant ces quatres années. Cet homme charismatique, à la voix grave et aux idées innovantes, m'a acceuilli au sein de son équipage et m'a encadré tout au long de ce voyage. Ses enseignements didactiques et son enthousiasme sans pareil ont été des facteurs stimulants et déterminants dans la réussite de ce projet. Je le remercie aussi pour m'avoir donné l'opportunité de faire part de mes travaux de recherche lors de plusieurs congrès organisés en Belgique et à l'étranger. Ces escales ont été l'occasion de découvrir d'autres paysages et de rencontrer des personnalités du monde scientifique.

J'exprime également toute ma gratitude au Professeur Charles-André Fustin qui, aux côtés du Professeur Gohy, a manié la barre et le gouvernail pour que jamais je ne perde le cap. Sa rigueur, sa patience et sa grande connaissance scientifique font de lui un cartographe hors pairs,

qu'il est toujours bon de consulter avant de s'aventurer en eaux troubles. Je souligne sa grande complémentarité avec le Professeur Gohy et je les remercie tous deux pour leur écoute, leur disponibilité et surtout pour la confiance qu'ils m'ont témoignée. Finalement, je leur tire mon chapeau pour leur rapidité de correction qui donne l'impression que les écrits peuvent être corrigés avant même d'être rédigés...

Je remercie aussi les Professeurs Jacqueline Marchant-Brynaert et Sophie Demoustier-Champagne pour avoir intégré l'aventure depuis le départ. Leur présence s'est d'abord traduite en tant que membres de mon comité d'encadrement puis en tant que juges de ce travail en acceptant, sans hésitation, de rejoindre mon jury de thèse. Je n'oublie pas non plus leur précieuse aide lorsque je préparais mon examen du FRIA qui fût mon ticket d'embarquement pour la thèse.

Je tiens également à remercier les Professeurs Benjamin Elias, Filip Duprez et Philippe Dubois pour avoir accepté de lire et de juger ce travail. Leurs commentaires judicieux et pertinents ont contribués à l'amélioration de ce manuscrit.

I would like to acknowledge Professor Ulrich S. Schubert for welcoming me in his research group during two weeks in June 2008. It was a great pleasure for me to work in his laboratory with Professor Richard Hoogenboom and Aydin Can. Moreover, I would like to warmly thank the former for the time he devoted to me and for the fruitfull discussions we had.

Après ce petit intermède en anglais, je voudrais saluer tous les matafs du laboratoire avec qui, chaque jour, j'ai hissé les voiles. Mes premiers remerciements vont tout droit au Dr. Pierre Guillet que j'ai rencontré lors de ma première foulée sur le pont. Derrière son allure altière et son humour un peu spécial, se cache un collègue et un camarade généreux, dévoué et toujours prêt à rendre service. Je me souviens avec joie de nos nombreuses discussions et de l'ambiance quelque peu chahutée que nous entretenions dans le laboratoire. Je souligne également son côté *ingénieur* et *toujours à la pointe de la technologie*. Si les bâteaux sont aujourd'hui équipés de radars et de système GPS, c'est sans conteste grâce à lui... Mes pensées vont ensuite aux Dr. Alexendru Vlad. Je lui dis merci pour avoir quitté sa Moldavie d'origine et être venu s'échouer

ici, sur les côtes de Louvain-la-Neuve. Sans ce véritable corsaire, les pitas, les muffins, les clics-clics, les pcc's, les images SEM, la vodka piquante et son alcool de mouche auraient été bien moins agréables. Un tout grand merci aussi au Dr. Guillaume De Bo qui m'avait déjà encadré en mémoire. Son esprit vif, sa culture générale et son côté un peu kamikaze vont me manquer lorsqu'il quittera le laboratoire. Je pense aussi à Clément Muguemana dont j'admire le calme, la gentillesse et la force tranquille qui émane de lui.

Je remercie également mes petits mousses, à savoir Bruno, Nathalie et Olivier pour leur aide et leur implication dans mon travail de thèse. Je fais un clin d'oeil tout particulier à Olivier dont j'ai apprécié l'aide et la compagnie lors de son mémoire (mais pas son orthographe). Je suis fier de ce jeune moussaillon qui s'est, lui aussi, embarqué pour l'aventure *thèse*. Merci aussi à mon ami Greg, à Julien (le jeune padawan) et à tous les autres membres du labo ainsi qu'à Axel, Brigitte, Cécile, Edwouard, Hubert et Jacques pour tous les petits coups de rames qui ont contribué à faire avancer ma barque.

A l'instar d'une brise iodée, les pensées du marin pour sa famille lui redonnent force et courage lorsque, loin de tout rivage, le mal de mer le tiraille. Je remercie donc particulièrement mes parents qui m'ont toujours soutenu dans mes choix et qui m'ont continuellement poussé à faire ce que j'aime pour que, simplement, je sois heureux. Il y a plusieurs années, j'ai été envoûté par le charme et le chant d'une sirène nommée Séverine. Sa présence, ses conseils, ses sacrifices et surtout son amour m'ont été indispensables pour arriver au bout du voyage. Finalement, mes dernières pensées vont à ma fille Léane dont les sourires quotidiens sont de véritables arcs-en-ciel. Le bonheur de la voir grandir tous les jours me rempli de joie. Et qui sait? Peut-être qu'un jour, elle aussi prendra le large...

CONTENTS

SYMBOLS AND ABBREVIATIONS

χ	Interaction parameter of Flory-Huggins
ΔG_m	Free energy of mixing
ΔH_m	Enthalpy of mixing
ΔS_m	Entropy of mixing
γ	Interfacial tension
λ	Wavelength
λ_{C-C}	Center-to-center interdistance
λ_{max}	Wavelength at the maximum of absorption
ν	Frequency
ϕ_{S}	Solvent gradient
c	Light velocity
E_a	Energy of activation
e_c	Click efficiency
e_g	Grafting efficiency
e_i	Initiation efficiency
h	Planck constant
M_{n}	Number average molar mass
M_{p}	Molar mass at the top of the GPC peak
M_{w}	weight average molar mass
r	Mass fraction
R_h	Hydrodynamic radius
5CB	p-n-penthyl-p'-cyanobiphenyl
Ø	Diameter
AA	Acrylic acid
AcOEt	Ethyl acetate
AFM	Atomic force microscopy
AIBN	Azobis(isobutyronitrile)

Ar	Argon
ATRP	Atom transfer radical polymerization
BA	Benzoic acid
BCC	Body centered cubic
BSA	Bovine serum albumine
CBDB	2-Cyano-2-butyl dithiobenzoate
CEA	2-Cinnamoyloxyethyl acrylate
CGC	Critical gel concentration
CMC	Critical micellar concentration
CMT	Critical micellar temperature
conv.	Conversion
CPDA	Cumyl phenyldithioacetate
CPS	Close-packed spheres
CRP	Controlled radical polymerization
CTA	Chain transfer agent
CuAAC	Copper(I)-catalyzed azide-alkyne cycloaddition
DCM	Dichloromethane
DE	Diffraction efficiency
DFT	Density functional theory
Dis	Disordered
DLS	Dynamic light scattering
DMAP	4-dimethylaminopyridyne
DMF	*N,N*-dimethylformamide
dNPy	4,4'-dinonyl-2,2'-dipyridyl
DP	Degree of polymerization
EBiB	Ethyl 2-bromoisobutyrate
EBP	Ethyl 2-bromopropionate
equiv.	Equivalent
Et_3N	Triethylamine
FCC	Face centered cubic
FD	Functionalization degree
FT-IR	Fourier transform infrared
GC	Gas chromatography
GPC	Gel permeation chromatography
HDD	Hard disk drive
HEX	Hexagonally packed cylinders
IR	Infrared
ISL	Intermediate segregation limit
LAM	Lamellae

LC	Liquid crystal
LCST	Lower critical solution temperature
LRBC	Light-responsive block copolymer
Me_6Tren	tris[2-(dimethylamino)ethyl]amine
MLAM	Modulated lamellae
NBA	*o*-nitrobenzyl acrylate
NBMA	*o*-nitrobenzyl methacrylate
NHPMI	N-hexyl-2-pyridylmethanimine
NIR	Near infrared
NMP	Nitroxide mediated polymerization
NMR	Nuclear magnetic resonance
NRET	Non-radiative energy transfer
ODT	Order-disorder transtition
PAz	Poly(acrylate of azobenzene moieties)
PBD	Polybutadiene
PCEMA	Poly(2-cinnamoylethyl methacrylate)
PCMA	Poly(methacrylate of coumarine moieties)
PDEAEMA	Poly(2-(diehtylamino)ethylmethacrylate)
PDI	Polydispersity index
PDMAEMA	Poly(dimethylaminoethylene methacrylate)
PE	Polyethylene *or* petroleum ether
PEE	Poly(ethylethylene)
PEO	Poly(ethylene oxide)
PEP	poly(ethylene-*co*-propylene)
PETEGA	Poly(ethyleneglycol acrylate)
PHEMA	Poly(hydroxyethyl methacrylate)
PI	Polyisoprene
PLAM	Perforated lamellae
PMA	Polymethylacrylate
PMAA	Poly(methylacrylatic acid)
PMAz	Poly(methacrylate of azobenzene moieties)
PMDETA	N,N,N',N',N"-pentamethyldiethylenetriamine
PMMA	Polymethylmethacrylate
PMSP	Poly(methacrylate of spyropyran moieties)
PNBA	Poly(*o*-nitrobenzyl acrylate)
PNBMA	Poly(*o*-nitrobenzyl methacrylate)
PNIPAM	Poly(N-isopropylacrylamide)
POEGMA	Poly(oligoethyleneglycol methacrylate)
ppm	Part per million

PPy	Polypyrenylmethyl
PS	Polystyrene
PtBA	Poly(*tert*-butylacrylate)
RAFT	Reversible addition-fragmentation chain transfer
RIG	Refractive-index grating
rpm	Revolution per minute
SAM	Self-assembled monolayer
SBS	Polystyrene-*b*-polybutadiene-*b*-polystyrene
SEM	Scanning electronic microscopy
SOG	Spin on glass
SP	Spyropyran
SRG	Surface relief grating
SSL	Strong segregation limit
TEM	Transmission electron microscopy
TFA	Trifluoroacetic acid
Tg	Glass-transition temperature
THF	Tetrahydrofuran
TsCl	Tosyl chloride
UV	Ultraviolet
Vis	Visible
VUV	Vacuum ultraviolet
WSL	Weak segregation limit

CHAPTER
ONE

INTRODUCTION

Abstract

Block copolymers are quite fascinating tools as they are able to self-assemble into well-organized structures at the nanoscale. The principle underpinning such an amazing behavior is a phase separation process which remains limited in space and is called microphase separation. Depending on some parameters, such as the incompatibility and the composition of the polymer blocks, several types of morphologies are available (spheres, cylinders,...). They can be further used to produce a wide range of nano and microstructured materials such as nanoparticles, nanoporous materials. This introduction chapter settles some basic principles of block copolymer self-assembly whether it happens in bulk, in thin films or in solution. In addition, some elements of photochemistry are also discussed as this thesis deals with photo-responsive block copolymers. The question of what is light and its interplay with matter from a chemist's point of view is approached at the end of this introductive chapter.

1.1 What are block copolymers?

Polymers are formed by an ensemble of macromolecular chains constituted of a large number of repetitive units called *monomers*. While homopolymers are made of only one type of monomer, copolymers are characterized by several of them. In the case of block copolymers, blocks (or sequences) of different polymerized monomers are linked together through a covalent bond. Among them, the AB linear diblock is the simpliest encountered and consists of two different linear homopolymers (so-called A and B) linked end to end. The number of the different sequences, their composition and the way they are linked to each other can be controlled by the synthetic procedure, and a wide range of architectures or topologies, can be achieved, *e. g.*, linear, branched, star-like or cyclic (Figure 1.1).

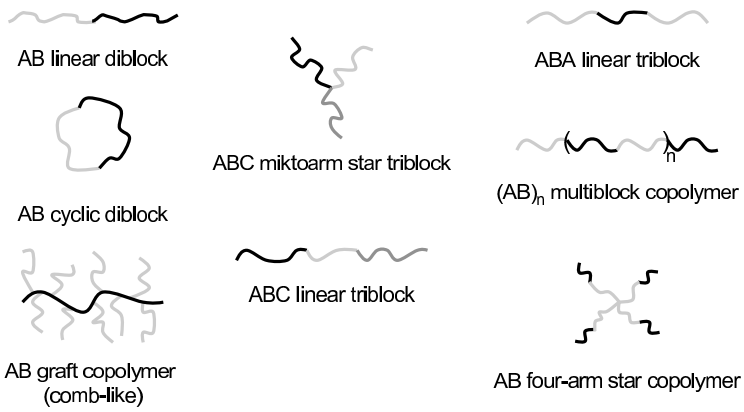

Figure 1.1: Typical architectures of block copolymers. Reproduced from Ref. [1]

Since the beginning of the science of block copolymers, the method of choice for their preparation is living anionic polymerization [2, 3]. In this technique, the polymer chain grows by the addition of monomers to the anionic reactive chain end. One drawback of this technique is the extreme reactivity of the anionic species towards interfering electrophiles (such as carbon dioxide, oxygen, water, etc.) which imposes the use of extra-pure chemicals and solvents as well as special glassware. In the

1990's, controlled-radical polymerizations (CRPs) emerged as powerful tools for the preparation of well-defined polymers, block copolymers, and other type of architectures with narrow molar mass distributions. They widely contributed to the spreading of block copolymer science because they are less sensitive than the traditional anionic polymerizations.

The success story of block copolymers stems from their self-assembly properties leading to materials with a structural organization in the range of the nanometer. Such *nano* materials have a wide number of (potential) applications. For instance, in the bulk and the rubbery state, they are industrially used as thermoplastic elastomer for impact modification and compatibilization. When organized in thin films, their potentials as nano-templates, nano-lithographic masks, nano-filtration membranes, make them of great interest in microelectronics and biofiltration. On the other side, block copolymers can self-assemble in solution into micelles and vesicles which can be used as drug carriers or for cosmetic applications. In regards, to the number of the resulting applications, the field of block copolymers seems to be endless and only limited by our mind. As a result, a lot of books and reviews are dedicated to this science and some references are given here [4–19].

1.2 Tools for block copolymer synthesis

1.2.1 Controlled radical polymerizations

Controlled radical polymerizations (CRPs) are radical chain growth polymerizations in which transfer and termination reactions are limited (controlled) by the establishment of a dynamic equilibrium between the growing free radicals and dormant species (Figure 1.2). This equilibrium, displaced towards the dormant species, decreases drastically the concentration in free radicals and, in turn, the rate of propagation overcomes largely the rate of the transfer and termination side reactions. Three main types of CRPs, based on the type of dormant species, are commonly used: reversible addition-fragmentation chain transfer (RAFT) based on thiocarbonylthio type compounds [20–23], atom transfer radical polymerization (ATRP) involving alkyl halide dormant species [24], and nitroxide-mediated polymerization (NMP) making use of alkoxyamines [25]. Further details on ATRP and RAFT processes are giving in the two next sections as they have been the synthetic

tools used during the thesis.

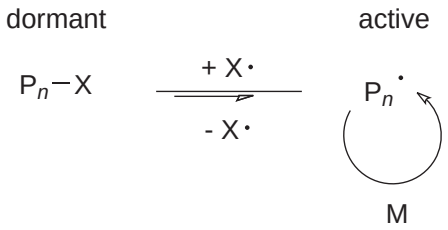

Figure 1.2: Equilibrium between the dormant species (P_n-X) and the active free radicals ($P_n^{\bullet}$) of the growing polymeric chain in controlled radical polymerizations. X stands for the controlling agent and M for the monomers.

1.2.1.1 Highlights on the ATRP process

As already mentioned, ATRP stands for *atom transfer radical polymerization* and is one of the most versatile chain-growth polymerization technique [24, 26]. Monomer derivatives of styrene, (meth)acrylamide, (meth)acrylate, and acrylonitrile have been successfully polymerized by ATRP and a wide range of polymeric architectures can be reached by this technique.

ATRP relies on the establishement of a redox equilibrium between active and dormant radical species. This equilibrium is mediated by a metal-ligand complex. Several transition metals are able to catalyze ATRP but the more efficient in terms of versatility and cost is copper (I). Copper bromide (CuBr) and chloride (CuCl) are usually used in association with bidentate or tridentate nitrogen ligands such as bipyridine (bpy) and PMDETA[1]. The role of the ligand is not only to solubilize the metal salt but also to adjust the redox potential of the catalyst thereby changing its (re)activity.

Figure 1.3 depicts the mechanism of ATRP polymerization catalyzed by a copper halide salt (CuX). The process starts with the formation of free radicals ($R^{\bullet}$) able to react with the first monomer unit (initiation).

[1]PMDETA = N,N,N',N",N"-pentamethyldiethylenetriamine

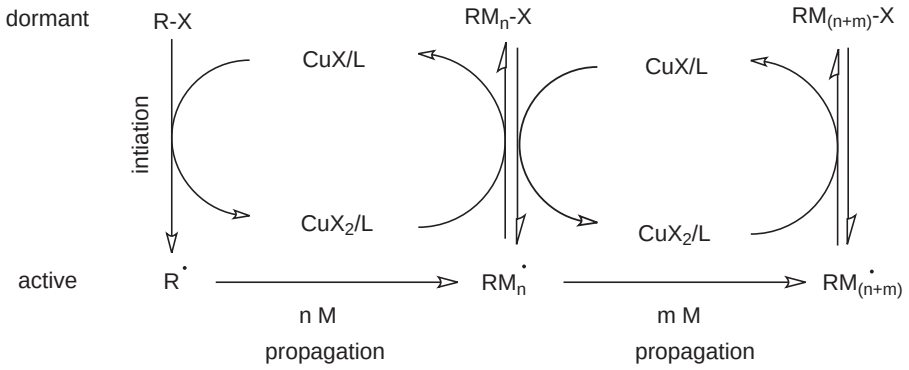

Figure 1.3: Mechanism of ATRP catalyzed by copper halides.

These radicals are formed by the reduction of alkyl halide initiators (RX) by Cu^{I} (CuX) which is in turn oxidized in Cu^{II}. During the propagation step, CuX_2 will transfer one halide back to the free radical of the growing chains, leading to dormant species (RM_n-X). Those inactive dormant chains will be re-activated by a second reduction step as Cu^{I} has been regenerated through the formation of dormant species. The monomer addition starts again and those successive oxydo-reduction cycles are controlling the process all over the polymerization reaction. The redox equilibrium established between the active and dormant species enables to decrease significally the rate of propagation in comparaison to the rate of initiation, to decrease dramatically the concentration in free radicals and consequently to limit the transfer and termination reactions. These two points are characteristic of a *controlled* polymerization.

1.2.1.2 Highlights on the RAFT process

As for ATRP, *Reversible addition-fragmentation chain transfer* polymerization (RAFT) is based on the establishement on an equilibrium between active and dormant species. In the case of RAFT polymerization, that equilibrium is mediated by chain transfer agents (CTAs) which are usually dithioester compounds. RAFT is able to polymerize a wide range of monomers such as styrene, methacrylates or acrylates. However, contrary to ATRP, this polymerization technique is a fully organic system, which makes the polymerization of amino and carboxylic

acid containing monomers easier as no competitive complexation with a metal catalyst can take place. Moreover, RAFT allows to work at lower temperature (60-80 °C) and is also water tolerant. Polymerization in water or in emulsion are thus possible.

Figure 5.4 shows the mechanism of RAFT polymerizations. A traditional initiation step allows the start of the polymerization of the first monomer units (1st initiation). The growing chain will quickly reacts with the C=S bond of the CTA leading to the intermediate I_1 followed by its reversible fragmentation either toward the initial growing chain ($M_m^{\bullet}$) or to the corresponding macro-CTA and radical $R^{\bullet}$ (1st addition-fragmentation). A second initiation step occurs due to the presence of $R^{\bullet}$ leading to other growing chains ($M_n^{\bullet}$). In that manner, the initial CTA will be entirely consumed leading to the main equilibrium described in Figure 5.4 between macro-CTAs and free-radical growing chains. That equilibrium allows to all the chains to grow at the same rate leading to polymers with narrow molar mass distribution.

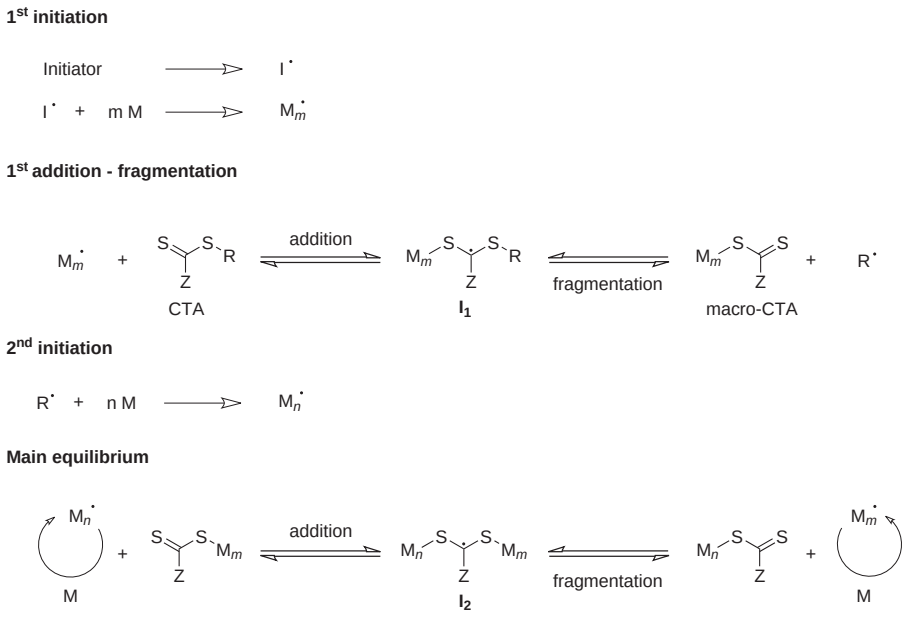

Figure 1.4: Mechanism of RAFT polymerization.

1.2.2 The CuAAC-click reaction

Beside polymerization techniques, one recent emerging tool for the formation of polymer architectures is the copper(I) azide-alkyne cycloaddition (CuAAC) click reaction. Click chemistry is a concept introduced by Sharpless and coworkers in 2001 which groups together fast and reliable reactions for the synthesis of useful new substances and combinatorial libraries [27]. The authors have settled a set of stringent criteria that the reactions need to fulfil to be qualified as click reactions. They have to be *modular, wide in scope, give very high yields, generate only inoffencive byproducts that can be removed by non-chomatographic methods, and be stereospecific* [27]. Among them, the well-known Huisgen 1,3-dipolar cycloaddition is a powerful reaction which enables to couple two molecules bearing, respectively, an azide function and an triple bond, leading to a triazole link. However, this reaction requires elevated temperature and usually leads to a mixture of the 1,4 and 1,5 regioisomers.

In 2002, this reaction proved to be efficiently catalyzed by copper(I) at room temperature leading exclusively to the 1,4 regioisomer [27, 28]. Since then, in less than ten years, this copper(I)-catalyzed azide-alkyne cycloaddition (CuAAC) has been extensively and widely used in organic synthesis [29–31] as well as in polymer synthesis [32–37].

Figure 1.5 presents the most commonly accepted mechanism for the CuAAC-click reaction. The real mechanism remains actually quite unclear and may certainly involves catalytic species with two or more metal atoms [30]. The first step (**a**) of the catalytic cycle is the formation of the Cu^{I} acetylide **2** from the alkyne **1** followed by the complexation of the copper center by the azide (**b**). The triazolide **5**, leading to the final product **6**, is presumably reached through the formation of a six membered metallacycle **4**. The mechanism is thus not concerted compared with the thermal and uncatalysed Huisgen 1,3-cycladdition.

Making use of CuAAC-click reaction and ATRP polymerization in the same synthetic plan has not been firstly thought as a possible one-pot process but as two powerful tools to reach the desired polymer architectures [38–49]. Indeed, ATRP polymerization was chosen because it enables the easy introduction of functional groups such as azides and alkynes which are the coupling reagents for the highly efficient CuAAC-click reaction.

As CuAAC-click reaction and ATRP polymerization make use of the same copper(I) catalyst, the idea of combining both reactions in a one-pot step emerged [48, 50–54]. Among them, tandem and simultaneous one-pot reactions can be distinguished. In both cases, the click and the ATRP are carried out in the same reaction vessel. However, while in the latter, both of the reactions are performed in the same time (simultaneously) [52–55], in the former, one reaction is performed before the other one either by adding one reagent after the first reaction is completed [50], or by clicking first at room temperature and then polymerizing after an increase of temperature [51].

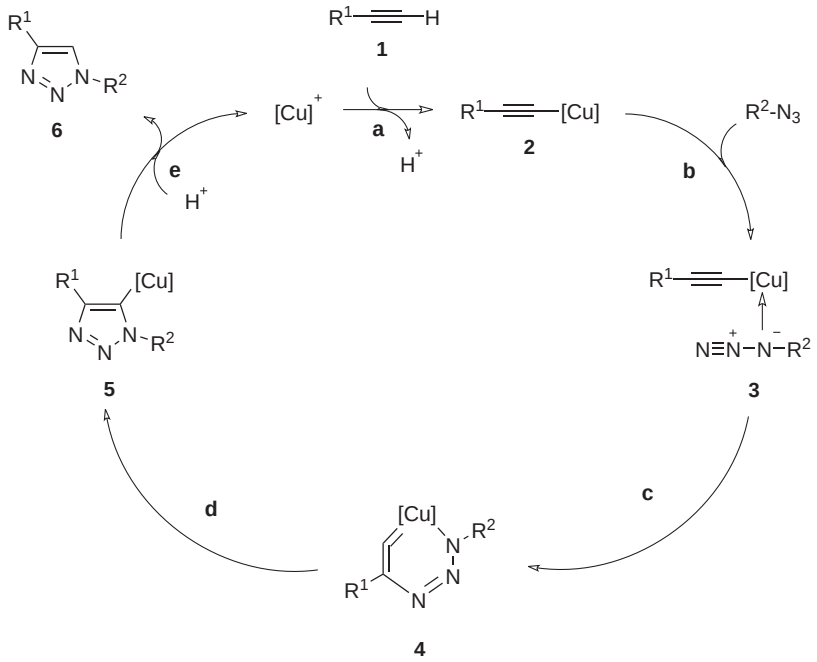

Figure 1.5: Simplified mechanism of the CuAAC click reaction.

1.3 Focus on the self-assembly of block copolymers

As previously introduced, the interest on block copolymers stems from their ability to self-assemble into periodic nanoscale structures. Self-assembly can be defined as *the autonomous organization of components into patterns or structures without human intervention* [56]. This definition is quite simple but also somehow hazy and can lead to some overuses. In order to avoid any misleading interpretation, we rely on the specifications given by Whitesides *et al.* who limit the term *self-assembly* to processes that involve pre-existing components, that are reversible, and that can be controlled by a proper design of the components [56].

In the case of block copolymers, the self-organization is the consequence of a microphase separation process due to, firstly, the inherent immiscibility of the majority of polymer blocks and to, secondly, the existence of a link between the different blocks. While the former induces the phase separation, the latter keeps the process limited in space. As a result, no macrophase separation occurs and the formation of a wide range of mesoscopic patterns can be observed either in the bulk or in solution (see Figure 1.6).

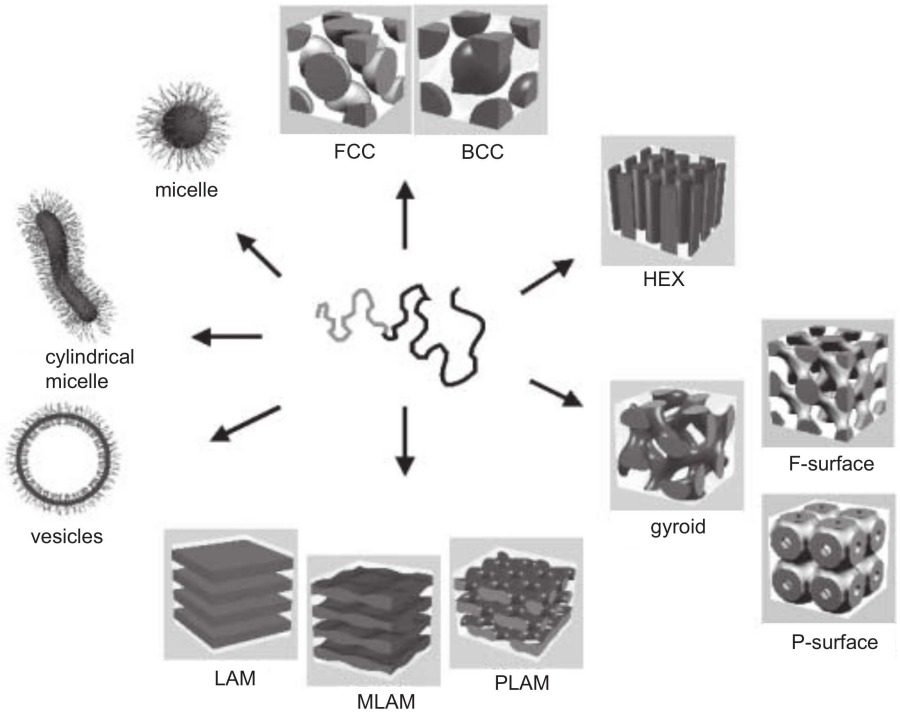

Figure 1.6: Typical self-organized structures obtained from block copolymers: spherical and cylindrical micelles, vesicles, face and body centered cubic packed spheres (FCC, BCC), hexagonally packed cylinders (HEX), various minimal surfaces (gyroid, F surface, P surface), simple lamellae (LAM), as well as modulated and perforated lamellae (MLAM, PLAM). Reproduced form Ref. [57].

1.3.1 In bulk

In bulk, block copolymers are usually observed in a microphase separated state [4, 11, 18, 58–60]. Their behavior is governed by thermodynamics and phase separation occurs spontaneously when the free energy of mixing of the system is positive ($\Delta G_m > 0$).

The free energy of mixing is defined as :

$$\Delta G_m = \Delta H_m - T\Delta S_m \tag{1.1}$$

where ΔH_m is the enthalpy of mixing and ΔS_m is the entropy of mixing [61].

Unless specific attraction interactions such as hydrogen bonding occur, the enthalpy never favors the mixing ($\Delta H_m > 0$). On the other hand, the blending is always entropically favoured as a greater disorder is achieved after mixing ($\Delta S_m > 0$). In that manner, mixing is observed when the entropic gain balances the repulsion of the molecules:

$$T\Delta S_m > \Delta H_m \tag{1.2}$$

In the case of polymers, the relation is often balanced towards phase separation ($\Delta G_m > 0$) due to low entropic contributions resulting from the constrains on chain configuration ($T\Delta S_m < \Delta H_m$) .

The phase separation can be rationalized by the reduced parameter χN, where χ is the Flory-Huggins interaction parameter and, N is the total degree of polymerization of the copolymer. The enthalpic contribution is represented by the Flory-Huggins parameter, which is based on the incompatibility of repeating units, while the degree of polymerization N reflects the entropy. In that manner, phase separation is favoured by increasing the degree of polymerization and by decreasing the temperature as the parameter χ is found to be inversely proportional to the temperature (see eq. 1.3).

$$\Delta G_m \propto \chi N \propto \frac{1}{\mathrm{T}} N \tag{1.3}$$

For block copolymers, the macrophase separation is prevented by the covalent bonds holding the blocks together. This leads to a microphase

segregation, in which a separation of the components into nanoscale domains occurs below this order-disorder transition (ODT) (Figure 1.7).

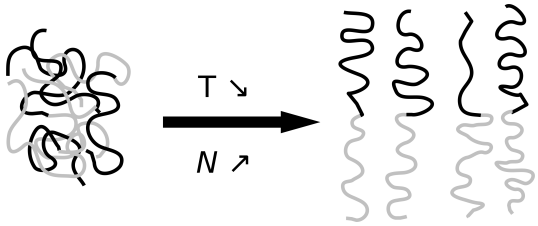

Figure 1.7: Influence of temperature (T) and of the total degree of polymerization (N) on the microphase separation in the bulk state.

The microphase separation is also affected by the composition of the copolymer, *i. e.* the volume fraction f of the blocks. To each volume fraction f corresponds a critical value of χN which determines the ODT. A phase diagram, predicting which nano-structures are accessed, can be formed by plotting χN versus f. Figure 1.8 illustrates the theoretical phase diagram for diblock copolymers [57]. For a symmetric diblock copolymer ($f = 0.5$), the $(\chi N)_{\mathrm{ODT}} = 10.5$. Below that value, the blocks are entirely miscible regardless of the composition. Above that limit, the separation occurs and nano-structures begin to appear. Depending on the value of χN, three regimes describing the phase separation are distinguished: the weak segregation limit (WSL) with $\chi N \approx$ 10-12, the intermediate segregation limit (ISL) with $12 \lessapprox \chi N \lessapprox 100$ and the strong segregation limit (SSL) with $\chi N > 100$.

Symmetric block copolymers form lamellar phases (LAM), with alternating layers of the constituent block. When the block copolymer becomes more asymmetric, it becomes energetically more favorable to form curved phases. Indeed, the shape of those structures are determined by the interfacial mean curvature that lowers the surface of the interface. On increasing f of one component, the following sequence of morphologies appeared: gyroid phase, hexagonally packed cylinders (HEX) cylinders and body centered cubic packed spheres (BCC).

The nanostructures and their stability are depending on the three regimes described above and the higher the value of χN is, the more stable will be the structure. Indeed, for high χN , block copolymers adopt a sharp interface between strongly stretched blocks in different microdomains (SSL), while for low χN, there is broad interphase between the two microdomains (WSL). In the WSL and ISL, other morphologies such as perforated layers or closed packed spheres are possible but are also less stable and more difficult to achieve. Most of the experimental work has been performed in the SSL regime. In that regime, the segregation occurs for almost all compositions and it is commonly assumed that only the three classical morphologies BCC, HEX and LAM are stable. Moreover, and thanks to phase diagrams, one can specifically adjust the morphologies by changing the composition and the chain length of block copolymers leading to tailormade nanostructured materials.

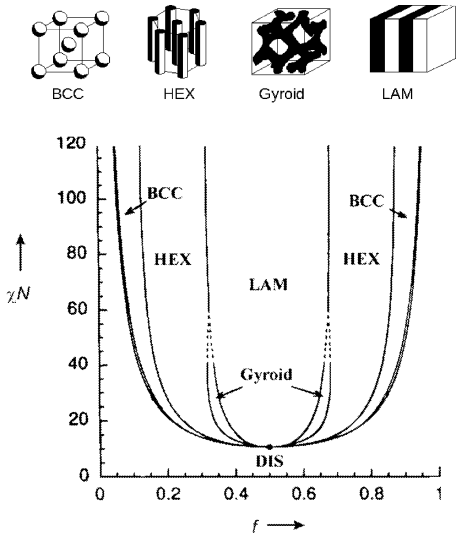

Figure 1.8: Theoretical phase diagram of diblock copolymers (down) with the representation of the four main morphologies (top). BBC, HEX, LAM and Dis stand respectively for body centered cubic packed spheres, hexagonally packed cylinders, simple lamellae and disordered phase. Reproduced form Ref. [18] and [57].

1.3.2 In thin films

Block copolymer thin films are polymer layers with thickness equal to or less than 1 μm. There are usually made through spin-coating or dip-coating from diluted solutions of copolymers and are of great interest due to the possibility of obtaining highly ordered two-dimensional patterns at the nanoscale. For instance, self-assembled block copolymers are used as lithographic masks, in order to transfer nanoscale patterns into a desired material. Such applications are useful in the semiconductor industry where the need of higher bit density is always increasing. By loading microdomains with nanoparticles or catalysts, block copolymer thin films are also developed for nanofabrication and nanoreactors. After self-assembly and removal of one sacrificial domains, nanoporous materials are obtained and can be used for nanofiltration and other templating applications [8, 9, 18, 19, 62].

The presence of defects in domain orientations and long-range order is however one of the main limitation for industrial applications. In order to reduced them, annealing is often used. Such a treatment enables the reorganization of the polymer chains in a structure close to the thermodynamic equilibrium morphology. Thermal annealing is the most used and consists in heating the films between the T_g and T_{ODT} of the constituents. The use of plasticizers such as solvent vapors or supercritical CO_2 are alternative to thermal annealing [63].

1.3.2.1 Interface and confinement effects

As in the bulk state, the behavior of block copolymers in thin films is governed by molecular weight, Flory-Huggins interaction parameters, temperature and volume fraction of each component. However, two additional factors play an important role in the case of thin films: interfacial interactions (film/superstrate and film/substrate) and geometrical constraints induced by confinement (thickness). These additional parameters play on the morphology and on the orientation of the microdomains resulting in a higher variety of structures and a better periodicity than in the bulk state [9, 15, 63–65].

In general, microdomains of diblock copolymers are orientated parallel to the substrate because of preferential interactions between one of the components and one interface (Figure 1.9, (a)) [66]. When those

interactions are removed, *i. e.* when the interfacial tensions (γ) between the different blocks and the substrate (or the superstrate) are the same, the microdomains orient perpendicular to the substrate (Figure 1.9, (b)) [18, 67–69]. This effect has been nicely demonstrated by Hawker and coworkers by controlling the orientation of the lamellar domains in a thin film made from a polystyrene-*block*-poly(methylmethacrylate) (PS-*b*-PMMA) diblock copolymer [70]. The authors showed that in the absence of any control at the film/air interface, the lamellae orient parallel to the air surface due to the lower surface energy of the polystyrene block. On the contrary, when the film was confined between two non-preferential surfaces, the alignment of the lamellae was normal to the surface. The non-preferential surfaces were made of a random (r) copolymer composed of the same monomeric units as the diblock (PS-*r*-PMMA).

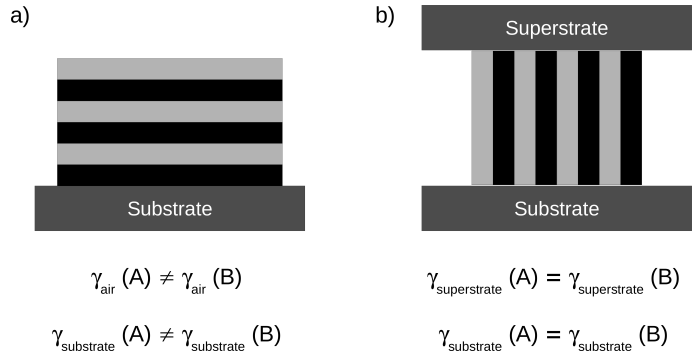

Figure 1.9: Influence of the interface on the orientation of lamellar microdomains for an AB diblock. With (a) and without (b) preferential interactions. γ = interfacial tension.

Besides the interfacial interactions, the block copolymer confinement plays also a great role as it was clearly shown by Knoll *et al.* in 2002 [71]. A polystyrene-*block*-polybutadiene-*block*-polystyrene (SBS) triblock was spin-coated onto a silicon substrate and subsequently annealed in chloroform vapors. The annealing introduced variations in the height of the film and the morphology revealed to be thickness dependent (Figure 1.10). At the thinnest parts of the film (10 nm), no lateral structure was observed. This is explained by the existence of, either a disordered

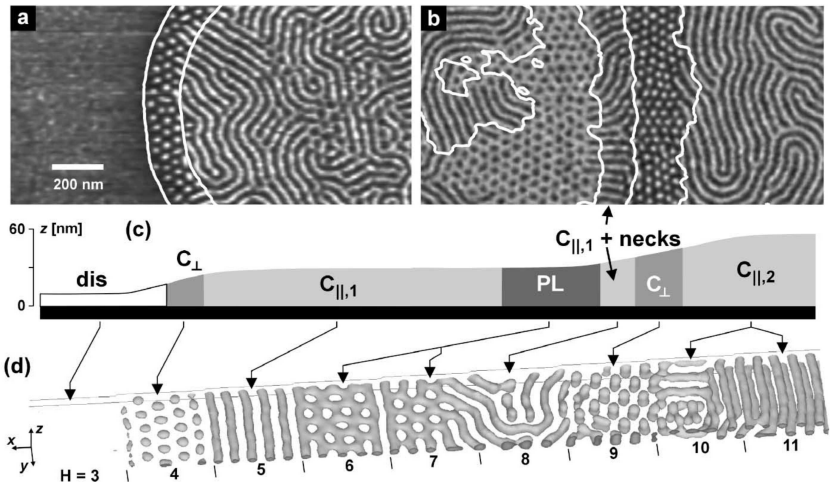

Figure 1.10: Influence of the thickness on block copolymers morphology. Tapping-mode atomic force microscopy (AFM) phase pictures (a and b) of two thin films of SBS with different initial thickness after solvent annealing showing a sequence of phases as a function of the height profile (c). Simulation profile of the same triblock copolymer film (d). Reproduced from Ref. [71].

phase (dis) or a lamellar wetting layer. With thickness increasing, the following morphologies were found: hexagonal pattern of PS cylinders oriented perpendicularly to the surface ($C_\perp$), PS cylinders parallel to the substrate ($C_\parallel$), perforated lamellae (PL), $C_\perp$ again and finally, two layers of $C_\parallel$.

1.3.2.2 Control of the orientation and of the long range order

Playing on the nature of the interfaces and/or on the thickness has proved to be efficient for controlling the morphology and/or orientation of the microdomains in thin films. In addition to the previously discussed annealing processes, preferential or non-preferential wettings and thickness variations, other methods based on the application of external fields and on specific film-surface interactions have been developed. In this respect, the orientation of polymeric domains in thin films can be controlled by applying to the sample external fields such as mechanical

flow fields, electric fields or gradient of solvents.

In the beginning, mechanical flow fields have been developed to induce alignment in microphase separated copolymers in the melt. Roll-casting and shear-alignment are two examples of the adaptation of flow fields to thin films [63]. Electric fields have been widely used to induce microdomains orientation in the bulk. In thin films, applying an electric field in the viscous state, but below the T_{ODT}, enables the orientation of the polymer microdomains parallel to the field lines. This behavior comes from the existence of a difference in the dielectric constants of the micro-separated phases. For example, Thurn-Albrecht *et al.* studied the orientation of PS-*b*-PMMA microdomains perpendicularly to the substrate in order to use them as nanowire templates after removal of the PMMA phase (see below section 1.3.2.3) [72, 73]. With electric fields, the orientation is a consequence of the interaction between the electrical fields and a change in the dielectric constant in the material.

Another method to orient perpendicularly the domains is the use of solvent gradients. In this technique, the solvent evaporation from the swollen film, induces a gradient of concentration which spreads from the substrate (more concentrated) to the surface (less concentrated) (Figure 1.11). The decrease in solvent content leads to the transition from the disordered to the ordered state at the surface. This transition extends afterwards towards the substrate in the opposite direction of the gradient (perpendicular orientation to the substrate). This technique has been successfully applied, for example, to thin films made from PS-*b*-PEO diblocks and PS-*b*-PMMA-*b*-PEO triblocks [74–76].

Controlling the organization within thin films is also possible by playing with surface effects. As previously shown, the presence or the absence of preferential interactions between one block and an interface can lead to the parallel or perpendicular orientation of microdomains (see section 1.3.2.1). Besides those simple effects, other methods based on specific film-surface interactions have been developed in order to orient microdomains. For block copolymers containing at least one crystallizable sequence, *epitaxy* proved to be efficient. This technique consists in an orientated growth of a crystal onto the surface of another crystal. The growth occurs in one of the crystallographic direction determined by the crystalline lattice of the substrate. One example is the crystallization

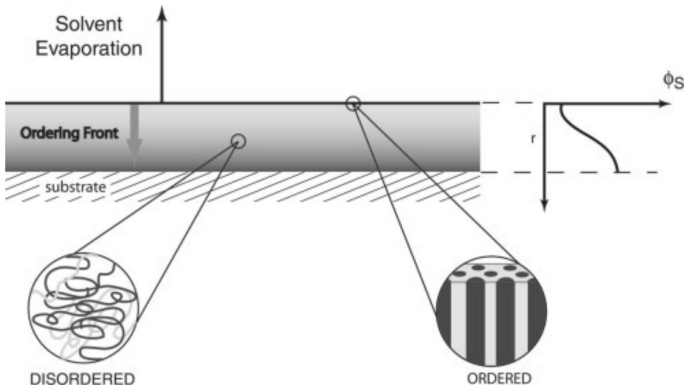

Figure 1.11: Schematic illustration of ordering in block copolymer thin films during the solvent annealing process via solvent evaporation. A solvent gradient (ϕ_S) appears trough the film thickness (r). Reproduced form Ref. [75].

of the polyethylene (PE) sequence of the triblock polyethylene-*block*-poly(ethylene-*co*-propylene)-*block*-polyethylene (PE-*b*-PEP-*b*-PE) on a crystal of benzoic acid (BA) [77]. The morphology obtained is a lamellar structure perpendicular to the crystalline substrate (Figure 1.12).

Directional crystallization also enables to orient polymeric domains and, contrary to epitaxy, this method is also applicable for non crystallizable copolymers. It consists in, firstly, solubilizing the copolymer in a crystallizable solvent. While the mixture is cooled down, the solvent crystallizes and the associated increase in concentration causes the microphase separation of the block copolymer while the orientation of the domains is determined by the fast directional growth of the solvent crystals. Two conditions are nevertheless required: the solvent has to efficiently solubilize the copolymer and must have the tendency to crystallize directionally in large crystalline areas [9, 15, 63, 78].

Another way to control the growth of polymeric crystals in thin films is the so-called g*raphoepitaxy* which uses an artificial topography of the surface of a crystalline or an amorphous substrate. A distinction has to be done between graphoepitaxy and the *templated self-assembly on nanopatterned surfaces*. Indeed, the term graphoepitaxy is used

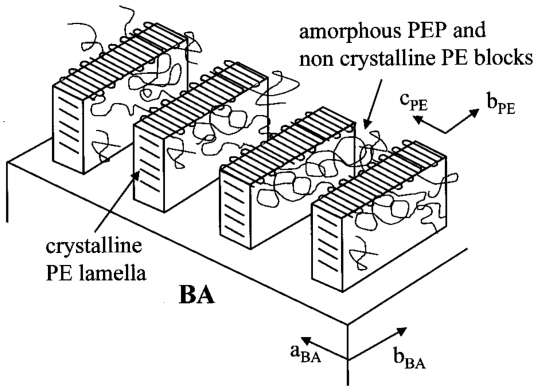

Figure 1.12: Schematic model of the lamellar structure obtained by epitaxy of PE-*b*-PEP-*b*-PE onto a benzoic acid crystal. a, b, c : crystallographic directions. Reproduced form Ref. [77].

when the morphology is controlled by a spatial confinement (in straight grooves for instance). On the other hand, templated self-assembly on nanopatterned surfaces stands for methods based on the chemical affinity for the pattern on the substrate [9, 15, 63]. For instance, Nealy and coworkers demonstrated long-range orientation of lamellae of PS-*b*-PMMA on a silicon surface covered with a nanopatterned self-assembled monolayer (SAM) (Figure 1.13). The orientation was achieved thanks to polar affinity between PMMA and the SAM [79].

The development of methods which allow the control over the alignment of microdomains is driven by the high potentials of block copolymers in nanotechnological applications. The current trend is to combine different methods in order to tend to zero defect structures.

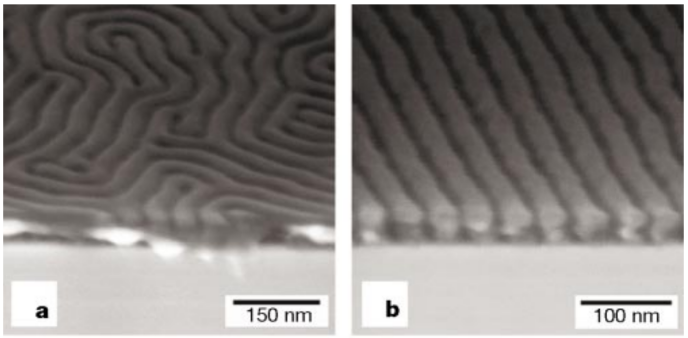

Figure 1.13: Cross-sectional SEM pictures of PS-*b*-PMMA on unpatterned (a) and chemically nanopatterned (b) surfaces. Reproduced form Ref. [79].

1.3.2.3 Applications

In a near future, block copolymers will undoubtedly play a major role in nanotechnology. In order to illustrate the potentials of block copolymers thin films, three representative examples of potential applications are presented here. For further information on the topic, the reader is invited to consult the non exhaustive references given here [8,9,18,19,62].

The first example of application deals with the fabrication of nanowires and was published in 2000 by Russell and coworkers [73]. The authors presented the formation of magnetic nanowires of cobalt which could be used as ultra high-density magnetic storage media. The strategy consisted in three steps as illustrated in Figure 1.14. A PS-*b*-PMMA copolymer was firstly self-assembled into perpendicular cylinders of PMMA in a PS matrix. The perpendicular orientation was controlled by applying an electrical field. The film thickness was approximately of 1 μm and the diameter of the cylinders of 14 nm. A deep ultraviolet (UV) exposure was then performed in order to degrade the PMMA and cross-link the PS. After removal of the degraded PMMA with acetic acid, a nanoporous material with vertical holes was obtained. Finally, nanowires were formed by electrodeposition of cobalt inside the pores leading to arrays of magnetic wires with a high density ($1.9 \times 10^{11} \mathrm{cm}^{-2}$).

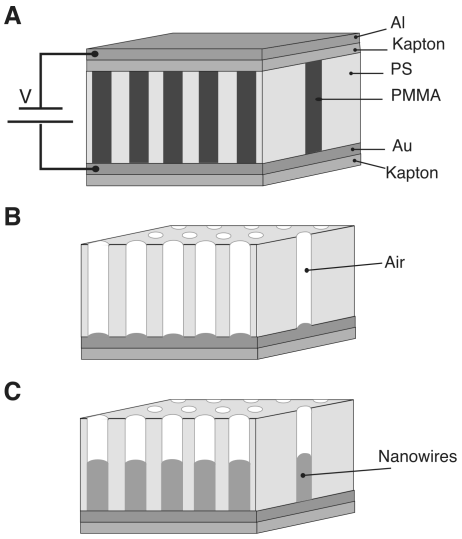

Figure 1.14: Illustration of nanowire formation from a PS-*b*-PMMA block copolymer. Block copolymer self-assembly controlled by applying an electrical field (a). Nanoporous film obtained after removal of the minor component (b). Nanowires formed by electrodeposition (c). Reproduced form Ref. [73].

Nano-magnetic materials for high density media storage can also be reached by nanolithography methods as was nicely illustrated by Naito *et al.* in 2002 [80]. A 2.5-inch hard disk drive (HDD) containing magnetic nano-dots has been produced using self-assembly of block copolymers (Figure 1.15, a and b). The preparation of this media started with a glass disk covered with a magnetic film made of a mixture of cobalt and platinum (Figure 1.15, c). The disk was then pressed with a nickel master possessing spiralic patterns. The resulting material contained grooves with a height of 110 nm and different width (from 100 to 250 nm). The imprinted grooves were filled with PS-*b*-PMMA and, after annealing, a self-assembled PMMA-dot structure was obtained. The PMMA was then selectively removed by oxygen plasma treatement and the resulting holes were filled by spin-on-glass (SOG)[2]. Finally, the un-

[2]Spin-on-glass (SOG) is a mixture of silicates and dopants (either boron or phosphorous) that is suspended in a solvent solution and is used in microelectronics as a planarizing dielectric for the fabrication of integrated circuits.

derlying magnetic film was patterned by ion milling using the SOG as a mask.

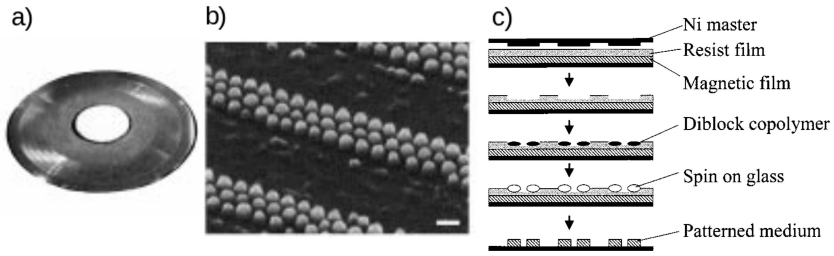

Figure 1.15: 2.5-inch HDD patterned medium prepared by self-assembly of PS-*b*-PMMA. Picture of the whole disk (a). SEM picture of the magnetic medium with 40 nm diameter dots; scale: 100 nm (b). Schematic preparation of the magnetic disk (c). Reproduced from Ref. [80].

Block copolymer thin films not only find applications in microelectronics, but in biomedical sciences too. For instance, the following example describes the use of nanoporous thin film as filtration membrane for the separation of viral solutions [81]. The schematic preparation of such membranes is depicted in Figure 1.16. The starting point was a thin film made of a self-assembled blend of PS-*b*-PMMA and homo-PMMA (Figure 1.16, a). The film exhibited PMMA cylinders oriented normal to the substrate and the homo-PMMA was found to be mixed within the PMMA microdomains of the block copolymers.

The film was prepared on a silicon substrate presenting a silicon oxide top layer allowing the transfer of the film onto a supporting membrane, after an exposure to hydrofluoric acid (HF). Indeed, the HF treatement destroyed the silicon oxide layer detaching the thin film from its silicon substrate (Figure 1.16, b). As block copolymer thin films were relatively brittle, the supporting membrane provides enough mechanical strength for further applications. Washing the membrane with acetic acid yielded porosity in the thin film as it selectively removed the homo-PMMA from the microdomains (Figure 1.16, c). The final membrane was made of well-ordered arrays of about 15 nm diameter pores which completely

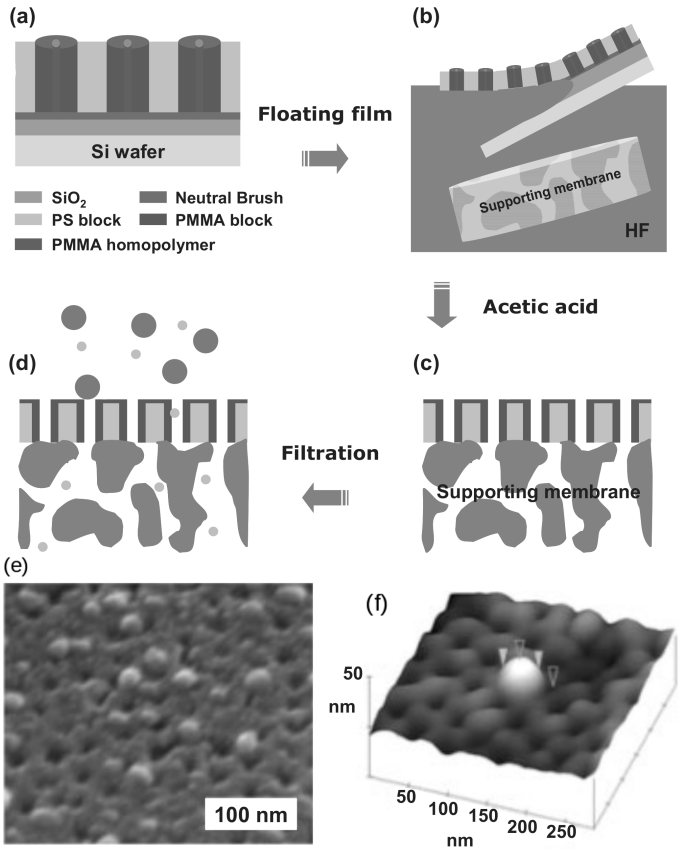

Figure 1.16: Fabrication of nanoporous membranes for nanoseparation. Schematic procedure for their preparation (a-d). SEM (e) and AFM (f) Pictures of the membrane surface after filtration of a solution containing HRV-14 rhinoviruses. Reproduced form Ref. [81].

prevent the penetration of HRV-14 rhinoviruses in the pores (virus size = 30 nm). On the contrary, proteins, such as bovine serum albumin (BSA), are able to freely pass through the pores of the membrane (BSA size = 7.2 nm) (Figure 1.16, d).

1.3.3 In solution

When dissolved in a selective solvent, block copolymers may self-assemble into micellar aggregates [4,13,18]. A selective solvent is defined as a thermodynamically good solvent for one block and a precipitant for the other one. Due to that incompatibility, the insoluble, or poorly solvated polymer sequences will associate to form a *core*, while the soluble blocks will spread out in the solution forming the so-called *corona* which will stabilize the core (Figure 1.17). Although this behavior is often described for water solution of amphiphilic block copolymers, micellar behavior is not limited to aqueous medium and is also observed in organic solvents. Micellization is an association process leading to a dynamic equilibrium between micelles and free copolymer chains called *unimers*. However, the obtained structures can be kinetically frozen and may not represent the thermodynamic equilibrium. This is the case when micelles display a core made of a polymer block possessing a high glass transition temperature (T_g) such as polystyrene for example.

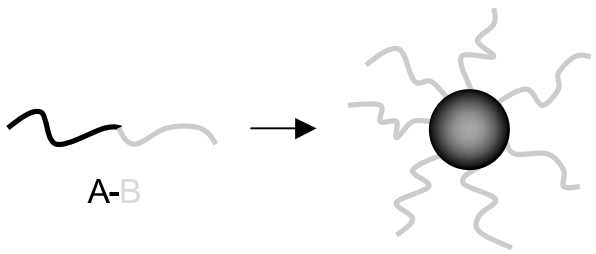

Figure 1.17: Schematic representation of a micelle made from a AB-diblock. Reproduced form Ref. [1].

The behavior of block copolymers in solution is characterized by several parameters. The first one is the *critical micellar concentration* (CMC) which rules the micellization process (Figure 1.18). Below that concentration, no micelles are observed, while above it micellization oc-

curs. For a given temperature, the CMC is thus defined as the concentration in block copolymers for which the first micelle is formed. Likewise, for a given concentration, a *critical micellar temperature* (CMT) characterizes micellar systems too. In that case, micellization can occur above or below the CMT depending on whether the self-assembly process is endothermic or exothermic, respectively. At higher concentration, above a *critical gel concentration* (CGC), micelles can order into a lattice and show gel behaviors (Figure 1.18).

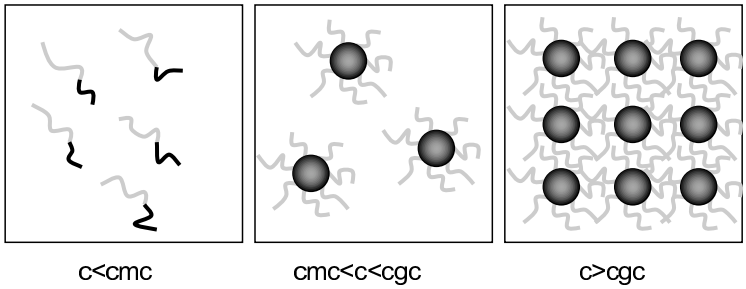

Figure 1.18: Theoretical phase diagram of diblock copolymers. Reproduced form Ref. [1].

Like in the solid state, the self-assembly of block copolymers in solution may display different morphologies. The main three are schematically represented in Figure 1.6 (spherical micelle, cylindrical micelle and vesicle). Discher and al. proposed a rule based on the mass fraction of the hydrophilic block to the total mass of the copolymer, $f_{hydrophilic}$. For $f_{hydrophilic} > 45\%$ spherical micelles are expected while rod-like micelles are observed for $f_{hydrophilic} < 50\%$. Vesicles are formed for $f_{hydrophilic} \sim 35\%$ and finally inverted microstructures such as large compound micelles are observed for $f_{hydrophilic} < 25\%$ [82]. This general rule should be seen as a trendline, because it is based on the study of mainly two systems (PEO-*b*-PBD and PEO-*b*-PEE)[3]. Moreover the sensitivity of the morphologies to chemical composition and to molecular weight has not yet been fully probed. Finally, block copolymer micelles find possible applications mainly as drug carrier [83, 84] and as template for nanoparticle synthesis [85–87].

[3]PBD=polybutadiene; PEE=poly(ethylethylene)

1.4 Elements of photochemistry

This thesis deals with block copolymers that can cleave through illumination with appropriate light. In order to understand how it works, some elements of photochemistry are explained in this section [88–90]. Concerning the use of light as stimulus in block copolymers in particular, a full chapter reviews the different photo-responsive moieties that have been so far incorporated in block copolymers and some of their potential applications (see chapter two).

1.4.1 Wave-particle duality of light

For a long time scientists were wondering whether light acted as a particle or a wave. This debate on the nature of light ended in the first part of the 20^{th} century with the concept of *wave-particle duality*. It was demonstrated that light is an electromagnetical wave characterized by a wavelength λ and a frequency ν such as:

$$\lambda\nu = c \tag{1.4}$$

where c is the velocity of light. Meanwhile, light can also be seen as a flow of particles called *photons* that possess an energy E being proportional to frequency according to

$$E = h\nu \tag{1.5}$$

where h is Planck's constant. By combining eq. 1.4 and eq. 1.5, the energy is found to be inversely proportional to the wavelength:

$$E = hc/\lambda \tag{1.6}$$

The theory of relativity states the equivalence between mass (m) and energy:

$$E = mc^2 \tag{1.7}$$

By combining the equation which relates energy and frequency (eq. 1.5) with that of energy and mass (eq. 1.7), the fundamental equation of De Broglie (eq. 1.9) is obtained:

$$E = h\nu = mc^2 \tag{1.8}$$

$$\Downarrow$$

$$\lambda = h/p \tag{1.9}$$

where $p = mc$. This relationship provides the bridge over corpuscular physics and wave physics since the momentum p is then related to the wavelength λ. That equation implies deep implications since it confers a wave-particle duality behavior not only to light, but also to every particles.

1.4.2 Light and chemistry

Light displays a very broad electromagnetical spectrum and only a small portion of it gives rise to photochemistry. In order to promote chemical processes, radiations with energies similar to those of chemical bonds are needed. According to equation 1.6, such energies matches the wavelengths ranging from 100 to 1000 nm corresponding to visible (vis), near-infrared (NIR) and ultra-violet (UV) radiations (Figure 1.19). Such radiations affect the electronic state of molecules and are the basis of photochemistry. At higher energies, ionization of molecules can be obtained with vacuum ultra-violet (VUV), X-ray or γ-ray radiations, while infrared (IR) radiations confer vibrational motion to molecules at lower energies.

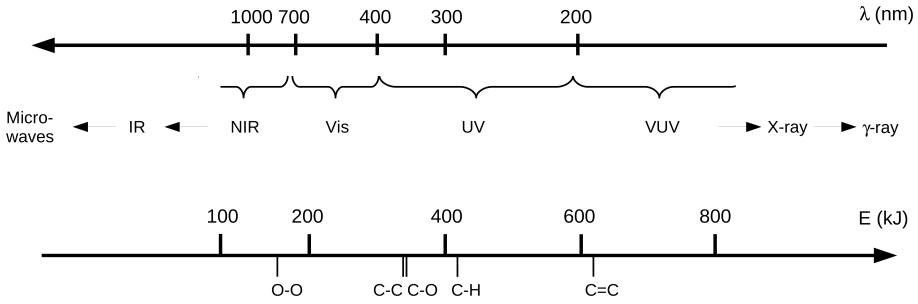

Figure 1.19: Electromagnetic continuum and energy of chemical bonding.

Photochemistry is based on a change in the electronic configuration of molecules by the absorption of one or several photons. This change does not affect directly the atomic structure of the molecule, but one or several electrons are promoted to orbitals of higher energy and molecules. Initially in a *ground* state, they reach an *excited* (E*) state by the absorption of the energy of photon(s) (Figure 1.20, a). The excited states may then lead to structural changes in the molecules and are thus the start of photochemical processes.

The exchange of energy between light and molecules results from the interaction between the oscillating electric field of light and the transition moment of the molecule. The transition moment is a transient oscillating electric field induced in the molecule by the light wave. Since the frequency of the transition moment and the light frequency are the same, resonance occurs and the exchange of energy may take place.

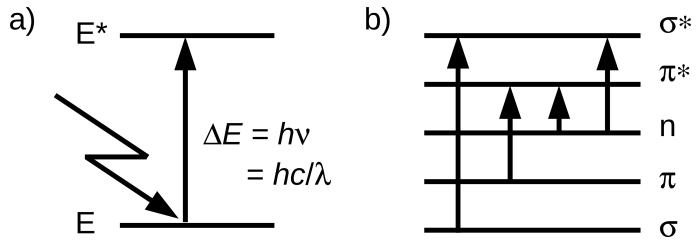

Figure 1.20: Light absorption by molecules (a) and electronic transitions in organic compounds (b).

In the ground state, electrons are only present in bonding orbitals (σ, π) or as lone pair (n). After absorption of a photon, one electron moves from an occupied molecular orbital to an unoccupied one which is an anti-bonding orbital (σ^*, π^*). Four electronic transitions are encountered in organic chemistry: $\sigma\sigma^*$, $\pi\pi^*$, $n\pi^*$, and $n\sigma^*$ (Figure 1.20, b). $\sigma\sigma^*$ transitions are generally observed in alcanes and $n\sigma^*$ in ethers and halogenated compounds while the majority of transitions are encountered in conjugated systems ($\pi\pi^*$) and in molecules with heteroatoms ($n\pi^*$).

Photochemical processes can be depicted by a state diagram such

as the well-known Jablonski diagram (Figure 1.21). The initial ground state is the singlet state S_0 and is the electronic state of the molecule with the lowest energy. The following states are S_1 and S_2 which correspond to the singlet states of $n\pi^*$ and $\pi\pi^*$ transitions. To those transitions correspond, respectively, the triplets state T_1 and T_2. These electronical states are subdivided into vibrational states (doted lines in Figure 1.21) and after the absorption of a photon, the molecule jumps to a higher state which energy corresponds exactly to that of the absorbed photon ($\Delta E = h\nu_a$).

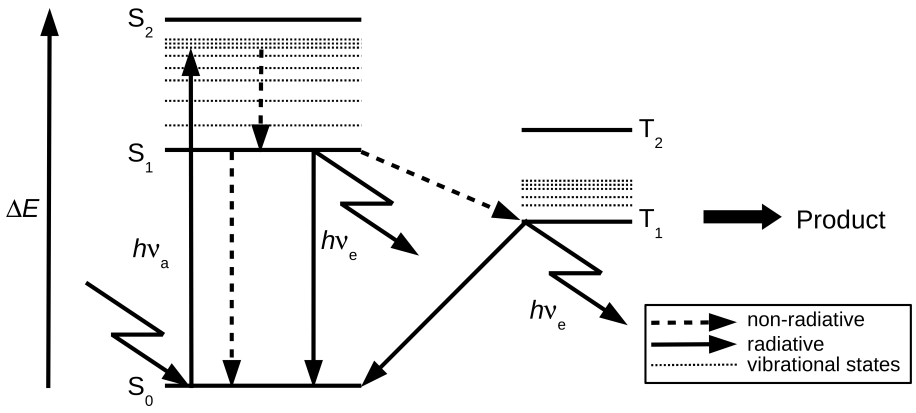

Figure 1.21: Jablonski state diagram.

As the excited states are not the most stable configurations, the system tends to return to its ground state. Different pathways are possible (Figure 1.21) and the system can decrease its energy through non-radiative or radiative relaxation. With non-radiative transitions the system reorganizes the energy of the molecule internally and eventually transfers it to the surroundings in form of heat. The molecule can also relax through the emission of a photon (luminescence). This emission takes place from the relaxed excited state S_1 (fluorescence) or T_1 (phosphorescence). A third way to reduce the excess of energy is to change the structure of the molecule leading to new products. Photochemistry deals precisely with this latter pathway.

1.4.3 Photochemistry vs thermochemistry

In chemical reactions, the path from the reagents towards the products is controlled by energetic barriers which have to be overcome in order to yield the products. The energy necessary to get over such barriers is called the activation energy (E_a) (Figure 1.22). In photochemistry, the excitation of molecules allows to start chemical transformation from excited states which are more energetic than their corresponding ground states (Figure 1.22). Starting from excited states makes then the crossing of the energetic barrier easier as the activation energy is lower or already overcome and some reactions which are not allowed in traditional chemistry (thermochemistry) are allowed in photochemistry.

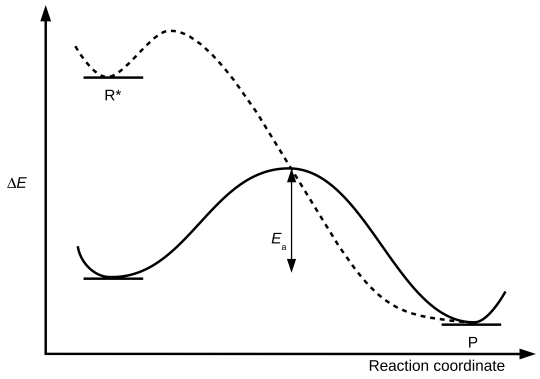

Figure 1.22: Energetic pathways from reagents (R) to products (p) in thermochemistry (solid line) and in photochemistry (dashed line). Starting from excited state (R*) enables to shortcut the thermal activation energy (E_a).

In order to illustrate this concept, the example of the *cis-trans* photoisomerization in alkenes is presented here. In alkenes, the interconversion between cis and trans isomers is not possible thermally as the presence of a double bond blocks the rotation around it. On the contrary, when alkenes are photo-excited, one electron from the bonding π orbital moves to the anti-bonding π^* orbital and the double bond character is almost reduced to zero. Consequently, rotation is made possible as the excited state can be assimilated to a single bond (Figure 1.23). The relaxation follows the potential energy surface S* where the mini-

mum corresponds to a twisted form of the molecule with the orbitals of the two unpaired electrons being orthogonal. However, this molecular shape is also that of the least stable ground state geometry. The way from the excited state to the ground state is possible by non-radiative crossing from S* to S_0 because the energy surfaces come very close together at this point.

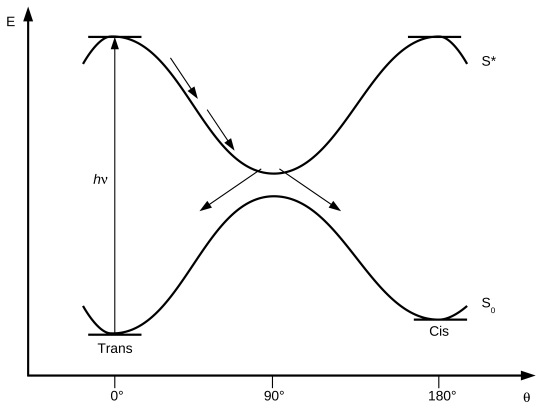

Figure 1.23: Energetic pathways for *cis-trans* photoisomerization in alkenes. The excited surface (S*) may be singlet or triplet.

As the excited states are characterized by a very high reactivity, the chemical processes are also several orders of magnitude faster than associated thermal reactions. Finally, photoactivation is highly selective as the light energy can be tuned in order to be concentrated in the target molecule while in thermal activation, everything is heated (reactor, solvent, other reagents,...).

1.5 Conclusions

Due to their intrinsic chemical composition and architecture, block copolymers are able to undergo a microphase separation allowing the obtention of well-organized structures at the nanoscale. Materials characterized by such nanostructures have a lot of potential applications in

the polymer industry, in microelectronics and for medical, biological and cosmetic applications. Those block copolymers are obtained from chain growth polymerizations and especially from controlled radical polymerization techniques.

Block copolymer self-assembly can be observed in the solid state or in solution. In the solid state, spheres, cylinders and lamellae are the typical morphologies encountered for diblocks. More complex patterns can be obtained with triblocks and with other architecture but have not been developed here. When block copolymers are processed in thin films, confinement and interface effects play also an important role and enable a better control of the morphologies and the orientation of the microdomains. Among polymer thin films, those which display a porosity are quite interesting because they can be employed as nano-filtration membranes or as templates for inorganic nanodots.

The aim of the thesis is precisely the development of a new kind of block copolymers which can lead to such nanoporous materials. The particularity of the project is to introduce photo-sensitive junctions into diblocks which can then be cleaved upon light irradiation. After self-assembly, irradiation with the appropriate light and extraction of the minor phases, those light-responsive block copolymers (LRBCs) will lead to nanoporous thin films.

Photocleavage is possible because light and matter can interact with each other through an energy transfer between light and molecules. After the absorption of a photon, the excited molecule has an excess of energy that the system tends to drain off by different kinds of relaxation, including chemical reactions such as photocleavage.

Before discussing the photocleavable block copolymers developed during the thesis and their processing into nanoporous thin films, an overview of the light-responsive block copolymers (LRBCs) that combine characteristic self-assembly of block copolymers and light-responsive systems is presented in the next chapter.

Bibliography

[1] Guillet, P. Ph.D. thesis, Université catholique de Louvain (UCL), 2008.

[2] Hadjichristidis, N.; Pitsikalis, M.; Pispas, S.; Iatrou, H. *Chem. Rev.* **2001**, *101*, 3747–3792.

[3] Baskaran, D.; Müller, A. H. E. *Prog. Polym. Sci.* **2007**, *32*, 173–219.

[4] Hamley, I. W. *The Physics of Block Copolymers*; Oxford University Press, inc., New-York, 1998.

[5] Bates, F. S.; Fredrickson, G. H. *Phys.Today* **1999**, *52*, 32–38.

[6] Hadjichristidis, N.; Pipas, S.; Floudas, G. A. *Block Copolymers: Synthetic Strategies, Physical Properties and Applications*; Wiley-Interscience, New-York, 2003.

[7] Lodge, T. P. *Macromol. Chem. Phys.* **2003**, *204*, 265–273.

[8] Hamley, I. W. *Angew. Chem. Int. Ed.* **2003**, *42*, 1692–1712.

[9] Park, C.; Yoon, J.; Thomas, E. L. *Polymer* **2003**, *44*, 6725–6760.

[10] Hadjichristidis, N.; Pitsikalis, M.; Iatrou, H. *Adv. Polym. Sci.* **2005**, *189*, 1–124.

[11] Abetz, V.; Simon, P. F. W. *Adv. Polym. Sci.* **2005**, *189*, 125–212.

[12] Muller, A. J.; Balsamo, V.; Arnal, M. L. *Adv. Polym. Sci.* **2005**, *190*, 1–63.

[13] Gohy, J. F. *Adv. Polym. Sci.* **2005**, *190*, 65–136.

[14] Hillmyer, M. A. *Adv. Polym. Sci.* **2005**, *190*, 137–181.

[15] Li, M. Q.; Coenjarts, C. A.; Ober, C. K. *Adv. Polym. Sci.* **2005**, *190*, 183–226.

[16] Darling, S. B. *Prog. Polym. Sci.* **2007**, *32*, 1152–1204.

[17] Olson, D. A.; Chen, L.; Hillmyer, M. A. *Chem. Mater.* **2008**, *20*, 869–890.

[18] Abetz, V.; Bosschetti-de Fierro, A.; Gohy, J.-F. In *Controlled and living Polymerizations*; Müller, A. H. E., Matyjaszweski, K., Eds.; Wiley-VCH, Weinheim, 2009; Chapter 9, pp 493–544.

[19] Kim, H. C.; Park, S. M.; Hinsberg, W. D. *Chem. Rev.* **2010**, *110*, 146–177.

[20] Perrier, S.; Takolpuckdee, P. *J. Polym. Sci. Part A* **2005**, *43*, 5347–5393.

[21] Moad, G.; Rizzardo, E.; Thang, S. H. *Polymer* **2008**, *49*, 1079–1131.

[22] Barner-Kowollik, C.; Perrier, S. *J. Polym. Sci. Part A* **2008**, *46*, 5715–5723.

[23] Barner-Kowollik, C. *Handbook of RAFT Polymerization*; Wiley-VCH: Weinheim, 2008.

[24] Matyjaszewski, K.; Xia, J. H. *Chem. Rev.* **2001**, *101*, 2921–2990.

[25] Hawker, C. J.; Bosman, A. W.; Harth, E. *Chem. Rev.* **2001**, *101*, 3661–3688.

[26] Kamigaito, M.; Ando, T.; Sawamoto, M. *Chem. Rev.* **2001**, *101*, 3689–3746.

[27] Kolb, H. C.; Finn, M. G.; Sharpless, K. B. *Angew. Chem. int. Ed.* **2001**, *40*, 2004–2021.

[28] Tornoe, C. W.; Cristensen, C.; Meldal, M. *J. Org. Chem.* **2002**, *67*, 3057–3064.

[29] Bock, B. D.; Hiemstra, H.; van Maarseveen, J. H. *Eur. J. Org. Chem.* **2006**, 51–68.

[30] Meldal, M.; Tornoe, C. W. *Chem. Rev.* **2008**, *108*, 2952–3015.

[31] Hein, J. E.; Fokin, V. V. *Chem. Soc. Rev.* **2010**, *39*, 1302–1315.

[32] Lutz, J.-F. *Angew. Chem. Int. Ed.* **2007**, *46*, 1018–1025.

[33] Fournier, D.; Hoogenboom, R.; Schubert, U. S. *Chem. Soc. Rev.* **2007**, *36*, 1369–1380.

[34] Binder, W. H.; Sachsenfofer, R. *Macromol. Rapid Commun.* **2007**, *28*, 15–54.

[35] Binder, W. H.; Sachsenhofer, R. *Macromol. Rapid commun.* **2008**, *29*, 952–981.

[36] Meldal, M. *Macromol. Rapid Commun.* **2008**, *29*, 1016–1051.

[37] Iha, R. K.; Wooley, K.; Nyström, A. M.; Burke, D. J.; Kade, M. J.; Hawker, C. J. *Chem. Rev.* **2009**, *109*, 5620–5686.

[38] Sumerlin, B. S.; Tsarevsky, N. V.; Louche, G.; Lee, R. Y.; Matyjaszewski, K. *Macromolecules* **2005**, *38*, 7540–7545.

[39] Lutz, J.-F.; Börner, H. G.; Weichenhan, K. *Macromol. Rapid Commun.* **2005**, *26*, 514–518.

[40] Gao, H.; Matyjaszewski, K. *Macromolecules* **2006**, *39*, 4960–4965.

[41] Laurent, B. A.; Grayson, S. M. *J. Am. Chem. Soc.* **2006**, *128*, 4238–4239.

[42] Ladmiral, V.; Mantovani, G.; Clarkson, G. J.; Cauet, S.; Irwin, J. L.; Haddleton, D. M. *J. Am. Chem. Soc.* **2006**, *128*, 4823–4830.

[43] Johnson, J. A.; Finn, M. G.; Koberstein, J. T.; Turro, N. J. *Macromolecules* **2007**, *40*, 3589–3598.

[44] Van Camp, W.; Germonpré, V.; Mespouille, L.; Dubois, P.; Goethals, E. J.; Du Prez, F. E. *React. Funct. Polym.* **2007**, *67*, 1168–1180.

[45] Gao, H.; Matyjaszweski, K. *J. Am. Chem. Soc.* **2007**, *129*, 6633–6639.

[46] Geng, J.; Mantovani, G.; Tao, L.; Nicolas, J.; Chen, G.; Wallis, R.; Mitchell, D. A.; Johnson, B. R. G.; Evans, S. D.; Haddleton, D. M. *J. Am. Chem. Soc.* **2007**, *129*, 15156–15263.

[47] Liu, Q.; Zhao, P.; Chen, Y. *J. Polym. Sci. Part A.* **2007**, *45*, 3330–3341.

[48] He, X.; Liang, L.; Xie, M.; Zhang, Y.; Lin S.,; Yan, D. *Macromol. Chem. Phys.* **2007**, *208*, 1797–1802.

[49] Urbani, C. N.; Bell, C. A.; Lonsdale, D.; Whittaker, M. R.; Monteiro, M. J. *Macromolecules* **2008**, *41*, 76–86.

[50] Mantovani, G.; Ladmiral, V.; Tao, L.; Haddleton, D. M. *Chem. Commun.* **2005**, 2089–2091.

[51] Mespouille, L.; Vachaudez, M.; Suriano, F.; Gerbaux, P.; Coulembier, O.; Degée, P.; Flammang, R.; Dubois, P. *Macromol. Rapid Commun.* **2007**, *28*, 2151–2158.

[52] Xu, Q. L.; Yao, F.; Fu, G.-D. *Macromolecules* **2009**, *42*, 6385–6392.

[53] Damiron, D.; Desorme, M.; Ostaci, R.-V.; Al Akhrass, A.; Hamaide, T.; Drockenmuller, E. *J. Polym. Sci. Part A* **2009**, *47*, 3803–3813.

[54] Zhang, Y.; Li, C.; Liu, S. *J. Polym. Sci. Part A* **2009**, *47*, 3066–3077.

[55] Geng, J.; Lindqvist, J.; Mantovani, G.; Haddleton, D. M. *Angew. Chem. Int. Ed.* **2008**, *47*, 4180–4183.

[56] Whitesides, G. M.; Grzybowski, B. *Science* **2002**, *295*, 2418–2421.

[57] Förster, S.; Plantenberg, T. *Angew. Chem. Int. Ed.* **2002**, *41*, 688–714.

[58] Leibler, L. *Macromolecules* **1980**, *13*, 1602–1617.

[59] Bates, F. S. *Science* **1991**, *251*, 898–905.

[60] Matsen, M. W.; Bates, F. S. *Macromolecules* **1996**, *29*, 1091–1098.

[61] Atkins, P.; de Paula, J. *Atkins' Physical Chemistry*, 7th ed.; Oxford University Press, 2002.

[62] Bang, J.; Jeong, U.; Ryu, D. Y.; Russell, T. P.; Hawker, C. J. *Adv. Mater.* **2009**, *21*, 4769–4792.

[63] Lazzari, M.; De Rosa, C. In *Block CoPolymers in Nanoscience*; Wiley-VCH, W., Ed.; Lazzari, M.; Liu, G.; Lecommandoux, S., 2006; Chapter 9, pp 191–229.

[64] Matsen, M. W.; Schick, M. *Curr. Opin. Colloid Interface Sci.* **1996**, *1*, 329–336.

[65] Fasolka, M. J.; Mayes, A. M. *Annu. Rev. Mater. Res.* **2001**, *31*, 323–355.

[66] Anastasiadis, S. H.; Russell, T. P.; Satija, S. K.; Majkrzak, C. F. *Phys. Rev. Lett.* **1989**, *62*, 1852–1855.

[67] Pickett, G.; Twitten, T. A.; Nagel, S. R. *Macromolecules* **1993**, *26*, 3194–3199.

[68] Kikuchi, M.; Binder, K. *J. Chem. Phys.* **1994**, *101*, 3367–337.

[69] Matsen, M. W. *J. Chem. Phys.* **1997**, *106*, 7781–7791.

[70] Huang, E.; Rockford, L.; Russell, T. P.; Hawkert, C. J. *Nature* **1998**, *395*, 757–758.

[71] Knoll, A.; Horvat, A.; Lyakhova, K. S.; Krausch, G.; Sevink, G. J. A.; Zvelindovsky, A. V.; Magerle, R. *Phys. Rev. Lett.* **2002**, *89*, 035501/1–4.

[72] Thurn-Albrecht, T.; Steiner, R.; DeRouchey, J.; Stafford, C. M.; Huang, E.; Bal, M.; Tuominen, M.; Hawker, C. J.; Russell, T. *Adv. Mater.* **2000**, *12*, 787–791.

[73] Thurn-Albrecht, T.; Schotter, J.; Kastle, C. A.; Emley, N.; Shibauchi, T.; Krusin-Elbaum, L.; Guarini, K.; Black, C. T.; Tuominen, M. T.; Russell, T. P. *Science* **2000**, *290*, 2126–2129.

[74] Bang, J.; Kim, S. H.; Drockenmuller, E.; Misner, M. J.; Russell, T. P.; Hawker, C. J. *J. Am. Chem. Soc.* **2006**, *128*, 7622–7629.

[75] Kim, S. H.; Misner, M. J.; Xu, T.; Kimura, M.; Russell, T. P. *Adv. Mater.* **2004**, *16*, 226–231.

[76] Lin, Z. Q.; Kim, D. H.; Wu, X. D.; Boosahda, L.; Stone, D.; LaRose, L.; Russell, T. P. *Adv. Mater.* **2002**, *14*, 1373–1376.

[77] De Rosa, C.; Park, C.; Lotz, B.; Wittmann, J. C.; Fetters, L. J.; Thomas, E. L. *Macromolecules* **2000**, *33*, 4871–4876.

[78] Park, C.; De Rosa, C.; Thomas, E. L. *Macromolecules* **2001**, *34*, 2602–2606.

[79] Kim, S. O.; Solak, H. H.; Stoykovich, M. P.; Ferrier, N. J.; de Pablo, J. J.; Nealey, P. F. *Nature* **2003**, *424*, 411–414.

[80] Naito, K.; Hieda, H.; Sakurai, M.; Kamata, Y.; Asakawa, K. *IEEE Trans. Mag.* **2002**, *38*, 1949–1951.

[81] Yang, S. Y.; Ryu, I.; Kim, H. Y.; Kim, J. K.; Jang, S. K.; Russell, T. P. *Adv. Mater.* **2006**, *18*, 709–712.

[82] Discher, D. E.; Eisenberg, A. *Science* **2002**, *297*, 967–973.

[83] Alarcon, C. D. H.; Pennadam, S.; Alexander, C. *Chem. Soc. Rev.* **2005**, *34*, 276–285.

[84] Rapoport, N. *Prog. Polym. Sci.* **2007**, *32*, 962–990.

[85] Vriezema, D. M.; Aragones, M. C.; Elemans, J. A. A. W.; Cornelissen, J. J. L. M.; Rowan, A. E.; Nolte, R. J. M. *Chem. Rev.* **2005**, *105*, 1445–1489.

[86] Gil, E. S.; Hudson, S. A. *Prog. Polym. Sci.* **2004**, *29*, 1173–1222.

[87] Rodriguez-Hernandez, J.; Checot, F.; Gnanou, Y.; Lecommandoux, S. *Prog. Polym. Sci.* **2005**, *30*, 691–724.

[88] Cowan, D. O.; Drisko, R. L. *Elements of Organic Photochemistry*; Plenum Press, New York, 1976.

[89] D. Coyle, J. *Introduction to Organic Photochemistry*; John Wiley & Sons Ltd, 1986.

[90] Suppan P., *Chemistry and Light*; Royal Society of Chemistry, 1994.

CHAPTER
TWO

LIGHT-RESPONSIVE BLOCK COPOLYMERS

Abstract

Stimuli-responsive polymers are the subject of intense research because they are able to show responses to various environmental changes. Among those stimuli, light has attracted much attention since it can be localized in time and space and it can also be triggered from outside of the system. In this chapter, light-responsive block copolymers (LRBCs) that combine characteristic features of block copolymers, e.g. self-assembly behavior, and light-responsive systems are reviewed. The different photo-responsive moieties that have been incorporated so far in block copolymers as well as the proposed applications are discussed.

2.1 Introduction

Since the mid 90's, the concept of *smart* polymeric materials has hatched out and briskly grown as attested by the number of articles published in the last years [1–5]. These stimuli-responsive polymers are able to show sharp responses to environmental changes such as pH, temperature, light, redox or chemical changes. Block copolymers are usually cornerstones for those systems. Indeed, they undergo microphase separation at the nanoscale leading to well-defined morphologies in solution and in the solid state [6–8]. The resulting nanostructures have potential applications in nanotechnology such as drug delivery, catalysis, filtration, templating, etc. In addition, as block copolymers display distinct sequences, the stimuli-responsiveness can be localized in only one part of the polymer and systems in which different blocks can distinctly respond to different stimuli can be designed. This paves the way towards multi-addressable systems showing very complex behavior. This recent burst in the field of stimuli-responsive block copolymers has to be related to the development of novel synthetic methods towards block copolymers. Actually, for almost 15 years, controlled-radical polymerizations (CRPs) encompassing atom transfer radical polymerization (ATRP), reversible addition-fragmentation chain transfer (RAFT), and nitroxide-mediated polymerization (NMP) have emerged as powerful tools for the preparation of stimuli-responsive block copolymers with well-defined structures and narrow molar mass distribution [9–14].

Among the aforementioned stimuli, light has attracted much attention since it can be localized in time and space and can also be triggered from outside of the system. Indeed, photo-processes usually start/stop when the light is switched on/off and generate only limited amount of by-products since no additional reagents are needed. Moreover, a lot of parameters such as the intensity and the wavelength of light can be adjusted during the reaction time which enables good control over the reaction.

Concerning light-responsive block copolymers (LRBCs) in particular, only some features have been previously pointed out [2–5]. We propose here a detailed review on the state of the art. This chapter summarizes the different photo-sensitive moieties that have been incorporated so far into block copolymers such as azobenzene and *o*-nitrobenzyl chro-

mophores and some of their related applications. The chapter is divided into two main parts. The first one reviews LRBCs in solution and the second one discusses their bulk behavior. Applications such as light-triggered drug delivery, holography and nanoporous materials will be presented in order to illustrate the potential of those materials.

2.2 Light-responsive block copolymers in solution

2.2.1 Light-induced disruption of micelles

Amphiphilic block copolymers are known to self-assemble into micelles when they are dissolved in a block-selective solvent [6]. Generally, water is the solvent used and the hydrophobic sequences gather together to form the micellar core while the hydrophilic chains spread out in water and form the corona which stabilizes the micellar core. A lot of attention is devoted to these systems because of their potential applications such as nanoreactors or nanocarriers for controlled drug and bioagent delivery. It is therefore not surprising that a plethora of studies are focused on the encapsulation and release of small molecules by block copolymer micelles [3,5]. Up to now, most of the efforts have been devoted to micellar systems responding to a change in temperature or pH [4]. However, light recently emerged as an interesting stimulus to trigger the release of active molecules from block copolymer micelles [2, 15, 16].

The general strategy for light-induced release is, firstly, the incorporation of small molecules in the core of block copolymer micelles. Upon irradiation, a change in the nature of the core-forming block occurs which further leads to the disruption of the micelles and the subsequent release of the trapped compounds (Figure 2.1). In the case of amphiphilic block copolymer micelles, light triggers a change in the polarity of the core-forming block which renders the block copolymers totally soluble. This kind of disruption can be either irreversible or reversible depending on the kind of used photo-sensitive moiety. The common feature of all the LRBCs encountered for this application is their structure which consists of one water-soluble linear block linked to an insoluble block bearing the chromophores as side groups.

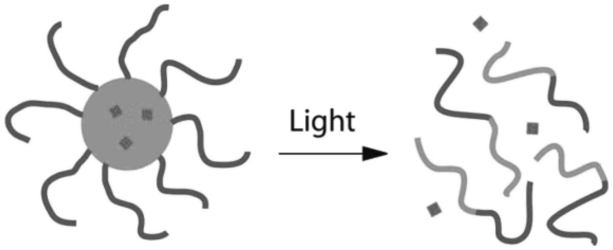

Figure 2.1: The concept of drug release triggered by light. Upon light illumination, micelles are disrupted, releasing their imprisoning contents. From Ref. [17].

2.2.1.1 Irreversible micelles disruption

Zhao and coworkers have described three amphiphilic LRBCs based on the same strategy [17–19]. They synthesized polymers containing one hydrophilic poly(ethylene oxide) (PEO) sequence linked to a hydrophobic polymethacrylate (PMA) block bearing photolabile side groups (Figure 2.2). The block copolymers were prepared by the ATRP of the photosensitive monomers initiated by a PEO macroinitiator. Light illumination induced the cleavage of the side chromophores, unmasking the protected acrylic acid (AA) functions. As the resulting PEO-*b*-PMAA was fully hydrophilic, the block copolymer became soluble in water. For micelles built from those photocleavable polymers in aqueous media, light stimulation resulted in the disruption of the micelles and in the subsequent release of the previously encapsulated molecules.

Esters of pyrenylmethyl (Py) were firstly proposed as photocleavable moieties to validate the concept of light-induced drug delivery (Figure 2.2) [18]. Nile Red fluorescent dyes were incorporated into micelles made of PEO-*b*-PPy. Upon UV irradiation, the photo-solvolysis of the pyrenyl groups caused the disruption of the micelles while releasing the encapsulated Nile Red (Figure 2.3). The black curve in Figure 2.3 represents the fluorescence emission spectrum of micellar solutions of PEO-*b*-PPy. The emission band with the wavelength at maximum intensity (λ_{max}) at 478 nm corresponds to the fluorescence of the pyrenyl groups. Micelles loaded with Nile Red show a band at λ_{max}= 620 nm (dark grey). The drastic decrease in the pyrenyl fluorescence is explained by

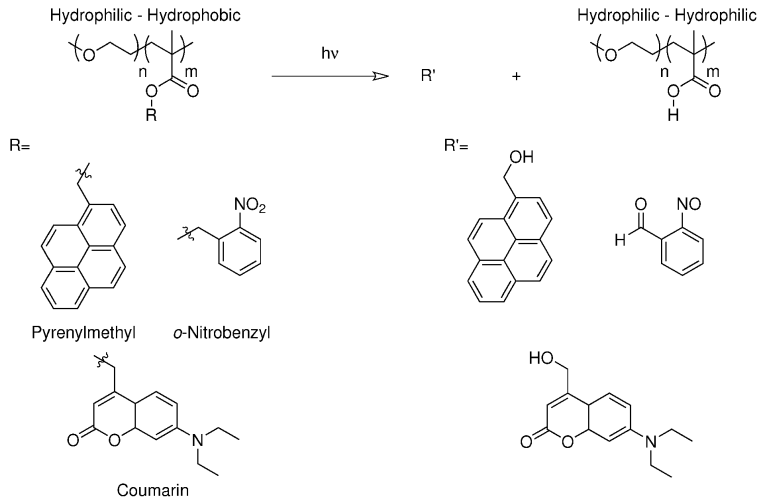

Figure 2.2: Changing the hydrophilic-hydrophobic balance of block copolymers by illumination.

the non-radiative energy transfer (NRET) between the two dyes due to the close distance between them as a result of the encapsulation of Nile Red in the micellar core. After UV irradiation at 365 nm, the fluorescent dyes are released due to the disruption of the micelles. As Nile Red is hydrophobic, it precipitates and no more fluorescence emission is observed (light grey).

Afterwards, the authors showed the possibility to control the release of encapsulated molecules by changing the intensity of the illumination. This behavior was demonstrated for block copolymers containing *o*-nitrobenzyl esters as side groups [17]. Such chromophores cleave themselves upon light excitation and, as the photocleavage proceed via a Norrish II type intra-molecular rearrangement, no molecule of solvent is needed to enable the process. Furthermore, *o*-nitrobenzyl esters are very interesting because they also undergo photocleavage upon the absorption of two near infrared (NIR) photons. For biomedical drug release applications, this point is very important because NIR radiations (vs UV) penetrate deeper through water and cell tissues, and they are less harmful for healthy cells. Even if the photo-dissociation of *o*-nitrobenzyl containing

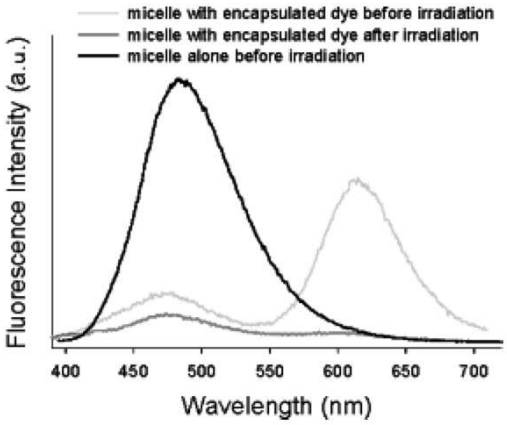

Figure 2.3: Fluorescence emission spectra of micellar solutions of PEO-*b*-PPy. Micelles without Nile Red dyes (black). Micelles with encapsulated Nile Red before irradiation (dark grey). Micelles with encapsulated Nile Red after irradiation (light grey). From Ref. [18].

micelles at 700 nm (NIR) was demonstrated, the process efficiency was lower than for UV irradiation (much longer irradiation time was needed in case of NIR) due to a much smaller absorption cross-section for the two NIR photons [17]. In order to address this problem, the chromophores were changed to esters of (diethylamino)methylcoumarinyl which display a larger two-photon absorption cross section and whose photosolvolysis occurs at 794 nm (Figure 2.2) [19].

A peculiar example of irreversible light-induced disruption of nano-objects has been reported by Stupp and coworkers (Figure 2.4) on photosensitive peptide oligomers containing an *o*-nitrobenzyl group [20,21]. Although those oligomers are not strictly speaking LRBCs, their unique photo-responsive behavior merits to be mentioned here. Those molecules were found to self-assemble into supramolecular quadruple helical nanofibers as observed by transmission electronic microscopy (TEM) (Figure 2.4, (a)). The helical structures were actually formed by the entanglement of two smaller helices themselves resulting from the entwining of two individual fibrils. Upon irradiation, the photochemical cleavage of the *o*-nitrobenzyl moiety led to the conversion of the quadruple helix

into non-helical single fibers (Figure 2.4, (b)). The diameter of those latter objects is equal to 11 nm which corresponds to about twice the length of a single oligomer.

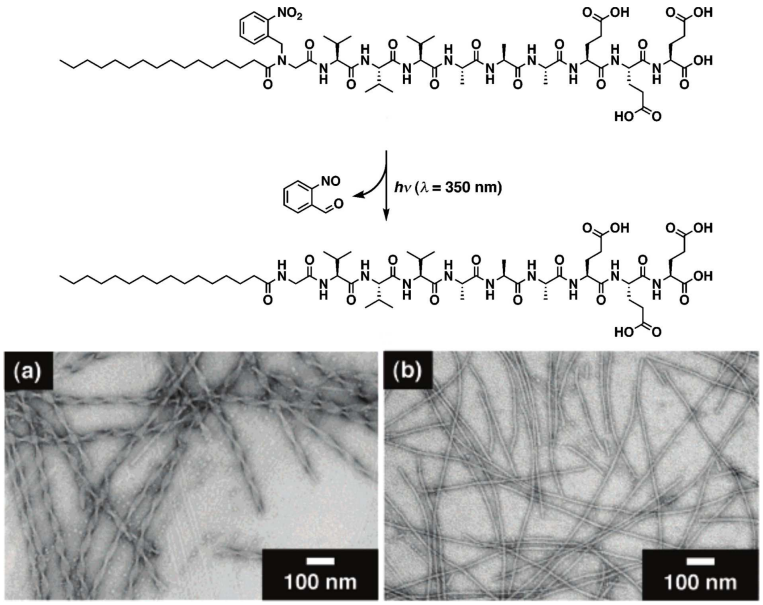

Figure 2.4: Structure and photochemical transformation of a peptide-based oligomer (up). TEM picture of the initial quadruple helical fiber (a) and the resulting structure formed after irradiation (b). Adapted from ref. [20].

The formation of quadruple helices is explained by the introduction of the bulky nitrobenzyl moiety at the junction between the two parts of the oligomer which hinders the packing of the molecules. In that manner, steric hindrance is believed to create opportunities for interactions among molecules in the surroundings of the fibrils (hydrogen bonding, hydrophobic interactions). Finally, the cleavage of the bulky moiety disables those interactions and the helices dissociate into single fibrils.

2.2.1.2 Reversible micelles disruption

Azobenzene moieties have been recognized early as candidates of choice for reversible light-induced micellization processes [22]. Indeed, these molecules are one of the most studied photo-responsive systems in polymer science since the mid 20th century [23–25]. Their great attractiveness is due to the easily reversible *trans*-*cis* photo-isomerization of their nitrogen-nitrogen double bond (N=N). In this process, the *trans* isomer can be converted to the *cis* one upon UV light irradiation and the back isomerization can be triggered by visible light.

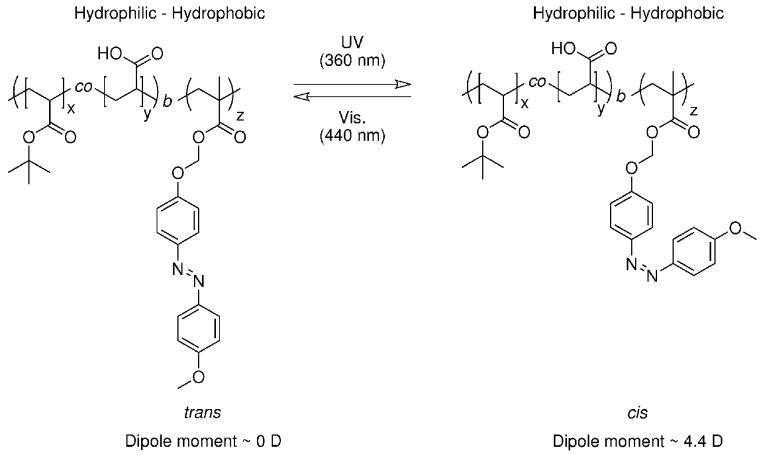

Figure 2.5: Reversible change in the polarity of P(tBA-*co*-AA)-*b*-PMAz copolymer induced by photoisomerization of azobenzene moieties. Adapted form Ref. [22].

As the photoisomerization is a reversible process, Zhao and coworkers designed a micellar system which can disintegrate upon UV irradiation and reform itself when irradiated with visible light [22,26]. They synthesized by ATRP a block copolymer containing one random poly(*t*-butyl acrylate-*co*-acrylic acid) sequence connected to a poly(methacrylate) bearing azobenzene chromophores as side chains, P(tBA$_{46}$-*co*-AA$_{22}$)-*b*-PMAz$_{74}$ (Figure 2.5, the numbers in subscript represent the average degree of polymerization of each block). Core-shell micelles and/or vesicles could be obtained from this polymer in a dioxane/water mixture

depending on the water percentage added to form those objects. For both morphologies, it was possible to disrupt the aggregates upon UV irradiation and reform them after exposure to visible light as shown in Figure 2.6. The scanning electronic microscopy (SEM) picture of the initial vesicles displayed large objects with a diameter between 100 and 300 nm (A). After UV irradiation, almost all vesicles disappeared (B) and they reformed themselves while being excited with visible light. The reversible process was followed by optical transmittance of a low power laser (λ=633 nm) through the vesicle solution (Figure 2.6, below) which confirmed the disruption and reformation of the nano-objects.

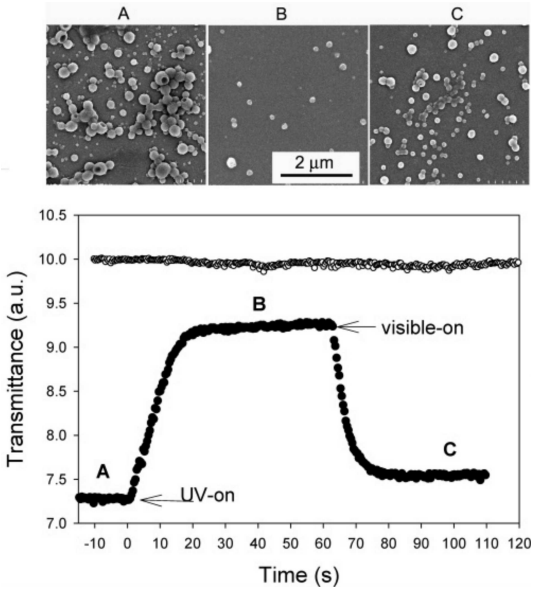

Figure 2.6: Above: SEM pictures of cast solution of vesicles of P(tBA$_{46}$-*co*-AA$_{22}$)-*b*-PMAz$_{74}$. Below: Changes in the transmittance for a vesicular solution P(tBA$_{46}$-*co*-AA$_{22}$)-*b*-PMAz$_{74}$. Before irradiation with UV light (A); after UV irradiation (B) and after exposure to visible light (C). The transmittance of the fully solubilized diblock in dioxane is also shown (regular line at 10 a.u.). Reproduced from Ref. [26].

This disruption-reformation process was explained by the change in the hydrophilic-hydrophobic balance of the block copolymer induced by

the photoisomerization of the azobenzenes side groups (Figure 2.5). Indeed, the azobenzene *trans* form is relatively apolar (dipole moment $\sim$ 0 D) while the *cis* form is on the other hand more polar. Using 4,4'-dimethoxyazobenzene as a model compound, the authors estimated the dipole moment of the *cis* isomer at about 4.4 D by Density Functional Theory (DFT) calculation. Those considerations account for the reversible dissociation-association of azobenzene containing micelles. Although a significant increase in the polarity of azobenzene moieties in the initially hydrophobic block happened after UV-irradiation, it may not be sufficient to dissociate micellar aggregates in all cases. Actually, a similar block copolymer but with a different composition (P(tBA_{19}-*co*-AA_{33})-*b*-$PMAz_{31}$) displayed limited response to UV and visible light irradiations certainly due to a too short azobenzene-containing sequence [26].

In order to enhance the efficiency of reversible photo-induced micellar dissociation-association process, Matyjaszweski and coworkers proposed the use of photo-sensitive spiropyran moieties [27]. They synthesized by ATRP a poly(ethylene oxide)-*block*-poly(methacrylate) whose methacrylate block bears spyropyran (SP) side-chains (PEO-*b*-PMSP) (Figure 2.7). The hydrophobic spiropyran moieties undergo photoisomerization into their hydrophilic zwitterionic merocyanine counterparts under UV irradiation and the reverse process is triggered by visible light (620 nm). This process is accompanied by a deep change in the hydrophobic to hydrophilic balance in the LRBC, which causes micellar disruption. Moreover, this system can be successfully used for the encapsulation and release of molecules of interest. In this respect, coumarin 102 was demonstrated to be encapsulated in micelles made of the PEO-*b*-PMSP and then released upon excitation at 365 nm. Moreover, the authors described the partial re-incorporation of the fluorescent dyes triggered by visible light (up to almost 50 % of the initially released coumarin 102). The very short spiropyranic sequence (8 monomer units) found in the reported LRBC proved the high degree of hydrophobic-to-hydrophilic contrast offered by spiropyrans in comparison to azobenzenes.

Following the works on azobenzene-containing LRBC micelles initiated by the group of Zhao, some interesting studies on the behavior of micellar nano- and micro- aggregates under photoisomerization such as shape deformation and morphological transformation of the nano-objects have been published [28–37]. Especially interesting is the

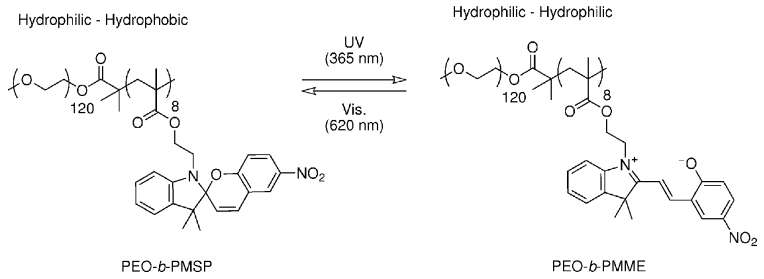

Figure 2.7: Reversible photoisomerization for the spiropyran-containing LRBC. Adapted from Ref. [27].

fusion process of giant block copolymer vesicles triggered by photo-irradiation, which mimics some biological processes [30, 33]. Fusion of giant micro vesicles self-assembled from poly(N-isopropylacrylamide)-*block*-poly(acrylate) bearing azobenzene chromophores as side-groups (PNIPAM-*b*-PAz) was investigated by Zhang and coworkers [33].The vesicles presented in Figure 2.8 (V3, V4, V5) were self-assembled in THF/water (50/50 vol.-%) and showed diameters between 4 and 5 μm. The fusion occurred as soon as they were exposed to UV light and was followed by optical microscopy.

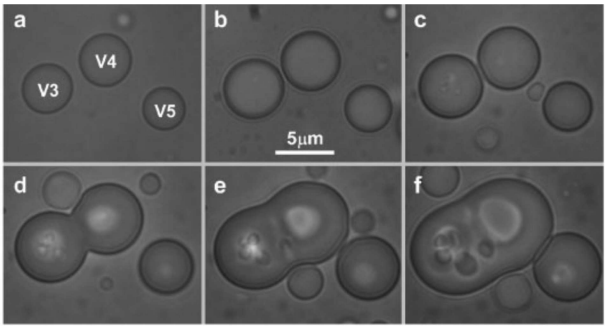

Figure 2.8: Photoinduced fusion process of the PNIPAM-*b*-PAz vesicles. Initial vesicles (a) and vesicles observed after irradiation of 16 (b), 33 (c), 42 (d), 58 (e), 80 (f) min. Reproduced from Ref [33].

This phenomenon was explained by a structural perturbation taking place in the azobenzene-containing bilayer during irradiation. Since the *trans*-to-*cis* isomerization induces a change in polarity, it also disturbs the packing of the *trans* azobenzenes in the vesicular membrane. Schematically, damages and defects are caused in the membrane by UV irradiation, decreasing its mechanical stability. Moreover, the associated surface expansion increases the surface free energy and, consequently, the fusion of vesicles appears to be the most likely way to reduce that excess of free energy and stabilize the objects. Recently, a quite interesting cycle of photo-induced damage, defect, fusion, disintegration and rearrangement of vesicles has been observed for self-assembled azopyridine-containing LRBC. All those processes were observed as long as the samples were exposed to UV irradiation. But once the light was switched off, the whole dynamics stopped and a stable state could be reached by visible illumination [30].

2.2.2 Photo-induced micellar cross-linking

Micelles are known to be dynamic structures which disintegrate themselves below their critical micellar concentration (CMC). In addition, they are sensitive to the nature of the solvent and to pH, ionic strength, light or temperature for the stimuli-responsive designed ones. One way to render those micelles more robust is to stabilize them by cross-linking. Numerous examples of chemical cross-linking either of the micellar core or of the corona can be found in the literature and non-exhaustive references are given herein [38, 39]. Light-induced cross-linking is a convenient route to stabilize micelles since chemical reagents and unwanted by-products are avoided.

2.2.2.1 Irreversible cross-linking

By using the [2+2] photo-cycloaddition of cinnamic esters, Liu and coworkers firstly demonstrated the light induced cross-linking of micelles and vesicles (Figure 2.9) [40–43]. For instance, they cross-linked the membrane of vesicles made of polyisoprene-*block*-poly(2-cinnamoylethyl methacrylate) (PI-*b*-PCEMA) in a THF/hexane mixture. As the PI chains formed the outer and the inner layer of the vesicle, they were able to semi and to fully ˝shave˝those hairy nano-objects by ozonolysis of the PI double bonds.

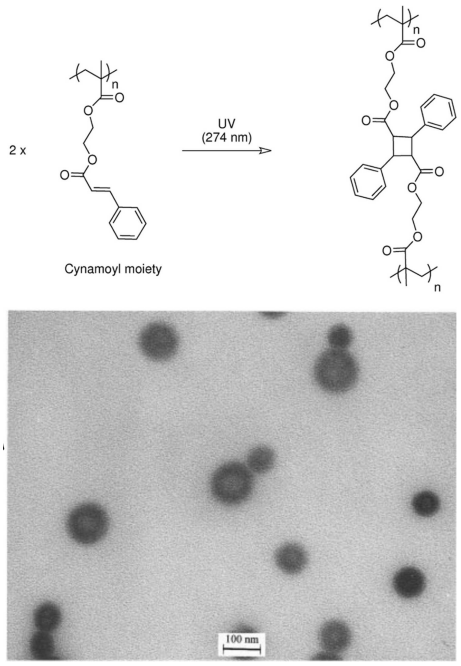

Figure 2.9: Photodimerization of cinnamic ester (top). TEM picture of fully shaved nanospheres made from PI-*b*-PCEMA. Reproduced from Ref. [41].

Recently, initially pH-responsive micelles have been rendered insensitive to that stimulus by photo cross-linking their cynamoyl containing core [43]. In this example, RAFT has been used to prepare poly(ethylene oxide)-*block*-poly(2-(diethylamino)ethylmethacrylate-*co*-2-cinnamoyloxyethyl acrylate). This PEO-*b*-P(DEAEMA-*co*-CEA) block copolymer is sensitive to pH due to the PDEAEMA sequence which undergoes nitrogen quaternization in acidic media. At pH>7, the deprotonated nitrogens render this block hydrophobic and micellization in water is observed (Figure 2.10). At pH<7, the PDEAEMA block is hydrophilic and no micelles are observed. However, when the cores of the micelles are cross-linked upon UV illumination due to the presence of the cynamoyl moieties, they maintain their integrity upon pH stimulation. Although the acidity cannot anymore destroy the micelles, they are nevertheless still sensitive to pH as the PDEAEMA nitrogens are still quaternizable.

For instance, 1-pyrenemethanol (hydrophobic dye) can be retained in the hydrophobic core at pH=10, while in acidic condition (pH=3) the polar hydrated core released the dye.

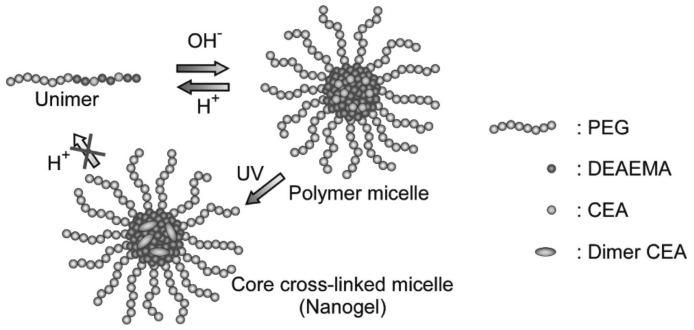

Figure 2.10: Schematic illustration of the pH-controlled micellization of PEO-*b*-P(DEAEMA-*co*-CEA) and the cross-linking upon UV irradiation. Reproduced from Ref. [43].

2.2.2.2 Reversible cross-linking

A more interesting feature is the possibility to cross-link micelles in a reversible way. Although cross-linking enables a much greater stability of the micelle, the release of encapsulated molecules might not be always easy in cross-linked micelles. On the other hand, if the cross-linking is reversible, it allows a good robustness of the micelles in the cross-linked state while not interfering with the release in the non-cross-linked state. Zhao and coworkers incorporated coumarin moieties in block copolymers in order to stabilize either the core or the shell of micelles (Figure 2.11) [44, 45]. Coumarin moieties are able to undergo a reversible [2+2] photo-cycloaddition upon UV irradiation. The authors firstly demonstrated the core photo-cross-linking of aqueous micellar aggregates prepared from PEO_{112}-*b*-$PCMA_{20}$ and PEO_{112}-*b*-P(CMA_8-*co*-MMA_{20}) where PCMA is a poly(methacrylate) bearing coumarin side-chains [44]. The irradiation wavelength was above 310 nm and the photo-decross-linking occurred below 260 nm. Although the latter appeared to be incomplete, a certain degree of reversibility can be achieved as shown in Figure 2.12. It was also demonstrated that cross-linked micelles slow down the release of encapsulated molecules compared to the non-cross-

linked ones.

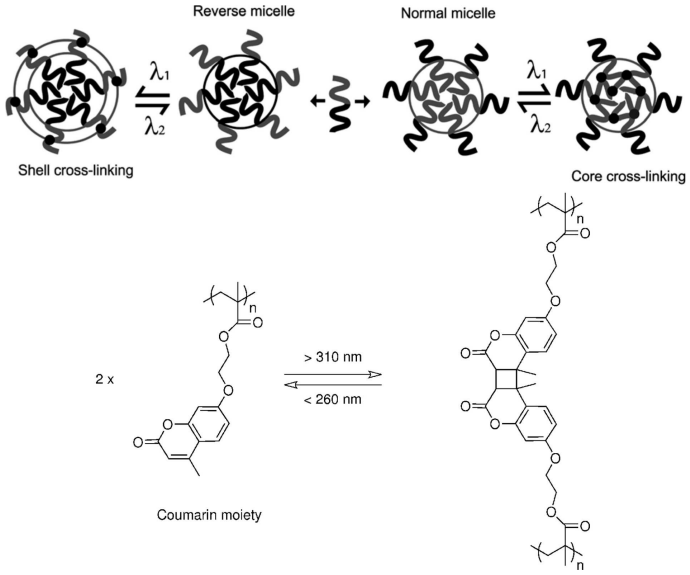

Figure 2.11: UV cross-linking of the core and the shell of micelles (top). Photodimerization of coumarin moieties in PCMA (bottom). Adapted from Ref. [15].

In the case of shell photo-cross-linking, Zhao and coworkers firstly prepared reverse micelles from a poly(dimethylaminoethylmethacrylate)-*block*-poly(methyl methacrylate-*random*-coumarin methacrylate) (PDMAEMA-*b*-P(MMA-*r*-CMA)) [45]. The micelles were formed by quaternazing the amino groups in a THF/DCM mixture. This reaction led to the collapse of the PDMAEMA sequences inducing the formation of the core of the micelles. The outer P(MMA-*r*-CMA) shell was then cross-linked by the photodimerization of the coumarin moieties upon UV irradiation. Afterwards, those shell-cross-linked-micelles were decorated by extra PDMAEMA chains grafted by a subsequent ATRP of DMAEMA initiated by chloride groups remaining at the surface of the cross-linked shell (the chloride end groups come from the ATRP synthesis of the initial PDMAEMA-*b*-P(MMA-*r*-CMA) copolymer). In that manner, the authors obtained micelles in water which could not be made from direct micellization of block copolymers. Indeed, the micelles con-

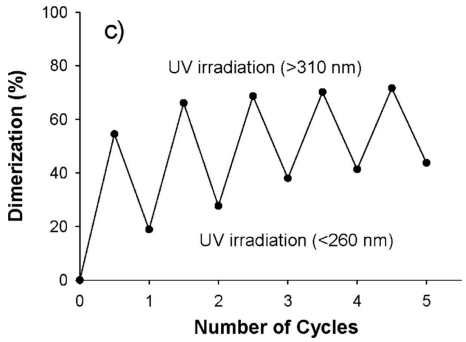

Figure 2.12: Reversible photodimerization of the coumarin moieties in PEO_{112}-*b*-$PCMA_{20}$ micelles exposed to alternated illuminations. Reproduced From ref [44].

tained both the core and the outer shell of the micelles are made of hydrophilic PDMAEMA, and are separated by a cross-linked P(MMA-*r*-CMA) intermediate shell.

2.2.3 Thermo- and light-responsive block copolymers

Multi-responsive systems are of great interest because they offer the possibility to tune their properties in different ways. As far as LRBCs are concerned, most of the examples involve temperature as an additional stimulus [35,36,46–48]. A first example of thermo- and light-sensitive block copolymers based on azobenzene moieties was reported in 2005 [35]. The authors synthesized a PDMAEMA-*b*-PAz LRBC in which the PDMAEMA sequence provides a LCST behavior. The LCST of the PDMAEMA-*b*-PAz LRBC increased upon irradiation from 41 ℃ for the *trans* form to 44 ℃ for the *cis* form.

Another example, showing a greater change in the LCST upon illumination, involves *o*-nitrobenzyl groups (Figure 2.13) [46]. In that paper, the synthesis of thermo- and light- sensitive hydrophilic poly(ethylene oxide)-*b*-poly(ethoxytri-(ethyleneglycol)acrylate-*co*-nitrobenzylacrylate) (PEO-*b*-P(ETEGA-*co*-NBA)) block copolymers by ATRP was described. The PETEGA sequence confers the thermo-sensitivity to the block copolymer which displays a LCST at around 25 ℃ ($LCST_1$). Upon UV irradiation, the irreversible cleavage of the *o*-nitrobenzyl esters into car-

boxylic acids renders the PETEGA sequence more hydrophilic and consequently increases the LCST by more than 10 °C ($LSCT_2$= 36 °C). To illustrate this shift in the LCST, Nile Red molecules have been encapsulated in the micelles at the first LCST ($LCST_1$), and have been released upon irradiation and subsequently re-encapsulated in micelles after increasing the temperature above the second LCST ($LCST_2$).

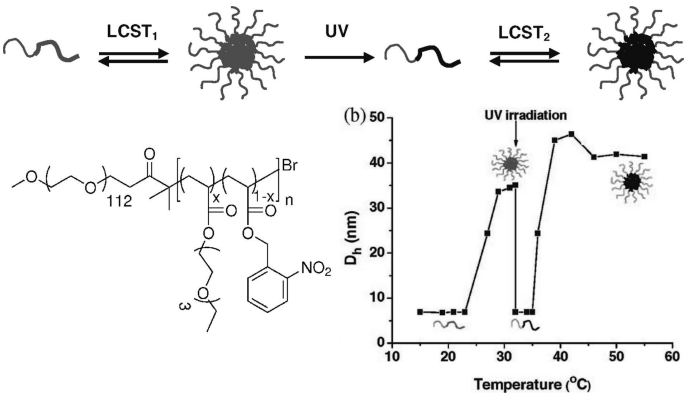

Figure 2.13: Multiple micellization and dissociation transitions of the PEO-*b*-P(ETEGA-*co*-NBA) (top). Chemical structure of the PEO-*b*-P(ETEGA-*co*-NBA) copolymer (left). Change in hydrodynamic diameter (D_h) upon temperature and light illumination (right). Adapted from Ref. [46].

As already mentioned, stimuli-responsive micelles are less sensitive to stimuli if they have been previously cross-linked, but can nevertheless keep interesting properties. He *et al.* described systems in which the photo-cross-linking of coumarin moieties enables new thermosensitive behavior [47, 48]. In the first example, thermo- and photo-responsive nanogels from cross-linked micelles have been prepared (Figure 2.14) [48]. The cross-linking of the coumarin groups in the core allows to keep the micellar structure below the LCST. Moreover, the size of the nano-objects can be controlled by the degree of cross-linking which determines the swelling of the micelles. The reversibility of all those changes is ensured by the reversibility of the photodimerization of the coumarin moieties (see above). In the same way, large reversible volume changes in vesicles have been described by the same authors [45].

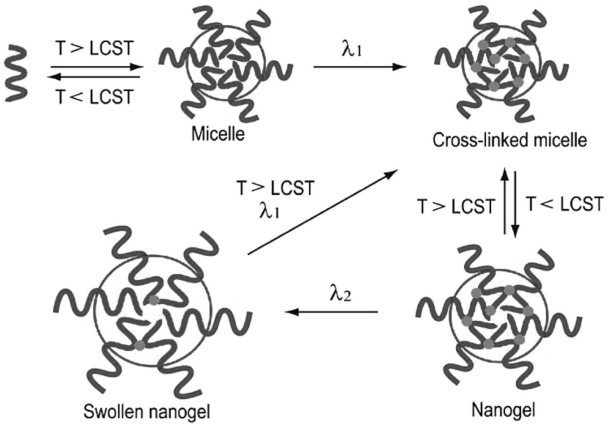

Figure 2.14: Thermo- and photo-responsive nanogels. Reproduced from Ref. [48].

2.3 Light-responsive block copolymers in the solid state

2.3.1 Azobenzene based copolymers

As previously introduced, azobenzenes and their derivatives undergo reversible photoisomerization upon illumination by light (see Section 2.2.1.2). Despite the photo-responsivity of azobenzene-containing polymers being known for a long time [23–25, 49, 50], azobenzene moieties were initially incorporated in block copolymers only for their mesogenic properties due to their rigid rod-like structure in the *trans* form [51–56]. In those systems, one block contains the azobenzenes as side groups which confers a mesogenic character to the block copolymers. The other(s) sequence(s) is (are) composed of traditional coil-like chain(s).

Later on, studies comparing the structure and photochromic behaviors of azobenzenes in homo and block copolymer films were published [57–65]. Azobenzene moieties usually organize themselves in the liquid crystalline phase in different kinds of aggregates. Side-by-side (H-type) and head-to-head (J-type) aggregates coexist together with the non-associated azobenzenes (Figure 2.15). It was found that the microstructures generated by the self-assembly of block copolymers gener-

ally hinder the organization of the mesophase, and thus less aggregates are found in block copolymer films than in those made of homopolymers [57].

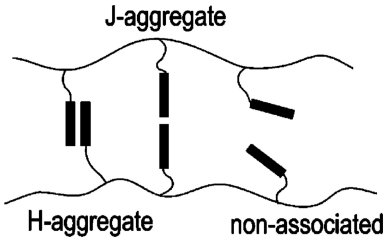

Figure 2.15: Types of aggregation present in azobenzene containing polymers. Reproduced from Ref. [60].

In 2004, Schmidt and coworkers compared the properties of PS-*b*-PAz block copolymers with different compositions to their corresponding homo-PAz and random PS-*co*-PAz copolymers [62]. Block copolymers displaying no phase separation, spherical and cylindrical morphology were synthesized. Figure 2.16 shows the evolution of the position (λ_{max}) of the π-π^* transition of azobenzene moieties in the different polymers. The shift of this band is characteristic of the type of aggregates present. In solution, no aggregates are formed and no differences can be observed in the absorption spectra of the different polymers. On the other hand differences appear for thin films. No change was observed for the random copolymer, reflecting the non-associated form of its azobenzene moieties. The hypsochromic shift in the π-π^* band for the homo-PAz reflects the presence of H-aggregates (*vs* bathochromic shift for J-aggregates). For the PS-*b*-PAz, a steady shift towards the formation of H-aggregates is observed with the increase of the azobenzene fraction. This increase can however not be attributed to the concentration of azobenzene moieties contained in the copolymer. Indeed, as no association is observed for the PS-*co*-PAz at the same concentration, the shift has to be attributed to the microphase separation observed with block copolymers. Moreover, the shift increases with the change in morphology (miscible-to-spherical-to-cylinders). Actually, microphase separation provides confined domains enabling the aggregation of azobenzenes.

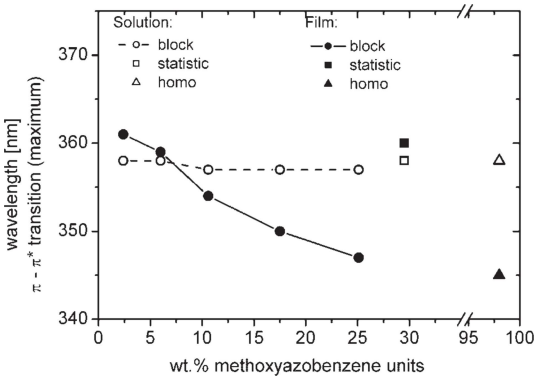

Figure 2.16: Maximum absorption of the π-π^* transition of block copolymers containing azobenzene (PS-*b*-PAz) and of the corresponding PS-*co*-PAz and homo-PAz in solution and in the solid state. Reproduced from Ref. [62]

As the mesogenic character is due to the rod-like shape of *trans*-azobenzenes, an isotropic state can be reached by their photo-isomerization into the *cis* form. Actually, the bent shape of the *cis* isomer prevents the orientated packing of the molecules. In this manner, reversible order-disorder transition (LC vs non-LC) can be modulated by light. However, the most important feature is the ability of azobenzenes to align themselves perpendicularly to the polarization direction of linearly polarized light. Indeed, absorption of light requires that the transition dipole moment of the molecule has a component parallel to the direction of the electric field (E) of light. As *trans*-azobenzenes present π-π^* transition moment approximately parallel to their molecular long axis, an angular selection for their photoisomerization takes place. Roughly, only the molecules which are not oriented perpendicularly to the polarization direction of light will isomerize into the *cis* form (Figure 2.17, (a)).

As the relaxation of the *cis* form is isotropic, successive *trans*-*cis*-*trans* cycles lead to a progressive enrichment of the medium in the *trans* isomers oriented perpendicularly to the polarized light (Figure 2.17). This phenomenon is well-known as the *Weigert effect* [66]. In block copolymers films, the confinement of azobenzenes in the microdomains (generated by self-assembly) hinders their photo-alignment by the polar-

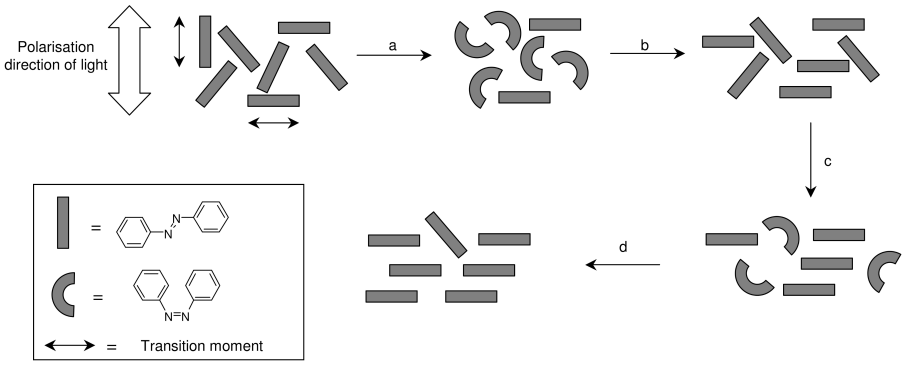

Figure 2.17: Photoalignment of azobenzene by *trans-cis-trans* isomerization (Weigert effect).

ized light. Consequently, the photochemical order-to-disorder transition (and reverse) is slowed down compared to the homopolymer counterparts.

When azobenzenes are bound to polymeric materials which display some degree of intrinsic order (liquid crystal, semi-crystal microphase separated domains) a cooperative motion phenomenon can be observed [25]. In this case, azobenzenes carry the polymeric chains along during the photo-alignment process, and a reorientation of the ordered domains is consequently achieved. The efficiency of this behavior is quite high, as a change of only 1 mol-% of the LC molecules is enough to lead to the reorganization of the whole system.

2.3.1.1 Photo-controlled change in morphology and alignment of microdomains

In 2005, Seki *et al.* demonstrated the possibility to control the morphology of self-assembled block copolymers by illumination [67]. They synthesized an ABA triblock containing a PEO middle-chain surrounded by two polymethacrylate sequences bearing azobenzene moieties as side groups (Figure 2.18 (top)). This triblock copolymer was self-assembled on water in a Langmuir trough and subsequently transferred onto a mica surface. This Langmuir-Blodgett film is formed of azobenzene do-

mains having spherical or rod-like shapes (Figure 2.18, (a)). When the monolayer is irradiated at 365 nm, before its transfer onto the solid substrate, a stripe pattern composed of azobenzene domains is observed (Figure 2.18, (b)). This change in morphology is explained by a change in polarity induced by the *trans*-to-*cis* isomerization of the azobenzenes. Indeed, the *cis* form presents a larger dipolar moment which favors the contact with water, resulting in the expansion of the azo microdomains. Concerning the reversibility of the process, it was found that thermal *cis*-to-*trans* back process led to the initial morphology after six days at room temperature. Illumination with visible light did not lead to a faster process.

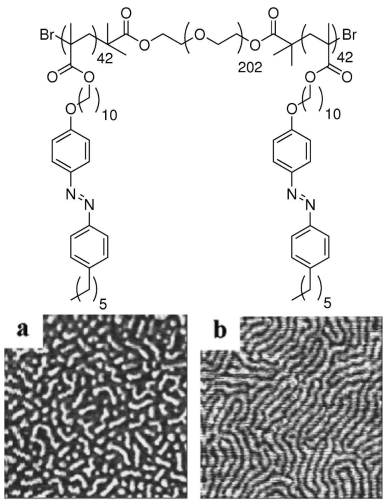

Figure 2.18: Top: Structure of the amphiphilic PAz-*b*-PEO-b-PAz triblock synthesized by ATRP. Bottom: AFM height pictures of the Langmuir-Blodgett film made from the PAz-*b*-PEO-*b*-PAz triblock (1 μm^2), (a) Without irradiation (*trans* form), (b) Irradiated at 365 nm (*cis* form). AFM Pictures reproduced from Ref. [67]

Taking advantage of the cooperative effect promoted by azobenzenes, Ikeda *et al.* demonstrated the possibility to control the alignment of microdomains in block copolymer thin films (Figure 2.19) [68]. They self-assembled a PEO_{113}-*b*-PAz_{80} coil-LC block copolymer into a thin film ($\pm$ 100 nm thick) with a cylindrical morphology. The cylinders,

orientated perpendicularly to the film surface, were formed by the PEO block while the matrix was the liquid crystalline (LC) phase made of the PAz sequence. The azobenzene chromophores were aligned parallel to the PEO cylinders. When the film was exposed to linearly polarized visible light at 488 nm and subsequently annealed at 140 ℃, the irradiated regions showed a reorientation of the PEO cylinders parallel to the substrate (perpendicular to the polarization of light). This is due to the cooperative motions as the irradiation induces the alignment of the azobenzene chromophores perpendicularly to the polarization plane of the light. The reorganization of the LC matrix in turn induces the reorientation of the PEO cylinders. A thermal annealing at a temperature close to the temperature of the smectic-to-isotropic transition is however needed to enhance the mobility of the polymeric chains and reach a high degree of order.

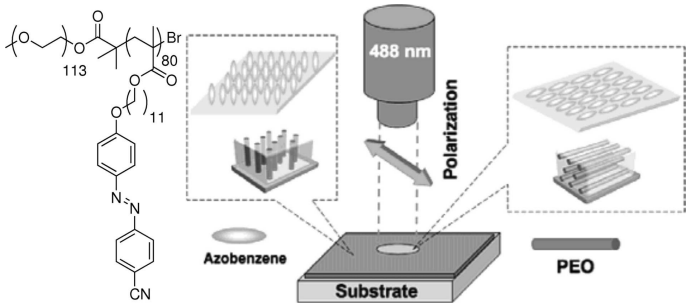

Figure 2.19: Structure of the PEO_{113}-*b*-PAz_{80} and the photoinduced reorientation of PEO domains triggered by cooperative motion. Adapted from Ref. [69].

A similar photo-patterning has been described for a PS_{76}-*b*-PAz_{140} system where the non-LC block displays a higher glass transition temperature (T_g) (Figure 2.20). The T_g of the PS sequence is equal to 102 ℃, and the realignment of the microphase separated structure required irradiation at a temperature above the order-disorder transition temperature (T_{odt} = 118 ℃ for PS_{76}-*b*-PAz_{140}) [69]. An interesting observation is the sharp transition between the parallel and the perpendicular PS cylinders regions without any radient region showing an mixture of both orientations.

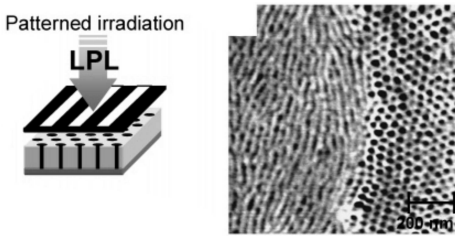

Figure 2.20: Photopatterning of the PS_{76}-*b*-PAz_{140} with linear polarized light (LPL). AFM picture after the photopatterning (left). Reproduced from Ref [68].

2.3.1.2 Holographic gratings

Improving the data storage capacity of recordable disks is a never ending quest as the amount of information needed to be stored and shared is vastly increasing every year. In that field, optical holographic storage is one of the most promising technology [70,71]. This technique is based on the possibility to imprint light interference patterns on photosensitive materials. The data are stored in the form of a change in the diffraction properties of these materials and the restitution is ensured by the diffraction of a reference light beam by the recorded medium. For that reason, the diffraction efficiency (DE) of the material used is one of the most important parameter to control.

In the case of holographic gratings imprinted on azobenzene containing LC polymer films, the diffraction efficiency is mainly governed by two kinds of contributions (Figure 2.21) [49,72,73]. Firstly, a refractive-index grating (RIG) is imprinted by a spatially selective photo-isomerization (alternation of LC and isotropic phases). Secondly, this RIG is usually accompanied by a deformation of the surface which contributes often in great part to the DE. This surface relief grating (SRG) process is due to a massive transportation of polymeric material thanks to a cooperative motion process [25]. The surface relief pattern is made of crests and troughs similar to the interference pattern.

Studying the optical behavior of azobenzene polymers and copolymers, Frenz *et al.* demonstrated that the surface relief process usu-

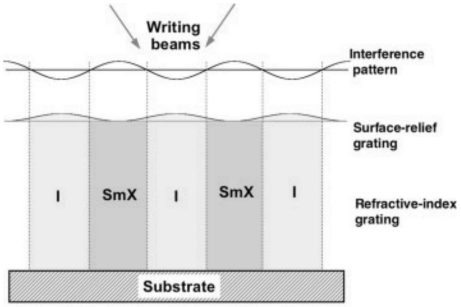

Figure 2.21: Refractive index grating (RIG) and surface relief grating (SRG) in azobenzene containing polymeric materials. Reproduced from Ref. [73]

ally observed during the formation of RIG can be inhibited by the microphase separation of block copolymers as the mass transport cannot take place because of the confinement of the azobenzenes in the microdomains [62]. In 2008, Ikeda and coworkers compared the holographic behavior of PMMA-*b*-PAz of different compositions [74]. For all copolymers, photo-induced alignment of the azobenzenes and formation of holographic gratings were observed. However, different behaviors were described depending on the relative composition in azobenzene chromophores. It was found that the magnitude of SRG depends on the amount of azobenzene contained in the polymers, and that surface relief grating was rarely observed when azobenzenes are confined in a spherical microdomain. However, large variation of the refractive index can still be obtained enabling good holographic grating.

SRG depends on the architecture of the azobenzene containing polymer. Generally, homopolymers offer greater SRG than random copolymers. Concerning block copolymers, the amount of azobenzenes contained in the polymer and the type of morphology of the microphase are two important parameters. Usually, none or poor SRG is observed for block copolymer thin films. To force surface relief grating or to enhance small initial SRG, additives and/or thermal annealing can be applied.

Morikawa *et al.* made use of 5CB (p-n-penthyl-p'-cyanobiphenyl) as plasticizer to produce surface relief gratings on thin films made of a

PEO_{114}-*b*-PAz_{67} copolymer which in itself is not prompt to mass transport [75]. The authors were interested in aligning microdomains and patterning block copolymer thin films using holographic writing. For their experiment, a PEO-*b*-PAz similar to the one shown in Figure 2.19 was used. The composition of this coil-LC block copolymer was chosen in order to obtain cylindrical microdomains. They firstly showed that, as expected, the orientation of the PEO cylinders depends on the film thickness [76, 77]. Below a thickness of the order of the diameter of the cylinders no microstructure is observed (< 20 nm). At 30 nm, a parallel orientation of the cylinders is observed, and at 70 nm they are perpendicular to the substrate. Afterwards, they imprinted a regular thickness pattern on the polymer film by a surface relief process.

In order to enable the SRG, 5CB was mixed with the polymer to facilitate the mobility of the chains and to reinforce the LC nature of the material [75, 78]. After a pre-irradiation of the film at 365 nm (to obtain the photostationary state with the highest content of the *cis* isomer) the authors exposed the film to the interference pattern generated by two coherent laser beams (488 nm) in order to obtain a succession of crests and troughs in the film. After thermal annealing, 5CB was evaporated and the fringe periodicity was equal to 4 μm (interference periodicity). Perpendicular and parallel cylinders were present in the troughs and in the crests respectively. The thickness of the film was around 30 nm and 70 nm at the troughs and the crests respectively. Moreover, similarly as in Ref. [70], a control of the in-plane alignment of the cylinders in the troughs was obtained due to the orientation of the azobenzene chromophores perpendicularly to the polarization plane of light (Figure 2.22). Indeed, depending on the polarization direction used, the direction of hthe cylinders was either parallel (Figure 2.22 (a)) or perpendicular (Figure 2.22 (e)) to the groove direction.

When only a weak SRG appears during the holographic grating, a simple thermal annealing may be enough to enhance the SRG as it was demonstrated by Yu *et al.* (Figure 2.23) [73]. Holographic writing on a film of PEO_{40}-*b*-PAz_{37} produced an initial SRG with a magnitude of around 16 nm in height (Figure 2.23 (a)). After the annealing of the film at 100 ℃ for 24 h, the height between the crests and the troughs was about 110 nm. Despite the fact that SRG are of great interest due to their important contribution to the diffraction efficiency, they are some-

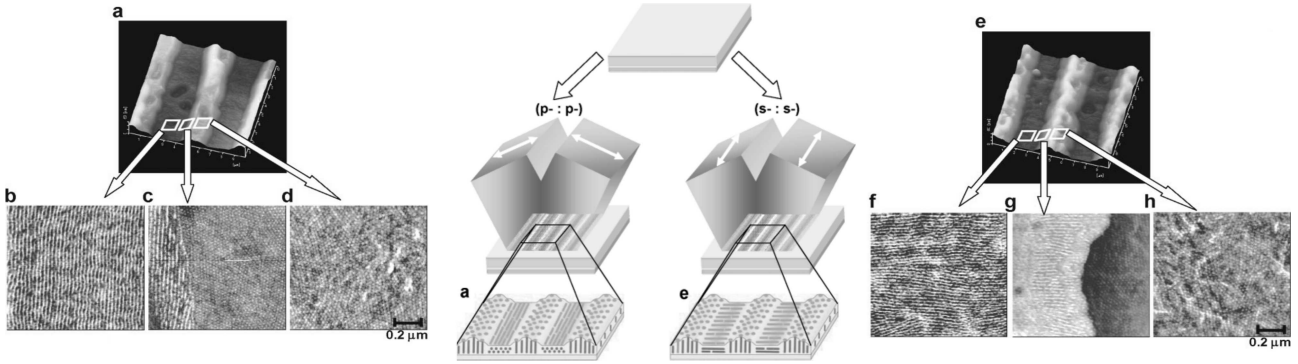

Figure 2.22: Schematic representation of the structure of the PEO-*b*-PAz thin film. In the non-irradiated regions (crests) PEO cylinders are perpendicular to the substrate. In the irradiated regions (troughs), the PEO cylinders are oriented parallel to the substrate. The left and right panels present the AFM images recorded on different areas of PEO-b-PAz thin films irradiated with interference patterns using p and s polarized light, respectively. Adapted from Ref. [75].

times undesirable. Indeed, the surface deformation is often irreversible (or at least difficult to erase) and can be a drawback for efficient and fast re-writable data storage. Moreover, SRG is unsuitable for achieving high angular selectivity which is a key feature for volume holography [79,80]. When thicker films are needed, for example to achieve high angular selectivity allowing to superimpose volume gratings at the same spot, another requirement is the adequate optical response of those films. Azobenzene containing polymers provide generally too much optical density because of their high absorption efficiency. One way to decrease the optical density is to dilute the chromophores by using block copolymers. Indeed, the microphase separation of block copolymers generates nano domains in which a gathering of the chromophores can occur. This confinement enables the dilution of the azobenzene moieties while keeping a good optical response.

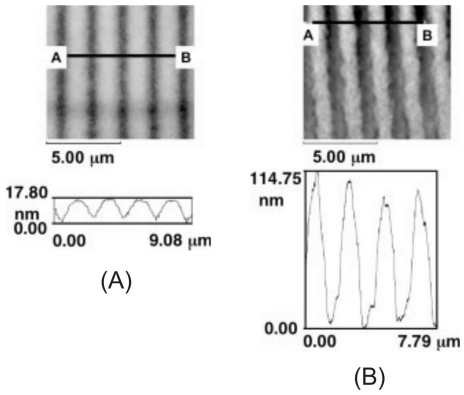

Figure 2.23: Thermal enhancement of SRG in a PEO_{40}-*b*-PAz_{37} film. AFM pictures before (A), and after (B) annealing. Reproduced from Ref [73].

In this optic, Schmidt and coworkers investigated the photo-addressability of different PS-*b*-P(Az-*co*-BP) copolymers in which azobenzenes coexist with other biphenyl based mesogens (BP) in the second block [79]. The block copolymers have the same degree of polymerization but different azobenzene to biphenyl mesogens ratios. The introduction of non-photosensitive mesogenic moieties contributes to lower the optical density while keeping a good photo-controlled organization through co-

operative motions. Successful holographic inscriptions were performed on 10 μm thick films made from such PS-*b*-P(Az-*co*-BP). The long-term stability of the gratings was also demonstrated since the refractive-index modulations imprinted were still stable after 270 or 480 days depending on the block copolymer used.

In order to further decrease the optical density, the same authors blended a polystyrene-block-poly(hydroxyethyl methacrylate), PS-*b*-P-HEMA, where the HEMA block is partially grafted with azobenzenes and biphenyl mesogens, with polystyrene [81]. The chemical structure of the block copolymer is shown in Figure 2.24. The blend of this di-block (5 wt.-%) with PS (95 wt.-%) was processed by injection-molding in order to obtain a film with a diameter of 25 mm and a thickness of 1.1 mm (Figure 2.24 , (b)). Thanks to this thickness, angular multiplexing of a large number (up to 80) of stable holographic gratings was demonstrated. Moreover, re-writing was also tested and several writing and erasure cycles (1000 cycles) were performed without degradation of the material. However, the introduction of non-photosensitive mesogen groups slows down the writing time. This is explained by the time needed for the cooperative motion to take place. This issue could be circumvented by using mesogenic azobenzene chromophores which form a liquid-crystalline phase without additional mesogenic side chains.

Finally, in addition to all those considerations, the nature of the block bearing the chromophores is also a key feature for holographic media. For instance, PEO is a soft polymer with a low glass-transition temperature (T_g) which facilitates the movement of the polymer chains in a cooperative motion. However, its low Tg and its relatively high hydrophilicity limit the use of PEO in recording media [74]. Polystyrene, on the other hand displays much more stability ($T_g \sim 100$ °C) and for the moment, PMMA is attracting a lot of attentions because of its good optical transparency. Studies on PMMA based homopolymers and random and block copolymers containing azobenzenes, as well as on blends, have been recently published and are on going [74, 81, 82].

Some interesting features involving holographic gratings on elastic materials have been reported [83–87]. In those studies, the well-known thermoplastic elastomer polystyrene-*block*-polybutadiene-*block*-polystyrene (SBS) has been used. When the PS content is equal to

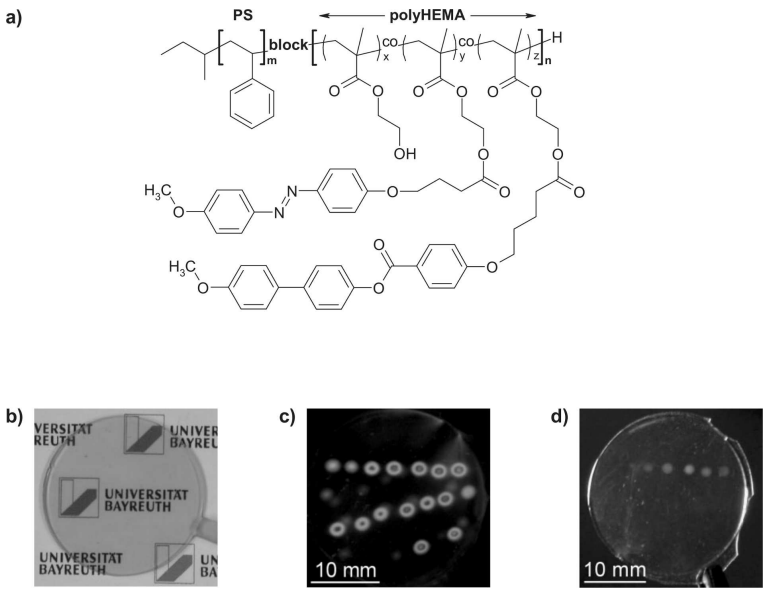

Figure 2.24: a) Structure of the PS-*b*-PHEMA with photoaddressable azobenzenes and BP mesogenic side chains in the HEMA block forming the minority phase (m = 528, n = 40) b) Picture of an injection-molded sample with a diameter of 25 mm and a thickness of 1.1 mm. c) Sample with several inscribed holograms between crossed polarizers. d) Sample showing the first diffraction order of some of these holograms under illumination with white light. Adapted from Ref. [80].

20-30 %, the microphase separation provides PS nano-cylinders which act as cross-linkers for the rubbery PB chains. In order to give a photo-responsive nature to SBS, the authors performed a free radical polymerization of azobenzene LC monomers in the presence of SBS. Radical transfer from the initiator onto the PB sequence enables the subsequent initiation and polymerization from the PB chains. In that manner, SBS with azobenzene polymer side chains grafted on the PB block was obtained [83].

Polymer films made from azobenzene grafted SBS display some interesting properties (Figure 2.25). The azobenzene molecules in the unstretched films are in a non-oriented *trans* state (Figure 2.25 (1)). Upon

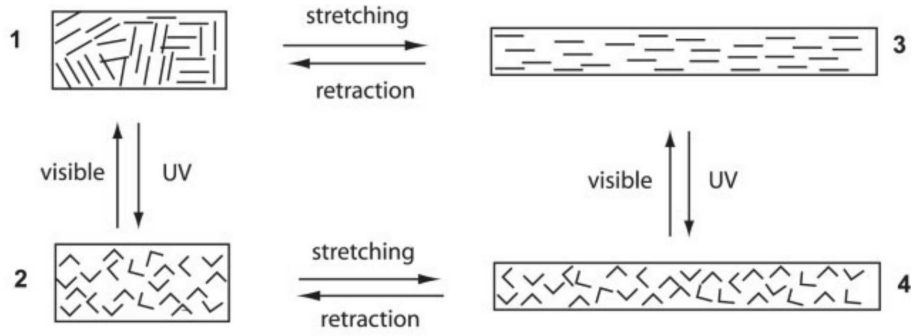

Figure 2.25: Schematic illustration of the reversible switching of films of SBS grafted with azobenzenes under mechanical stress and light illumination. Reproduced from Ref. [86].

UV irradiation, a reversible isotropic *cis* rich state is formed (Figure 2.25 (2)) which can undergo reversible stretching (Figure 2.25 (4)). Starting form the unstrectched *trans* state (1), azobenzene moieties are able to orient themselves upon deformation with their long axis parallel to the stretching direction (Figure 2.25 (3)). This chromophore alignment is reversible and the degree of order can be tuned by the intensity of the deformation: the more the film is stretched, the more the chromophores are aligned. Finally, the oriented state (3) can be erased by UV irradiation, and completely recovered upon visible irradiation. Interestingly, the azobenzenes in the stretched film are not prompt to photo-alignment as both polarized and non-polarized illumination restores the alignment in the strain direction.

The inscription of birefringent diffraction gratings was demonstrated by photo-patterning stretched films at different extension degrees [87]. Parallel and perpendicular fringes were inscribed by irradiating stretched films (state 3) at 360 nm (Figure 2.26). The non-illuminated regions keep the *trans* oriented configuration of the chromophores while the disordered *cis* state was observed in the illuminated areas. It was shown that the diffraction efficiency (DE) is proportional to the draw ratio and can be reversibly switched back and forth upon retractation/restretching. Another writing method consisting in photo-patterning the disordered stretched films (state 4) was also studied. While gratings were suc-

cessfully obtained, they were however not as clear and stable as those obtained by the first method.

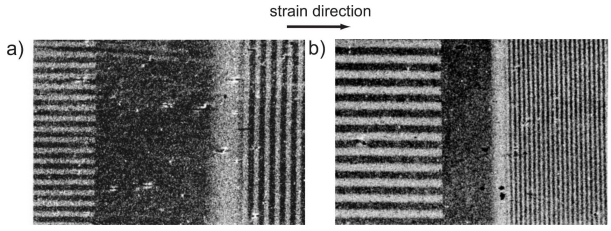

Figure 2.26: Polarized optical micrographs of two inscribed gratings (10 μm fringe spacing) recorded on a film under a 300 % stretching (a), and the same film after a retraction of the half of the length (b). Reproduced from Ref. [85]

An intriguing behavior was observed when the photosensitive SBS film was subjected to holographic gratings. Figure 2.27 clearly shows that DE increases with the strain intensity. Surprisingly, this first grating is erased and replaced with a second one as the irradiation time increases. The second grating displays higher DE, long term stability, and no erasure upon UV or visible light was possible. This phenomenon can be explained by in depth reorganizations of the polymeric chains inside the material. Upon irradiation, the illuminated regions become disordered because the azobenzene *cis*-isomers display no LC feature. As those regions are no more able to endure the constraint, a relaxation of the PB chains occurs and causes an in depth reorganization in the internal structure of the film. This feature is undesirable for rewriting applications but might be useful for potential secure and long-term recording.

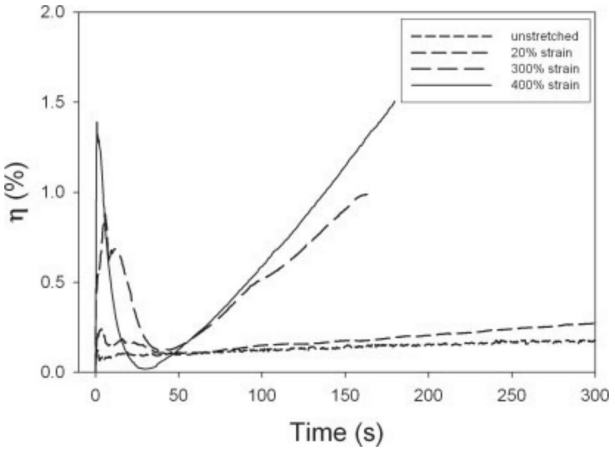

Figure 2.27: First-order diffraction efficiency *vs.* exposure time for films stretched at different strains. Irradiation wavelength: 350 nm; gratings periodicity: 2 μm. Reproduced from Ref. [85].

2.3.2 Linear photocleavable block copolymers

The great majority of the light-responsive block copolymers encountered bear the chromophores as side groups. Such architectures lead to a modification of the sequence bearing the chromophores after exposure to the appropriate light. On the other hand, when a photocleavable moiety is inserted at the junction between the blocks, the copolymer can split into its distinct sequences upon exposure to light. Block copolymers in which the blocks are held together by a cleavable junction are notably interesting because they can be used as precursors for generating hollow structures (hollow micelles and nanoporous polymeric materials) [88–90]. The underlying strategy is the self-assembly of the block copolymer into the desired structures followed by the cleavage of the junction to release the minor block and its removal to create the porosity. Several examples of cleavable junctions sensitive to chemical stimuli have been reported [91–93]. Those junctions were based on supramolecular interactions (such as hydrogen bonding or metal-ligand complexes), tritylether linkage, or disulfide bond. As already mentioned, turning to photocleavable junctions has the advantage to avoid any chemical reagents and to control the reaction from outside of the system, which is especially important for solid state applications.

2.3.2.1 Anthracene based junction

Anthracene [4+4] photo-dimerization has been widely studied in organic chemistry, notably because of the reversible feature of the reaction [94, 95]. Müllen and coworkers described the photo-coupling and the reverse photocleavage of, respectively, PMMA and PS end-capped with an anthracene group [96, 97]. For instance, when irradiated at 366 nm, the PS chains combine themselves to yield the dimeric form (Figure 2.28). After irradiation at 280 nm, the anthracene moieties are quantitatively recovered leading to the cleavage of the dimer into the native polymeric material. Of note, no degradation of the end groups nor of the polymer chains has been observed, even after 10 dimerization-dissociation cycles. Although the obtained dimers were A-*b*-A homopolymers, they have paved the way toward the incorporation of photolabile junctions into block copolymers.

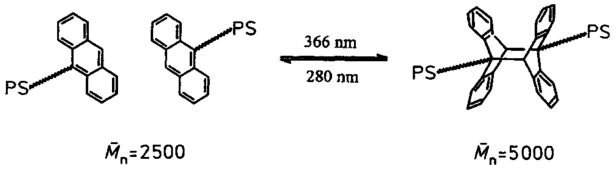

Figure 2.28: Reversible photo-dimerization of ω-anthrylpolystyrene. Reproduced from Ref. [97].

Following those lines, Russell and coworkers described the synthesis of the first photocleavable A-*b*-B diblock [98]. The diblock synthesis proceeded through a UV coupling between anthracene end-capped PS and PMMA, leading to a PS-*AA*-PMMA copolymer containing a photocleavable anthracenic dimer junction (Figure 2.29). Despite long reaction time and side homo-coupling of PS and PMMA, the diblock was successfully obtained. The morphology of thin films prepared from this copolymer was then studied. Dissociation of the anthracenic junction was observed during thermal annealing of the thin films. For an annealing at 135 °C , the thermal cleavage was estimated to around 30 %. Nevertheless, a self-assembled morphology composed of PMMA cylinders perpendicular to the substrate in a PS matrix was observed. Above this temperature, the thermal cleavage is too important and a macrophase

separation is observed. To circumvent this problem, annealing in supercritical CO_2 was performed, and the thermal cleavage was used to alter the morphologies of the thin films and to create porosity [99]. Although the cleavage by UV irradiation in solution was demonstrated, no characterization of the thin films under UV irradiation was mentioned.

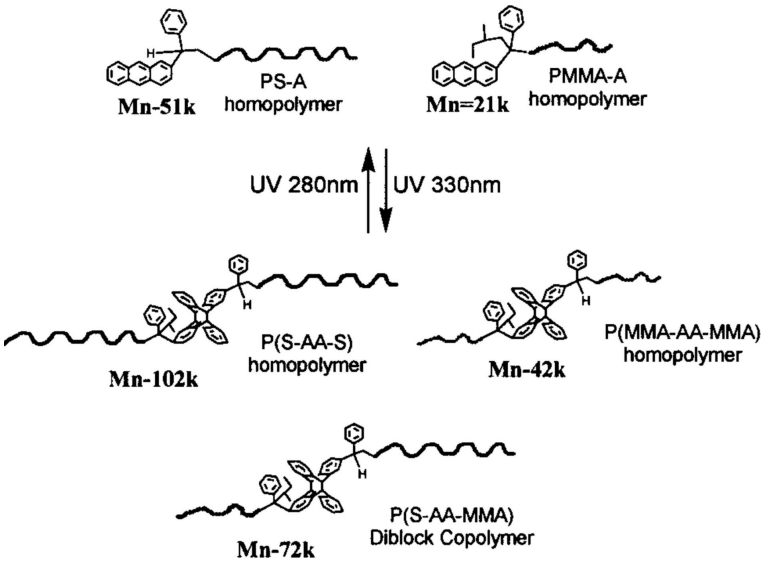

Figure 2.29: UV coupling of anthracene end-functionalized PS and PMMA. Reproduced from Ref. [98].

2.3.2.2 Nitrobenzyl ester based junction

Kang and Moon were the first to demonstrate the possibility to achieve nanoporous thin films from a photocleavable PS-*b*-PEO copolymer bearing an *o*-nitrobenzyl junction [100]. The block copolymer was synthesized by the ATRP of styrene initiated by a PEO macroinitator bearing the photocleavable group at the initiator chain end. The self-assembly of this block copolymer led to thin films presenting a PS matrix with PEO cylinders oriented perpendicular to the substrate. Upon UV irradiation at 350 nm, the *o*-nitrobenzyl junction was cleaved and the PEO phase was selectively removed with a methanol/water mixture (a non-solvent of PS). The film porosity was demonstrated by transmis-

sion electronic microscopy (TEM) and scanning electronic microscopy (SEM) measurements. Thanks to an intra-molecular mechanism (Norrish II type), the photocleavage could be performed in the solid state since only light is necessary to trigger the process.

2.4 Conclusions

This chapter has highlighted the interest of light-responsive block copolymers. The different photo-sensitive moieties incorporated so far in block copolymers have been presented and their related potential applications have been discussed.

Firstly we focused on the irreversible and reversible light-induced destabilization of micelles. Pyrene, nitrobenzyl, and coumarin moieties have been essentially considered in irreversible pathways while reversible processes are based on the isomerization of azobenzene and spiropyran chromophores. Photo-controlled cross-linking of micelles was then tackled with the photodimerization of cinnamic and coumarin groups as they can improve the stability of these nano-objects. Finally, the combination with thermal responsiveness showed some interesting changes in the LSCT of the used block copolymers. The main motivation of those works is to provide nanocontainers for the light-triggered encapsulation and release of molecules since light enables the use of mild conditions and a good spatial and temporal control. However, reversible isomerization processes should still be improved. Indeed, the change in polarity induced by the isomerization of azobenzene is, in most cases, not large enough, and the bulkiness and the presence of nitro groups in spiropyran can be annoying. Thus, there is a clear need to improve the existing systems or to find other suitable photo-sensitive moieties exhibiting large change in polarity upon illumination. The kinetics of those reversible isomerization processes is also a crucial feature for the practical application of such systems that has been often poorly discussed in the published examples.

The second part of this chapter dealt with the behavior of light-responsive block copolymers in the solid state. In that field, azobenzene-containing block copolymers are on top, notably because of the liquid crystal feature they can show. Indeed, they enable molecular cooper-

ative motions which is the key point in microdomain photo-alignment and holographic writing. In some cases, such phenomenon lead to massive transport of the polymeric material and surface relief processes take place. In addition, elastic holographic materials can be achieved when azobenzene chromophores are incorporated in thermoplastic elastomers. Azobenzene moieties revealed to be good candidates for holography. However, the thermal *cis*-to-*trans* isomerization might be an issue for long-term data storage and has to be kept in mind for the design of applications. Finally diblocks presenting a photocleavable junction between the blocks have been discussed. Those polymers have potential applications as precursors of nanoporous materials. Important issues related to such copolymers are the choices of the cleavable group itself and of the synthetic method allowing its incorporation in the block copolymer architecture. Finally, the use of light as stimulus is particularly interesting in the solid state because it can penetrates the matter better than other reagents.

Throughout this variety of examples, the aim of this work was to convince the readers of the versatility and usefulness of light as a stimulus in polymer science. Indeed, this *often underestimated reagent* presents some advantages not shown by others and has to be considered for itself and also as a complement to other stimuli.

Bibliography

[1] Gil, E. S.; Hudson, S. A. *Prog. Polym. Sci.* **2004**, *29*, 1173–1222.

[2] Alarcon, C. D. H.; Pennadam, S.; Alexander, C. *Chem. Soc. Rev.* **2005**, *34*, 276–285.

[3] Rapoport, N. *Prog. Polym. Sci.* **2007**, *32*, 962–990.

[4] Rodriguez-Hernandez, J.; Checot, F.; Gnanou, Y.; Lecommandoux, S. *Prog. Polym. Sci.* **2005**, *30*, 691–724.

[5] Dai, S.; Ravi, P.; Tam, K. C. *Soft Matter* **2009**, *5*, 2513–2533.

[6] Gohy, J. F. *Adv. Polym. Sci.* **2005**, *190*, 65–136.

[7] Hamley, I. W. *Angew. Chem. Int. Ed.* **2003**, *42*, 1692–1712.

[8] Kim, H. C.; Park, S. M.; Hinsberg, W. D. *Chem. Rev.* **2010**, *110*, 146–177.

[9] Matyjaszewski, K.; Xia, J. H. *Chem. Rev.* **2001**, *101*, 2921–2990.

[10] Hawker, C. J.; Bosman, A. W.; Harth, E. *Chem. Rev.* **2001**, *101*, 3661–3688.

[11] Perrier, S.; Takolpuckdee, P. *J. Polym. Sci. Part A* **2005**, *43*, 5347–5393.

[12] Barner-Kowollik, C.; Perrier, S. *J. Polym. Sci. Part A* **2008**, *46*, 5715–5723.

[13] Moad, G.; Rizzardo, E.; Thang, S. H. *Polymer* **2008**, *49*, 1079–1131.

[14] Barner-Kowollik, C. *Handbook of RAFT Polymerization*; Wiley-VCH: Weinheim, 2008.

[15] Zhao, Y. *J. Mater. Chem.* **2009**, *19*, 4887–4895.

[16] Ercole, F.; Davis, T. P.; Evans, R. A. *Polym. Chem.* **2010**, *1*, 37–54.

[17] Jiang, J. Q.; Tong, X.; Morris, D.; Zhao, Y. *Macromolecules* **2006**, *39*, 4633–4640.

[18] Jiang, J. Q.; Tong, X.; Zhao, Y. *J. Am. Chem. Soc.* **2005**, *127*, 8290–8291.

[19] Babin, J.; Pelletier, M.; Lepage, M.; Allard, J. F.; Morris, D.; Zhao, Y. *Angew. Chem. Int. Ed.* **2009**, *48*, 3329–3332.

[20] Muraoka, T.; Cui, H.; Stupp, S. I. *J. Am. Chem. Soc.* **2008**, *130*, 2946–2947.

[21] Palmer, L. C.; Stupp, S. I. *Acc. Chem. Res.* **2008**, *41*, 1674–1684.

[22] Wang, G.; Tong, X.; Zhao, Y. *Macromolecules* **2004**, *37*, 8911–8917.

[23] Kumar, G. S.; Neckers, D. C. *Chem. Rev.* **1989**, *89*, 1915–1925.

[24] Ichimura, K. *Chem. Rev.* **2000**, *100*, 1847–1873.

[25] Natansohn, A.; Rochon, P. *Chem. Rev.* **2002**, *102*, 4139–4175.

[26] Tong, X.; Wang, G.; Soldera, A.; Zhao, Y. *J. Phys. Chem. B* **2005**, *109*, 20281–20287.

[27] Lee, H. I.; Wu, W.; Oh, J. K.; Mueller, L.; Sherwood, G.; Peteanu, L.; Kowalewski, T.; Matyjaszewski, K. *Angew. Chem. Int. Ed.* **2007**, *46*, 2453–2457.

[28] Su, W.; Zhao, H.; Wang, Z.; Li, Y. M.; Zhang, Q. J. *Eur. Polym. J.* **2007**, *43*, 657–662.

[29] Sin, S. L.; Gan, L. H.; Hu, X.; Tam, K. C.; Gan, Y. Y. *Macromolecules* **2005**, *38*, 3943–3948.

[30] Su, W.; Luo, Y. H.; Yan, Q.; Wu, S.; Han, K.; Zhang, Q. J.; Gu, Y. Q.; Li, Y. M. *Macromol. Rapid Commun.* **2007**, *28*, 1251–1256.

[31] Wang, D. R.; Ye, G.; Wang, X. G. *Macromol. Rapid Commun.* **2007**, *28*, 2237–2243.

[32] Han, K.; Su, W.; Zhong, M. C.; Yan, Q.; Luo, Y. H.; Zhang, Q. J.; Li, Y. M. *Macromol. Rapid Commun.* **2008**, *29*, 1866–1870.

[33] Lin, L.; Yan, Z.; Gu, J. S.; Zhang, Y. Y.; Feng, Z.; Yu, Y. L. *Macromol. Rapid Commun.* **2009**, *30*, 1089–1093.

[34] Wang, D. R.; Liu, J. P.; Ye, G.; Wang, X. G. *Polymer* **2009**, *50*, 418–427.

[35] Ravi, P.; Sin, S. L.; Gan, L. H.; Gan, Y. Y.; Tam, K. C.; Xia, X. L.; Hu, X. *Polymer* **2005**, *46*, 137–146.

[36] Jochum, F. D.; Theato, P. *Polymer* **2009**, *50*, 3079–3085.

[37] Tang, X. D.; Gao, L. C.; Fan, X. H.; Liang, X. C.; Zhou, Q. F. *Macromol. Chem. Phys.* **2009**, *210*, 1556–1562.

[38] O'Reilly, R. K.; Hawker, C. J.; Wooley, K. L. *Chem. Soc. Rev.* **2006**, *35*, 1068–1083.

[39] Read, E. S.; Armes, S. P. *Chem. Commun.* **2007**, 3021–3035.

[40] Guo, A.; Liu, G. J.; Tao, J. *Macromolecules* **1996**, *29*, 2487–2493.

[41] Ding, J. F.; Liu, G. J. *Chem. Mater.* **1998**, *10*, 537–542.

[42] Sandholzer, M.; Bichler, S.; Stelzer, F.; Slugovc, C. *J. Polym. Sci. Part A: Polym. Chem.* **2008**, *46*, 2402–2413.

[43] Yusa, S.; Sugahara, M.; Endo, T.; Morishima, Y. *Langmuir* **2009**, *25*, 5258–5265.

[44] Jiang, J. Q.; Qi, B.; Lepage, M.; Zhao, Y. *Macromolecules* **2007**, *40*, 790–792.

[45] Babin, J.; Lepage, M.; Zhao, Y. *Macromolecules* **2008**, *41*, 1246–1253.

[46] Jiang, X.; Lavender, C. A.; Woodcock, J. W.; Zhao, B. *Macromolecules* **2008**, *41*, 2632–2643.

[47] He, J.; Tong, X.; Tremblay, L.; Zhao, Y. *Macromolecules* **2009**, *42*, 7267–7270.

[48] He, J.; Tong, X.; Zhao, Y. *Macromolecules* **2009**, *42*, 4845–4852.

[49] Ikeda, T. *J. Mater. Chem.* **2003**, *13*, 2037–2057.

[50] Delaire, J. A.; Nakatani, K. *Chem. Rev.* **2000**, *100*, 1817–1845.

[51] Bohnert, R.; Finkelmann, H. *Macromol. Chem. Phys.* **1994**, *195*, 689–700.

[52] Walther, M.; Bohnert, R.; Derow, S.; Finkelmann, H. *Macromol. Rapid Commun.* **1995**, *16*, 621–629.

[53] Martin, A.; Tefehne, C.; Gronski, W. *Macromol. Rapid Commun.* **1996**, *17*, 305–311.

[54] Walther, M.; Finkelmann, H. *Prog. Polym. Sci.* **1996**, *21*, 951–979.

[55] Mao, G. P.; Wang, J. G.; Clingman, S. R.; Ober, C. K.; Chen, J. T.; Thomas, E. L. *Macromolecules* **1997**, *30*, 2556–2567.

[56] Walther, M.; Faulhammer, H.; Finkelmann, H. *Macromol. Chem. Phys.* **1998**, *199*, 223–237.

[57] Moriya, K.; Seki, T.; Nakagawa, M.; Mao, G. P.; Ober, C. K. *Macromol. Rapid Commun.* **2000**, *21*, 1309–1312.

[58] Tian, Y. Q.; Watanabe, K.; Kong, X. X.; Abe, J.; Iyoda, T. *Macromolecules* **2002**, *35*, 3739–3747.

[59] Cui, L.; Zhao, Y.; Yavrian, A.; Galstian, T. *Macromolecules* **2003**, *36*, 8246–8252.

[60] Tong, X.; Cui, L.; Zhao Y., *Macromocecules* **2004**, *37*, 3101–3112.

[61] Yu, H. F.; Iyoda, T.; Okano, K.; Shishido, A.; Ikeda, T. *Mol. Cryst. Liq. Cryst.* **2005**, *443*, 191–199.

[62] Frenz, C.; Fuchs, A.; Schmidt, H. W.; Theissen, U.; Haarer, D. *Macromol. Chem. Phys.* **2004**, *205*, 1246–1258.

[63] Yu, H. F.; Shishido, A.; Ikeda, T.; Iyoda, T. *Macromol. Rapid Commun.* **2005**, *26*, 1594–1598.

[64] Yu, H. F.; Asaoka, S.; Shishido, A.; Iyoda, T.; Ikeda, T. *Small* **2007**, *3*, 768–771.

[65] Zhao, Y.; Qi, B.; Tong, X.; Zhao, Y. *Macromolecules* **2008**, *41*, 3823–3831.

[66] Weigert, T. *Verh. Phys. Ges. Berlin* **1919**, *21*, 485.

[67] Kadota, S.; Aoki, K.; Nagano, S.; Seki, T. *J. Am. Chem. Soc.* **2005**, *127*, 8266–8267.

[68] Morikawa, Y.; Kondo, T.; Nagano, S.; Seki, T. *Chem. Mater.* **2007**, *19*, 1540–1542.

[69] Yu, H. F.; Iyoda, T.; Ikeda, T. *J. Am. Chem. Soc.* **2006**, *128*, 11010–11011.

[70] Hesselink, L.; Orlov, S. S.; Bashaw, M. C. *P. IEEE* **2004**, *92*, 1231–1280.

[71] Ashley, J.; Bernal, M. P.; Burr, G. W.; Coufal, H.; Guenther, H.; Hoffnagle, J. A.; Jefferson, C. M.; Marcus, B.; Macfarlane, R. M.; Shelby, R. M.; Sincerbox, G. T. *IBM J. Res. Dev.* **2000**, *44*, 341–368.

[72] Yamamoto, T.; Hasegawa, M.; Kanazawa, A.; Shiono, T.; Ikeda, T. *J. Phys. Chem. B* **1999**, *103*, 9873–9878.

[73] Yu, H. F.; Okano, K.; Shishido, A.; Ikeda, T.; Kamata, K.; Komura, M.; Iyoda, T. *Adv. Mater.* **2005**, *17*, 2184–2188.

[74] Yu, H.; Naka, Y.; Shishido, A.; Ikeda, T. *Macromolecules* **2008**, *41*, 7959–7966.

[75] Morikawa, Y.; Nagano, S.; Watanabe, K.; Kamata, K.; Iyoda, T.; Seki, T. *Adv. Mater.* **2006**, *18*, 883–886.

[76] Knoll, A.; Horvat, A.; Lyakhova, K. S.; Krausch, G.; Sevink, G. J. A.; Zvelindovsky, A. V.; Magerle, R. *Phys. Rev. Lett.* **2002**, *89*, 035501/1–4.

[77] Lazzari, M.; De Rosa, C. In *Block CoPolymers in Nanoscience*; Wiley-VCH, W., Ed.; Lazzari, M.; Liu, G.; Lecommandoux, S., 2006; Chapter 9, pp 191–229.

[78] Ubukata, T.; Seki, T.; Ichimura, K. *Adv. Mater.* **2000**, *12*, 1675–1678.

[79] Hackel, M.; Kador, L.; Kropp, D.; Frenz, C.; Schmidt, H. W. *Adv. Funct. Mater.* **2005**, *15*, 1722–1727.

[80] Hackel, M.; Kador, L.; Kropp, D.; Schmidt, H.-W. *Adv. Mater.* **2007**, *19*, 227–231.

[81] Breiner, T.; Kreger, K.; Hagen, R.; Hackel, M.; Kador, L.; Muller, A. H. E.; Kramer, E. J.; Schmidt, H. W. *Macromolecules* **2007**, *40*, 2100–2108.

[82] Forcen, P.; Oriol, L.; Sanchez, C.; Rodriguez, F. J.; Alcala, R.; Hvilsted, S.; Jankova, K. *Eur. Polym. J.* **2007**, *43*, 3292–3300.

[83] Bai, S. Y.; Zhao, Y. *Macromolecules* **2001**, *34*, 9032–9038.

[84] Bai, S. Y.; Zhao, Y. *Macromolecules* **2002**, *35*, 9657–9664.

[85] Zhao, Y.; Bai, S. Y.; Dumont, D.; Galstian, T. V. *Adv. Mater.* **2002**, *14*, 512–514.

[86] Zhao, Y.; Bai, S. Y.; Asatryan, K.; Galstian, T. *Adv. Funct. Mater.* **2003**, *13*, 781–788.

[87] Cui, L.; Tong, X.; Yan, X. H.; Liu, G. J.; Zhao, Y. *Macromolecules* **2004**, *37*, 7097–7104.

[88] Guo, M. Y.; Jiang, M. *Soft Matter* **2009**, *5*, 495–500.

[89] Chen, D. Y.; Jiang, M. *Acc. Chem. Res.* **2005**, *38*, 494–502.

[90] Hillmyer, M. A. *Adv. Polym. Sci.* **2005**, *190*, 137–181.

[91] Fustin, C. A.; Lohmeijer, B. G. G.; Duwez, A. S.; Jonas, A. M.; Schubert, U. S.; Gohy, J. F. *Adv. Mater.* **2005**, *17*, 1162–1165.

[92] Zhang, M. F.; Yang, L.; Yurt, S.; Misner, M. J.; Chen, J. T.; Coughlin, E. B.; Venkataraman, D.; Russell, T. P. *Adv. Mater.* **2007**, *19*, 1571–1576.

[93] Ryu, J. H.; Park, S.; Kim, B.; Klaikherd, A.; Russell, T. P.; Thayumanavan, S. *J. Am. Chem. Soc.* **2009**, *131*, 9870–9871.

[94] Becker, H. D. *Chem. Rev.* **1993**, *93*, 145–172.

[95] Bouas-Laurent, H.; Castellan, A.; Desvergne, J. P.; Lapouyade, R. *Chem. Soc. Rev.* **2000**, *29*, 43–55.

[96] Bartz, T.; Klapper, M.; Mullen, K. *Macromol. Chem. Phys.* **1994**, *195*, 1097–1109.

[97] Coursan, M.; Desvergne, J. P.; Deffieux, A. *Macromol. Chem. Phys.* **1996**, *197*, 1599–1608.

[98] Goldbach, J. T.; Russell, T. P.; Penelle, J. *Macromolecules* **2002**, *35*, 4271–4276.

[99] Goldbach, J. T.; Lavery, K. A.; Penelle, J.; Russell, T. P. *Macromolecules* **2004**, *37*, 9639–9645.

[100] Kang, M.; Moon, B. *Macromolecules* **2009**, *42*, 455–458.

CHAPTER
THREE

OBJECTIVES

Abstract

The general aim of the thesis is the development of photocleavable block copolymers which can be further used to form nanoporous materials. The general frame of the project is presented here as well as the objectives of the thesis. The synthesis of new photocleavable block copolymers, their self-assembly into thin films and to the formation of nanopores in these thin films are the goals to be reached.

3.1 The project

In the past decade, block copolymers have emerged as powerful tools for preparing nanostructured materials [1, 2]. They are indeed able to self-assemble at the nanoscale into well-ordered morphologies and this property makes them of great importance in the field of nanotechnology. These self-assembled structures can be used, among other things, for the preparation of nanoporous materials by selectively removing the minor phase from the structure. These materials exhibit the pore topology and the pore size of their parent structures and can be further used as separation membranes and templates for other nanomaterials [2, 3].

Most methods reported up to now for the creation of nanopores rely on the degradation of the minor block by, for example, ozonolysis of polydienes, UV etching of polymethylmethacrylate, hydrolysis of polyesters, or HF etching, and offer thus a rather poor control over the functionality of the pore walls [4–7]. Several examples of cleavable junctions sensitive to chemical stimuli have also been reported [8–10]. Those junctions were based on, supramolecular interactions (such as metal-ligand complexes) [8], tritylether linkage [9], or disulfide bond [10]. Such junctions enable the use of mild conditions and in some cases lead to functionalized nanoporous materials. However, these strategies do not offer the possibility to tune the type of functionality, available into the pores.

In this thesis, a new approach towards nanoporous materials displaying chemical functionalities is proposed (Figure 3.1). The first step of this project is the synthesis of block copolymers containing one or several photocleavable moieties. Secondly, these copolymers are self-assembled in order to obtain a thin film with a cylindrical morphology displaying a perpendicular orientation of the cylinders. Finally, the film is exposed to UV-Visible light and washed with a selective solvent leading to a nanoporous thin film containing pores covered by chemical functions.

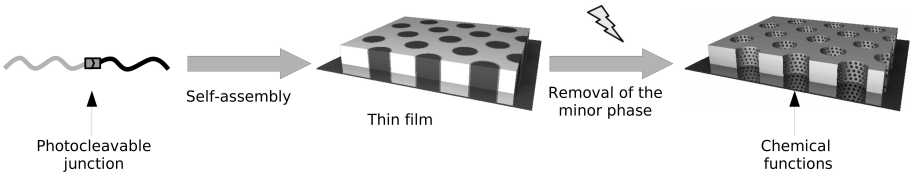

Figure 3.1: Strategy towards nanoporous materials with functionalized pore walls.

This strategy is inspired from organic chemistry where photocleavable moieties are often used as protecting groups [11, 12]. As already mentioned, turning to photocleavable junctions has the advantage to avoid chemical reagents and to control the reaction from outside of the system, which is especially important for solid state applications. Moreover, depending on the structure of the photo-sensitive derivative used, it will be possible to control the chemical functions.

The nanoporous materials made from those photocleavable copolymers may have two main applications. The first one is their use as selective membranes for protein filtration. After pore creation, a specific protein ligand could be fixed into the pores thanks to the chemical functions inside the pores (Figure 3.2). In this way, this system could be used to filter a solution containing different kinds of proteins by playing on steric effects (only the smallest proteins will go through the membrane) and on affinity (the proteins having affinity with the specific ligand will remain in the membrane).

The second application is the creation of inorganic nanodots. Actually, it is possible to fill the pores with metals. After the removal of the polymeric matrix, metallic nanodots can be obtained. Such materials can be used, for example, as high density data storage media. The advantage of a photocleavable approach is the possibility of creating heterogeneous nanoporous materials. In fact, a lithographic mask can be used to irradiate only some areas of the film. In this way, only the part of the materials which has been irradiated will provide porosity (Figure 3.3).

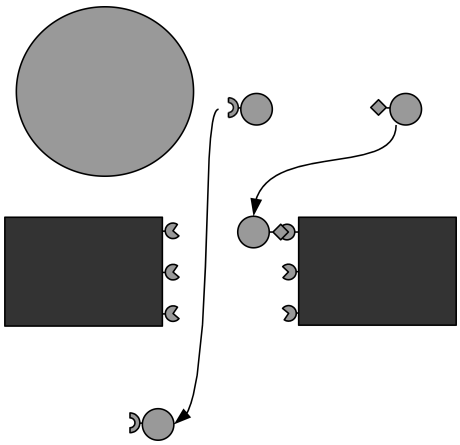

Figure 3.2: Nanofiltration based on the pore sizes and on the affinity.

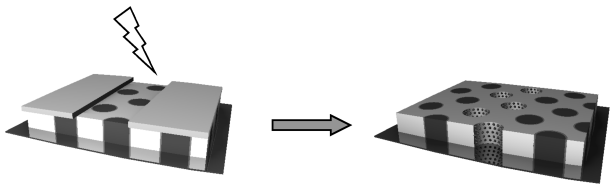

Figure 3.3: Formation of a heterogeneous nanoporous material using a lithographic mask.

3.2 The objectives

The aim of this thesis is to develop new block copolymers containing *o*-nitrobenzyl ester photocleavable groups. These moieties are one of the most used photocleavable protecting groups in organic synthesis [11,12]. Upon UV irradiation, these groups undergo a cleavage of the ester bond leading to carboxylic acid and nitroso-benzaldehyde counterparts (Figure 3.4). Depending on the structure of the *o*-nitrobenzyl derivatives, different chemical functions can be obtained. Indeed, like esters yield carboxylic acids, *o*-nitrobenzyl carbamates and carbonates provide amines and alcohols, respectively.

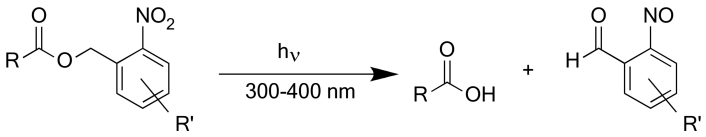

Figure 3.4: Photocleavage of *o*-nitrobenzyl ester.

3.2.1 Synthesis of photocleavable block copolymers

The synthesis of two families of photocleavable copolymers is proposed in this thesis (Figure 3.5). The first one is a linear polystyrene-*block*-poly(ethylene oxide) diblock copolymer with a nitrobenzyl junction ($h\nu$) between the two blocks (PS-$h\nu$-PEO). The second type of copolymer is made of a PS block and a poly(nitrobenzyl(meth)acrylate) sequence which bears photocleavable side groups (PS-*b*-PNB(M)A)). Once self-assembled, the linear photocleavable block copolymer (first family) will provide, after photocleavage, a material in which pore walls are covered with functional groups (Figure 3.5, top). On the other hand, the block copolymer bearing photocleavable side groups (second family) will lead to pore walls covered with functional polymer brushes (Figure 3.5, bottom). These nanopores will display a high density of chemical functions and will be able to open and close themselves depending on the swelling of the brushes that could be controlled by the used solvent.

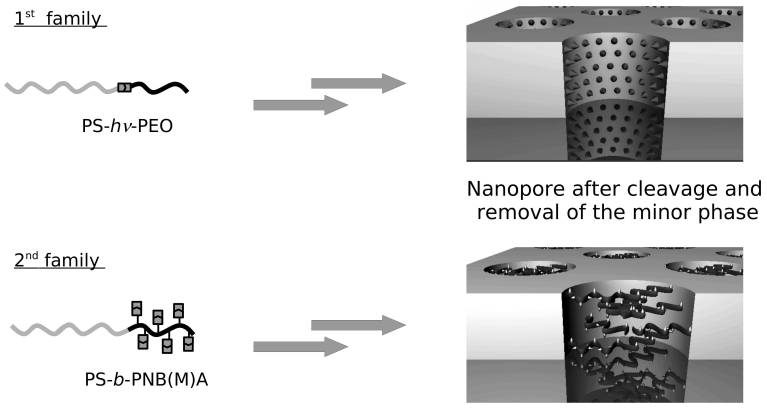

Figure 3.5: The two families of block copolymer considered in the thesis

For the first family, the synthetic key step is the quantitative incorporation of the photocleavable junction between the two blocks. Different strategies have been designed and are presented in Chapter 4. Concerning the second family, several strategies have also been considered and are described in Chapter 5. The pathways considered imply either the direct polymerization of photocleavable monomers (acrylate and methacrylate of *o*-nitrobenzyl ester (NBA and NBMA)) or the post-functionalization of a polystyrene-*block*-poly(acrylic acid) (PS-*b*-PAA) with *o*-nitrobenzyl derivatives.

After the synthesis of those photocleavable block copolymers, their behavior upon UV irradiation will be studied in solution in order to determine the optimal conditions for their photocleavage (see Chapter 6). Techniques such as UV-visible spectroscopy (UV-Vis), gel permeation chromatography (GPC) and nuclear magnetic resonance (NMR) will be used to investigate their photocleavage.

3.2.2 Self-assembly into a cylindrical morphology

The different synthetized photocleavable copolymers will be then self-assembled onto surfaces in order to obtain nanostructured thin films (see Chapter 7). Among the different possible nanostructures, a cylindrical morphology with a normal orientation of the cylinders is targeted. Atomic force microscopy (AFM) will provide information on the mor-

phology of the films and will be used for the optimization of the self-assembly conditions. Beside this technique, scanning and transmission electron microscopies (SEM and TEM) will also be performed to complete the characterization of the films.

As already discussed in the introduction, the morphology can be controlled by the volumic fraction, f, of the different blocks (see Section 1.3.1). For a cylindrical morphology, f should be roughly in a range of 0.2-0.3. For the first family based on PS-*b*-PEO (the PEO forming the cylinders), a total molar mass of the copolymer between 20,000 to 25,000 g/mol with a PEO block of 5,000 g/mol is targeted. Indeed, such a composition in PS/PEO is well-known to produce the desired cylindrical morphology [9, 13, 14]. For the second family, the composition of PS-*b*-PNB(M)A giving rise to cylinders is not available in the literature and the self-assembly of copolymers with different compositions will thus be investigated. The desired composition is estimated by the mass fraction r which is used as an estimate of the volume fraction f, since the density of PNB(M)A is not known. Values of r between 0.2 and 0.3 will be targeted for the synthesis of the PS-*b*-PNB(M)A copolymers.

3.2.3 Creation of the porosity

Exposing the thin films to UV radiations with the appropriate wavelength will cleave the photo-sensitive junctions. Nanoporosity will be obtained after extraction of the minor phase with a selective solvent. The porosity will be demonstrated with UV-vis and FT-IR spectroscopy as well as SEM and TEM microscopies (see Chapter 7).

Bibliography

[1] Hamley, I. W. *Angew. Chem. Int. Ed.* **2003**, *42*, 1692–1712.

[2] Park, C.; Yoon, J.; Thomas, E. L. *Polymer* **2003**, *44*, 6725–6760.

[3] Hillmyer, M. A. *Adv. Polym. Sci.* **2005**, *190*, 137–181.

[4] Park, M.; Harrison, C.; Chaikin, P. M.; Register, R. A.; Adamson, D. H. *Science* **1997**, *276*, 1401–1404.

[5] Thurn-Albrecht, T.; Steiner, R.; DeRouchey, J.; Stafford, C. M.; Huang, E.; Bal, M.; Tuominen, M.; Hawker, C. J.; Russell, T. *Adv. Mater.* **2000**, *12*, 787–791.

[6] Zalusky, A. S.; Olayo-Valles, R.; Wolf, J. H.; Hillmyer, M. A. *J. Am. Chem. Soc.* **2002**, *124*, 12761–12773.

[7] Ndoni, S.; Vigild, M. E.; Berg, R. H. *J. Am. Chem. Soc.* **2003**, *125*, 13366–13367.

[8] Fustin, C. A.; Lohmeijer, B. G. G.; Duwez, A. S.; Jonas, A. M.; Schubert, U. S.; Gohy, J. F. *Adv. Mater.* **2005**, *17*, 1162–1165.

[9] Zhang, M. F.; Yang, L.; Yurt, S.; Misner, M. J.; Chen, J. T.; Coughlin, E. B.; Venkataraman, D.; Russell, T. P. *Adv. Mater.* **2007**, *19*, 1571–1576.

[10] Ryu, J. H.; Park, S.; Kim, B.; Klaikherd, A.; Russell, T. P.; Thayumanavan, S. *J. Am. Chem. Soc.* **2009**, *131*, 9870–9871.

[11] Pillai, V. *Synthesis* **1980**, 1–26.

[12] Bochet, C. G. *J. Chem. Soc., Perkin Trans. 1* **2002**, 125–142.

[13] Lin, Z. Q.; Kim, D. H.; Wu, X. D.; Boosahda, L.; Stone, D.; LaRose, L.; Russell, T. P. *Adv. Mater.* **2002**, *14*, 1373–1376.

[14] Kim, S. H.; Misner, M. J.; Xu, T.; Kimura, M.; Russell, T. P. *Adv. Mater.* **2004**, *16*, 226–231.

CHAPTER
FOUR

SYNTHESIS OF LINEAR PHOTOCLEAVABLE DIBLOCK COPOLYMERS

Abstract

The synthesis of linear diblock copolymers, in which the link between the two blocks can be cleaved upon light illumination, is described. Three synthetic pathways have been investigated with a PEO-hν-PS block copolymer as target, the latter containing an o-nitrobenzyl ester photocleavable junction. The third strategy, involving a CuAAC-click reaction and an ATRP polymerization combined in a one-pot simultaneous process, turned out to be the best route for the synthesis of the desired PEO-hν-PS. Finally, several types of block copolymers have been successfully synthetized using this one-pot reaction, demonstrating the versatility of the approach.

4.1 Introduction

This chapter focuses on the synthesis of a photocleavable PEO-$h\nu$-PS able to self-assemble into thin films with a cylindrical morphophogy. As already mentioned in Chapter 3, this morphology can be obtained from PEO-*b*-PS diblocks having a molar mass (M_n) of about 20,000-25,000 g/mol and with the M_n of PEO equal to 5,000 g/mol. In order to obtain such a composition, the starting point of the synthesis is a commercially available mono-hydroxy poly(ethylene oxide) (PEO_{113}-OH[1], **7**) which M_n is precisely equal to 5,000 g/mol. Concerning the PS sequence, M_n's ranging from 15,000-20,000 g/mol are targeted and will be obtained, either by a commercial source or by ATRP polymerization of styrene. The two blocks will be linked together by an *o*-nitrobenzyl ester. This junction needs to be introduced in such a way that after photocleavage, a carboxylic acid function will be present on the chain end of the polystyrene block.

Three synthetic pathways towards PEO-$h\nu$-PS have been investigated and are presented in Figure 4.1. The first route (coupling strategy) consists in directly coupling two commercially available end-functionalized PEO and PS homopolymers. Some chemical modifications of the chain ends are however needed in order to introduce the desired *o*-nitrobenzyl moiety and to allow the coupling reaction. In this strategy, the photocleavable junction is not pre-existing and is formed during the coupling through the esterification between the carboxylic acid functionalized PS and the *o*-nitrobenzyl alcohol terminated PEO.

In the second strategy, the photocleavable moiety is firstly grafted on the PEO block which will be subsequently transformed into a photocleavable macroinitiator of polymerization (macroinitiator strategy). In a second step, the ATRP of styrene initiated by this macroinitiator will lead to the desired block copolymer.

The last route will perform the grafting of the photocleavable moiety and the polymerization of the second block in a simultaneous one pot process (one-pot strategy). The grafting of the *o*-nitrobenzyl is however not carried out in the same way than in the second route. Indeed, while the *o*-nitrobenzyl moiety will be introduced by an etherification reaction

[1]The number in subscript is the degree of polymerization of the polymer.

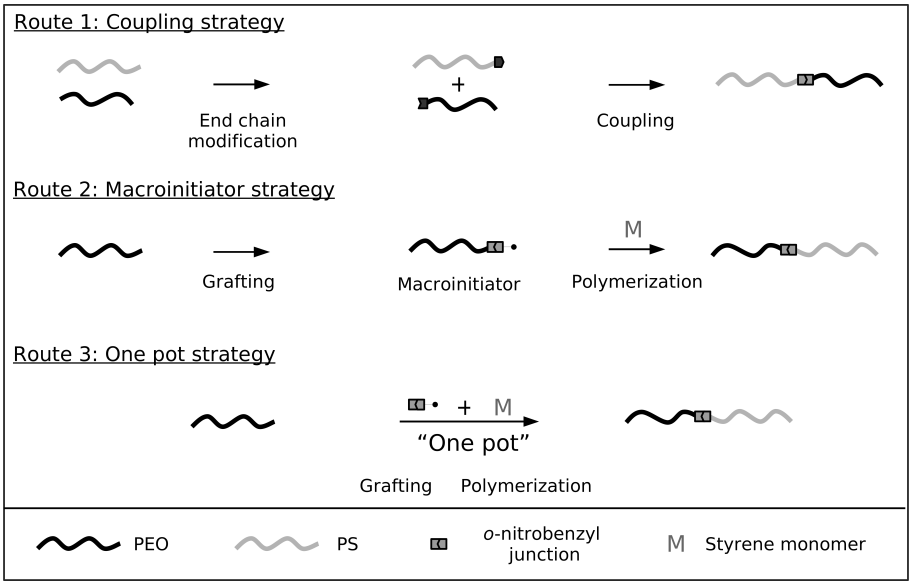

Figure 4.1: Synthesis strategies towards photocleavable PEO-$h\nu$-PS block copolymers.

in the second pathway, a CuAAC-click reaction will be used as linking tool in the third one.

4.2 Coupling strategy

The coupling strategy towards PS-$h\nu$-PEO is a three-step synthesis as depicted in Figure 4.2. A tosylate moiety (OTs), which is a good leaving group, is firstly grafted onto a mono-hydroxy terminated PEO of 5,000 g/mol (PEO_{113}-OH, **7**), to provide the PEO_{113}-OTs **8**. In a second step, the tosylate (OTs) is replaced by the *o*-nitrobenzyl alcohol **9** to produce **10**. Finally, the PS-$h\nu$-PEO (**12**) copolymer is obtained by coupling **10** with a carboxylic acid terminated PS of 16,500 g/mol (PS_{158}-COOH, **11**) via an esterification reaction. Those two functionalized homo-polymers are commercially available (Polymer Source, Inc.) and were prepared by anionic polymerization. They are thus characterized by a very narrow molar mass distribution (PDI < 1.10).

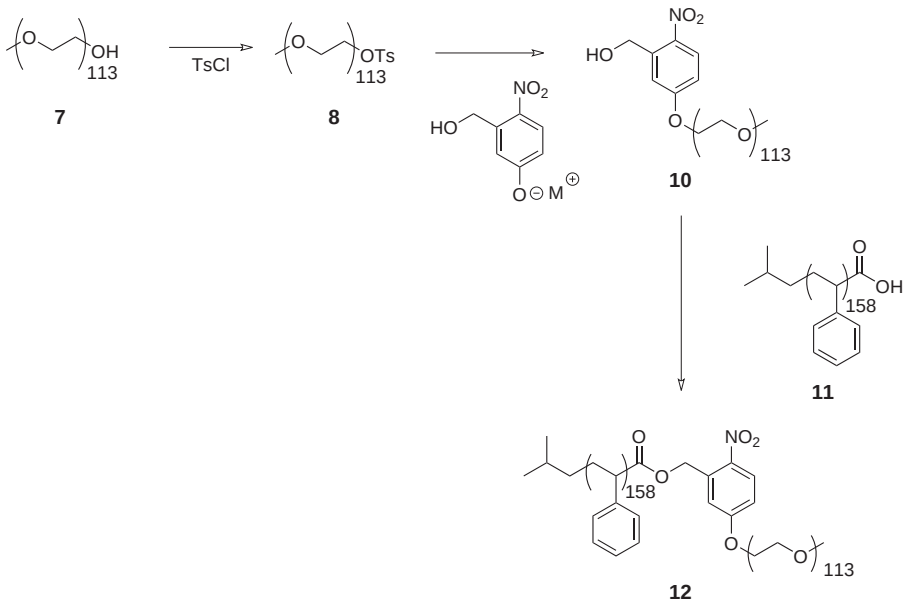

Figure 4.2: Coupling strategy. Toward PS-$h\nu$-PEO.

4.2.1 PEO-OH functionalization

The PEO_{113}-OH functionalization into PEO_{113}-OTs is presented in Figure 4.3. The starting PEO-OH (M_n=5,000 g/mol, PDI=1.05) is reacted with 20 equivalents of tosyl chloride (TsCl) and triethylamine in THF during 24 h at 40 ℃. The yield of the reaction is equal to 93 % and the PEO is 100 % functionalized as determined by ^{1}H NMR by comparing the integration signal of the methoxy chain end and the tosylate moiety.

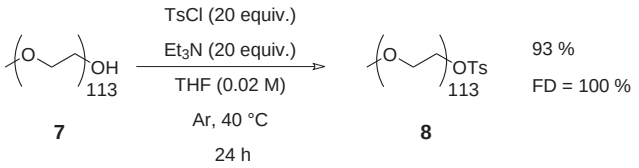

Figure 4.3: Tosylation of PEO_{113}-OH.

4.2.2 PEO-OTs substitution

The second step of the PS-*hν*-PEO synthesis is the nucleophilic substitution of PEO_{113}-OTS by the *o*-nitrobenzyl alcohol **9** (Scheme 4.4). The reaction consists in, firstly deprotonating the phenolic alcohol of **9** with a base to provide the phenolate **13**. In a second step, a SN_2 between **13** and **8** yields the *o*-nitrobenzyl substituted PEO **10**.

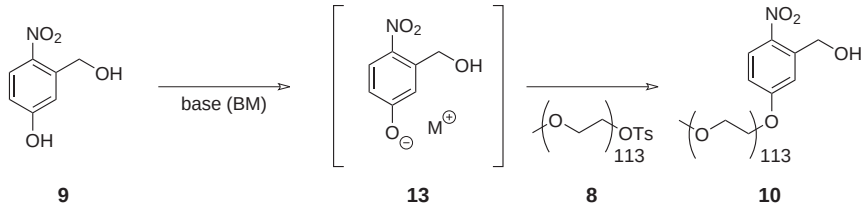

Figure 4.4: PEO-OTs substitution.

Several experimental conditions were tried for the PEO-OTs substitution and are presented in Table 4.1. These results show that the NaH/THF system provides better functionalization than the traditional K_2CO_3/DMF system (entries 2 & 3). Indeed, NaH is a stronger base than K_2CO_3. So, the NaH/THF system produces the phenolate **13** more efficiently than the K_2CO_3/DMF one. The conditions showed at entry 3 are the best ones and yield a functionalization degree equals to 90 %. Increasing the equivalents of base did not improve the functionalization degree (FD) and 90 % was the maximum substitution possible.

Table 4.1: Optimization of the PEO-OTs substitution.

					Equiv.			
Entry	Solvent[a]	Base	T (°C)	t (h)	**9**	Base	**13**	FD[b] (%)
1	DMF	K_2CO_3	70	45	1.2	3.6	1.2	40
2	DMF	K_2CO_3	70	40	4.5	13.5	4.5	69
3	THF	NaH	reflux	40	7	4.5	4.5	90
4	THF	NaH	reflux	48	12	9	9	90
5	THF	NaH	reflux	48	24	20	20	90

[a] C_{PEO}= 0.02 M. [b]Determined by ^{1}H NMR.

4.2.3 PS-PEO coupling

Once the intermediate **10** was synthesized, its direct esterification with the PS-COOH **11** was investigated (Scheme 4.5). Thionyl chloride ($SOCl_2$) was firstly used as activating agent but no reaction was observed in the conditions presented in Scheme 4.5. Changing to oxalyl chloride ($(COCl)_2$), a milder chlorinating agent, yielded some product. The conversion was however limited to 20%. In addition, using 4-dimethylaminopyridine (DMAP), instead of Et_3N did not improve the yield.

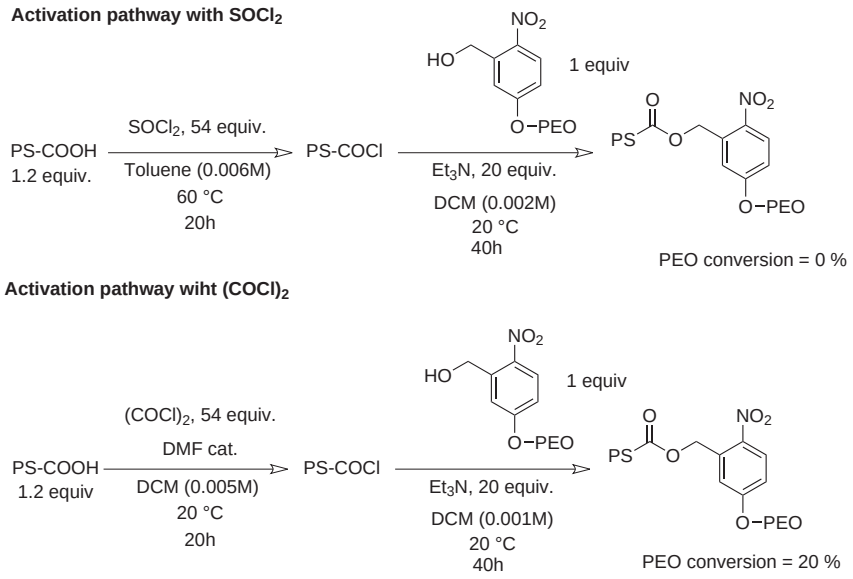

Figure 4.5: PS-PEO coupling via esterification.

An investigation on model molecules has shown that this esterification in dilute conditions is not efficient (Figure 4.6 and Table 4.2). Phenylacetic acid (**14**) and *o*-nitrobenzyl alcohol (**16**) have been used as model compounds for PS-COOH and PEO-$h\nu$-OH respectively. Conditions of dilution similar to the polymer coupling have been investigated. After 18 h reaction time (Table 4.2, Entry 1), only 18 % of PEO conversion were achieved. Increasing the number of equivalent of Et_3N and the reaction time improved the conversion up to 38 % (Entry 2) while heating the medium revealed to be inefficient (Entry 3). Finally, DMAP was used instead of Et_3N and *o*-nitrobenzyl alcohol **16** was previously reacted with NaH in order to start the esterification with the alcoholate form which is much more reactive, but no conversion was observed (Entry 4).

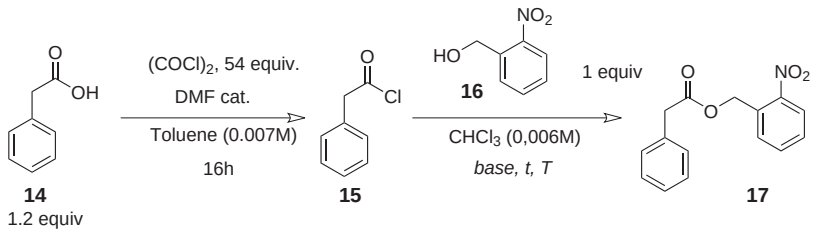

Figure 4.6: Esterification on model compounds in dilute conditions.

During these experiments, the esterification reaction revealed to be the critical step. Indeed, ^{13}C NMR measurements demonstrated the quantitative formation of the acyl chloride **15** during the activation step. The chemical shift (δ) of the phenilic -CH_2- in the acid form is 41.2 ppm while the acyl chloride form displays a peak shifted to 53.0 ppm, in agreement with the theoritical chemical shift.

Table 4.2: Esterification on model compounds in dilute conditions.

Entry	Base	Base (equiv)	T (°C)	t (h)	**16** Conv. (%)
1	Et_3N	20	20	18	12
2	Et_3N	40	20	50	38
3	Et_3N	40	60	50	0
4[a]	DMAP	26	20	48	0

[a]Performed in THF with the sodium alcoholate form of **16**.

The poor reaction yield might be due to the high dilution of the active species. The reactive centers are indeed only located at the end of the polymer chains. Moreover, large amounts of solvent are needed to solubilize the polymeric chains. These two points contribute to the high dilution of the active centers which increases the probalility of deactivation of the acyl chloride chain ends. For that reason the next strategy has been considered.

4.3 Macroinitiator strategy

As shown in the previous section, the esterification between the functionalized PEO **10** and the carboxylic acid terminated PS **11** is not an efficient reaction (section 4.2.3). For that reason, another synthetic strategy has been proposed to obtain the desired PS-*hν*-PEO **12** (Figure 4.7). This strategy is based on the polymerization of styrene initiated by a photocleavable PEO macroinitiator **18**. The grafting of the *o*-nitrobenzyl moiety followed by its conversion into an initiator of polymerization has to be carried out first. Concerning the polymerization method, ATRP has been chosen because of the possibility to easily modify the PEO end-terminated by the *o*-nitrobenzyl alcohol (**10**) into the ATRP macroinitator **18** in only one step.

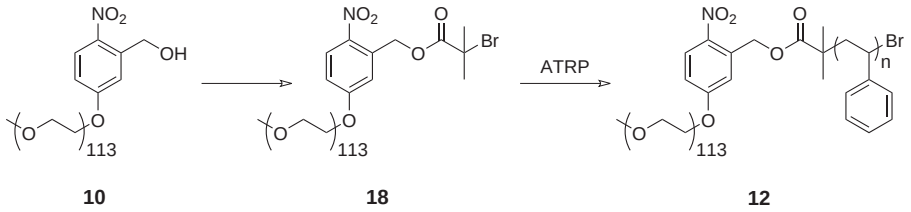

Figure 4.7: Macroinitiator synthetic strategy for PS-*hν*-PEO.

4.3.1 Photocleavable PEO-*hν*-Br macroinitiator

The synthesis of the photocleavable PEO macroinitiator PEO-*hν*-Br (**18**) is presented in Figure 4.8(a). The ATRP macroinitiator is obtained by esterifying the PEO-*hν*-OH **10** with bromo-isobutyrate bromide. These conditions have been previously tested on a PEO-OH providing a 100 % functionalized PEO macroinitiator **20** (Figure 4.8(b)). However, the obtained PEO-*hν*-Br was contaminated with about 10% of non-photocleavable chains (PEO-Br **20**). Indeed, as the starting PEO-*hν*-OH **10** was functionalized at only 90%, the residual PEO-OH has also reacted with bromo-isobutyrate bromide leading to PEO-Br **20**. The contamination could be evidenced by ^{1}H NMR as shown in Figure 4.9.

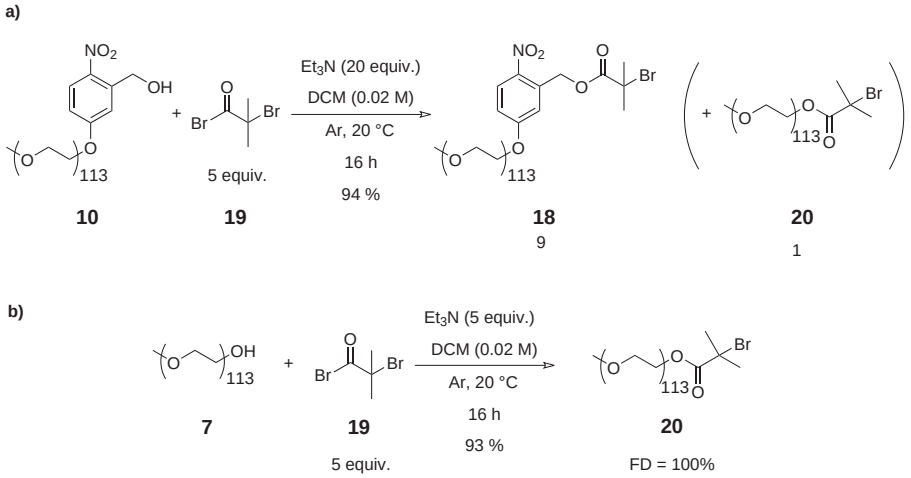

Figure 4.8: Photocleavable (a) and non-photocleavable (b) PEO macroinitiator synthesis.

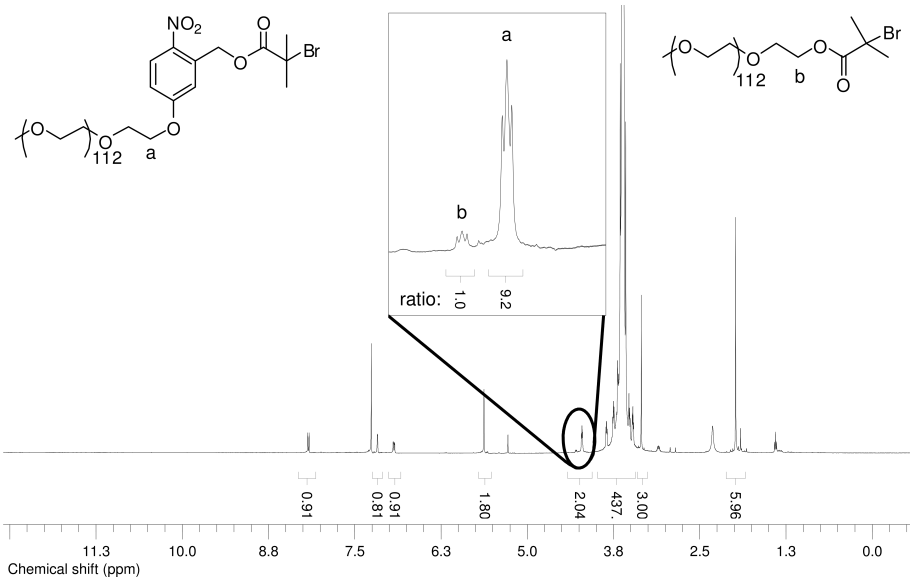

Figure 4.9: ^{1}H NMR spectrum of PEO-*hν*-Br **18**. Zoom shows the presence of $\sim$ 10 % residual PEO-Br **20**.

4.3.2 ATRP of styrene with PEO-$h\nu$-Br macroinitiator

Before polymerizing styrene with the photocleavable macroinitiator PEO-$h\nu$-Br **18**, ATRP conditions were tested with the non-photocleavable PEO macroinitiator **20** (Figure 4.10 and Table 4.3).

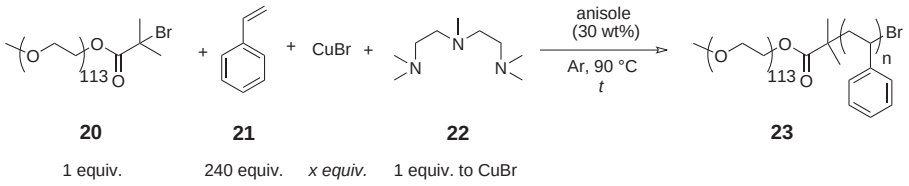

Figure 4.10: ATRP of styrene with PEO_{113}-Br macroinitiator.

The experimental set-up is composed of the macroinitiator **20**, styrene, CuBr and PMDETA. Conditions presented in Entry 1 yielded a copolymer with a low polydispersity index (PDI=1.16). However, even if the PDI value was low, the shape of the GPC chromatogram[2] was very asymetric, displaying a shoulder towards the higher masses which indicates coupling reactions during the reaction. By reducing the amount of copper bromide, lower monomer conversions were achieved and more defined block copolymers were thus obtained (Entries 2 and 3).

Table 4.3: ATRP of styrene initiated by PEO_{113}-Br **20**.

Entry	CuBr (equiv.)	t (h)	Conv.[a] (%)	$M_{n,\,th}$ (g/mol)	$M_{n,\,NMR}$ (g/mol)	$M_{n,\,GPC}$ (g/mol)	PDI (GPC)
1[b]	2.0	17	99	25,800	29,900	49,300	1.16
2	1.5	18	72	23,300	19,600	27,100	1.12
3	1.0	19	43	15,700	15,400	21,400	1.06

[a]Determined by ^{1}H NMR. [b]Performed with 200 equiv. of styrene in 20 wt-% anisole.

[2]Chromatogram not shown here

The ATRP of styrene initiated by the PEO-*hν*-Br macroinitiator **18** was investigated under similar conditions to those presented at the Entry 2 of Table 4.3. Under these conditions, a copolymer with a molar mass (M_n) of 14,300 g/mol and a PDI of 1.13 was obtained after 19 h reaction time (Figure 4.11). Another experiment using Me_6Tren[3] as ligand instead of PMEDTA yielded a copolymer with higher PDI (1.45) and with a PS block of M_n = 8,100 g/mol. Moreover, other experiments in similar conditions displayed no polymerization or quite low monomer conversions (< 5 %) indicating some problems with this system.

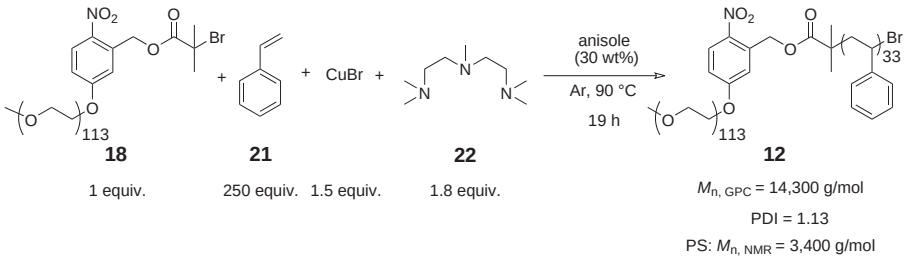

Figure 4.11: ATRP of styrene with PEO-*hν*-Br macroinitiator.

As successful polymerizations were obtained with the macroinitiator **20** under similar conditions, the problems encountered with the photocleavable system could arise from the PEO-*hν*-Br macroinitiator. Some residual impurities coming from the etherification step of PEO-OTs by the *o*-nitrobenzyl diol **9** might be the source of the problems as the final PEO-*hν*-OH compound displayed an abnormal dark yellow coloration. After several precipitation and dialysis purification steps, the disappearence of the color was observed, but no improvement in the polymerizations was observed.

Since problems were encountered with the polymerization and no 100 % photocleavable chains could be obtained by that way, this macroinitiator strategy has been abandoned. However, it is important to note that Moon and coworkers successfully synthesized a photocleavable PEO-*hν*-PS copolymer in 2009 by using exactly this strategy [1].

[3] Me_6Tren = tris[2-(dimethylamino)ethyl]amine

4.4 One-pot strategy

The PS-$h\nu$-PEO obtained by the pathway described in the previous section (Section 4.3.2) suffers from two drawbacks: the first is that problems have been encountered to polymerize styrene from the macroinitiator **18**, and secondly that this macroinitiator is composed of 90 % of photocleavable chains and 10 % which are not. This means that the final block copolymer will contain 10 % of non-photocleavable chains too. Consequently, thin films formed from such materials will also display, after photocleavage, pore walls covered by 90 % of carboxylic acid functions and by 10 % of remaining PEO chains.

To circumvent these drawbacks, another strategy has been designed and is presented in Figure 4.12. This new way consists in performing the polymerizaton of styrene in the same time than creating the photocleavable junction between the PS and the PEO block through a copper(I)-catalyzed alkyne-azide cycloaddition (CuAAC-click reaction).

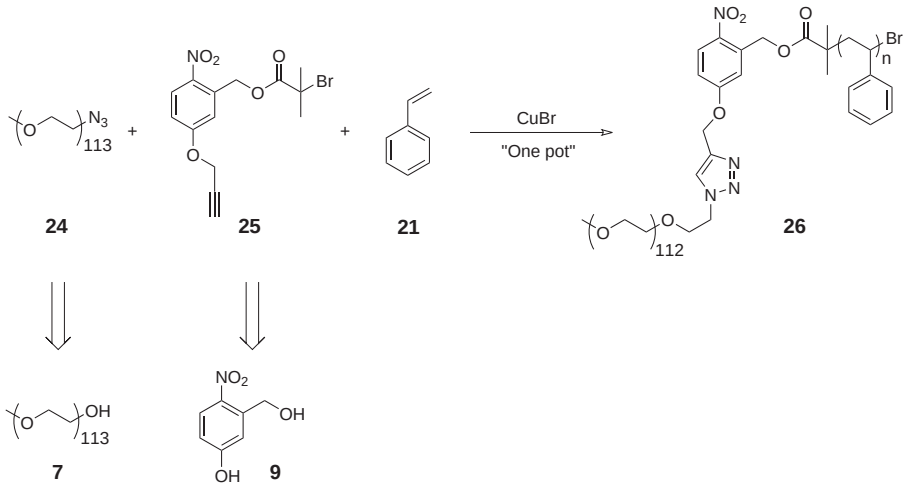

Figure 4.12: Click & ATRP strategy.

The photocleavable ATRP initiator **25** has to be synthetized first from the diol **9** while the PEO terminated azide (**24**) can be easily obtained from the monohydroxyl PEO **7**. The initiator **25** bears the

alkyne function which can be coupled to the azide function of the PEO leading to a triazole junction. Both reactions are catalyzed by the same copper catalyst (Cu^{I}) making a one-pot reaction possible.

4.4.1 Photocleavable initiator synthesis

The photocleavable initiator **25** has been synthesized as presented in Figure 4.13. The diol **9** is reacted with propargyl bromide in a K_2CO_3/DMF mixture to selectively etherify the phenol. The second step is the esterification between **27** and bromo-isobutyrate bromide to yield the photocleavable initiator **25**.

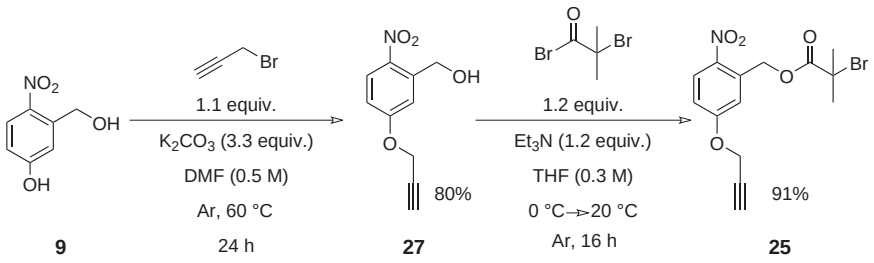

Figure 4.13: Photocleavable initiator synthesis.

4.4.2 PEO-N_3 synthesis

The azide terminated PEO **24** is obtained by nucleophilic substitution of tosylated PEO **8** by sodium azide (NaN_3) with a functionalization degree >90 % as presented in Figure 4.14. Even if the PEO functionalization is not quantitative it will not lead to non-photocleavable block copolymers after the coupling because the residual PEO-OH will not perform the CuAAC-click coupling.

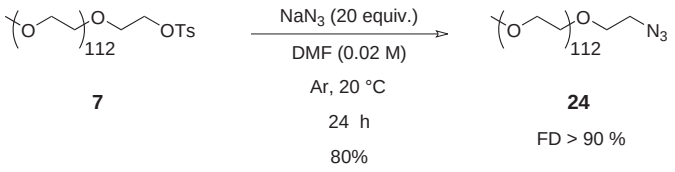

Figure 4.14: PEO-N_3 synthesis.

4.4.3 ATRP of styrene using the photocleavable initiator

The ATRP of styrene initiated by **25** has been studied and the general reaction is presented in Figure 4.15. The results of this study are presented in Table 4.4. The starting conditions are shown in Entry 1 and led to a PS polymer possessing a molar mass (M_n) of 23,400 g/mol and a polydispersity index equal to 1.55. The GPC chromatogram of this PS shows an important shoulder similar to the one depicted in Figure 4.16 (**a**). The PSs obtained for Entries 2 and 3 display the same chromatogram shape. On the other hand, the PSs obtained from conditions of entries 4 to 6 show a single symetrical peak (see Figure 4.16; **b**).

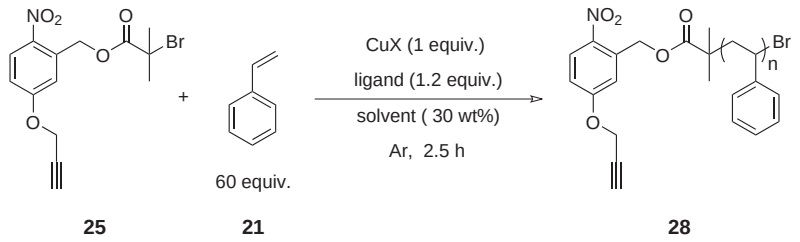

Figure 4.15: ATRP of styrene initiated by a photocleavable initiator.

The main difference between Entries 1-3 and 4-6 resides in the experimental conditions. Indeed, for Entries 1-3, the initiator is already present when the complexation between CuX and its ligand occurs.[4] For entries 4-6, the initiator is injected after the CuX/ligand complexation. These experiments suggest that the alkyne moiety of the initiator might

[4]CuX = CuBr or CuCl

be a ligand for CuX, and thus a competitor of PMDETA or Me_6Tren. When the alkyne initiator is injected after CuX/ligand complexation, no side reaction occurs and polymerization goes on normally. On the other hand, when the initiator is injected before the CuX/ligand complexation, the initiator can complex the CuX and some side reactions occur, which increase the PDI. Additionally, the use of Me_6Tren and DMF instead of PMDETA and anisole was directed by their stronger complexation properties. However, as suggested by the results, the key point is the order of addition of the initiator.

The shape of the GPC chromatograms obtained for Etries 1-3 strongly looks like the ones obtained for the polymerizaton of propargyl methacrylate with a CuBr/bpy complex as catalyst [2]. The authors explained that behavior by two facts. Firstly, the possibility of radical addition to the acetylene groups leading to radical side reactions (transfer and termination reaction). The authors justified this explanation by the observation of insoluble gel formation for propargyl methacrylate at high conversion. The second explanation is the possibility of the coordination of the copper by the alkyne, perturbing the course of the polymerization.

Even if better shapes of molar mass distributions have been obtained by changing the order of the initiator injection, the efficiency of the initiation step e_i remains quite low for all experiments ($0.2<e_i<0.6$, Table 4.4). In order to improve it, CuCl catalyst has been used instead of CuBr as the exchange of halide is known to enable a better initiation step due to a stronger bonding strength of the C-Cl bond compared to the C-Br one [3, 4]. An improvement in the efficiency up to $e_i = 0.6$ has been reached, but it still remains far away from that of other isobutyrate counterparts. In comparaison, ATRP of styrene initiated with the macroinitiator **20** presented in Table 4.3 displays e_i above 0.9.

Entry	CuX	Ligand	Solvent	T (℃)	Initiator injection[a]	Conv.[b] %	$M_{n,\,th}$[c] (g/mol)	$M_{n,\,GPC}$[d] (g/mol)	PDI	Peak shape[e]	e_i[f]
1[g]	CuBr	PMDETA	anisole	100	before	32	7,300	23,400	1.55	a	0.3
2	CuBr	PMDETA	anisole	90	before	50	3,100	7,000	1.31	a	0.4
3	CuCl	Me_6Tren	DMF	110	before	39	2,400	7,100	1.41	a	0.3
4	CuCl	Me_6Tren	DMF	110	after	24	1,500	2,400	1.46	b	0.6
5	CuBr	Me_6Tren	DMF	90	after	17	1,100	4,800	1.23	b	0.2
6	CuBr	Me_6Tren	anisole	90	after	30	1,900	5,400	1.35	b	0.4

[a]before = initiator injection before the CuBr/ligand complexation; after = initiator injection after the CuBr/ligand complexation. [b]Determined by ^{1}H NMR. [c] Theoritical M_n = monomer equivalents × molar mass of monomer × conv. [d]Measured with a PS calibration. [e]Peak shape as defined at Figure 4.16. [f] e_i: initiation efficiency = $M_{n,\,th}/M_{n,\,GPC}$ [g]Reaction time = 15 h; styrene equiv. = 250; anisole = 10 wt%.

Table 4.4: Optimization of ARTP of styrene initiated by **25**.

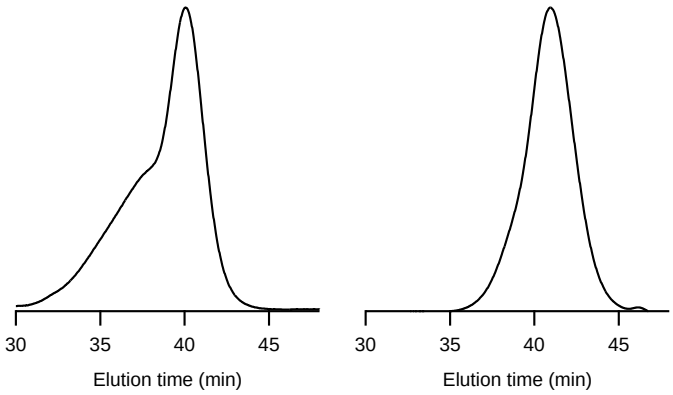

Figure 4.16: GPC chromatograms of Entries 2 (a) and 5 (b) from Table 4.4.

4.4.4 CuAAC-Click and ATRP one-pot reaction

The low initiation efficiencies encountered with the photocleavable initiator **25** during the ATRP of styrene might be due to either the nitro group or to the triple bond. As the triple bond was already involved in some side reactions, it was decided to firstly try to cancel out its effect. Protecting the triple bond, with a silane group for instance, was initially considered [5–8]. However, this implies to extend the synthesis with two additional steps: the protection of the alkyne and its further deprotection. Another way to get round, was to click the initiator to the PEO block followed by the polymerization of styrene in a second reaction. In this manner, the alkyne would be transformed in a triazole moiety which is no more able to interfer (or interfer less) with the polymerization step.

Performing these two reactions in a one-pot process seemed also to be a viable option as the CuAAC click reaction takes place faster than the polymerization reaction. Indeed, only catalytic amount of copper bromide are needed to perfom a CuAAC-click at room temperature while ATRP needs higher temperature and one equivalent of CuBr is often used. In a one-pot process, click reaction should thus occur faster than the polymerization, preventing any interferences coming from side reac-

tions involving the triple bond.

Table 4.5 presents PEO-$h\nu$-PS block copolymers synthetized by the one-pot method. Conditions presented at Entry 1 yielded a PEO_{113}-$h\nu$-PS_{135} characterized by a PDI equal to 1.29. Although a good initiation efficiency was reached (e_i= 1), the coupling efficiency, *i.e.*, the click efficiency, was however low (∼40 %) implying the presence of a large amount of non-coupled blocks after the reaction. These homo-polymers were removed by washing with selective solvents (diethyl ether for PS and water/methanol mixture for PEO). Moreover, the shape of the GPC chromatogram of PEO_{113}-$h\nu$-PS_{135} was quite asymetric indicating some chain coupling reaction probably due to a too high viscosity of the reaction medium. High viscosity might also explain the low click efficiency as the diffusion of reactive chain ends is slowed down.

In order to decrease the viscosity of the system, the next polymerizations were performed in more diluted conditions (Table 4.5, Entries 2-4). Moreover, in order to narrow the molar mass distributions, Me_6Tren was replaced by PMDETA and the temperature was lowered to 90 °C as these two factors decrease the rate of propagation. In these conditions, the click reaction and the initiation step were very efficient with yields higher than about 85% and 90%, respectively.

Entry[a]	Block copolymer[b]	Ligand	Styrene (equiv.)	Anisole (wt-%)	T (℃)	t (h)	Conv.[c] (%)	$M_{n,\,NMR}$ (g/mol)	$M_{n,\,GPC}$ (g/mol)	PDI	e_i[d]
1	PEO_{113}-$h\nu$-PS_{135}	Me_6Tren	300	20	100	5.5	45	19,400	33,600	1.29	1.0
2	PEO_{113}-$h\nu$-PS_{119}	PMDETA	300	40	90	15.0	35	17,900	25,300	1.14	0.9
3	PEO_{113}-$h\nu$-PS_{133}	PMDETA	300	40	90	20.0	40	19,100	30,100	1.15	0.9
4[e]	PEO_{113}-$h\nu$-PS_{176}	PMDETA	400	30	90	20.0	44	23,600	37,700	1.16	1.0

[a]Reaction conditions: initiator **25**/PEO-N_3 **24**/CuBr/ligand = 1:1:1:1.5. [b]DP of polystyrene determined by ^{1}H NMR. [c]Determined by ^{1}H NMR. [d]e_i: initiation efficiency = $M_{n,\,th}$ (PS)/$M_{n,\,NMR}$ (PS).

Table 4.5: Synthesis of PEO-$h\nu$-PS by a CuAAC click and ATRP one-pot reaction.

The efficiency of the click reaction is determined by ^{1}H NMR (500 MHz) on the crude copolymer by comparing the integrations of the methoxy chain end of PEO with the signal of the triazole proton (H_t) of the junction. Figure 4.17 shows the NMR spectrum of the crude PEO_{113}-$h\nu$-PS_{133} (Table 4.5, Entry 3). The click efficiency is equal to 92 % ($H_t \times 100$) when H_m is calibrated to 3 (3 protons).

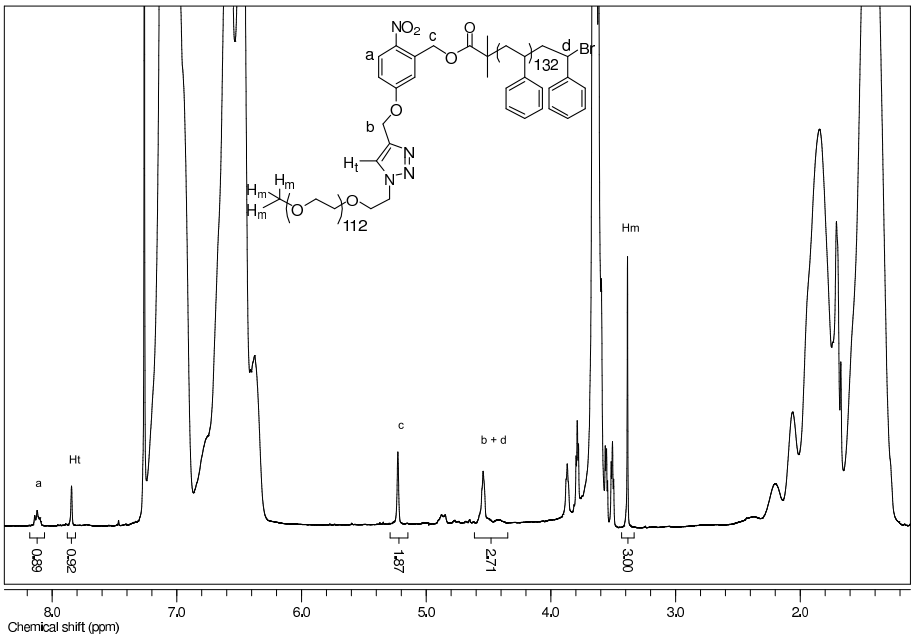

Figure 4.17: ^{1}H NMR spectrum of the crude PEO_{113}-$h\nu$-PS_{133} (Table 4.5, entry 3).

After removal of the residual non-coupled blocks, the PEO-$h\nu$-PS copolymers (Entries 2-4, Table 4.5) display narrow molar mass distributions as evidenced by their GPC chromatograms shown in Figure 4.18. Finally, PEO_{113}-$h\nu$-PS_{176} possesses the proper composition for the desired cylindrical morphology after self-assembly into thin films. Its self-organization behavior in the solid state will be discussed in Chapter 7.

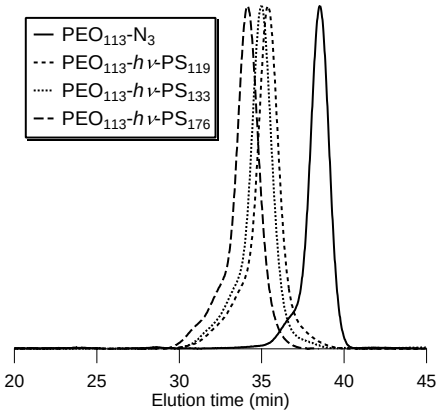

Figure 4.18: GPC traces of PEO-$h\nu$-PS from Table 4.5 (Entries 2-4) and their starting azide-functionalized PEO block.

4.4.5 One-pot strategy, a versatile strategy?

After the successful obtention of well-defined PEO-$h\nu$-PS block copolymers via the CuAAC-click and ATRP one-pot synthesis, the scope and the limitations of the method have been investigated. In addition to the PEO-$h\nu$-PS block copolymers, three kinds of systems have been studied: PEO-$h\nu$-PtBA, PS-$h\nu$-PMMA and PMMA-$h\nu$-PS. Those systems are very interesting because they involve the polymerization of monomers displaying different reactivities (styrenic, acrylic and methacrylic monomers). Moreover, the click efficiency can be tested on different azide chain end. Indeed, the azide moiety is connected to a primary, secondary or tertiary carbon whether the starting block is a PEO, a PS or a PMMA block, respectively.

Figure 4.19 shows the different azide starting blocks and monomers used in the study. The synthesis of the azide terminated PEO has been already presented in section 4.4.2. PS-N_3 and PMMA-N_3 have been synthetized by ATRP of styrene and methyl methacrylate respectively, followed by the azide substitution of the bromide chain-end. These syntheses are described in the experimental section at the end of the chapter.

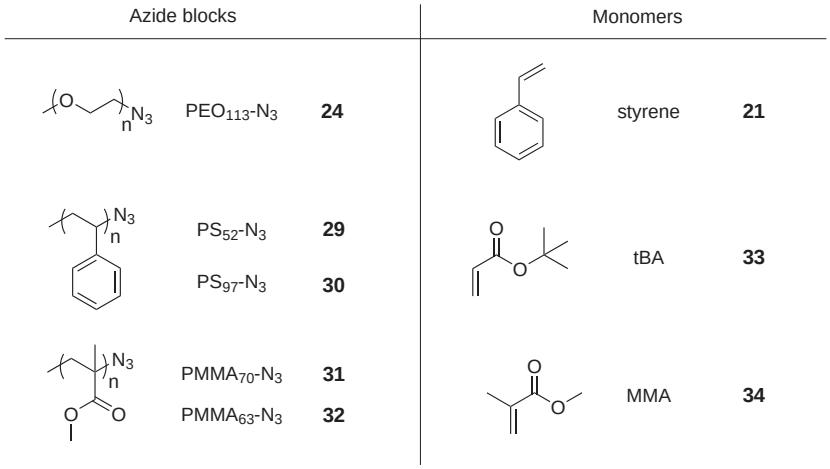

Figure 4.19: Azide functionalized blocks and monomers used for the investigation of the scope and the limitations of the CuAAC and ATRP one-pot reaction.

The results of the scope and limitations study are summarized in Table 4.6. One PEO-$h\nu$-PtBA (Entry 1) and three PS-$h\nu$-PMMA copolymers with different compositions (Entries 2-4) displaying narrow mass distribution (PDI < 1.3) have been successfully synthesized. Molar masses ($M_{\mathrm{n,\,NMR}}$) ranging from 20,000 to 48,500 g/mol have been reached and the click reaction was very efficient with yields higher than 85 % even for shorter reaction times (2 h). The click efficiency (e_c) has been estimated by ^{1}H NMR by comparing the polymer signals, chain-ends and/or main chain, and the signals of the junction, triazole and/or -CH_2- group next to the triazole. As in the case of PEO-$h\nu$-PS, the small amounts of residual homopolymers were easily extracted by washing the copolymers with selective solvents of the blocks to be removed. Homo-PEO, PtBA, PS and PMMA were respectively extracted with water/methanol, hexane, diethyl ether/hexane and nitromethane/methanol mixtures. Finally, Figures 4.20(a) (b) and (c) present the GPC chromatograms of the synthesized photocleavable block copolymers. The clear shift towards the higher molar masses (shorter elution time) indicates the formation of the block copolymers.

Entry[a]	Block copolymer[b]	**25**:CuBr:L[c]	Monomer (equiv.)	R-N_3	Anisole (wt-%)	t (h)	Conv. (%)	e_c^e (%)	$M_{n,\,NMR}$ (g/mol)	$M_{n,\,GPC}$[f] (g/mol)	PDI
1[g]	PEO_{113}-*hν*-$PtBA_{305}$	1:1.0:1.50	300	**24**	40	2	90	90	48,500	63,100	1.15
2	PS_{52}-*hν*-$PMMA_{278}$	1:1.0:1.50	300	**29**	40	2	72	85	33,200	37,300	1.25
3[h]	PS_{97}-*hν*-$PMMA_{33}$	1:1.2:1.80	125	**30**	95	2	33	85	13,600	15,700	1.12
4[h]	PS_{97}-*hν*-$PMMA_{100}$	1:1.2:1.80	250	**30**	88	4	43	86	20,100	24,200	1.10
5	$PMMA_{63}$-*hν*-PS_x	1:1.5:2.25	400	**31**	30	20	47	31	/	/	/
6	$PMMA_{63}$-*hν*-PS_x	1:1.5:2.25	500	**31**	50	18	30	23	/	/	/
7	$PMMA_{63}$-*hν*-PS_x	1:1.5:2.25	800	**31**	20	7	32	/	/	/	/
8	$PMMA_{70}$-*hν*-PS_x	1:1.0:1.50	300	**32**	40	15	47	18	/	/	/

[a]Reactions performed at 90 ℃. [b]DP of polymer determined by ^{1}H NMR. [c]L = PMDETA. [d]Determined by ^{1}H NMR. [e]e_c = click efficiency, determined by ^{1}H NMR. [f]Determined with a PS calibration. [g]Reaction performed with Me_6Tren at 80 ℃. [h]Performed with 1.2 equiv. of R-N_3 at 60 ℃.

Table 4.6: Scope and limitations of CuAAC-click & ATRP one pot.

On the other hand, performing the one-pot reactions with an azide functionalized PMMA reveals to be much more tricky. Indeed, in the conditions tested (Table 4.6, Entries 5-8), although styrene polymerization occured, only low click efficiencies ($e_c \leq 31$ %) have been observed. This can be explained by the tertiary nature of the end carbon of the PMMA backbone which hinders the bromide substitution during the azide functionalization lowering the functionalization degree. Moreover the tertiary nature could also hinder the triazole formation. Indeed, it has been demonstrated on model compound that a methacrylate-type azide reacts 10 times slower with propargyl alcohol than an acrylate-type azide [9].

Figure 4.20(d) depicts the GPC chromatogram of the crude mixture obtained under conditions of Entry 6. The peak at longer elution time is attributed to the starting azide functionalized PMMA while the peak at shorter elution time represents the block copolymer. This chromatogram clearly shows that a large part of the starting azide block has not clicked as only a tiny shoulder is visible on the GPC chromatograms of the crude mixture.

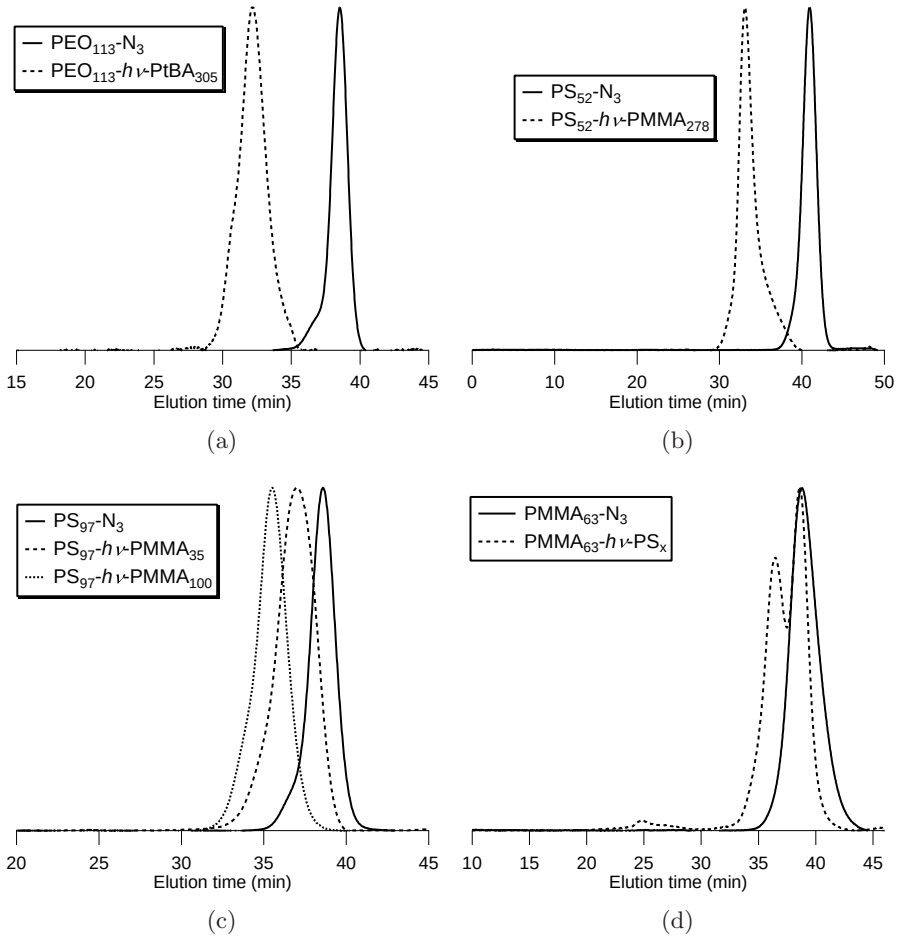

Figure 4.20: GPC chromatograms of photocleavable block copolymers presented in Table 4.6 and their starting azide blocks. (a) Entry 1, (b) Entry 2 , (c) Entries 3-4, (d) crude mixture of Entry 6.

4.5 Conclusions

The aim of the study presented in this chapter, was the obtention of a photocleavable PEO-$h\nu$-PS copolymer displaying a suitable composition for further self-assembly into a cylindrical morphophogy. Different pathways have been investigated.

Firstly, an esterification reaction between an *o*-nitrobenzyl alcohol end-functionalized PEO and a carboxylic acid terminated PS was considered. Unfortunately, the transposition of a well-known esterification reaction to polymer chain end chemistry failed probably due to a too high dilution of the reactive chain ends.

The second route was based on the polymerization of styrene initiated by a photocleavable PEO macroinititator. However, some unidentified polymerization issues were encountered.

Finally, the third strategy considered reveals to be efficient. This strategy relies on a functional ATRP initiator bearing the photocleavable moiety and an alkyne as anchoring group for the CuAAC-click reaction. Thus, in one step, the second block is grown by ATRP and clicked to the azide functionalized first block. By this approach, a large variety of block copolymers can be prepared thanks to the vast number of polymers accessible by ATRP, and to the easy introduction of the azide moiety as a chain end on many polymers. However, the methacrylate type azides should not be used as first block because of their smaller rate constant towards the formation of the triazole ring.

Using this one-pot reaction, several photocleable block copolymers have been successfully obtained and the photocleavable ability upon UV irradiation will be discussed in Chapter 6. The self-assembly of PEO_{113}-$h\nu$-PS_{176}, which displays the good compositon for cylindrical morphology, will be described in Chapter 7.

Experimental part

Materials and Instrumentation. Poly(ethylene oxide) mono methyl ether (PEO_{113}-OH, M_n=5,000 g/mol, PDI=1.04) and polystyrene end-functionalized with carboxylic acid (PS_{156}-COOH, M_n=16,500 g/mol, PDI=1.06) were purchased from Polymer Source Inc. and were dried by azeotropic cycles with toluene prior to use. Styrene (sty, Aldrich, 99 %), tert-butylacrylate (tBA, Acros, 99 %) and methyl methacrylate (MMA, Aldrich, 99 %) were passed through activated basic alumina (Acros) columns prior to use. Triethylamine (Et_3N) was dried over KOH. Potassium carbonate (K_2CO_3, 99 %) was dried 24 h in a vacuum oven at 100°C. 5-hydroxy-2-nitrobenzyl alcohol (Aldrich, 97 %), 2-nitrobenzyl alcohol (Aldrich, 97 %) and phenyl acetid acid (Aldrich, 99 %) were dried in vacuo prior to use. N,N-dimethylformamide (DMF) and toluene were distilled on CaH_2 prior to use. Dichloromethane (DCM) and chloroform ($CHCl_3$) were distilled on P_2O_5 prior to use. Tetrahydrofuran (THF) was distilled on sodium/benzophenone prior to use. Propargyl bromide (Aldrich, 80 wt-% in toluene), 1-bromoethylbenzene (Aldrich, 97 %), sodium azide (NaN3, Acros, 99 %), tosyl chloride (TsCl, Fluka, 99 %), 4,4'-dinonyl-2,2'-dipyridyl (dNPy, Aldrich, 97 %), CuBr (Aldrich, 99.999 %), N,N,N',N",N"-pentamethyldiethylenetriamine (PMDETA, Aldrich, 98 %), $CuBr_2$ (Aldrich, >99 %), CuCl (Aldrich, >99 %), ethyl 2-bromoisobutyrate (EBiB, Acros, 98 %), anisole (Acros, 99 %), ethylenediaminetetraacetic acid disodium salt dehydrate (EDTA, Fluka, 97 %) and all the other chemicals were used as received. Flash chromatography was performed on silica gel (0.040-0.063 μm grade).

Proton and carbon nuclear magnetic resonance spectra were recorded on a 300 MHz or 500 MHz (Bruker Avance II). Infrared (IR) spectra were recorded on thin films deposited from a dichloromethane solution on a ATR accessory with a Shimadzu FTIR-8400S FT-IR spectrometer. Mass spectra were obtained using chemical ionization (100 eV, ionization gas: methane). Molar masses (M_n) and polydispersity indices (PDIs) of the polymers were measured on a Waters (GPC) system equipped with a Waters 510 pump and a 410 differential refractometer (40 °C; eluent: DMF; flow rate of 0.5 mL/min). The calibration was performed using polystyrene standards.

Section 4.2

Synthesis of PEO_{113}-OTs (8). To a solution of PEO_{113}-OH (2.60 g, 0.52 mmol) in dry THF (25 mL, 0.2 M), dry triethylamine (1.45 mL, 10.4 mmol, 20 equiv.) and tosyl chloride (1.98 g, 10.4 mmol, 20 equiv.) were added. The light yellow solution was stirred under argon at 35 °C for 24 h. THF was removed under reduced pressure. The residue was diluted in CH_2Cl_2 and washed with water. The organic phases were combined, dried over Na_2SO_4, filtered and the solvent was removed under reduced pressure. The light yellow solid was precipitated in Et_2O, filtered and dried one night in vacuo at 30 °C, affording a white powder (2.45 g, 91 %, FD: 100 %).

^{1}H NMR (500 MHz, $CDCl_3$): δ 7.77 (d, 2H, ^3J = 8.0 Hz, H_{Ar}), 7.32 (d, 2H, ^3J = 8.0 Hz, H_{Ar}), 4.31 (t, 2H, ^3J = 4.5 Hz, -CH_2-OTs), 3.62 (s, 449H, CH_2(PEO)), 3.36 (s, 3H, CH_3-O), 2.43 (s, 3H, CH_3 (Ar)).

Typical procedure for PEO-$h\upsilon$-OH (10). (Table 4.1, Entry 3) To a NaH suspension (25 mg, 0.63 mmol, 4.5 equiv.) in dry THF, *o*-nitrobenzyl alcohol (167 mg, 0.98 mmol, 7 equiv.) was added at 0 °C under argon. After 45 min. of stirring, a solution of PEO_{113}-OTs (725 mg, 0.14 mmol, 1 equiv.) in dry THF was added and the mixture was stirred at reflux for 40 h (0.02 M). THF was removed under reduced pressure and the residue was diluted with CH_2Cl_2 and washed with water. The organic phases were combined, dried over Na_2SO_4, filtered and the solvent was removed in vacuo. The solid residue was precipitated in Et_2O, filtered and dried in vacuo at 30 °C for 24 h, affording a yellow powder (629 mg, 87 %; FD = 90 %).

^{1}H NMR (500 MHz, $CDCl_3$): δ (ppm) 8.14 (d, 1H, ^3J = 9.1 Hz, H_{Ar}), 7.36 (d, 1H, ^4J = 2.0 Hz, H_{Ar}), 6.88 (dd, 1H, ^3J = 9.1 Hz, ^4J = 2.0 Hz, H_{Ar}), 5.00 (d, 2H, ^4J = 4.6 Hz, CH_2-O, ester; junction), 4.25 (t, 2H, ^3J = 4.5 Hz, -CH_2-O, ether junction), 3.62 (s, 449H, CH_2(PEO)), 3.36 (s, 3H, CH_3-O, PEO chain end).

Typical procedure for the esterification between PEO (10) and PS (11) with oxalyl chloride. To a solution of PS_{158}-COOH (267 mg, 0.016 mmol,1.2 equiv.) in dry toluene (3.2 mL, 0.005 M), oxalyl chloride (103 mg, 0.810 mmol, 54 equiv.) was added dropwise at 0 °C. Two drops of DMF were added at 0 °C and the mixture was stirred at 20 °C for 20 h under argon. Toluene was distilled in vacuo. The residue was diluted in dry toluene and toluene was distilled in vacuo. This

procedure was repeated 3 times. The residue was then diluted with dry CH_2Cl_2 and a solution of PEO_{113}-$h\nu$-OH **10** (70 mg, 0.013 mmol. 1 equiv.) and Et_3N (38 μL, 0.271 mmol, 20 equiv.) in dry CH_2Cl_2 was added dropwise via a cannula. The mixture (0.001 M) was stirred for 40 h at 20 °C. The mixture was washed with water and the organic phases were combined, dried over Na_2SO_4, filtered and the solvent was removed in vacuo. The solid residue was precipitated in hexane, filtered and dried in vacuo at 30 °C for 24 h, affording a white powder. A conversion of 20 % was determined by ^{1}H NMR by comparing the integrations of the benzylic CH_2-O (δ (ppm): 5.02 and 5.66 for the alcohol and the ester respectively).

Typical procedure for the esterification between the phenylacetic acid (14) and *o*-nitrobenzyl alcohol (11). (Table 4.2, Entry 2) To a solution of phenylacetic acid (50 mg, 0.37 mmol, 1.2 equiv.) in dry toluene (0.007 M), oxalyl chloride (1.55 mL, 18.36 mmol, 54 equiv.) was added dropwise at 0 °C. Two drops of DMF were added at 0 °C and the mixture was stirred at 20 °C for 20 h under argon. Toluene was distilled in vacuo. The residue was diluted in dry toluene and toluene was distilled in vacuo. This procedure was repeated 3 times. The residue was then diluted with dry $CHCl_3$ and a solution of *o*-nitrobenzyl alcohol (**11**, 47 mg, 0.31 mmol, 1 equiv.) and Et_3N (1.72 mL, 12.33 mmol, 40 equiv.) in dry $CHCl_3$ was added dropwise via a cannula. The mixture (0.006 M) was stirred for 40 h at 20 °C. The mixture was washed with water and the organic phases were combined, dried over Na_2SO_4, filtered and the solvent was removed in vacuo. The residue was kept in $CHCl_3$, filtered on SiO_2 and the solvent was removed in vacuo. A conversion of 40 % was determined by ^{1}H NMR based on the crude product by comparing the integrations of the benzylic CH_2-O (δ (ppm): 4.71 and 5.14 for the alcohol and the ester respectively).

Section 4.3

Synthesis of PEO-$h\nu$-Br (18). To a solution of PEO_{113}-$h\nu$-OH (**10**, 300 mg, 0.06 mmol, 1 equiv.) and Et_3N (162 μL, 1.16 mmol, 20 equiv.) in dry CH_2Cl_2 (2.90 mL, 0.02M), bromoisobutyrate bromide (36 μL, 0.29 mmol, 5 equiv.) was added dropwise under argon at 0 °C. The mixture was stirred for 16 h at 20 °C, then washed with water. The organic phases were combined, dried over Na_2SO_4, filtered and the solvent was removed in vacuo. The solid residue was precipitated in Et_2O, filtered

and dried in vacuo at 30 °C for 24 h, affording a yellow powder (289 mg, 94 %; FD = 90 %).

^{1}H NMR (500 MHz, $CDCl_3$): δ (ppm) 8.18 (d, 1H, ^3J = 9.0 Hz, H_{Ar}), 7.18 (d, 1H, ^4J = 2.5 Hz, H_{Ar}), 6.94 (dd, 1H, ^3J = 9.0 Hz, ^4J = 2.5 Hz, H_{Ar}), 5.64 (s, 2H,CH_2-O, ester), 4.22 (t, 2H, ^3J = 4.0 Hz, -CH_2-O, ether junction), 3.63 (s, 449H, CH_2 (PEO)), 3.36 (s, 3H,CH_3-O, PEO chain end), 1.99 (s, 6H, CH_3, isobutyrate chain end).

Synthesis of PEO-Br (20). To a solution of PEO_{113}-OH (**7**, 573 mg, 0.11 mmol, 1 equiv.) and Et_3N (80 μL, 0.57 mmol, 5 equiv.) in dry CH_2Cl_2 (5.73 mL, 0.02M), bromoisobutyrate bromide (71 μL, 0.57 mmol, 5 equiv.) was added dropwise under argon at 0 °C. The mixture was stirred for 16 h at 20 °C then washed with water. The organic phases were combined, dried over Na_2SO_4, filtered and the solvent was removed in vacuo. The solid residue was precipitated in Et_2O, filtered and dried in vacuo at 30 °C for 24 h, affording a white powder (533 mg, 93 %; FD = 100 %).

^{1}H NMR (500 MHz, $CDCl_3$): δ (ppm) 4.30 (t, 2H, ^3J = 4.5 Hz, CH_2-O, ester), 3.63 (s, 449H, CH_2(PEO)), 3.36 (s, 3H, CH_3-O, PEO chain end), 1.92 (s, 6H, CH_3, isobutyrate chain end).

ATRP of styrene initiated by PEO-Br (20). (Table 4.3 Entry 3) Under argon, a Schlenk tube containing CuBr (2.1 mg, 0.015 mmol, 1 equiv.) was filled with a solution of PEO-Br **20** (76 mg, 0.015 mmol, 1 equiv.), styrene (419 μL, 3.65 mmol, 240 equiv.), PMDETA (2.63 mg, 0.015 mmol, 1 equiv.) and anisole (30 wt%) previously degassed by three freeze-pump-thaw cycles. The mixture was degassed by three freeze-pump-thaw cycles, filled with argon and stirred in an oil bath at 90 °C for 19 h. The polymerization was quenched by quickly cooling the tube in a water-ice bath. Reaction mixture was filtered on neutral Al_2O_3 (eluent: CH_2Cl_2) and solvents were removed under reduce pressure. The viscous residue was precipitated in hexane affording a white powder (43 %). M_n (GPC) = 21,400 g/mol; PDI (GPC) =1.06.

ATRP of styrene initiated by PEO-$h\nu$-Br (18). (Section 4.3.2) Under argon, a Schlenk tube containing CuBr (3.52 mg, 0.024 mmol, 1.5 equiv.) was filled with a solution of PEO-$h\nu$-Br **18** (87 mg, 0.016 mmol, 1 equiv.), styrene (470 μL, 4.09 mmol, 250 equiv.), PMDETA (5. mg, 0.030 mmol, 1.2 equiv.) and anisole (30 wt%) previously degassed

by three freeze-pump-thaw cycles. The mixture was degassed by three freeze-pump-thaw cycles, filled with argon and stirred in an oil bath at 90 ℃ for 15 h. The polymerization was quenched by quickly cooling the tube in a water-ice bath. Reaction mixture was filtered on neutral Al_2O_3 (eluent: CH_2Cl_2) and solvents were removed under reduce pressure. The viscous residue was precipitated in hexane affording a light yellow powder (54 %). M_n (GPC) = 14,300 g/mol; PDI (GPC) =1.13.

Section 4.4

Synthesis of 5-propargylether-2-nitrobenzyl alcohol (27). A mixture of 5-hydroxy-2-nitrobenzyl alcohol (856 mg, 5.2 mmol, 1 equiv.) and K_2CO_3 (2.16 g, 15.6 mmol, 3 equiv.) was stirred in DMF (10.4 mL) for 1 hour at 60 ℃. Propargyl bromide (80 % in toluene, 0.7 mL, 6.3 mmol, 1.2 equiv.) was added dropwise. The mixture was stirred for 24 hours at 60 ℃. DMF was removed under reduced pressure. The residue was dissolved in AcOEt and washed with water. The organic phases were combined, dried over $MgSO_4$, filtered and the solvent was removed in vacuo. The yellow-brown solid was recrystallized in AcOEt/cyclohexane, affording slightly iridescent white crystals (860 mg, 80 %).

^{1}H NMR (300 MHz, $(CD_3)_2SO$): δ (ppm) 8.15 (d, 1H, ^3J = 9.0 Hz, H_{Ar}), 7.41 (s, 1H, H_{Ar}), 7.10 (d, 1H, ^{3} J = 9.0 Hz, H_{Ar}), 5.60 (t, 1H, ^4J = 5.4 Hz, C≡C-H), 4.98 (s, 2H, -CH_2-OH), 4.85 (d, 2, ^4J = 5.1 Hz, C≡C-CH_2-), 3.67 (s, 1H, -OH). ^{13}C NMR (75 MHz, $(CD_3)_2SO$) δ (ppm) 161.5 (C_{Ar}-O-), 142.2 (C_{Ar}-NO_2), 139.9 (C_{Ar}-CH_2-), 127.4 (H-C_{Ar}), 113.8 (H-C_{Ar}), 113.1 (H-C_{Ar}), 79.1 (H-C≡C-), 78.3 (H-C≡C-), 60.1 (C≡C-CH_2), 56.1 (H_2C-OH). FTIR (film, cm^{-1}): 3265 b, 3182 b, 2123 w, 1608 s, 1587 s, 1508 s, 1248 s, 1336 s, 858, w. MS (CI) : m/z = 208 ($[M+H]^+$, 56), 190 ($[C_{10}H_8NO_3]^+$, 100). Anal. Calcd. For $C_{10}H_9NO_4$: C, 57.97; H, 4.38; N, 6.76. Found: C, 58.27; H, 4.44; N, 6.84.

Synthesis of 5-propargylether-2-nitrobenzyl bromoisobutyrate (25). A solution of bromoisobutyrate bromide (538 μL, 4.35 mmol, 1.2 equiv.) in dry THF (4 mL) was added dropwise to a stirred solution of 5-propargylether-2-nitrobenzyl alcohol **27** (700 mg, 3.62 mmol) and dry Et_3N (606 μL, 4.35 mmol, 1.2 equiv.) in dry THF (8 mL) at 0 ℃ and under argon. The mixture was slowly brought to 20 ℃ and stirred overnight. Distilled water (100 μL) was added dropwise to quench the reaction. THF was removed under reduced pressure and the residue was dissolved in CH_2Cl_2 and washed with water. The organic phases were

combined, dried over $MgSO_4$, filtered and the solvent was removed in vacuo. The yellow-brown residue was purified on flash chromatography (eluent: $CHCl_3$) affording a light yellow solid (1.20 g, 91%).

^{1}H NMR (300 MHz,$CDCl_3$): δ (ppm) 8.19 (d, 1H, ^3J = 9.1 Hz, H_{Ar}), 7.26 (s, 1H, H_{Ar}), 7.02 (d, 1H, ^3J = 9.1 Hz, H_{Ar}), 5.64 (s, 2H, -CH_2-OCO-), 4.80 (d, 2H, ^4J = 2.1 Hz, C≡C-CH_2-), 2.60 (d, 1H, -C≡CH), 2.01 (s, 6H, CH_3). ^{13}C NMR (75 MHz,$CDCl_3$): δ (ppm) 170.8 (C=O), 161.8 (C_{Ar}-O-), 140.4 (C_{Ar}-NO_2), 135.3 (C_{Ar}-CH_2-), 127.9 (H-C_{Ar}), 114.5 (H-C_{Ar}), 113.4 (H-C_{Ar}), 77.1 (H-C≡C-), 77.0 (H-C≡C-), 64.4 (-CH_2-OCO-), 56.4 (C≡C-CH_2), 55.7 (C-Br), 30.8 (CH_3). FTIR (film, cm^{-1}): 3290 m, 2123 w, 1737 s, 1610 s, 1581 s, 1514 s, 1336 s, 1249, s, 1151 s, 858 w. MS (CI) : m/z = 356 ($[M+H]^+$, 2), 190 ($[C_{10}H_8NO_3]^+$, 100). Anal. Calcd. For $C_{10}H_9NO_4$: C, 47.21; H, 3.96; N, 3.93. Found : C, 47.55; H, 3.94; N, 4.08.

Synthesis of PEO_{113}-N_3 (24). To a solution of PEO-OTs **8** (996 g, 0.19 mmol, 1 equiv.) in dry DMF (9.66 mL, 0.02 M), sodium azide (251 mg, 3.86 mmol, 20 equiv.) was added. The solution was stirred under argon at 20 ℃ for 24 h. DMF was removed under reduced pressure. The residue was diluted in CH_2Cl_2 and washed with water. The organics phases were combined, dried over Na_2SO_4, filtered and the solvent was removed under reduced pressure. The residue was precipitated in Et_2O, filtered and dried one night in vacuo at 30 ℃, affording a white powder (850 mg, 87 %, FD: 90 %).

^{1}H NMR (500 MHz, $CDCl_3$): δ (ppm) 3.62 (s, 452H, CH_2 (PEO)), 3.36 (m, 5H, CH_2-O ;CH_2-N_3).

Synthesis of Me_6Tren (48). A mixture of formaldehyde 37 % (w/w) (4.83 mL, 128.1 mmol, 20 equiv.), formic acid (3.82 mL, 51.2 mmol, 8 equiv.) and distilled water (0.90 mL) was stirred 1 hour at 0 ℃. A solution of Tren (1.00 mL, 6.4 mmol, 1 equiv.) in 1.00 mL of water was added dropwise at 0 ℃. The mixture was refluxed 16 h at 105 ℃. Volatile fractions were removed under reduced pressure. The brown residue was treated with a $NaOH_{sat}$ aqueous solution until pH > 10. The product was extracted into CH_2Cl_2. The organic phase was dried over $MgSO_4$, filtered and the solvent was removed in vacuo. The yellow residue was disolved in pentane, dried again over $MgSO_4$, filtered and the solvent was removed in vacuo affording a pale yellow oil (1.11 g, 75 %).

^{1}H NMR (300 MHz, $CDCl_3$): δ (ppm) 2.42 (dd, 6H, ^3J = 6.1 Hz, ^3J = 8.6 Hz, CH_2), 2.18 (dd, 6H, ^3J = 6.1 Hz, ^3J = 8.6 Hz, CH_2), 2.03 (s, 18H, CH_3). ^{13}C NMR (75 MHz, $CDCl_3$): δ (ppm) 57.2 (CH_2), 52.7 (CH_2), 45.6(CH_3) . IR (film, cm^{-1}): 2941 s, 2856 m, 2825 s, 2763 s, 1460 s, 1261 m, 1122 s, 1031 s, 935 m, 856 m, 752 m. MS (CI): *m/z* = 231 ([M+H]$^+$, 100), 72 ([$C_4H_{103}N$]$^+$, 49)

General procedure for the synthesis of PS in condition "*before*". (Entry 2, Table 4.4) Under argon, a Schlenk tube containing CuBr (19.6 mg; 0.137 mmol; 1 equiv.) was filled with a solution containing styrene (853 mg; 8.20 mmol; 60 equiv.), PMDETA (28.4 mg; 0.164 mmol; 1.2 equiv.), photocleavable initiator **25** (48.7 mg, 0.136 mmol, 1 equiv.) and anisole (368 μL, 30 wt-%). The mixture was degassed by three freeze-pump-thaw cycles, filled with argon and stirred in an oil bath at 90 °C for 2.5 h (styrene conversion = 39 %). The polymerization was quenched by quickly cooling the tube in a water-ice bath. The reaction mixture was diluted with CH_2Cl_2 and washed with an aqueous solution of EDTA (0.04 M). The organic phase was dried over Na_2SO_4, filtered and the solvent was removed under reduced pressure. The residue was precipitated in hexane (2 ×), filtered and dried in vacuo at 30 °C for 24 h, affording a white powder.

M_n (GPC) = 7,000 g/mol; PDI (GPC) = 1.31.

General procedure for the synthesis of PS in condition "*after*". (Entry 6. Table 4.4) Under argon, a Schlenk tube containing CuBr (9.6 mg; 0.067 mmol; 1 equiv.) was filled with a solution containing styrene (418 mg; 4.02 mmol; 60 equiv.) and Me_6Tren (18.5 mg; 0.0803 mmol; 1.2 equiv.) previously degassed by three freeze-pump-thaw cycles. The mixture was stirred for 10 minutes and was then frozen. Under argon, a solution of the photocleavable initiator **25** in anisole (180 μL (C = 133 g/L), 0.067 mmol, 1 equiv.) was added. The mixture was degassed by three freeze-pump-thaw cycles, filled with argon and stirred in an oil bath at 90 °C for 2.5 h (styrene conversion = 30 %). The polymerization was quenched by quickly cooling the tube in a water-ice bath. The reaction mixture was diluted with CH_2Cl_2 and washed with an aqueous solution of EDTA (0.04 M). The organic phase was dried over Na_2SO_4, filtered and the solvent was removed under reduced pressure. The residue was precipitated in hexane (2 ×), filtered and dried in vacuo at 30 °C for 24 h, affording a white powder.

M_n (GPC) = 5,400 g/mol; PDI (GPC) = 1.35.

General procedure for the synthesis of PEO-$h\nu$-PS (PEO_{113}-$h\nu$-PS_{119}, entry 2 table 4.5). Under argon, a schlenk tube containing CuBr (4.5 mg; 0.031 mmol; 1 equiv.) was filled with a solution containing styrene (sty; 980 mg; 9.41 mmol; 300 equiv.), PMDETA (8.2 mg; 0.042 mmol; 1.5 equiv.), PEO_{113}-N_3 (158 mg; 0.031 mmol, 1 equiv.) and anisole (545 μL) previously degassed by three freeze-pump-thaw cycles. The mixture was stirred for 10 minutes and was then frozen. Under argon, a solution of the photocleavable initiator **25** in anisole (112 μL (C = 100 g/L), 0.031 mmol, 1 equiv.) was added. The mixture was degassed by three freeze-pump-thaw cycles, filled with argon and stirred in an oil bath at 90 °C for 15 h (styrene conversion = 40 %). The polymerization was quenched by quickly cooling the tube in a water-ice bath. The reaction mixture was diluted with CH_2Cl_2 and washed with an aqueous solution of EDTA (0.04 M). The organic phase was dried over Na_2SO_4, filtered and the solvent was removed under reduced pressure. The residue was precipitated in hexane (2 ×), filtered and dried in vacuo at 30 °C for 24 h, affording a white powder (372 g, 68%). Residual homo-PEO and/or homo-PS was/were removed by extraction with selective solvents (Et_2O for PS and H_2O:MeOH (90:10) for PEO).

M_n (GPC) = 30,100 g/mol; PDI (GPC) = 1.15. ^{1}H NMR (500 MHz, $CDCl_3$): δ (ppm) 8.12 (m, 1H, H_{Ar} in ortho position of NO_2, junction), 7.86 (s, 1H, =CH triazole; junction) 7.40-6.20 (m, 665H, H_{Ar}; PS + junction), 5.23 (s, 2H, CH_2-O, ester; junction), 4.6-4.3 (m, 3H, CH_2-O, ether; junction + CH-Br, end chain), 3.62 (s, 452H, CH_2; PEO), 3.39 (s, 3H, CH_3-O; PEO), 2.3-1.2 (m, 399 H, $H_{backbone}$; PS).

Synthesis of PS_{52}-Br. Under argon, a round bottom flask, with a side stopcock, containing CuBr (35 mg; 0.24 mmol; 1 equiv.) was filled with a solution containing 1-bromoethylbenzene (45 mg; 0.24 mmol, 1 equiv.), styrene (5.08 g; 48.8 mmol; 200 equiv.), dNPy (299 mg; 0.73 mmol; 3 equiv.) and anisole (1.27g; 20 wt-%) previously degassed by three freeze-pump-thaw cycles. The mixture was degassed by three freeze-pump-thaw cycles, filled with argon and stirred in an oil bath at 100 °C for 20 h (styrene conversion = 30 %). The polymerization was quenched by quickly cooling the tube in a water-ice bath. The reaction mixture was filtered on neutral Al_2O_3 (eluent: CH_2Cl_2). The organic phase was dried over $MgSO_4$, filtered and the solvent was removed under

reduced pressure. The residue was precipitated in hexane (2 ×), filtered and dried in vacuo at 30 ℃ for 24 h, affording a white powder (844 mg, 54 %).

M_n (GPC) = 5,400 g/mol; PDI (GPC) =1.08. ^{1}H NMR (300 MHz, $CDCl_3$): δ (ppm) 7.50-6.30 (m, 296H, H_{Ar}), 4.65-4.35 (m, 1H, CH-Br), 2.60-1.20 (190H, $H_{backbone}$).

Synthesis of PS_{97}-Br. Under argon, a round bottom flask, with a side stopcock, containing CuBr (47 mg; 0.32 mmol; 1.5 equiv.) was filled with a solution containing EBiB (43 mg; 0.22 mmol, 1 equiv.), styrene (9.10 g; 87.37 mmol; 400 equiv.), PMDETA (68 mg; 0.39 mmol; 1.8 equiv.) and anisole (3.90 g; 30 wt%) previously degassed by three freeze-pump-thaw cycles. The mixture was degassed by three freeze-pump-thaw cycles, filled with argon and stirred in an oil bath at 90 ℃ for 5 h (styrene conversion = 23 %). The polymerization was quenched by quickly cooling the tube in a water-ice bath. The reaction mixture was diluted with CH_2Cl_2 and washed with an aqueous solution of EDTA (0.04 M). The organic phase was dried over $MgSO_4$, filtered and the solvent was removed under reduced pressure. The residue was precipitated in hexane, filtered and dried in vacuo at 30 ℃ for 24 h, affording a white powder (2.01 g, 96 %).

M_n (GPC) = 10,100 g/mol; PDI (GPC) =1.06. ^{1}H NMR (300 MHz, $CDCl_3$): δ (ppm) 7.20-6.10 (m, 549H, H_{Ar}), 4.60-4.30 (m, 1H, CH-Br), 3.65-3.49 (m, 2H, CH_3-CH_2-O, ester), 2.40-1.10 (343H, $H_{backbone}$).

General procedure for synthesis of PMMA-Br ($PMMA_{70}$-Br). Under argon, a round bottom flask, with a side stopcock, containing CuBr (50 mg; 0.35 mmol; 1.0 equiv.) was filled with a solution containing EBiB (68 mg; 0.35 mmol, 1 equiv.), MMA (3.49 g; 34.86 mmol; 100 equiv.), dNPy (427 mg; 1.05 mmol; 3 equiv.) and anisole (5.23 g; 60 wt%) previously degassed by three freeze-pump-thaw cycles. The mixture was degassed by three freeze-pump-thaw cycles, filled with argon and stirred in an oil bath at 60 ℃ for 30 min (MMA conversion = 54 %). The polymerization was quenched by quickly cooling the tube in a water-ice bath. The reaction mixture was diluted with CH_2Cl_2 and washed with an aqueous solution of EDTA (0.04 M). The organic phase was dried over $MgSO_4$, filtered and the solvent was removed under reduced pressure. The residue was precipitated in hexane, filtered and dried in vacuo at 30 ℃ for 24 h, affording a white powder (0.68 g, 40 %).

M_n (GPC) = 9,600 g/mol; PDI (GPC) = 1.12. ^{1}H NMR (300 MHz, $CDCl_3$): δ (ppm) 4.01 (m, 2H, CH_2-O, ethoxy chain end), 3.58 (s, 210H, CH_3-O, ester), 2.0-1.30 (140H, $CH_{2,\ backbone}$), 1.2-0.6 (210H, $CH_{3,\ backbone}$).

General procedure for the synthesis of PS-N_3 and PMMA-N_3. Scheme 4.19) To a solution of PS_{52}-Br (800 mg, 0.15 mmol, 1 equiv.) in dry DMF (7.41 mL, 0.02 M), sodium azide (193 mg, 2.96 mmol, 20 equiv.) was added. The solution was stirred under argon at 20 ℃ for 24 h. Distilled H_2O (50 mL) was added to the mixture inducing the precipitation of the polymer which was extracted with CH_2Cl_2. The organic phases were combined, dried over $MgSO_4$, filtered and the solvent was removed under reduced pressure. The residue was precipitated in MeOH, filtered and dried one night in vacuo at 30 ℃, affording a white powder (707 mg, 95 %).

PS_{52}-N_3: ^{1}H NMR (300 MHz, $CDCl_3$): δ (ppm) 7.50-6.30 (m, 324H, H_{Ar}), 4.20-3.80 (m, 1H, CH-N_3), 2.60-1.20 (190H, $H_{backbone}$).

$PMMA_{70}$-N_3: ^{1}H NMR (300 MHz, $CDCl_3$): δ (ppm) 4.08 (m, 2H, CH_2-O, ethoxy chain end), 3.56 (s, 210H, CH_3-O, ester), 2.0-1.30 (140H, $CH_{2,\ backbone}$), 1.2-0.6 (210H, $CH_{3,\ backbone}$).

Procedure for the synthesis of PEO_{113}-$h\nu$-$PtBA_{305}$. (Entry 1, Table 4.6) Under argon, a Schlenk tube containing CuBr (4.1 mg; 0.029 mmol; 1 equiv.) was filled with a solution containing tert-butyl acrylate (tBA; 1099 mg; 8.57 mmol; 300 equiv.), Me_6Tren (9.9 mg; 0.043 mmol; 1.5 equiv.), PEO_{113}-N_3 (143 mg; 0.29 mmol, 1 equiv.) and anisole (634 μL) previously degassed by three freeze-pump-thaw cycles. The mixture was stirred for 10 minutes and was then frozen. Under argon, a solution of the photocleavable initiator **25** in anisole (102 μL (C = 100 g/L), 0.29 mmol, 1 equiv.) was added. The mixture was degassed by three freeze-pump-thaw cycles, filled with argon and stirred in an oil bath at 80 ℃ for 2 h (tBA conversion = 90 %). The polymerization was quenched by quickly cooling the tube in a water-ice bath. The reaction mixture was diluted with CH_2Cl_2 and washed with an aqueous solution of EDTA (0.04 M). The organic phase was dried over Na_2SO_4, filtered and the solvent was removed under reduced pressure. The residue was precipitated in MeOH:H_2O 50:50, filtered and dried in vacuo at 30 ℃ for 24 h, affording a white solid (1.045 g, 92 %). Residual homo-PEO and/or homo-PtBA were removed by extraction with selective solvents

(hexane for PtBA and H_2O:MeOH (90:10) for PEO).

M_n (GPC) = 63,100 g/mol; PDI (GPC) =1.15. ^{1}H NMR (500 MHz, $CDCl_3$): δ (ppm) 8.16 (d, 1H, ^3J = 9.0 Hz, H_{Ar}; junction), 7.87 (s, 1H, =CH triazole; junction), 7.15 (s, 1H, H_{Ar}; junction), 7.12 (m, 1H, H_{Ar}; junction), 5.49 (s, 2H, CH_2-O, ester; junction), 4.29 (s, 2H, CH_2-O, ether; junction), 3.63 (s, 452H, CH_2; PEO), 3.39 (s, 3H, CH_3-O; PEO), 2.4-2.1 (s, 305 H, $CH_{backbone}$; PtBa). 1.9-1.2 (m, 3355 H, $CH_{2,\ backbone}$ + CH_3; PtBa).

General procedure for the synthesis of PS-*hν*-PMMA. (PS_{97}-*hν*-$PMMA_{35}$, Entry 3, Table 4.6) Under argon, a Schlenk tube containing CuBr (5.0 mg; 0.035 mmol; 1.2 equiv.) was filled with a solution containing methyl methacrylate (MMA; 349 mg; 3.49 mmol; 125 equiv.), PMDETA (9.1 mg; 0.052 mmol; 1.8 equiv.), PS_{97}-N_3 (352 mg; 0.035 mmol, 1.2 equiv.) and anisole (6.53 mL) previously degassed by three freeze-pump-thaw cycles. The mixture was stirred for 10 minutes and was then frozen. Under argon, a solution of the photocleavable initiator **25** in anisole (100 μL (C = 100 g/L), 0.028 mmol, 1 equiv.) was added. The mixture was degassed by three freeze-pump-thaw cycles, filled with argon and stirred in an oil bath at 60 ℃ for 2 h (MMA conversion = 33 %). The polymerization was quenched by quickly cooling the tube in a water-ice bath. The reaction mixture was diluted with CH_2Cl_2 and washed with an aqueous solution of EDTA (0.04 M). The organic phase was dried over Na_2SO_4, filtered and the solvent was removed under reduced pressure. The residue was precipitated in hexane (2 ×), filtered and dried in vacuo at 30 ℃ for 24 h, affording a white powder (373 mg, 80 %). Residual homo-PS and/or homo-PMMA were removed by extraction with selective solvents (Et_2O:hexane (50:50) for PS and CH_3-NO_2:MeOH (30:70) for PMMA).

M_n (GPC) = 15,700 g/mol; PDI (GPC) = 1.12. ^{1}H NMR (500 MHz, $CDCl_3$): δ (ppm) 8.13 (m, 1H, H_{Ar} in ortho position of NO_2, junction), 7.30-6.20 (m, 585H, H_{Ar}; PS + junction), 5.45 (m, 2H, CH_2-O, ester; junction), 4.20 (m, 2H, CH_2-O, ether; junction), 3.62 (s, 105H, CH_3-O; PMMA), 2.2-0.8 (m, 331H, $H_{backcone}$; PS + PMMA).

General procedure for the polymerization of styrene from starting $PMMA$-N_3. (Entry 6, Table 4.6) Under argon, a Schlenk tube containing CuBr (8.3 mg; 0.058 mmol; 1.5 equiv.) was filled with a solution containing styrene (2.00 g; 19.290 mmol; 500 equiv.), PMDETA

(15.0 mg; 0.087 mmol; 1.8 equiv.), $PMMA_{62}$-N_3 (239 mg; 0.038 mmol, 1 equiv.) and anisole (2.22 mL) previously degassed by three freeze-pump-thaw cycles. The mixture was stirred for 10 minutes and was then frozen. Under argon, a solution of the photocleavable initiator **25** in anisole (135 μL, C=100 g/L), 0.038 mmol, 1 equiv.) was added. The mixture was degassed by three freeze-pump-thaw cycles, filled with argon and stirred in an oil bath at 90 ℃ for 18 h (styrene conversion = 29 %). The polymerization was quenched by quickly cooling the tube in a water-ice bath. The reaction mixture was diluted with CH_2Cl_2 and washed with an aqueous solution of EDTA (0.04 M). The organic phase was dried over Na_2SO_4, filtered and the solvent was removed under reduced pressure. The residue was precipitated in hexane (2 ×), filtered and dried in vacuo at 30 ℃ for 24 h, affording a white powder (422 mg, 50 %).

The block copolymer was not purified and only the crude product was analyzed: GPC analysis showed the presence of two peaks (see Figure 4.20(d)): one corresponding to the homo-PMMA and the other to the block copolymer (see Figure 4.20(d)). Click efficiency (e_c) was estimated to 23 % by ^{1}H NMR (500 MHz, $CDCl_3$) by comparing the PMMA signal (δ = 3.60 ppm, s, 189H, CH_3-O) and the signal of the triazole junction ((δ = 7.85 ppm, s, 0.23H, =CH, triazole).

Bibliography

[1] Kang, M.; Moon, B. *Macromolecules* **2009**, *42*, 455–458.

[2] Sumerlin, B. S.; Tsarevsky, N. V.; Louche, G.; Lee, R. Y.; Matyjaszewski, K. *Macromolecules* **2005**, *38*, 7540–7545.

[3] Matyjaszewski, K.; Xia, J. H. *Chem. Rev.* **2001**, *101*, 2921–2990.

[4] Shipp, D. A.; Wang, J.-L.; Matyjaszewski, K. *Macromolecules* **1998**, *31*, 8005–8008.

[5] Opsteen, J. A.; van Hest, J. C. M. *Chem. Commun.* **2005**, 57–59.

[6] Ladmiral, V.; Mantovani, G.; Clarkson, G. J.; Cauet, S.; Irwin, J. L.; Haddleton, D. M. *J. Am. Chem. Soc.* **2006**, *128*, 4823–4830.

[7] Geng, J.; Mantovani, G.; Tao, L.; Nicolas, J.; Chen, G.; Wallis, R.; Mitchell, D. A.; Johnson, B. R. G.; Evans, S. D.; Haddleton, D. M. *J. Am. Chem. Soc.* **2007**, *129*, 15156–15263.

[8] Urbani, C. N.; Bell, C. A.; Lonsdale, D.; Whittaker, M. R.; Monteiro, M. J. *Macromolecules* **2008**, *41*, 76–86.

[9] Golas, P. L.; Tsarevsky, N. V.; Matyjaszewski, K. *Macromol. Rapid Commun.* **2008**, *29*, 1167–1171.

CHAPTER
FIVE

SYNTHESIS OF DIBLOCK COPOLYMERS BEARING PHOTOCLEAVABLE SIDE GROUPS.

Abstract

The synthesis of diblock copolymers made of a linear sequence and of a block bearing photocleavable o-nitrobenzyl esters as side groups is described. The first part of this chapter deals with the controlled radical polymerizations (CRPs) of the photocleavable monomers NBA and NBMA. RAFT, NMP and ATRP conditions have been investigated in order to define the best conditions leading to well-defined polymers. After this study, the polymerization of styrene using a PNBMA macroinitiator and the reverse approach, i.e., the polymerization of NBMA with a PS macroinitiator, in order to obtain photocleavable PNBMA-b-PS block copolymers are presented. Finally, a different strategy involving the grafting of o-nitrobenzyl moieties on PAA-b-PS precursors leading to photocleavable PNBA-b-PS is considered.

5.1 Introduction

The synthesis of block copolymers made of a (meth)acrylate sequence bearing photocleavable *o*-nitrobenzyl esters as side groups and of a linear PS block (PNB(M)A-*b*-PS) is described in this chapter. Similarly to the PEO-$h\nu$-PS system, different synthetic pathways have been investigated and are presented in Figure 5.1.

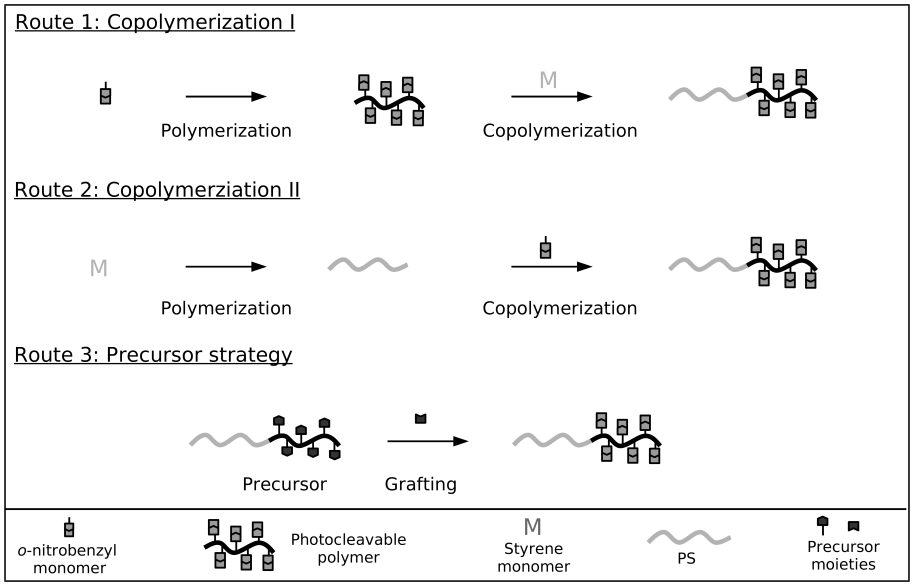

Figure 5.1: Synthesis strategies towards photocleavable PS-*b*-PNB(M)A block copolymers.

The first route consists in firstly polymerizing photocleavable *o*-nitrobenzyl acrylate (NBA) or methacrylate (NBMA) and subsequently polymerizing styrene in order to yield PNB(M)A-*b*-PS block copolymers (Copolymerization I). The approach of the second pathways is the same as for route number one, except that the order of the block synthesis is inverted (Copolymerization II). Finally, the third route implies the use of a poly(acrylic acid)-*block*-polystyrene (PAA-*b*-PS) as precursor of PNBA-*b*-PS (precursor strategy). Indeed, photocleavable block copolymers can be reached after the grafting of PAA-*b*-PS with *o*-nitrobenzyl

bromide. As far as PAA-*b*-PS copolymers are concerned, they can be obtained after hydrolysis of poly(tert-butyl acrylate)-*block*-polystyrene (PtBA-*b*-PS) precursors, the latter being easily produced by CRP.

The first and second strategies are based on the polymerization of acrylate and methacrylate of *o*-nitrobenzyl alcohol (NBA and NBMA). Before discussing the synthesis of the photocleavable block copolymers, the behavior of these monomers under CRPs conditions has been investigated and is presented here. This study was carried out in collaboration with Dr. Richard Hoogenboom and Aydin Can from the group of Prof. Ulrich S. Schubert at the Laboratory of Macromolecular Chemistry and Nanoscience from the Eindhoven University of Technology (TU/e, The Netherlands). This laboratory uses high-throughput experimentation (HTE) workflows (automated synthesizers) enabling a screening a large number of parameters (solvent, time, reagent, etc.) in short time periods. The experiments using HTE technique were performed on a Chemspeed ASW2000 automated synthesizer equiped with 16 parallel 13 mL reactors and coupled to gas chromatography analyzer (GC).

5.2 CRPs of NBA and NBMA

5.2.1 Introduction

As already mentioned, *o*-nitrobenzyl derivatives are commonly used as photolabile protecting groups for carboxylic acid or amine groups in organic and polypeptide synthesis [1, 2]. Their easy accessibility and their quantitative cleavage upon UV exposure have both contributed to their popularity. *o*-Nitrobenzyl derivatives have also attracted interest in the field of material science. Since the early 80's, *o*-nitrobenzyl esters are incorporated into polymers for the production of photoresist materials [3–14], and more recently, they are encountered in networks [15], in biodegradable polymers [16], in star polymers [15, 17], and also in block copolymers (see chapter 2).

Surprisingly, to the best of our knowledge only one example dealing with the CRP of an *o*-nitrobenzyl containing monomer can be found in the literature [18]. The authors reported the ATRP of *o*-nitrobenzyl methacrylate (NBMA) initiated by a PEO macroinitiator to synthesize poly(ethylene oxide)-*block*-poly(nitrobenzylmethacrylate) block copoly-

mers (PEO-*b*-PNBMA). Despite the use of CRP, these diblocks showed broad molar mass distribution (PDI = 1.8) indicating a poor control over the polymerization.

A similar behavior has been described in 1999 by Pan *et al.* where the homopolymerization of another nitro-aromatic monomer, *p*-nitrophenyl methacrylate (NPMA), by ATRP was poorly controlled (1.57<PDI< 2.45) [19]. The use of polystyrene (PS) or PEO macroinitiator narrows the polydispersity index (1.25<PDI<1.40 for PS, and 1.15<PDI<1.30 for PEO), which can be ascribed to the narrow molar mass distribution of the macroinitiator rather than improved control over the polymerization [19, 20]. On the other hand, homopolymers of *p*-nitrophenyl acrylate (NPA) with molar masses up to 12,000 g/mol and with narrow polydispersity indices (PDI<1.20) have been successfully synthesized by RAFT [21].

The difficulty in controlling the polymerization of monomers containing nitro-aromatic groups by CRP is inherent to their chemical structure. Actually, nitro-aromatic compounds are known to act as inhibitors/retardators in radical polymerizations and to produce radicals when heated [22–33].

Two complementary mechanisms describing the polymerization inhibition by nitro-aromatic compounds have been proposed (Figure 5.2) [24, 25, 33]. The first one, proposed by Price and Durham in 1943, involves the attack of the propagating radical onto the aromatic ring in the *para* position. Afterwards, hydrogen abstraction by another propagating radical (1), or a radical transfer to the monomer (2) ends the process [24,33]. A few years later, a complementary mechanism implying the direct attack of the propagating radical onto the nitro group, and consequently the termination of the growing chains, has been suggested by Hammond and Bartlett (3-5) [25, 33].

Besides those inhibition mechanisms, the controlled polymerization process might also be disturbed by radicals produced by the nitro-aromatic compounds themselves. Indeed, studies on the pyrolysis of nitro-aromatic compounds have revealed some distinct decomposition pathways leading to different kinds of free radical species. For instance, phenyl and phenol radicals are formed after the loss of the NO_2

group [28,29,31]. It was also shown that nitrobenzyl derivatives generate free radicals at relatively low temperature (80-140 °C) in concentration ranging from 10^{-4} to 10^{-6} M depending on the temperature, due to the inter- and intra-molecular hydrogen transfer from the benzylic methylene [27, 30]. These concentrations are high enough to perturb the controlled polymerization process but are too low to affect the composition of the desired polymers.

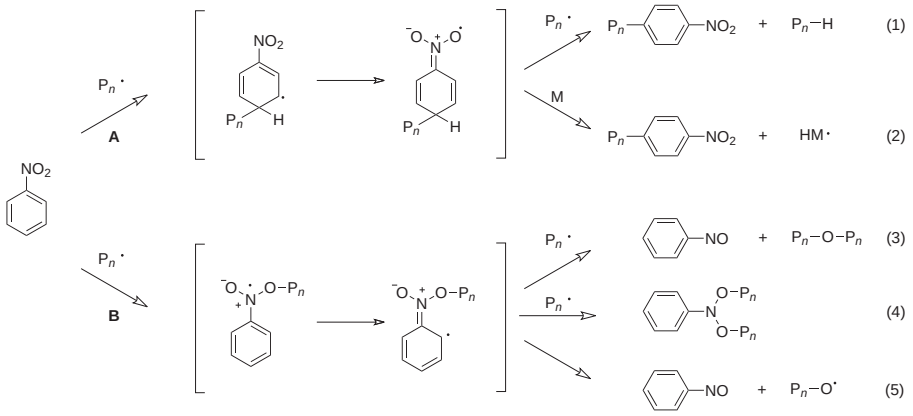

Figure 5.2: Polymerization inhibition by nitro-aromatic compounds. Mechanism proposed by Price and Durham (**a**). Complementary pathways suggested by Hammond and Bartlett (**b**)

In regard to those considerations, *o*-nitrobenzyl acrylate (NBA) and methacrylate (NBMA) represent very challenging monomers to polymerize by CRP techniques, but remain nonetheless highly interesting in the field of light sensitive polymers. This section discusses the behavior of those photocleavable monomers under RAFT, ATRP and NMP conditions, with the aim of defining their limits, and finding exploitable experimental conditions leading to well-defined polymers.

5.2.2 NBA and NBMA synthesis

Before studying the polymerizations of NBA **36** and NBMA **38**, they have been successfully synthesized by an esterification reaction between *o*-nitrobenzyl alcohol **16** and acryloyl **35** and methacryloyl **37** chloride respectively (Figure 5.3).

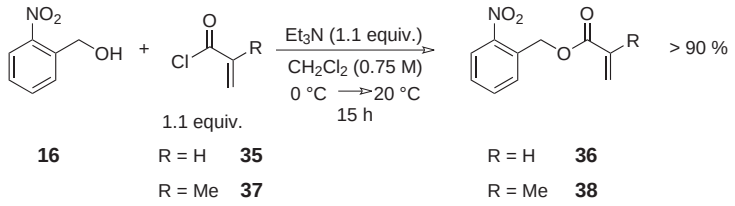

Figure 5.3: Synthesis of NBA and NBMA.

5.2.3 RAFT polymerization of NBMA and NBA

Successful RAFT polymerizations of methyl methacrylate (MMA), 1-ethoxyethyl acrylate (EEA), methacrylic acid (MA) and oligo(ethylene glycol)methacrylate (OEGMA) using high-throughput workflow procedures have been previously reported [34–36]. Similar reaction conditions for NBMA and NBA have been investigated using azobis(isobutyronitrile) (AIBN, **39**) as initiator in combination with 2-cyano-2-butyl dithiobenzoate (CBDB, **40**) or cumyl phenyldi-thioacetate (CPDA, **42**) as chain transfer agent (CTA) (Figure 5.4). The polymerizations were performed in DMF at 70 ℃ in parallel on a Chemspeed ASW2000 automated synthesizer. Butylbenzene was used as internal standard for GC measurements. The screened parameters were the following: the AIBN/CTA ratio (0.10, 0.25), the monomer/CTA ratio (100, 200), and, for NBA, the CTA type (CBDB, CPDA).

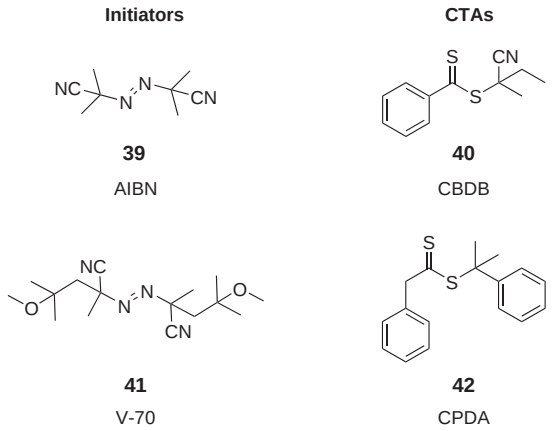

Figure 5.4: Chemical structure of the initiators and the CTAs used in RAFT experiments.

The results for NBMA are presented in Table 5.1. The polymerizations were rather slow, molar masses of only 6,000-11,000 g/mol could be obtained after 18 h reaction time. Although the molar mass distributions remain relatively broad (PDI∼1.5), some control over the polymerization can still be achieved as shown in Figure 5.5. For all tested polymerizations, a linear variation of the conversion with time in semi-logarithmic plots has been observed, indicating a constant concentration of active species in the medium (Figure 5.5(a)). Moreover, the molar masses can be predicted since they increase linearly with conversion (Figure 5.5(b)). Deviations from the ideal behavior, however, exist (all lines should cross the origin for both plots) that could be tentatively attributed to a low addition rate of the monomer radical to the thiocarbonyl moiety compared to the propagation rate. This would delay the setting of the reversible addition-fragmentation equilibrium and is known as hybrid behavior [37]. An initial burst of radicals derived from the decomposition of parts of the NBMA could also play a role in this behavior. Best results were obtained for an AIBN/CBDB ratio equal to 0.25.

Table 5.1: Experimental conditions and results obtained for RAFT polymerization of NBMA with CBDB performed on the Chemspeed ASW200 automated synthesizer.

Entry[a]	NBMA/CBDB (Molar Ratio)	AIBN/CBDB (Molar Ratio)	t (h)	Conv. (%)	M_n[b] (g/mol)	PDI
1	100	0.25	18	63	8,300	1.59
2	200	0.25	18	49	11,400	1.48
3	100	0.10	18	26	6,400	1.50
4	200	0.10	18	21	9,000	1.52

[a]The polymerizations were performed on a 4 mmol monomer scale, in DMF (1 M) at 70 ℃ and using CBDB as CTA. [b]Determined with a PS calibration.

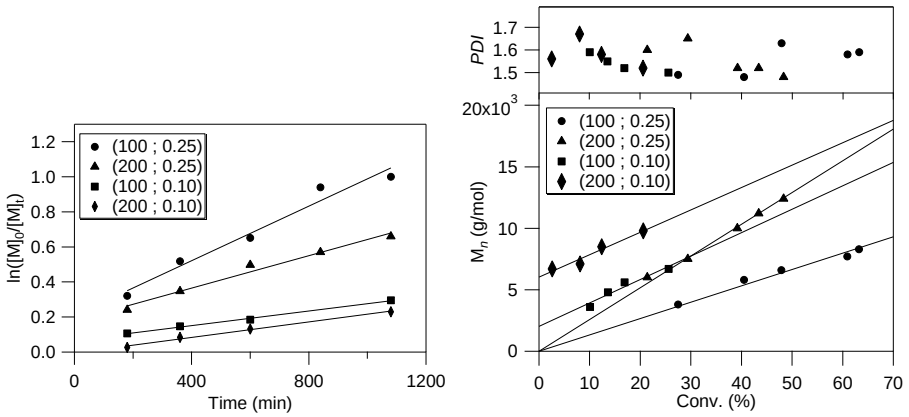

Figure 5.5: (a) Plot of $\ln([M]_0/[M])$ versus time for the RAFT polymerization of NBMA with CBDB at 70 ℃. Insert: ratio NBMA/CBDB; ratio AIBN/CBDB. (b) Plot of M_n (lower panel) and PDI (upper panel) versus conversion for the RAFT polymerization of NBMA with CBDB at 70 ℃. Insert: ratio NBMA/CBDB; ratio AIBN/CBDB.

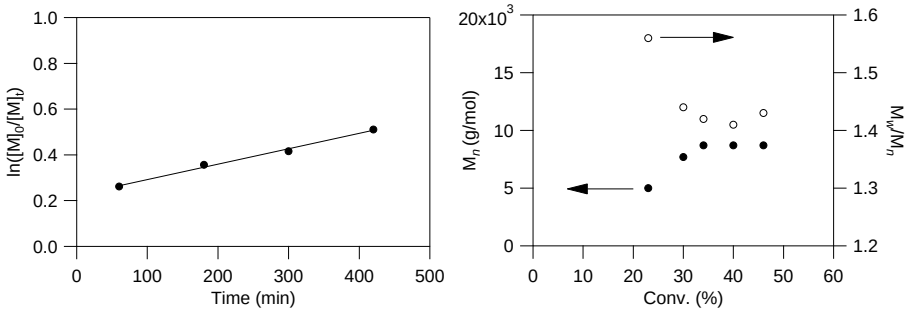

(a) (b)

Figure 5.6: (a) Plot of $\ln([M]_0/[M])$ versus time for the RAFT polymerization of NBMA with CBDB at 40 ℃. (b) Plot of M_n versus conversion (full circles) and M_w/M_n (PDI) versus conversion (open circles) for the RAFT polymerization of NBMA with CBDB at 40 ℃.

In order to try to improve the control over the polymerization of NBMA by minimizing the generation of radicals generated by the *o*-nitrobenzyl group, the polymerization temperature was decreased to 40 ℃. Ratios of AIBN/CBDB = 0.25 and NBMA/CBDB = 200 were used. To enable initiation at this low temperature, azobis(4-methoxy-2,4-dimethyl valeronitrile) (V-70, **41**) was employed as initiator instead of AIBN because of its lower decomposition temperature (10 h half-life decomposition temperature = 30 ℃; 65 ℃ for AIBN).

A linear increase of conversion with time was observed after a fast initial polymerization (Figure 5.6(a)), and smaller polydispersity indices (PDI down to 1.41) were obtained compared to 70 ℃. However, the plot of M_n versus conversion (Figure 5.6(b)) shows that the polymerization exhibits some controlled character only for conversions up to about 33 %, since the increase in molar mass saturates for higher conversions. It is not clear why the control is lost only after 30 % conversion, but the linear increase in the kinetic plot in combination with the saturation of molar mass indicates the occurrence of chain transfer reactions.

Concerning NBA, similar reaction conditions as the ones described in Table 5.1 have been applied, and another CTA (CPDA, **42**) has been

tested, but the obtained molar masses never exceeded 1,000 g/mol. The RAFT polymerization of NBA can thus be considered as almost completely inhibited. This unexpected behavior might be ascribed to the higher reactivity of the acrylate radical in comparison to the methacrylate one, being thus more prone to undergo side reactions with the *o*-nitrobenzyl group.

5.2.4 NMP polymerization of NBA

Since methacrylate type monomers are notoriously difficult to polymerize in a controlled manner by NMP, only the NBA has been used in this study by employing SG1 nitroxide **43** and MAMA-SG1 BlocBuilder^{TM} **44** as initiators (Figure 5.7) [38,39]. Unfortunately, no polymerization has been observed in the tested conditions which were previously optimized for acrylates [40, 41]. This is probably explained by the high temperatures used in NMP which favors the degradation of the *o*-nitrobenzyl moiety and thus the important generation of side radicals inhibiting the polymerization of NBA in addition to the complications already discussed for the RAFT polymerization of NBA.

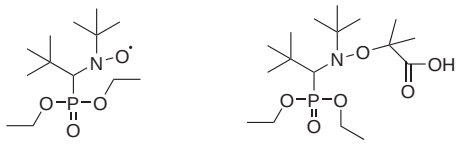

43 SG1 nitroxide

44 MAMA-SG1 BlocBuilder^{TM}

Figure 5.7: Chemical formula of SG1 and MAMA-SG1 BlocBuilder^{TM} used in NMP experiments.

5.2.5 ATRP polymerization of NBMA and NBA

A first set of experiments was performed in parallel on the Chemspeed ASW2000 automated synthesizer. The polymerizations were performed in anisole at 80 ℃ using ethyl 2-bromoisobutyrate (EBiB,**45**) as initiator. *N*-hexyl-2-pyridylmethanimine (NHPMI, **47**) and PMDETA **22** were used as ligands for the polymerization of NBMA, and PMDETA and Me_6Tren **48** were tried for NBA (Figure 5.8). The other varied parameters were the monomer concentration (1 and 2 M) and the monomer/initiator ratio (100, 200). The results for NBMA and NBA are presented in Tables 5.2 and 5.3, respectively.

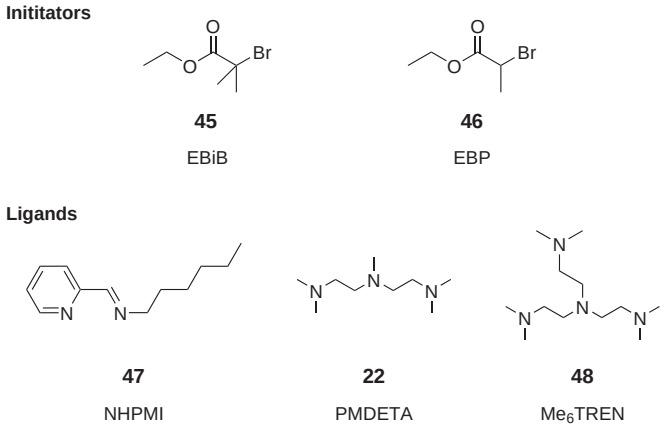

Figure 5.8: Chemical formula initiatiors and ligands used in ATRP experiments.

In the case of NBMA, no molar masses over 1,000 g/mol could be obtained when NHPMI was used as ligand. This system is thus not active enough to enable the polymerization of NBMA. The experiments with PMDETA, a more activating ligand, led to higher, albeit still rather low, molar mass (∼3,000 g/mol) polymers. Compared to the results obtained by RAFT, the molar masses are lower, but the polydispersity index is also smaller (PDI∼1.3-1.4 instead of 1.5). ATRP seems thus to be a more promising method than RAFT for the polymerization of NBMA, even if the molar masses achieved remained low, and merits further investigation (see below).

Table 5.2: Conditions and results for the ATRP of NMBA performed on the Chemspeed ASW2000 automated synthesizer.

Entry[a]	Ligand	C_{NBMA} (mol/L)	NBA/EBiB	t (h)	M_n[b] (g/mol)	PDI
1	NHPMI	1	100	18	900	/
2	NHPMI	1	200	18	500	/
3	NHPMI	2	100	18	1,000	1.29
4	NHPMI	2	200	18	800	/
5	PMDETA	1	100	3	2,500	1.40
6	PMDETA	1	200	3	1,600	1.35
7	PMDETA	2	100	3	1,800	1.34
8	PMDETA	2	200	3	2,700	1.32

[a]The polymerizations were performed on a 4 mmol monomer scale in anisole at 80 ℃; [EBiB]/[CuBr]=1;[NHPMI]/[CuBr]=2.4; [PMDETA]/[CuBr]=1.2.
[b]Determined with a PS calibration.

For NBA (Table 5.3), only very low molar masses were obtained, similarly to NBMA, but with a lower polydispersity index. By using the very active Me_6Tren instead of PMDETA the polymerization rate of NBA increased significantly since the same range of molar masses could be achieved in 3 hours instead of 18 hours with PMDETA. However, like in RAFT, the polymerization of NBA by ATRP seems thus strongly limited.

In order to obtain PNB(M)A of higher molar masses by ATRP, another set of polymerizations was carried out at higher concentration of NBA and NBMA. The results for NBA are shown in Table 5.4. Performing polymerization with ethyl 2-bromopropinoate (EBP, **46**) and at a concentration of 3.4 M in anisole (instead of 1 or 2 M) led indeed to polymers with larger molar masses (up to 5,300 g/mol), but showing large polydispersity indices. No controlled polymerization could thus be achieved for NBA despite variations in the amount of Cu(I) and ligand, and of the temperature.

Table 5.3: Conditions and results for the ATRP of NBA performed on the Chemspeed ASW2000 automated synthesizer.

Entry[a]	Ligand	C_{NBA} (mol/L)	NBA/EBiB	t (h)	M_n[b] (g/mol)	PDI
1	PMDETA	1	100	18	1,300	1.18
2	PMDETA	1	200	18	1,100	1.16
3	PMDETA	2	100	18	1,900	1.23
4	PMDETA	2	200	18	1,800	1.18
5	Me_6Tren	1	100	3	1,900	1.18
6	Me_6Tren	1	200	3	1,100	1.11
7	Me_6Tren	2	100	3	2,700	1.35
8	Me_6Tren	2	200	3	2,000	1.22

[a]The polymerizations were performed on a 4 mmol monomer scale in anisole at 80 ℃; [EBiB]/[CuBr]=1;[ligand]/[CuBr]=1.2. [b]Determined with a PS calibration.

For NBMA (Table 5.5), the experiments at higher monomer concentration revealed that polymers with higher molar masses (12,100-16,400 g/mol) and with low polydispersity indices (PDI<1.25) can been synthesized. Actually, good results have been obtained with polymerization in 3.4 M in anisole and with 1 or 2 equivalents of copper bromide (CuBr) and/or small amounts of copper(II) ($CuBr_2$). When DMF was used as solvent, the polymerization was faster but broader molar mass distributions were obtained even when $CuBr_2$ was added.

Entry[a]	NBA/CuBr/EBP (molar ratio)	Ligand	T (℃)	t (h)	Conv. (%)	$M_{n,\,th}$ (g/mol)	M_n[b] (g/mol)	PDI
1	200/1/1	PMDETA	80	20	/	/	/	/
2	100/2/1	Me_6Tren	90	16	42	7,800	3,800	2.62
3	200/1/1	Me_6Tren	80	10	10	4,100	2,500	1.47
4	200/2/1	Me_6Tren	80	20	25	10,300	5,300	1.71

[a]The polymerizations were performed on a 2.5 mmol monomer scale; C_{NBA}=3.4 mol/L. [b]Determined with a PS calibration.

Table 5.4: Conditions and results for the ATRP of NBA.

Entry[a]	NBMA/CuBr/EBiB (molar ratio)	Solvent	$CuBr_2$ (mol %)	t (h)	Conv. (%)	$M_{n,\,th}$ (g/mol)	M_n[b] (g/mol)	PDI
1	200/1/1	anisole	10	20	31	13,700	16,300	1.21
2	300/1/1	anisole	10	27	19	12,600	13,800	1.24
3	200/1/1	anisole	0	15	32	14,200	12,100	1.13
4	200/1/1	DMF	0	8	33	14,600	12,000	1.35
4	200/1/1	DMF	10	15	35	15,500	17,500	1.143

[a]The polymerizations were performed on a 2.5 mmol monomer scale; C_{NBA}=3.4 mol/L. [b]Determined with a PS calibration.

Table 5.5: Conditions and results for the ATRP polymerization of NBMA with PMDETA.

In order to illustrate the controlled character of the polymerization, the conditions presented at the Entry 3 of Table 5.5 were chosen for a kinetic study. Linear correlations of, firstly, the conversion versus time in semilogarithmic coordinates and, secondly, the molar mass versus conversion have been observed, and are shown in Figures 5.9(a) and 5.9(b), respectively. Moreover, a narrowing of the molar mass distribution with time, typical for a controlled polymerization, has also been observed (Figures 5.9(b) and 5.9(c)). Finally, it is important to note that conversions over 35-40 % could not, in general, be achieved without a significant broadening of the molar mass distribution.

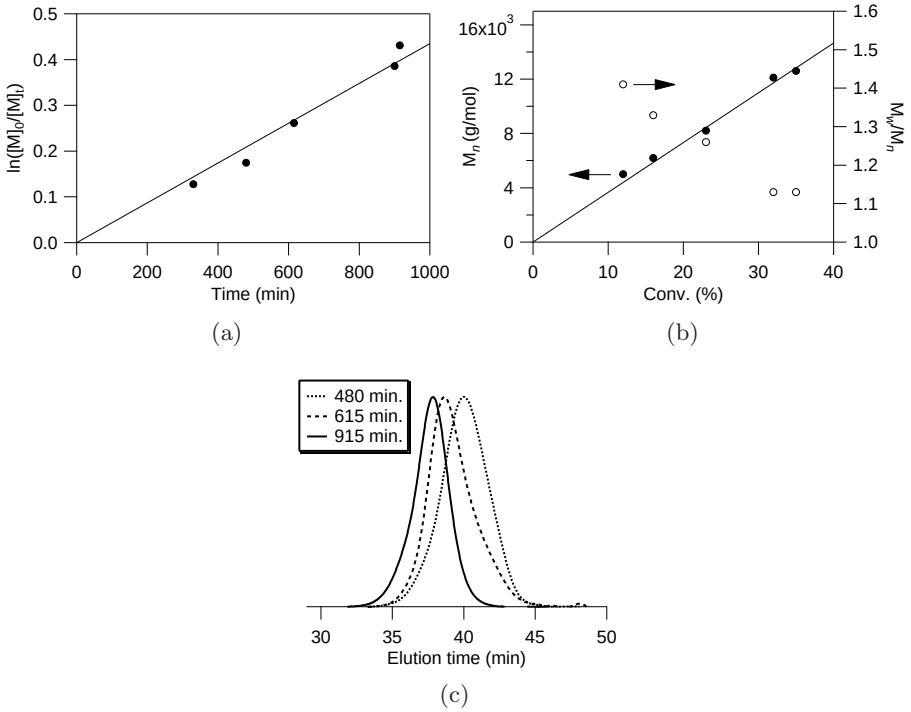

Figure 5.9: Plot of $\ln([M]_0/[M])$ versus time for the ATRP polymerization of NBMA (a). Plot of M_n versus conversion (full circles) and M_w/M_n (PDI) versus conversion (open circles) for the ATRP polymerization of NBMA (b). Evolution of the GPC chromatograms with time for the ATRP of NBMA (Table 5.5, Entry 3): after 480 (dotted line), 615 (dashed line), and 915 (full line) min. reaction time (c) .

5.2.6 Conclusions

o-Nitrobenzyl methacrylate and acrylate prove to be capricious and challenging monomers to polymerize by controlled radical polymerization techniques due to the sensitive nitro-aromatic group. This group can indeed generate free radicals and can also act as an inhibitor. Nevertheless, the global composition of all synthesized polymers was not affected by those side radicals as confirmed by ^{1}H NMR which showed that the different protons of the polymer (aromatic, benzylic, backbone) have the expected ratio. The nitrobenzyl acrylate (NBA) exhibited the greatest difficulties to be polymerized under controlled conditions. Actually, no polymerization was observed for RAFT and NMP, and ATRP only yielded low molar mass polymers with broad molar mass distributions in the tested experimental conditions. (Figure 5.10).

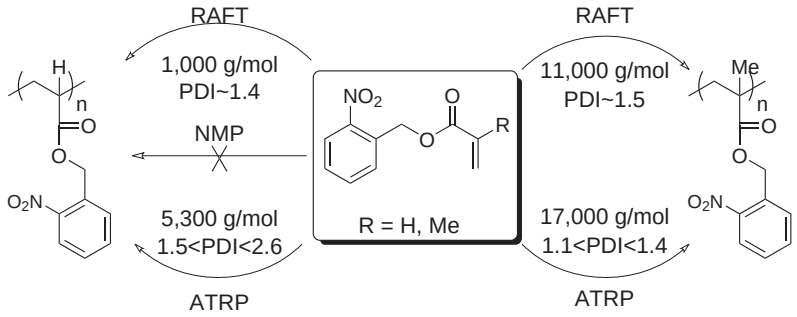

Figure 5.10: Summary of the results obtained for the CRPs of NB(M)A in the tested conditions.

On the contrary, the methacrylate version of the monomer, NBMA, showed much more promising results. Polymers with molar masses up to 11,000 g/mol only and with rather broad molar mass distributions (PDI∼1.5) were obtained by RAFT but the polymerizations exhibited, nevertheless, some controlled character. For ATRP, the controlled nature of the polymerization was successfully demonstrated after optimization of the catalytic system and monomer concentration, and is therefore the method of choice for the synthesis of poly(*o*-nitrobenzyl methacrylate). Moreover, it should be noted that the monomer conversion should be limited to 30 % to keep the control over the polymerization. In this case, polymers with molar masses up to 17,000 g/mol and polydispersity

index as low as 1.13 have been obtained.

5.3 Copolymerization I : ATRP of styrene initiated with a PNBMA macroinitiator

After the successful synthesis of photocleavable PNBMA homopolymers with narrow molar mass distributions by ATRP, the polymerization of styrene starting from the PNBMA macroinitiator presented at Entry 3 of Table 5.5 has been investigated. Conditions similar to those used for the ATRP of styrene initiated by a PEO macroinitiator (See Table 4.10) have been tested. Unfortunately, no polymerization of styrene has been observed under these conditions. This behavior could be explained either by a loss of the bromide chain end during the polymerization of NBMA or by the high reactivity of the styrene radicals which can easily undergo side reactions with the *o*-nitrobenzyl groups of the NBMA macroinitiator (behavior similar to the NBA described in Section 5.2). For that reason, this pathway has been rapidly abandoned.

5.4 Copolymerization II : ATRP of NBMA with a PS macroinitiator

One major problem encountered in the synthesis of block copolymers by chain extension from a macroinitiator in ATRP (and in CRPs in general) is the order of the block synthesis. Indeed, when this order in not well chosen, the copolymerization leads to a bimodal distribution of the molar masses due to a poor initiation efficiency [42, 43]. Successful chain extensions are observed when the rate of initiation is at least as fast as the rate of propagation. This is the case when the comonomers belong to the same class. However, when different kinds of monomers have to be copolymerized, the following order of polymerization must be respected: acrylonitrile, methacrylates, acrylates or styrenes [43]. This means that polyacrylonitrile and polymethylacrylates blocks must be synthesized first while the order of addition for styrenes and acrylates is not important.

As the polymerization of styrene with a PNBMA macroinitiator failed (see Section 5.3), the inverse strategy consisting in polymerizing NBMA from a PS macroinitator has been investigated. The technique

of the halogen exchange already mentioned in section 4.4.3 has been tested by using CuCl as catalyst with a bromide macroinitiator (Table 5.6) [42,43]. The GPC chromatograms of the block copolymer before and after purification are presented in Figure 5.11. After removal of the non-coupled PS, a PS-*b*-PNBMA with a M_{n} equal to 34,400 g/mol and a PDI of 1.37 has been obtained. The efficiency of the initiation has been estimated to about 64 % according to the ratio between the M_{n}'s of the PS block calculated before and after the extraction of the homo-PS.This poor efficiency encountered in the polymerization of NBMA with a PS macroinitiator in combination with the difficulty to polymerize NBMA in a controlled way led us to change to another strategy which is described in the next section.

Table 5.6: Polymerization of NBMA with a PS macroinitiator performed with CuCl in anisole (30 wt-%) at 110 °C.

Entry	PS-Br/CuCl/PMDETA/NBMA (equiv.)	t (h)	$M_{\mathrm{n,\ NMR}}$ (g/mol)	$M_{\mathrm{n,\ GPC}}{}^{b}$ (g/mol)	PDI
1	1 : 1.5 : 1.8 : 225	6	34,400	23,700	1.37

[b]Determined with a PS calibration after purification.

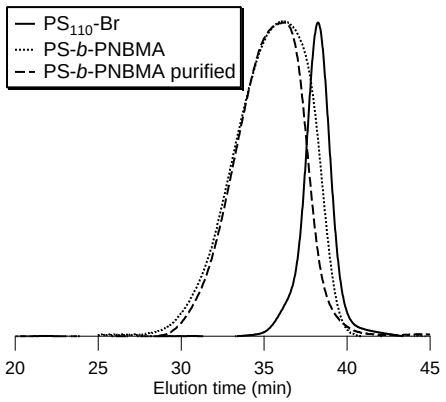

Figure 5.11: GPC chromatograms of the PS-*b*-PNBMA described in Table 5.6.

5.5 Precursor strategy

The last investigated strategy is presented in Figure 5.12. The first step is the polymerization of *tert*-butyl acrylate (tBA) by ATRP followed by that of styrene in order to obtain a PtBA-*b*-PS diblock copolymers (**50**). Hydrolysis of the *tert*-butyl esters of the PtBA sequence unmasks the carboxylic functions leading to the PAA-*b*-PS **51**. The last step of this strategy is the grafting of the *o*-nitrobenzyl groups on the PAA block thanks to a nucleophilic substitution of *o*-nitrobenzyl bromide by the carboxylates of the diblock. This strategy lengthens the synthesis but it circumvents the problems encountered with the polymerization of *o*-nitrobenzyl monomers. This strategy has been investigated by Olivier Bertrand during his master thesis [44].

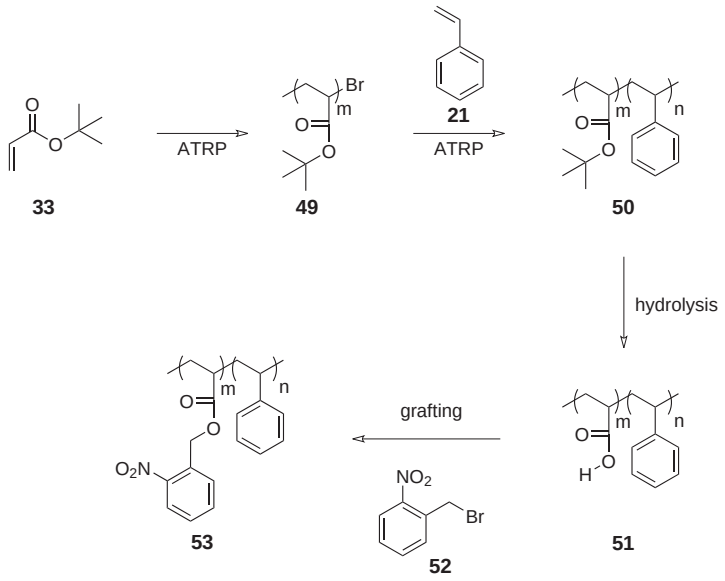

Figure 5.12: Strategy of the precursor route.

5.5.1 PtBA synthesis

Table 5.7 presents the experimental conditions and the results for the ATRP polymerizations of tBA. Polymerizations were conducted in anisole at 80 or 90 ℃ using CuBr/PMDETA as catalytic system in conjunction with either EBiB or EBP as the initiator. Several well-defined PtBA with molar masses from 3,500 to 14,600 g/mol (M_n, NMR) and with PDI less then 1.25 were produced in this way. Except for $PtBA_{148}$ (Entry 1), the monomer conversions were limited to maximum ∼50 % in order to keep a maximum of reactive chain-ends for the further chain extension with styrene. In fact, high monomer conversions increase the probability of transfer and termination reactions leading to inactive chain ends.

Entry[a]	PtBA[b]	Initiator[c]	T (℃)	t (h)	Conv. (%)	$M_{n,\,th}$ (g/mol)	$M_{n,\,NMR}$ (g/mol)	$M_{n,\,GPC}$[b] (g/mol)	PDI
1[d]	$PtBA_{148}$	EBiB	80	2.0	95	14,600	19,000	19,500	1.10
2	$PtBA_{74}$	EBiB	90	1.0	52	7,900	9,500	11,700	1.14
3	$PtBA_{27}$	EBiB	90	0.5	19	2,900	3,500	4,900	1.16
4	$PtBA_{31}$	EBiB	90	0.5	26	4,000	4,000	7,100	1.22
5	$PtBA_{49}$	EBP	80	2.0	41	6,300	6,300	8,600	1.13
6	$PtBA_{62}$	EBP	80	2.0	49	7,600	7,900	10,100	1.10

[a]Reactions conditions: Initiator/CuBr/PMDETA/PtBA = 1 / 1 / 1.1 / 120; anisole 40 wt-%.
[b]DP determined by ^{1}H NMR. [c]EBiB :ethyl 2-isobutyrate; EBP: ethyl 2-bromopropionate.
[d]Performed in 20 wt-% of anisole.

Table 5.7: Experimental conditions and results for the polymerization of tBA by ATRP.

5.5.2 PtBA-*b*-PS synthesis

Several PtBA-*b*-PS have been synthesized by polymerizing styrene with the PtBA macroinitiators described in the previous section. The experimental conditions and the results of these experiments are presented in Table 5.8. The polymerizations were carried out in anisole at 100 ℃ with the CuBr/PMDETA catalytic system. Well-defined block copolymers with molar masses between 14,700 and 70,000 g/mol and with PDIs lower than 1.3 have been successfully produced in these conditions.

Let us not forget that the aim is to obtain photocleavable block copolymers able to self-assemble into a cylindrical morphology. As already mentioned in Chapter 3, the composition leading to such a morphology is not known and block copolymers with different compositions have to be tested. For this reason, the mass fraction (r) of the photocleavable block is used as a guideline for the synthesis, and values of r between 0.2 and 0.3 are targeted for the final block copolymers. This is why the parameter $r_{100\ \%}$ is introduced here that represents the mass fraction of the photocleavable block if the grafting of the *o*-nitrobenzyl functions is quantitative, *i.e.*, is equal to 100 %.

According to the parameter $r_{100\%}$, PtBA-*b*-PS from Entries 4-7 from Table 5.8 are suitable candidates for the obtention of the cylindrical morphology after their transformation into photocleavable block copolymers. Concerning the PtBA-*b*-PS from Entries 1-3, they will be used to test and improve the conditions of the hydrolysis and grafting reactions.

Entry[a]	PtBA-*b*-PS	Styrene (equiv.)	Anisole (wt-%)	t (h)	Conv. (%)	$M_{\mathrm{n,\ th}}$ (g/mol)	$M_{\mathrm{n,\ NMR}}$ (g/mol)	$M_{\mathrm{n,\ GPC}}$[c] (g/mol)	PDI	$r_{100\%}$[d]
1[e]	$PtBA_{74}$-*b*-PS_{50}	120	40	2	44	15,000	14,700	16,000	1.17	0.75
2[f]	$PtBA_{27}$-*b*-PS_{443}	400	30	17	89	40,600	49,600	60,100	1.21	0.12
3	$PtBA_{62}$-*b*-PS_{213}	300	30	7	66	28,500	30,200	35,500	1.10	0.36
4	$PtBA_{49}$-*b*-PS_{280}	300	20	5	98	36,900	35,600	51,000	1.19	0.26
5	$PtBA_{31}$-*b*-PS_{168}	300	60	4	37	15,500	21,500	21,000	1.14	0.28
6	$PtBA_{74}$-*b*-PS_{415}	1000	40	15	37	48,000	52,700	58,900	1.22	0.29
7	$PtBA_{74}$-*b*-PS_{581}	1000	40	24	47	68,900	70,000	74,000	1.28	0.20

[a]Reactions conditions: PtBA/CuBr/PMDETA = 1 / 1 / 1.1; T=100 ℃. [c]Determined with a PS calibration. [d]$r_{100\%}$ = mass fraction of the future PNBA block at 100 % functionalization. [e]Performed with PtBA/CuBr/PMDETA = 1/ 0.9 / 0.9. [f]Performed with PtBA/CuBr/PMDETA = 1 / 1.5 / 1.7.

Table 5.8: Experimental conditions and results for the polymerization of styrene with PtBA macroinitiators.

5.5.3 Hydrolysis of PtBA-*b*-PS.

After the synthesis of PtBA-*b*-PS copolymers, the hydrolysis of the *t*-butyl esters into carboxylic acid functions has been performed. The transformation has been conducted in acidic conditions either by refluxing the polymers in dioxane with HCl (HCl/dioxane system) or by stirring them in dichloromethane with trifluoroacetic acid (TFA/CH_2Cl_2 system). The starting PtBA-*b*-PS and the corresponding PAA-*b*-PS obtained by hydrolysis are presented in Table 5.9. Quantitative transformations were obtained for the HCl/dioxane system (Entries 1, 5-7) while the hydrolysis remained limited to about 95 % when the TFA/CH_2Cl_2 was used (Entries 2-4).

Table 5.9: Hydrolysis of PtBA into PAA.

Entry	PtBA-Polymer		PAA-Polymer	Hydrolysis system[a]	e_h [b] (%)
1	homo-$PtBA_{148}$	→	homo-PAA_{148}	HCl/dioxane	> 99
2	$PtBA_{74}$-*b*-PS_{50}	→	PAA_{74}-*b*-PS_{50}	TFA/CH_2Cl_2	94
3	$PtBA_{49}$-*b*-PS_{280}	→	PAA_{49}-*b*-PS_{280}	TFA/CH_2Cl_2	95
4	$PtBA_{62}$-*b*-PS_{213}	→	PAA_{62}-*b*-PS_{213}	TFA/CH_2Cl_2	95
5	$PtBA_{31}$-*b*-PS_{168}	→	PAA_{31}-*b*-PS_{168}	TFA/CH_2Cl_2	96
6	$PtBA_{27}$-*b*-PS_{232}	→	PAA_{27}-*b*-PS_{232}	HCl/dioxane	> 99
7	$PtBA_{74}$-*b*-PS_{415}	→	PAA_{74}-*b*-PS_{415}	HCl/dioxane	> 99
8	$PtBA_{74}$-*b*-PS_{581}	→	PAA_{74}-*b*-PS_{581}	HCl/dioxane	> 99

[a]Reaction conditions: for HCl/dioxane system: C_{polymer} = 5 g/L; HCl = 50 equiv. compared to tBA; reflux, 24 h; for TFA/CH_2Cl_2 system: C_{polymer} = 10 g/L; TFA = 10 equiv. compared to tBA; 20 ℃, 48 h. [b]Hydrolysis efficiency (e_h) determined by ^{1}H NMR.

5.5.4 PNBA-*b*-PS synthesis

The last step of the synthesis is the grafting of the *o*-nitrobenzyl groups on the PAA sequence of the PAA-*b*-PS diblock copolymers (Figure 5.13). This grafting is a nucleophilic substitution (SN_2) which consists in firstly deprotonating the carboxylic acids with a base, affording carboxylate functions able to substitute the bromide of the *o*-nitrobenzyl bromide **52** in a second step. As carboxylates are poor nucleophiles, the reaction needs a non-nucleophilic base such as 1,8-diazabicyclo[5.4.0]undec-7-ene (DBU, **54**) that can not compete with the carboxylate for the bromide substitution. Moreover, performing the reaction in aprotic polar solvents such as DMF enables to increase the nucleophilicity of the carboxylate because of a good solvation of the counter-ion (protonated DBU).

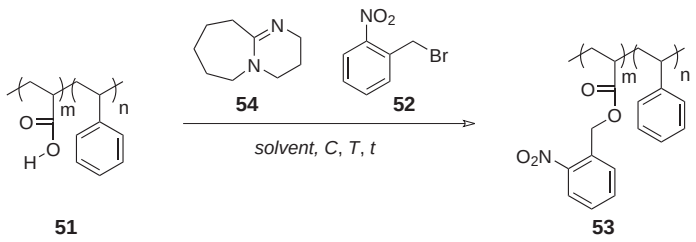

Figure 5.13: Grafting of *o*-nitrobenzyl bromide onto PAA-sequences.

Table 5.10 presents the experimental conditions and the results for the grafting of homo-PAA polymers and PAA-*b*-PS diblock copolymers. In 1990, Shimokawa and coworkers successfully synthesized PNBMA homo-polymers from PMAA by reacting it with *o*-nitrobenzyl bromide **52** using DBU as a base [45]. Similar conditions have been firstly tested on homo-PAA affording 100 % functionalized homo-PNBA (Entries 1-2). The reactions were performed at 30 ℃ in DMF for 3 hours using 2 equivalents of **52** and DBU.

Similar conditions were then applied to PAA_{49}-*b*-PS_{280} (Entries 3-4). In these cases, the efficiency of the grafting (e_g) was about 50 % even when 7 equivalents of **52** were used (Entry 4). Increasing the temperature to 50 ℃, with PAA_{62}-*b*-PS_{213}, improved the efficiency up to about

Entry[a]	Starting PAA-Polymer	C_{AA}[b] (mol/L)	NBBr **52** (equiv.)	T (℃)	t (h)	e_g[c] (%)	$M_{n,\,NMR}$ (g/mol)	$M_{n,\,GPC}$[d] (g/mol)	PDI
1	homo-PAA_{148}	0.50	2.0	30	3	99	30,300	24,200	1.13
2	homo-PAA_{139}	0.10	2.0	30	3	10	30,700	/	/
3	PAA_{49}-*b*-PS_{280}	0.15	2.0	30	3	48	34,200	55,200	1.14
4	PAA_{49}-*b*-PS_{280}	0.10	7.0	30	3	55	34,800	57,600	1.13
5	PAA_{62}-*b*-PS_{213}	0.10	2.3	50	3	89	33,600	36,500	1.11
6	PAA_{62}-*b*-PS_{213}	0.10	2.3	50	6	91	33,900	34,400	1.16
7	PAA_{62}-*b*-PS_{213}	0.10	5.3	50	16	89	33,600	36,400	1.10
8[e]	PAA_{74}-*b*-PS_{50}	1.00	2.2	50	24	93	14,700	18,400	1.20
9	PAA_{31}-*b*-PS_{168}	0.04	2.2	50	15	97	24,400	21,700	1.14
10	PAA_{27}-*b*-PS_{443}	0.04	2.0	50	15	81	50,600	59,000	1.22
11	PAA_{27}-*b*-PS_{443}	0.04	6.0	50	24	83	50,800	60,800	1.25
12	PAA_{27}-*b*-PS_{443}	0.10	6.0	50	64	78	50,500	60,000	1.25
13	PAA_{27}-*b*-PS_{443}	0.04	6.0	80	4	85	50,800	59,100	1.26
14[f]	PAA_{27}-*b*-PS_{443}	0.04	5.0	50	15	86	50,800	60,400	1.23
15[g]	PAA_{27}-*b*-PS_{443}	0.04	5.0	50	15	80	50,600	60,800	1.23
16[h]	PAA_{27}-*b*-PS_{443}	0.04	5.0	50	15	80	50,600	57,300	1.29
17	PAA_{74}-*b*-PS_{415}	0.05	4.0	50	15	85	56,000	57,700	1.23
18	PAA_{74}-*b*-PS_{581}	0.05	4.0	50	15	77	72,300	70,800	1.27

[a]Reactions performed in DMF with x equiv. of DBU (x = NBBr equiv.). [b]e_g: Grafting efficiency, determined by ^{1}H NMR. [c]Determined with a PS calibration. [e]Synthesis realized by Dr. Kuppan Chandrasekar. [f]Performed in dioxane. [g]Performed in DMF/dioxane (50/50). [h]Performed in DMF/THF (50/50).

Table 5.10: Experimental conditions and results for the functionalization of PAA-*b*-PS.

90 % (Entry 5). However, longer reaction times did not enhance the grafting efficiency (Entry 6), even in conjunction with 5.3 equivalents of **52** (Entry 7). Performing the reaction at higher concentration (1 M) with PAA_{74}-*b*-PS_{50}, led to a PNBA-*b*-PS functionalized at about 90 % (Entry 8). On the other hand, decreasing the concentration to 0.04 M with PAA_{31}-*b*-PS_{168} pushed the efficiency to 97 %.

Several experiments have been carried out with PAA_{27}-*b*-PS_{443} (Entries 10-16). The parameters investigated were the following: the dilution (0.1, 0.04 M), the number of equivalents of *o*-nitrobenzyl bromide (2, 5, 6), the reaction time (4 to 64 h), the temperature (50, 80 ℃), the solvent (DMF, dioxane, DMF/dioxane (50/50), DMF/THF (50/50)). Whatever the conditions, the grafting efficiency was about 80 %.

In regard to all these experiments, the grafting efficiency seems to be mostly determined by the composition of the block copolymer itself rather than by the reaction conditions. Indeed, while PAA homopolymers are easily functionalized at 30 ℃ (Entries 1-2), the introduction of a PS sequence limits the grafting to about 50 % (Entries 3-4). Increasing the temperature (50 ℃) improves the functionalization but the efficiency was limited to about 90% for PAA_{62}-*b*-PS_{213} (Entries 5-7) and to about 80 % for PAA_{27}-*b*-PS_{443} (Entries 10-16). The best results were obtained with short PS sequences (Entries 8-9). A possible explanation could be that the PS chains surround the PAA sequences, hindering the access to the carboxylate functions.

A quantitative functionalization is not necessary for the targeted applications with these block copolymer, and a degree of functionalization of about 80 % should be enough for the creation of porosity after photocleavage. Indeed, the key point is not to get a 100 % functionalized block copolymer, but to get enough photocleavage moieties able to free a significative volume after the cleavage. $PNBA_{74}$-*b*-PS_{415} and $PNBA_{74}$-*b*-PS_{581} presented at Entries 17-18, are good candidates for the cylindrical morphology as their final mass fraction r is equal to 0.25 and 0.18 respectively. Their self-assembly behavior will be discussed in Chapter 7. Because the grafting is not quantitative, a new labelling of the photocleavable block copolymers is introduced here. $PNBA_{74}$-*b*-PS_{415} and $PNBA_{74}$-*b*-PS_{581} will be called P(NBA-*co*-AA)$_{74}$-*b*-PS_{415} and P(NBA-*co*-AA)$_{74}$-*b*-PS_{581}, respectively. This labelling highlights the fact that

acrylic acid units are still present in the photocleavable sequence.

Figures 5.14(a) and 5.14(b) show the GPC chromatograms of P(NBA-*co*-AA)$_{74}$-*b*-PS$_{415}$ and of P(NBA-*co*-AA)$_{74}$-*b*-PS$_{415}$ with the corresponding PtBA-*b*-PS and PtBA macroinitiator. The shifts toward the lower elution times demonstrate the chain extension from the PtBA macroinitiator. Figure 5.14(c) shows the GPC chromatograms of the P(NBA-*co*-AA)-*b*-PS copolymers presented in Table 5.10, demonstrating the obtention of well-defined copolymers (one example per composition). For P(NBA-*co*-AA)$_{74}$-*b*-PS$_{415}$ and P(NBA-*co*-AA)$_{74}$-*b*-PS$_{581}$, a tailing at the longer elution time can be seen, indicating some termination reactions during the polymerization of styrene.

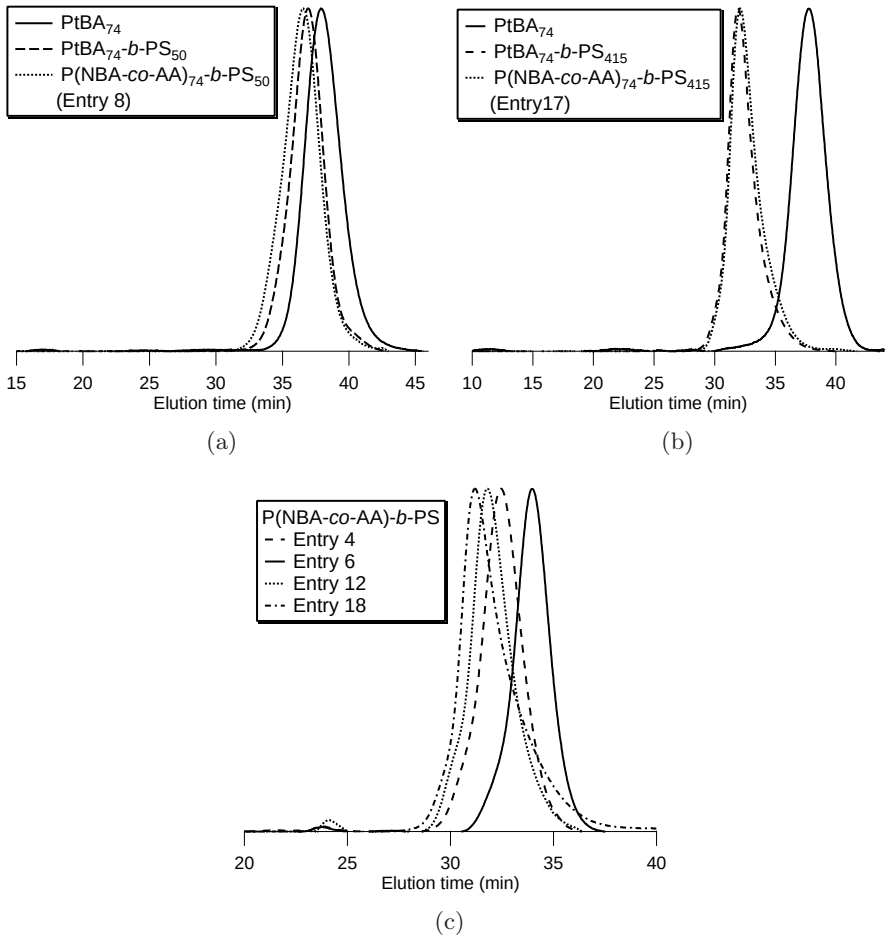

Figure 5.14: GPC chromatograms of the P(NBA-*co*-PAA)-*b*-PS presented in Table 5.10. (a) GPC traces of the macroinitiator $PtBA_{74}$, $PtBA_{74}$-*b*-PS_{50} and the corresponding P(NBA-*co*-AA)$_{74}$-*b*-PS_{50} of Entry 8. (b) GPC traces of the macroinitiator $PtBA_{74}$, $PtBA_{74}$-*b*-PS_{415} and the corresponding P(NBA-*co*-AA)$_{74}$-*b*-PS_{415} of Entry 17. (c) GPC traces of the grafted P(NBA-*co*-AA)-*b*-PS from Entries 4, 6, 12, 18.

5.6 Conclusions

Three synthetic strategies have been investigated in order to obtain diblock copolymers containing a linear PS sequence and a block bearing photocleavable *o*-nitrobenzyl esters as side groups. The first two strategies were based on the polymerization of the photocleavable NBA and NBMA monomers. For this reason, their behaviors under controlled radical polymerizations have been firstly investigated. The polymerization of these monomers revealed to be difficult as nitroaromatic compounds are perturbators of radical polymerizations. Despite this limitation, rather well-defined homo PNBMA polymers have been obtained by ATRP.

The further chain extension of a PNBMA used as macroinitiator for styrene polymerization was not successful since no block copolymers could be obtained in the studied conditions. On the contrary, the reverse strategy consisting in the polymerization of NBMA from a PS macroinitiator successfully led to a PS-*b*-PNBMA block copolymer. This strategy has however been abandoned due to the intrinsic low efficiency of the initiation step and to the inherent difficulty of polymerizing monomers containing nitroaromatic moieties.

A different strategy based on the grafting of *o*-nitrobenzyl bromide onto a PAA-*b*-PS led to well-defined photocleavable block copolymers. Even if the functionalization of the acid units was not quantitative, relatively high degrees of grafting (80-90 %) were nevertheless achieved, and two photocleavable block copolymers with potentially good composition for further yielding the desired cylindrical morphology have been obtained. The fact that acid functions are remaining in the block copolymers is not a problem for the targeted application. The grafting strategy is thus the best and fastest route for the obtention of photocleavable block copolymers with narrow molar mass distributions.

Experimental part

Materials and Instrumentation. Acryloyl chloride (Aldrich, 97 %) and methacryloyl chloride (Alfa Aesar, 97 %) were distilled under reduced pressure before use. Dichloromethane (CH_2Cl_2, Aldrich, 98 %) was distilled over P_2O_5. N,N-dimethylformamide (DMF, Aldrich, 99.8 %) was distilled on CaH_2 prior to use. Triethylamine was dried over KOH. Tris(2-(dimethylamino)ethyl)amine (Me_6Tren) was synthesized as described in the experimental part of Chapter 4. N-hexyl-2-pyridylmethanimine (NHPMI) and Cumyl phenyldithioacetate (CPDA) provided by the laboratory of Prof. Schubert (TU/e) and were synthesized as described in the literature [46,47]. Azobis(isobutyronitrile) (AIBN, Aldrich) was recrystallized from methanol. SG1 free nitroxide and the associated alkoxyamine MAMA-SG1 (BlocBuilder^{TM}) were generously given by Arkema. 2-Cyano-2-butyl dithiobenzoate (CBDB) was kindly provided by AGFA. Styrene (Aldrich, 99 %) and *tert*-butyl acrylate (tBA, Acros, 99 %) were passed through activated basic alumina (Acros) columns prior to use. 2-Nitrobenzyl alcohol (Aldrich, 97 %) and 2-nitrobenzyl bromide (NNBr, Acros, 97 %) were dried in vacuo at 30 ℃ for 48 h prior to use. CuBr (Aldrich, 99.999 %), CuBr2 (Aldrich, 99.999 %), ethyl 2-bromoisobutyrate (EBiB, Acros, 98 %), ethyl 2-bromopropionate (EBP, Aldrich, 99 %), anisole (Acros. 99 %), N,N,N',N",N"-pentamethyldiethylenetriamine (PMDETA, Aldrich, 98 %), butylbenzene (Aldrich, 95 %), 2,2'-azobis(4-methoxy-2.4-dimethyl valeronitrile) (V-70, Wako Chemicals), N,N-dimethylformamide (DMF, Aldrich, 99.8 %, anhydrous), ethylenediaminetetraacetic acid disodium salt dehydrate (EDTA, Fluka, 97 %), 1,8-diazabicyclo[5.4.0]undec-7-ene (DBU, Acros, 98 %), trifluoroacetic acid (TFA, Acros, 99 %) and all the other chemicals were used as recieved. Flash chromatography was performed on silica gel (0.040-0.063 μm grade).

Proton and carbon nuclear magnetic resonance spectra were acquired on a 300 MHz (Bruker Avance II) or on a 400 MHz spectrometer (Varian Mercury). Infrared (IR) spectra were recorded on thin films deposited on sodium chloride plates with a FT-IR spectrometer (Shimadzu FTIR-8400S). Mass spectra were obtained using chemical ionization (100 eV, ionization gas: methane). Parallel polymerizations were performed on a Chemspeed ASW2000 automated synthesizer couple to an Interscience gas chromatography (GC) auto-sampler equipped with a Rtx-

5 (Crosslinked 5% diphenyl/95% dimethyl polysiloxane) capillary column. Molar masses and polydispersity indices of the polymers were measured on a Shimadzu size exclusion chromatography (SEC) system equipped with a LC-10AD pump, a RID-10A refractive index detector (50 °C; eluent: chloroform/triethylamine/2-propanol (94/4/2); flow rate: 1 mL/min), and on a Waters SEC system equipped with a Waters 510 pump and a 410 differential refractometer (40 °C; eluent: DMF or DMF with NH_4PF_6 (2.5 mM)); flow rate of 0.5 mL/min). The calibration was performed using polystyrene standards.

Section 5.2.2

General procedure for the synthesis of NBMA 38 and NBA 36. To a stirred solution of *o*-nitrobenzyl alcohol (22.84 g, 145 mmol, 1.0 equiv.) and Et_3N (22 mL, 159 mmol, 1.1 equiv.) in CH_2Cl_2 (193 mL, 0.75 M), a solution of methacryloyl chloride (16 mL, 159 mmol, 1.1 equiv.) in CH_2Cl_2 (15 mL) was added dropwise at 0 °C. The mixture was stirred for 15 hours at 20 °C. The mixture was washed with water and the organic phase was dried over $MgSO_4$, filtered and the solvent was removed in vacuo. The yellow-brown crude product was purified by flash chromatography on silica gel (PE/AcOEt: 80/20) affording a viscous yellow liquid (31.08 g, 97 %).

NBMA: ^{1}H NMR (300 MHz, $CDCl_3$): δ (ppm) 8.05 (d, 1H, ^3J = 8.1 Hz, H_{Ar}), 7.61 (m, 2H, H_{Ar}), 7.46 (t, 1H, ^3J = 7.6 Hz, H_{Ar}), 6.18 (s, 1H, =CH_2), 5.62 (s, 1H, =CH_2), 5.56 (s, 2H, O-CH_2-), 1.96 (s, 3H, CH_3). ^{13}C NMR (75 MHz, $CDCl_3$): δ (ppm) 166.5 (C), 147.4 (C), 135.6 (C), 133.6 (CH), 132.2 (C), 128.6 (2 CH), 126.3 (=CH_2), 124.8 (CH), 62.9 (CH_2), 18.1 (CH_3). IR (film, cm^{-1}): 2958 w, 2927 w, 1716 s, 1637 m, 1614 m, 1521 s, 1448 m, 1340 s, 1147 s, 1049 m, 1014 s, 989 m, 943 s, 856 s, 788 s. MS (CI): m/z = 222 ($[M+H]^+$), 220 ($[M-H]^+$), 136 ($[C_7H_6NO_2]^+$), 69 ($[C_4H_5O]^+$).

NBA: ^{1}H NMR (300 MHz, $CDCl_3$): δ (ppm) 8.09 (d, 1H, ^3J = 8.2 Hz, H_{Ar}), 7.62 (m, 2H, H_{Ar}), 7.48 (t, 1H, ^3J = 7.6 Hz, H_{Ar}), 6.48 (dd, 1H, ^3J = 17.3 Hz ; ^2J = 1.2 Hz, =CH_2, trans), 6.20 (dd, 1H, ^3J = 17.3; Hz ^3J = 10.4 Hz, =CH), 5.90 (dd, 1H, ^3J = 10.4 Hz; ^2J = 1.2 Hz, =CH_2, cis), 5.59 (s, 2H, O-CH_2-). ^{13}C NMR (75 MHz, $CDCl_3$): δ (ppm) 165.3 (C), 147.3 (C), 133.7 (CH), 132.0 (C), 131.0 (=CH), 128.7 (CH), 128.6 (CH), 127.6 (=CH_2), 124.9 (CH), 62.7 (CH_2). IR (film, cm^{-1}):

1724 s, 1633 m, 1614 m, 1521 s, 1406 s, 1340 s, 1166 s, 1054 s, 981 s, 943 s, 856 s, 788 s. MS (CI): m/z = 208 ($[M+H]^+$), 136 ($[C_7H_6NO_2]^+$, 55 ($[C_3H_3O]^+$).

Section 5.2.3

General procedure for the parallel RAFT polymerizations of NBMA and NBA (TU/e). Polymerizations were performed on a Chemspeed ASW2000 automated synthesizer at the TU/e. The robot system was fitted with an array of 16 parallel 13 mL reactors with additional cold-finger reflux condensers. Stock solutions were prepared in DMF and bubbled with argon (30 min) before starting the experiment. Stock solutions of NBMA (16.7 mL; 2.10 M), NBA (16.7 mL; 2.10 M), CBDB (5.3 mL, 0.050 M), CPDA (5.3 mL, 0.050M), AIBN (7.4 mL; 0.013 M) and butylbenzene (10 mL, internal standard) were transferred into the reaction vessels resulting in 4.0 mL reaction mixtures with different AIBN/CTA ratios (0.1 and 0.25) and monomer equivalents relative to CTA (100 and 200). All polymerizations were performed with 1 M monomer concentration at 70 ℃ with vortex stirring (600 rpm) for 18 hours. Samples (0.1 mL) were taken after 3, 6, 10, 14 and 18 hours, and transferred to 1 mL vials which were prefilled with 0.9 mL chloroform. These samples were used for GC and GPC analysis.

RAFT polymerization of NBMA at 40 ℃ (TU/e). A solution containing CBDB (5.6 mg 0.025 mmol, 1 equiv.), NBMA (1.11 g; 5.0 mmol, 200 equiv.), V-70 (1.8 mg, 0.006 mmol, 0.25 equiv.) and DMF (2.3 mL) was bubbled with argon (30 min), then sealed and stirred at 40 ℃ (oil bath). Samples (0.1 mL) were taken after 1, 3, 5, 7 and 24 hours, and transferred to 1 mL vials which were prefilled with 0.9 mL chloroform. These samples were used for GC and GPC analysis.

Section 5.2.4

Typical procedure for the NMP of NBA (TU/e). A solution of Blockbuilder^{TM} (19.0 mg, 0.05 mmol, 1 equiv.), SG1 (1.5 mg, 0.005 mmol, 0.1 equiv.) and NBA (1 g, 4.8 mmol, 96 equiv.) in toluene (2.5 mL) was bubbled 30 minutes with argon and subsequently stirred at 110 ℃ for 20 hours. The polymerization was quenched by quickly cooling the reaction tube in a water-ice bath. A sample (0.1 mL) was taken at the end of the polymerization and transferred to a 1 mL vial

prefilled with 0.9 mL chloroform. This sample was used for GC and GPC analysis.

Section 5.2.5

General procedure for the parallel ATRP polymerizations of NBMA and NBA. (TU/e) Polymerizations were performed on a Chemspeed ASW2000 automated synthesizer. The robot system was fitted with an array of 16 parallel 13 mL reactors with additional cold-finger reflux condensers. Stock solutions were prepared in anisole and bubbled with argon (30 min) before starting the experiment. CuBr was weighted into the reactors and kept under argon before starting the experiment. Stock solutions of NBMA (15.8 mL; 3.33 M), NBA (15.8 mL, 3.33 M), EBiB (7.9 mL, 0.10 M), PMDETA (4.0 mL, 0.12 M), NHPMI (2.0 mL, 0.48 M) and Me_6Tren (2.0 mL, 0.10 M) were transferred into the reaction vessels (containing CuBr) resulting in 4.0 mL reaction mixtures with different monomer concentrations (1 M or 2 M), different ligands (PMDETA, NHPMI, Me_6Tren) and with different monomer equivalents relative to EBiB (100 and 200). All polymerizations were performed at 80 ℃ with vortex stirring (600 rpm) for 18 hours. Samples (0.1 mL) were taken after 3, 6, 10, 14 and 18 hours, and transferred to 1 mL vials that were prefilled with 0.9 mL chloroform. These samples were used for GC and GPC analysis.

Typical procedure for the ATRP of NBMA and NBA (entry 3, Table 5.5. A solution of EBiB (3.2 mg, 0.016 mmol, 1 equiv.), NBMA (720 mg, 3.25 mmol, 200 equiv.), PMDETA (3.4 mg, 0.020 mmol, 1.2 equiv.) and anisole (0.31 mL) was degassed by three freeze-pump-thaw cycles. A Schlenk tube containing CuBr (1.95 mg, 0.0136 mmol, 1 equiv.) and a magnetic bar was filled with 758 μL of the degassed solution (2.71 mmol of NBMA). The mixture was degassed by three freeze-pump-thaw cycles, filled with argon and stirred in an oil bath at 80 ℃ for 15 h. The polymerization was quenched by quickly cooling the tube in a water-ice bath. The reaction mixture was filtered over neutral Al_2O_3 (eluent: CH_2Cl_2) and the solvents were removed under reduce pressure. The viscous residue was precipitated in Et_2O affording a light yellow powder. Conversions were determined by ^{1}H NMR spectroscopy on the crude mixture.

M_n (GPC) = 12,100 g/mol; PDI (GPC) =1.13. M_n (NMR) = 15,100 g/mol. ^{1}H NMR (500 MHz, $CDCl_3$): δ (ppm) 8.01 (b, 67H, H_{Ar}), 7.61

(b, 134H, H_{Ar}), 7.46 (b, 67H, H_{Ar}), 5.29 (b, 134H, CH_2-O), 3.72 (q, 67H, CH_2-O, chain end), 2.2-1.3 (134H, $CH_{2,\ backbone}$), 1.3-0.6 (201H, $CH_{3,\ backbone}$).

Section 5.4

Typical procedure of the synthesis of PS-Br. (PS_{110}-Br, Table 5.6) Under argon, a schlenk tube containing CuBr (10 mg; 0.07 mmol; 1 equiv.) was filled with a solution containing EBiB (14 mg; 0.07 mmol, 1 equiv.), styrene (2.24 g; 21.54 mmol; 300 equiv.), PMDETA (15 mg; 0.08 mmol; 1.2 equiv.) and anisole (560 mg; 20 wt-%) previously degassed by three freeze-pump-thaw cycles. The mixture was degassed by three freeze-pump-thaw cycles, filled with argon and stirred in an oil bath at 100 °C for 5 h (styrene conversion = 30 %). The polymerization was quenched by quickly cooling the tube in a water-ice bath. The reaction mixture was diluted with CH_2Cl_2 and filtered on neutral aluminium oxide. The organic phase was dried over $MgSO_4$, filtered and the solvent was removed under reduced pressure. The residue was precipitated in hexane, filtered and dried in vacuo at 30 °C for 24 h, affording a white powder (502 mg, 74 %).

M_n (GPC) = 11,500 g/mol; PDI (GPC) = 1.05. ^{1}H NMR (300 MHz, $CDCl_3$): δ (ppm) 7.20-6.10 (m, 540H, H_{Ar}), 4.60-4.30 (m, 1H, CH-Br), 3.65-3.49 (m, 2H, CH_3-CH_2-O, ester), 2.40-1.10 (324H, $H_{backbone}$).

Typical procedure for the ATRP of NBMA initated by PS-Br macroinitiator. (Entry 2, Table 5.6) Under argon, a Schlenk tube containing CuCl (1.6 mg, 0.016 mmol, 1.5 equiv.) was filled with a solution containing PS_{110}-Br (126 mg, 0.011 mmol, 1 equiv.), NBMA (542 mg, 2.45 mmol, 225 equiv.), PMDETA (3.4 mg, 0.019 mmol, 1.8 equiv.) and anisole (0.29 mL, 30 wt-%) previously degassed by three freeze-pump-thaw cycles. The mixture was degassed by three freeze-pump-thaw cycles, filled with argon and stirred in an oil bath at 110 °C for 6 h (styrene conversion = 31 %). The polymerization was quenched by quickly cooling the tube in a water-ice bath. The reaction mixture was diluted with CH_2Cl_2 and filtered on neutral aluminium oxide. The organic phase was dried over $MgSO_4$, filtered and the solvent was removed under reduced pressure. The residue was precipitated in methanol, filtered and dried in vacuo at 30 °C for 24 h, affording a white powder (127 mg, 44 %). Homo-PS was selectively removed by extraction with Et_2O. Initiation efficiency has been estimated as follows: the initiation

efficiency is estimated by the ratio between the M_n of the PS block calculated before and after the extaction of the homo-PS. $M_{n,\ before}$= 7,000 g/mol; $M_{n,\ after}$= 11,000 g/mol. Initiation efficiency = (7,000/11,000) * 100 = 64 %.

M_n (GPC) = 23,700 g/mol; PDI (GPC) = 1.37. ^{1}H NMR (300 MHz, $CDCl_3$): δ (ppm) 8.02 (b, 105H, H_{Ar}, PNBMA), 7.61 (b, 210H, H_{Ar}, PNBMA), 7.46 (b, 105H, H_{Ar}, PNMBA), 7.20-6.10 (m, 550H, H_{Ar}, PS), 5.29 (b, 210H, CH_2-O, PNBMA), 2.40-1.10 (540H, $H_{backbone}$, PS + PNBMA), 1.2-0.4 (315H, $CH_{3,\ backbone}$, PNBMA). M_n (NMR) = 34,400 g/mol.

Section 5.5

Typical procedure for synthesis of PtBA. ($PtBA_{74}$, Entry 2, Table 5.7) Under argon, a round-bottom flask, with a stopcock, containing CuBr (82 mg; 0.57 mmol; 1 equiv.) was filled with a solution containing *tert*-butyl acrylate (tBA; 10.01 mL; 68.59 mmol; 120 equiv.), EBiB (112 mg; 0.57 mmol, 1 equiv.), PMDETA (109 mg; 0.62 mmol; 1.1 equiv.), and anisole (5.92 mL; 40 wt-%) previously degassed by three freeze-pump-thaw cycles. The mixture was degassed by three freeze-pump-thaw cycles, filled with argon and stirred in an oil bath at 90 ℃ for 1 h (tBA conversion = 52 %). The polymerization was quenched by quickly cooling the tube in a water-ice bath. The reaction mixture was diluted with CH_2Cl_2 and washed with an aqueous solution of EDTA (0.04 M). The organic phase was dried over $MgSO_4$, filtered and the solvent was removed under reduced pressure. The residue was precipitated in MeOH:H_2O 50:50, filtered and dried in vacuo at 30 ℃ for 24 h, affording a white solid (3.19 g, 70%).

M_n (GPC) = 11,700 g/mol; PDI (GPC) =1.14. ^{1}H NMR (300 MHz, $CDCl_3$): δ 4.1 (m, 3H, CH_2-O, CH-Br), 2.3- 2.0 (b, 73 H, CH backbone), 1.9-1.3 (s, 814H, CH_2 backone, CH_3 *t*-Butyl). M_n (NMR) = 9,500 g/mol

Typical procedure for synthesis of PtBA-*b*-PS ($PtBA_{74}$-*b*-PS_{50}, Entry 6, Table 5.8). Under argon, a round bottom flask with, a side stopcock, containing CuBr (22 mg; 0.15 mmol; 0.9 equiv.) was filled with a solution containing $PtBA_{74}$-Br (1.60 g; 0.17 mmol, 1 equiv.), styrene (2.11 g; 20,26 mmol; 120 equiv.), PMDETA (27 mg; 0.15 mmol; 0.9 equiv.) and anisole (1.56 g; 40 wt-%) previously degassed by three freeze-pump-thaw cycles. The mixture was degassed by three freeze-pump-thaw cycles, filled with argon and stirred in an oil bath at 100 ℃

for 2 h (styrene conversion = 44 %). The polymerization was quenched by quickly cooling the tube in a water-ice bath. The reaction mixture was diluted with CH_2Cl_2 and washed with an aqueous solution of EDTA (0.04 M). The organic phase was dried over $MgSO_4$, filtered and the solvent was removed under reduced pressure. The residue was precipitated in hexane, filtered and dried in vacuo at 30 ℃ for 24 h, affording a white powder (2.06 g, 82 %).

M_n (GPC) = 16,000 g/mol; PDI (GPC) =1.17. ^{1}H NMR (500 MHz, $CDCl_3$): δ 7.30-6.30 (b, 250H, H_{Ar}; PS), 4.1 (m, 2H, CH_2-O; Chain end), 2.3- 1.1 (b, 1038H, CH backbone, CH_2 backbone, CH_3 *t*-Butyl). M_n (NMR) = 14,700 g/mol.

Typical procedure for the hydrolysis of PtBA-polymers with the HCl/dioxane system. ($PtBA_{148}$, Entry 1, Table 5.9) In a round bottom flask, $PtBA_{148}$ (488 mg; 4.44 mmol in tBA units; 1 equiv.) was dissolved in dioxane (22.30 mL, 0.2 M). HCl 12M (1.11 mL, 13.32 mmol, 3 equiv.) was added and the solution was stirred in an oil bath at 85 ℃ for 15 h. The solvent was removed under reduced pressure. The polymer was precipitated in diethyl ether, filtered and dried in vacuo at 30 ℃ for 24 h, affording a white powder (165 mg, 76 %).

^{1}H NMR (300 MHz, CD_3OD): δ 2.4 (b, 148H, CH backbone), 2.1-1.4 (b, 296H, CH_2, backbone). M_n (NMR) = 10,600 g/mol.

Typical procedure for the hydrolysis of PtBA-polymers with the TFA/CH_2Cl_2 system. (synthesis of PAA_{74}-*b*-PS_{50}, Entry 7, Table 5.9) In a round bottom flask, $PtBA_{74}$-*b*-PS_{50} (500 mg; 2.52 mmol in tBA units; 1 equiv.) was dissolved in dichloromethane (23.09 mL, 0.11 M). TFA (0.88 mL, 11.50 mmol, 4.6 equiv.) was added and the solution was stirred at 20 ℃ for 24 h. The solvent was removed under reduced pressure and the residue was kept in a minimum amount of DMF and dialyzed against methanol. The polymer was precipitated in hexane, filtered and dried in vacuo at 30 ℃ for 24 h, affording a white powder (279 mg, 78%).

^{1}H NMR (300 MHz, DMF-d_7): δ 7.3-6.1 (b, 250H, H_{Ar}; PS), 2.2 (b, 74H, CH backbone PAA), 2.1- 1.1 (b, 300H, CH_2 backbone PAA + PS). M_n (NMR) = 10,500 g/mol.

Typical procedure for the grafting of *o*-nitrobenzyl bromide on PAA-Polymers. (grafting on PAA_{74}-*b*-PS_{50}, Entry 18, Ta-

ble 5.10) Under argon, in a Schlenck tube, PAA_{74}-*b*-PS_{50} (502 mg; 3.54 mmol in AA units; 1 equiv.) was dissolved in DMF (3.54 mL, 1 M). NBBr **52** (1.735 g, 8.03 mmol, 2.2 equiv.) and DBU (1.027 mL, 8.03 mmol, 2.2 equiv.) was added and the solution was stirred at 50 °C for 24 h. AcOH (241 μL, 4.18 mmol, 1.2 equiv.) was added to the medium. The mixture was then diluted with CH_2Cl_2 and washed with distilled water. The organic phase dried over $MgSO_4$, filtered and the solvent was removed under reduced pressure. The polymer was precipitated in hexane, filtered and dried in vacuo at 30 °C for 24 h, affording a light yellow powder (794 mg, 81 %).

M_n (GPC) = 18,400 g/mol; PDI (GPC) =1.20. ^{1}H NMR (300 MHz, $CDCl_3$): δ 8.0 (b, 70H, H_{Ar}, PNBA), 7.6-7.3 (b, 227H, H_{Ar}, PNBA), 7.3-6.1 (b, 249H, H_{Ar}; PS), 5.2 (b, 137H, CH_2-O, PNBA), 2.5 (b, 74H, CH backbone PNBA), 2.3-1.1 (b, 351H, CH_2 backbone PNBA + PS). M_n = 20,500 g/mol. Grafting efficiency = 93%. FTIR (film, cm^{-1}): 3082-2850 (C_{Ar}-H, PS), 1737 (C=O, PNBA), 1525 (NO_2, PNBA), 1492 (C_{Ar}=C_{Ar},PS), 1452 (C_{Ar}=C_{Ar}, PS), 1348 (NO_2, PNBA), 1228-1153 (C-O, PNBA).

Bibliography

[1] Pillai, V. *Synthesis* **1980**, 1–26.

[2] Bochet, C. G. *J. Chem. Soc., Perkin Trans. 1* **2002**, 125–142.

[3] Barzynski, H. *Angew. Makromol. Chem.* **1980**, *93*, 131–141.

[4] Reichmanis, E.; Wilkins, C. W.; Chandross, E. A. *J. Vac. Sci. Technol.* **1981**, *19*, 1338–1342.

[5] Kubota, S.; Moriwaki, T.; Ando, T.; Fukami, A. *J. Appl. Polym. Sci.* **1987**, *33*, 1763–1775.

[6] Kubota, S.; Yamawaki, Y.; Moriwaki, T.; Eto, S. *Polym. Eng. Sci.* **1989**, *29*, 950–953.

[7] Hanson, J. E.; Reichmanis, E.; Houlihan, F. M.; Neenan, T. X. *Chem. Mater.* **1992**, *4*, 838–842.

[8] Mathew, T.; Ajayaghosh, A.; Das, S. *J. Photochem. Photobiol. A* **1993**, *71*, 181–189.

[9] Ajayaghosh, A.; George, G., S. C. *Chem. Commun.* **1994**, 423–44.

[10] Ajayaghosh, A.; George, M. V.; Yamoaoka, T. *J. Mater. Chem.* **1994**, *4*, 1769–773.

[11] Doh, J.; Irvine, D. J. *J. Am. Chem. Soc.* **2004**, *126*, 9170–9171.

[12] Katz, J. S.; Doh, J.; Irvine, D. J. *Langmuir* **2006**, *22*, 353–259.

[13] Shin, G. J.; Jung, J. C.; Chi, J. H.; Oh, T. H.; Kim, J. B. *J. Polym. Sci. Part A* **2007**, *45*, 776–788.

[14] Chang, C.-C.; Leung, M.-K. *Chem. Mater.* **2008**, *20*, 5816–5821.

[15] Johnson, J. A.; Finn, M. G.; Koberstein, J. T.; Turro, N. J. *Macromolecules* **2007**, *40*, 3589–3598.

[16] Xie, Z.; Hu, X.; Chen, X.; Sun, J.; Jing, X. *Biomacromolecules* **2008**, *9*, 376–380.

[17] Johnson, J. A.; Baskin, J. M.; Bertozzi, C. R.; Koberstein, J. T.; Turro, N. J. *Chem. Commun.* **2008**, 3064–3066.

[18] Jiang, J. Q.; Tong, X.; Morris, D.; Zhao, Y. *Macromolecules* **2006**, *39*, 4633–4640.

[19] Liu, Y.; Wang, L.; Pan, C. *Macromolecules* **1999**, *32*, 8301–8305.

[20] Tang, X.; Hu, Y.; Pan, C. *Polymer* **2007**, *48*, 6354–6365.

[21] Hu, C., Y; Liu, Y.; Pan, C. *J. Polym. Sci. Part A* **2004**, *42*, 4862–4872.

[22] Foord, S. *J. Chem. Soc.* **1940**, 48–56.

[23] Price, C. C.; Kell, R. W.; Krebs, E. *J. Am. Chem. Soc.* **1942**, *64*, 1103–1106.

[24] Price, C. C.; Durham, D. A. *J. Am. Chem. Soc.* **1943**, *65*, 757–759.

[25] Hammond, G. S.; Bartlett, P. D. *J. Polym. Sci.* **1951**, *6*, 617–624.

[26] Bartlett, P. D.; Kwart, H. *J. Am. Chem. Soc.* **1952**, *74*, 3969–3973.

[27] Janzen, E. G. *J. Am. Chem. Soc.* **1965**, *87*, 3531–3532.

[28] Hand, C. W.; Merritt, C.; Dipietro, C. *J. Org. Chem.* **1997**, *42*, 841–844.

[29] Gonzalez, A. C.; Larson, C. W.; Mcmillen, D. F.; Golden, D. M. *J. Phys. Chem.* **1985**, *89*, 4009–4814.

[30] He, Y. Z.; Cui, J. P.; Mallard, W. G.; Tsang, W. *J. Am. Chem. Soc.* **1998**, *110*, 3754–3759.

[31] Minier, L. M.; Brower, K. R.; Oxley, J. C. *J. Org. Chem.* **1991**, *56*, 3306–3314.

[32] Bajpai, U. D. N.; Bajpai, A. K.; Bajpai, J. *J. Appl. Polym. Sci.* **1991**, *42*, 2005–2012.

[33] Odian, G. *Principles of Polymerization, 4th ed.*; Wiley: New York, 2004.

[34] Fijten, M. W. M.; Meier, M. A. R.; Hoogenboom, R.; Schubert, U. S. *J. Polym. Sci. Part A* **2004**, *42*, 5775–5783.

[35] Hoogenboom, R.; Schubert, U. S.; Van Camp, W.; Du Prez, F. E. *Macromolecules* **2005**, *38*, 7653–7659.

[36] Becer, C. R.; Hahn, S.; Fitjen, M. W. M.; Thijs, H. M. L.; Hoogenboom, R.; Schubert, U. S. *J. Polym. Sci. Part A* **2008**, *46*, 7138–7147.

[37] Barner-Kowollik, C.; Quinn, J. F.; Nguyen, T. L. U.; Heuts, J. P. A.; Davis, T. P. *Macromolecules* **2001**, *34*, 7849–7857.

[38] Couturier, J.-L.; Guerret, O.; Bertin, D.; Gigmes, D.; Marque, S. R. A.; Tordo, P.; Chauvin, F. *PCT WO2004/014, 926* **2004**.

[39] Chauvin, F.; Dufils, P.-E.; Gigmes, D.; Guillaneuf, Y.; Marque, S. R. A.; Tordo, P.; Bertin, D. *Macromolecules* **2006**, *39*, 5238–5250.

[40] Becer, C. R.; Paulus, R. M.; Hoogenboom, R.; Schubert, U. S. *J. Polym. Sci. Part A* **2006**, *44*, 6202–6213.

[41] Eggenhuisen, T. M.; Becer, C. R.; Fijten, M. W. M.; Eckardt, R.; Hoogenboom, R.; Schubert, U. S. *Macromolecules* **2009**, *41*, 5132–5140.

[42] Shipp, D. A.; Wang, J.-L.; Matyjaszewski, K. *Macromolecules* **1998**, *31*, 8005–8008.

[43] Matyjaszewski, K.; Xia, J. H. *Chem. Rev.* **2001**, *101*, 2921–2990.

[44] Bertrand O., M.Sc. thesis, catholic University of Louvain, 2009.

[45] Nishikubo, T.; IIzawa, T.; Takahashi, A.; Shimokawa, T. *J. Polym. Sci. Part A* **1990**, *105*, 117.

[46] Queffelec, J.; Gaynor, S. G.; Matyjaszewski, K. *Macromolecules* **2000**, *33*, 8629–8639.

[47] Prescott, S. W.; Ballard, M. J.; Rizzardo, E.; Gilbert, R. G. *Macromolecules* **2002**, *35*, 5417–5425.

CHAPTER

SIX

PHOTOCLEAVAGE OF BLOCK COPOLYMERS IN SOLUTION

Abstract

The photocleavage of block copolymers synthesized in Chapters 4 and 5 is described. The first part of the chapter deals with the first family of block copolymers. The photocleavage in solution of PEO-hν-PS, PEO-hν-PtBA and PS-hν-PMMA is discussed and is followed by a comparison between the photocleavage and the chemical cleavage of PEO-hν-PS block copolymers in solution as well as in a selective solvent. The second part is devoted to the photocleavage of P(NBA-co-AA)-b-PS block copolymers in solution. In that case, the formation of micellar objects upon irradiation has been demonstrated by dynamic light scattering.

6.1 Photocleavage of *o*-nitrobenzyl derivatives

o-Nitrobenzyl derivatives are famous photosensitive protecting groups used in organic chemistry, in biochemistry, in microbiology and in material science [1–6]. Carboxylic acids, amines and alcohols can be easily protected in the form of *o*-nitrobenzyl esters, carbamates and ethers or carbonates, respectively and their subsequent recovery is obtained after exposure to appropriate UV light.

The mechanism of photocleavage of *o*-nitrobenzyl esters is presented in Figure 6.1 and starts with the UV excitation (250-400 nm) of the nitro group by $n\pi^*$ or $\pi\pi^*$ transition leading to the diradical **58**. An intramolecular abstraction of the hydrogen in the γ position by the oxygen radical provides then the *aci*-nitro tautomer **59**. After isomerization and cyclization, a rearrangement enables the cleavage of the molecule releasing the deprotected acid **56** and the nitrosobenzaldehyde part **57**.

In the case of carbamates and carbonates, the reaction is accompanied with the release of carbon dioxide (CO_2) which has been used to determined the efficiency of the photocleavage [7, 8]. For carbamates, the release of CO_2 is quantitative although the yield in amine functions recovery is not. This is explained by the formation of imines via the reaction between the released nitrosobenzaldehyde and the amino function. Quantitative amine recovery has been however obtained by preventing the formation of imines thanks to the addition of sulfuric acid or aldehyde reagents such as semicarbazide hydrochloride. Another side reaction which may decrease the recovery efficiency is the formation of diazobenzene derivatives from the photocombination of two nitrosobenzaldehydes. Such diazobenzenes act as internal light filters and their formation is prevented by using α-substituted *o*-nitrobenzyl protecting groups [7, 8]. Concerning carboxylic and alcohol protected functions, high recovery yields have been obtained using *o*-nitrobenzyl or α-substituted *o*-nitrobenzyl derivatives as protecting groups [7–11].

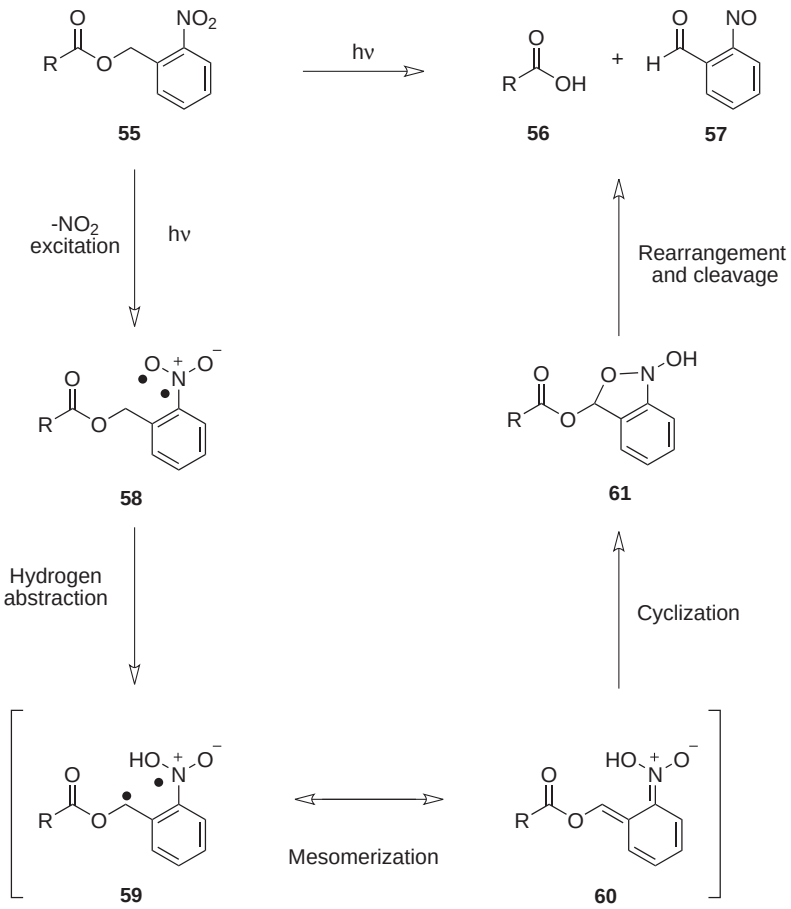

Figure 6.1: Mechanism of the photocleavage of *o*-nitrobenzyl ester into carboxylic acid and nitrosobenzaldehyde. Adapted from Ref. [2].

6.2 Photocleavage of linear block copolymers

6.2.1 Photocleavage in a non-selective solvent

The photocleavage of the linear block copolymers synthesized in Chapter 4 (PEO-$h\nu$-PS, PEO-$h\nu$-PtBA and PS-$h\nu$-PMMA) has been studied in solution. Upon UV irradiation, these block copolymers cleave into one block bearing the deprotected carboxylic acid and in another block end-functionalized with the *o*-nitrobenzylaldehyde counterpart (see Figure 6.2).

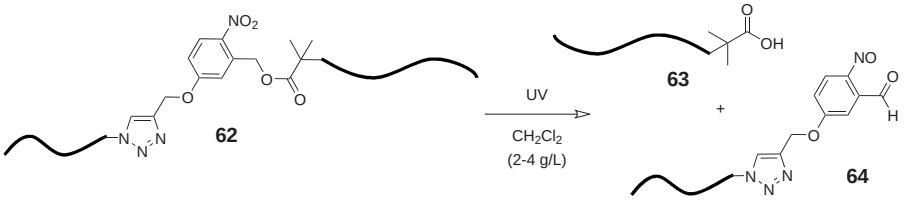

Figure 6.2: Cleavage of linear block copolymers into two dissociated blocks upon light irradiation.

Solutions of block copolymers in CH_2Cl_2 have been exposed to UV irradiation produced by lamps having their maximum emission wavelength at 300 and at 350 nm. The photocleavage at 350 nm has been followed with UV-visible spectroscopy and Figures 6.3(a), 6.3(c) and 6.3(e) show the evolution of the absorption spectra with irradiation time for one representative of each type of block copolymers. The photocleavage has been followed until no significant change in the spectrum could be seen (50 min.). All the starting block copolymers displayed the maximum of absorbance at a wavelength (λ_{max}) of 309 nm. This band is associated with the nitro-aromatic moiety and the corresponding molar extinction coefficients were found to be between 9,250 and 9,450 $L.mol^{-1}.cm^{-1}$ for each block copolymers. During the irradiation, the intensity of the band at λ_{max} decreases in favour of the bands associated to the nitrosobenzaldehyde counterpart (340, 450, 480 nm).

At the end of the irradiation (50 min.), the irradiated solutions were

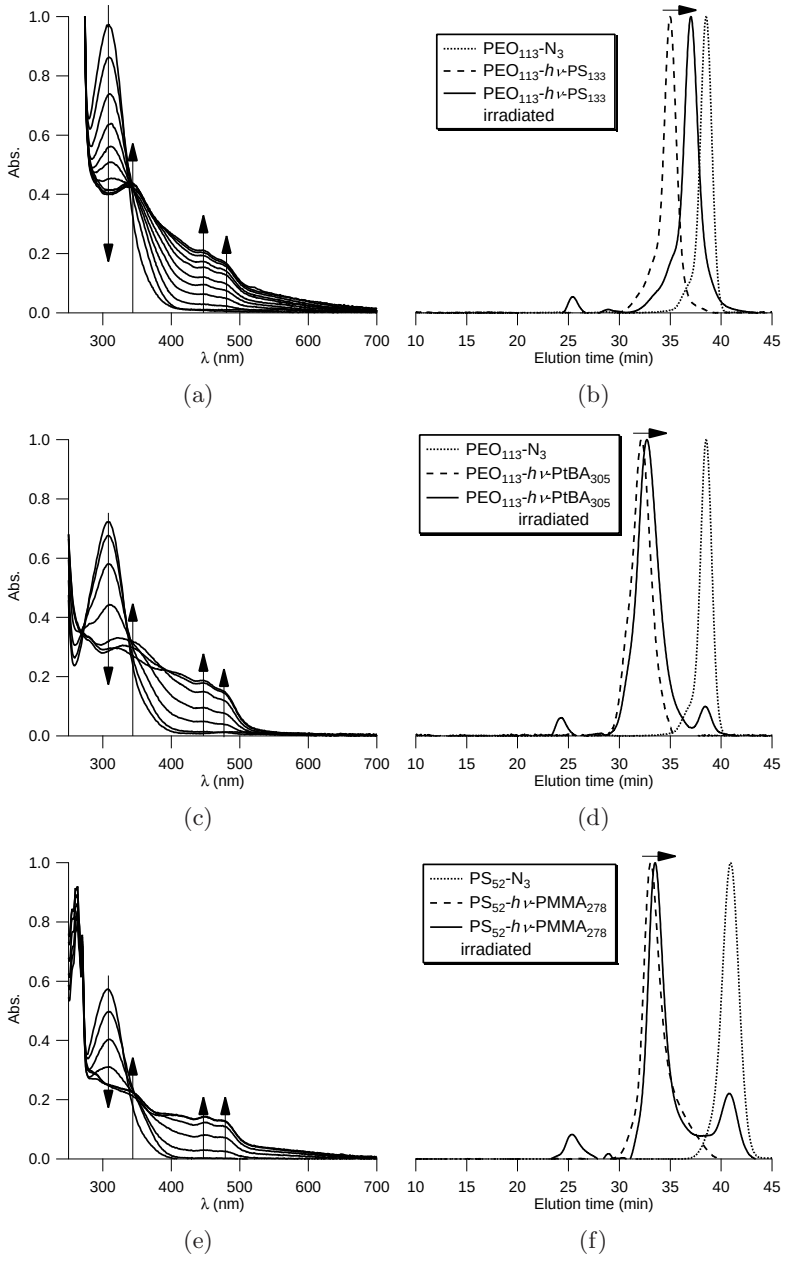

Figure 6.3: Photocleavage in solution (CH_2Cl_2, 350 nm) of PEO_{113}-$h\nu$-PS_{133} ((a), (b)) PEO_{113}-$h\nu$-$PtBA_{305}$ ((c), (d)) PS_{52}-$h\nu$-$PMMA_{278}$ ((e), (f)). Evolutions of the UV-visible absorption spectra of the solutions as a function of time: t(min)= 0, 2, 4, 6, 8, 10, 15, 20, 30, 40, 50 (a); t(min)= 0, 2, 5, 10, 20, 35, 50 (c), (e). GPC chromatograms of the block copolymers, of their azide-functionalized precursor blocks and of the products observed after 50 min. irradiation time (b), (d) and (f).

analyzed with GPC (Figures 6.3(b), 6.3(d) and 6.3(f)). After irradiation the peaks associated to the block copolymers are no longer observed, but new peaks are visible on the GPC chromatograms, corresponding to the dissociated blocks[1] (see Figures 6.3(d) and 6.3(f)). These results clearly indicate that the nitrobenzyl ester junction holding the two blocks together can be efficiently cleaved under light illumination.

The photocleavage efficiency has been improved by using UV lamps with a wavelength of maximum emission of 300 nm. The results presented in Figure 6.4(a) show the evolution of the UV-visible spectra of PEO_{113}-$h\nu$-PS_{176} with irradiation time at 300 nm. After 15 minutes, no change in the UV-visible spectrum could be seen. Moreover, the GPC chromatogram of the irradiated solution demonstrates the photocleavage into two distinct blocks (Figure 6.4(b)). The improved efficiency of the

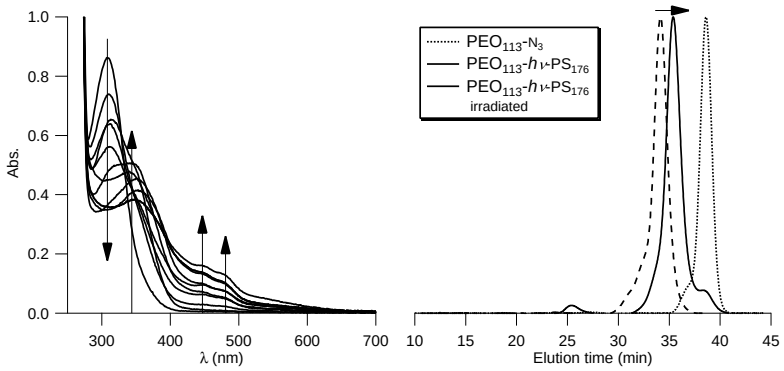

(a) (b)

Figure 6.4: Photocleavage of PEO_{113}-$h\nu$-PS_{176} (Table 4.5, Entry 4) in solution (CH_2Cl_2, 2 g/L); λ = 300 nm. Evolution of the UV-visible absorption spectra of the solution as a function of time (t(min)= 0, 1.5, 3, 5, 8, 10, 15, 20) (a). GPC chromatograms of the block copolymer with its starting azide block and after 15 min irradiation (b).

cleavage at 300 nm is explained by three factors. Firstly, the photosensitive *o*-nitrobenzyl junction of the block copolymers absorbs more light at 300 nm than at 350 nm because its λ_{max} is located at 309 nm. Sec-

[1] In the case of PEO_{113}-$h\nu$-PS_{133}, the signal corresponding to the dissociated PEO and PS are surimposed in the same peak 6.3(b).

ondly, the light intensity delivered by the lamps to the sample is 10 times greater in the case of the 300 nm emitting lamps than for those emitting at 350 nm[2]. Finally, the *o*-nitrosobenzylaldehydes produced during the photocleavage are also chromophores which absorb light (λ_{max} = 340 nm). Therefore, they act as competitors with *o*-nitrobenzyl moieties for light absorption at 350 nm. On the contrary, decreasing the wavelength to 300 nm enables to preferentially stimulate *o*-nitrobenzyl moieties, increasing thus the efficiency of cleavage.

The other linear photocleavable block copolymers have also been irradiated with UV light at 300 nm. Table 6.1 presents the GPC results for the block copolymers before and after photocleavage. M_p is defined as the molar mass at the top of the main peak of the GPC chromatograms[3]. Table 6.1 shows the values of M_p for the block copolymers before (column *BC*) and after (column $h\nu$) 15 minutes irradiation time. The difference in molar mass between the polymer before and after irradiation is also presented in the table (column *shift*) and corresponds to the mass that has been *"lost"* by the polymers after their cleavage. These values have to be compared with the M_p of the starting azide block (column *R-N₃*) and demonstrate qualitatively that the blocks have been splitted. For instance, shifts of about 10,000 g/mol towards lower molar masses have been observed for the PEO-$h\nu$-PS block copolymers (Entries 1-4). These shifts correspond to the molar mass[4] of the PEO block used as precursor in the synthesis. The same results have been observed for PEO-$h\nu$-PtBA (Entry 5). For PS_{52}-$h\nu$-$PMMA_{278}$ the shift in molar mass corresponds to the M_p of the starting PS block (Entry 6). In the case of PS_{97}-$h\nu$-$PMMA_{33}$, the main peak after irradiation (column $h\nu$) corresponds to the starting PS block (Entry 7). This observation is explained by the fact that this block copolymer is mainly composed by the sequence of the original azide block while the reverse situation prevails for the other copolymers.

[2]Light intensity at 300 nm = 38.5 mW/cm^2; light intensity at 350 nm = 4.58 mW/cm^2.

[3]The molar mass M_p is determined with a PS calibration and does not represent the exact molar mass of the polymers

[4]expressed in PS calibration

Table 6.1: Quantification of the shifts observed on the GPC chromatograms of the block copolymers before and after irradiation at 300 nm.

		M_p[a] (g/mol)			
Entry	Block copolymer	BC[b]	$h\nu$[c]	shift[d]	R-N_3[e]
1	PEO_{113}-$h\nu$-PS_{135}	36,600	25,600	10,000	10,300
2	PEO_{113}-$h\nu$-PS_{119}	25,000	15,700	9,300	10,300
3	PEO_{113}-$h\nu$-PS_{133}	28,100	17,900	10,200	10,300
4	PEO_{113}-$h\nu$-PS_{176}	35,500	24,900	10,600	10,300
5	PEO_{113}-$h\nu$-$PtBA_{305}$	68,100	58,600	10,200	10,300
6	PS_{52}-$h\nu$-$PMMA_{278}$	52,300	47,800	4,500	5,400
7	PS_{97}-$h\nu$-$PMMA_{33}$	15,800	10,400	5,400	10,200

[a] M_p = Molar mass at the top of the main peak of the GPC chromatogram; determined with a PS calibration. [b] M_p of the block copolymer (BC). [c] M_p of the main peak after irradiation. [d] Shift = M_p (BC) - M_p ($h\nu$) [e] R-N_3 = M_p of the starting azide functionalized block.

6.2.1.1 General remarks about the GPC chromatograms

On the GPC chromatograms of the irradiated block copolymers, the difference in intensity between the two peaks associated to the cleaved blocks may be somehow disturbing. However, this observation has been confirmed by GPC analysis of an equimolar mixture of a homo-PEO (5,000 g/mol) and a homo-PS (19,600 g/mol) as demonstrated in Figure 6.5(a). This behavior is due to the fact that chemically different polymer blocks have different refractive index increments (dn/dc) in solution, resulting in different magnitudes for the signal of the RI dectector.

The second comment concerns the appearance of a small peak on the GPC traces of the irradiated solutions at an elution time of about 25 minutes. This peak is certainly an artefact due to interactions between the nitroso- and/or the carboxylic groups and the columns of the GPC. This artefact disappeares completely when the GPC measurements are performed with an eluent containing salt (DMF + NH_4PF_6; 2.5 mM) as it can be seen on the GPC trace presented in Figure 6.5(b).

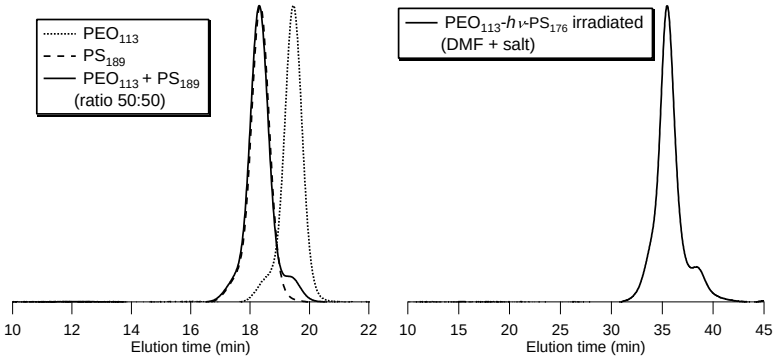

Figure 6.5: GPC chromatogram of an equimolar mixture of homo-PEO (5,000 g/mol) and homo-PS (19,600 g/mol) (a)). GPC chromatogram of irradiated PEO_{113}-$h\nu$-PS_{176} performed with salted eluent (DMF + NH_4PF_6) (b).

6.2.2 Photocleavage in a selective solvent

As described in Section 1.3.3 of the introduction chapter, block copolymers can self-assemble into micelles when dissolved in a selective solvent. In the present section, the photocleavage of micelles of PEO_{113}-$h\nu$-PS_{176} is discussed. The strategy is depicted in Figure 6.6. The micelles were obtained in a methanol/water mixture ($MeOH/H_2O$: 9/1) and consisted of a PS core surrounded by a corona composed of PEO. Once the micelles were formed, the solution was irradiated at 300 nm with an intensity of 38.5 mW/cm^2, in a similar way to that applied for the photocleavage of the block copolymers in a non-selective solvent.

Micelles were obtained by initially dissolving the block copolymer in DMF, a non-selective solvent for both blocks, and the solution was subsequently dialyzed against a $MeOH/H_2O$ (9/1) mixture in order to trigger micellization. Dynamic light scattering (DLS)[5] was finally used to demonstrate the formation of micelles. Figure 6.7 shows the relaxation

[5]DLS is a technique measuring the fluctuations of the scattering intensity with time in order to determine the hydrodynamic radius of molecules and nanoparticles in solution.

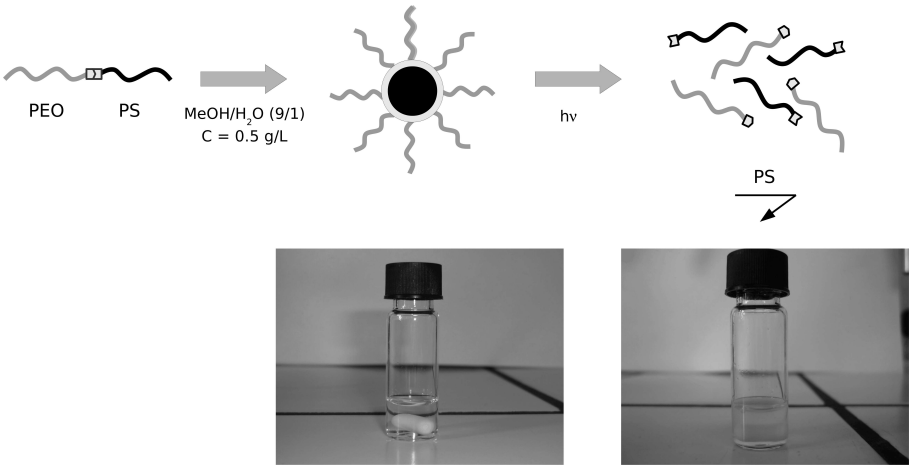

Figure 6.6: Formation and photocleavage of micelles of PEO_{113}-$h\nu$-PS_{176}. Strategy (above). Pictures of a micellar solution before (left) and after irradiation (right).

curve measured at an angle of 90° (intensity auto-correlation function) and the corresponding Contin analysis. A hydrodynamic radius (R_h) of 20.5 nm was determined for the micelles. The polydispersity index (PDI) of the micellar solution was equal to 0.089, indicating a quite narrow distribution of the sizes of the micelles.

The micellar solution was then irradiated at 300 nm for 15 minutes leading to the formation of a precipitate corresponding to the insoluble PS. Before irradiation, the solution diplayed the characteristic bluish color of micellar solutions and was optically clear (Figure 6.6, left picture). However, when the link between the blocks was cleaved, the solution became optically turbid since PS cores were no longer stabilized by the PEO chains leading to their precipitation in solution (Figure 6.6, right picture).

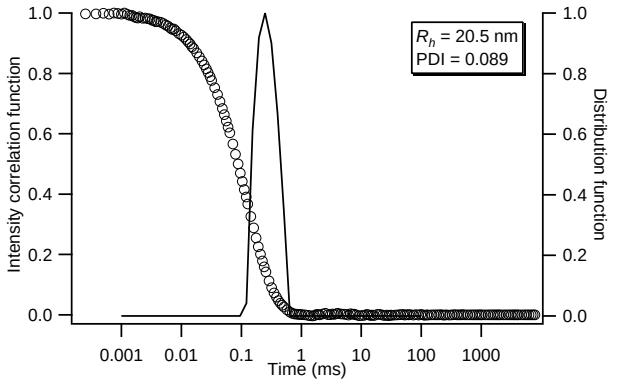

Figure 6.7: Intensity autocorrelation function (open circles) and Contin analysis of the DLS data (full line) of PEO_{113}-$h\nu$-PS_{176} in MeOH/H_2O (9/1).

6.2.3 Photocleavage *vs* chemical cleavage

6.2.3.1 Chemical cleavage

Beside their light-sensitivity, block copolymers containing *o*-nitrobenzyl ester moieties can also be cleaved by the hydrolysis of the ester bond present in the junction between the two blocks. This behavior was demonstrated by stirring the PEO_{113}-$h\nu$-PS_{176} block copolymer with NaOH in DMF at 20 ℃ (Figure 6.8). After 3 hours of reaction time, the block copolymer was cleaved as it was evidenced by GPC analysis (Figure 6.9). The chromatogram of the hydrolyzed mixture (full line curve) displays the shift of the main peak towards the lower molar masses and the appearance of a peak corresponding to the PEO block .

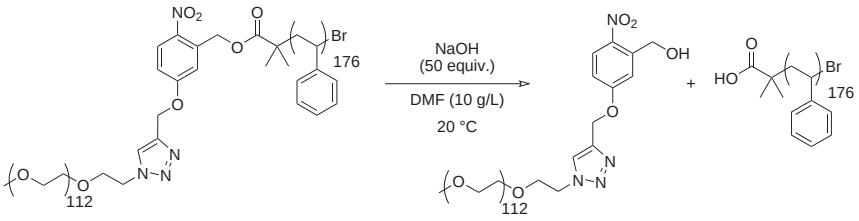

Figure 6.8: Chemical cleavage of PEO_{113}-$h\nu$-PS_{176}.

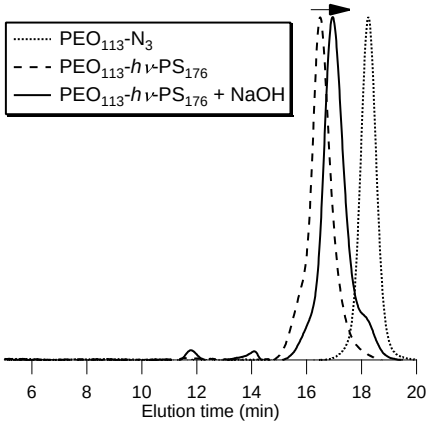

Figure 6.9: GPC chromatograms of the PEO_{113}-$h\nu$-PS_{176} block copolymer before and after its hydrolysis with NaOH.

As for the cleavage upon irradiation, the disruption of PEO_{113}-$h\nu$-PS_{176} micelles was investigated. To the same micellar solution as described in the previous section (Section 6.2.2), 1000 equivalents of NaOH were added. After 24 hours, a slight precipitate was visible, but 72 hours were needed to obtain a solution as turbid as that obtained for the irradiation at 300 nm after 15 minutes.

Table 6.2 summarizes the results for the photocleavage and the chemical cleavage of PEO_{113}-$h\nu$-PS_{176} in a non-selective solvent (fully solubilized) and in a selective solvent (micelles). When the block copolymer is self-assembled into micelles, its chemical cleavage is greatly slowed down in comparison with its cleavage in a non-selective solvent. Indeed, with 20 times more equivalents of base (1000 *vs* 50), the reaction needs much more time to be completed (72 h *vs* 3 h). On the other hand, no significant difference in reaction time is observed when light is used. Indeed, after 15 minutes at 300 nm, the reaction is completed for both entirely solubilized block copolymer chains in solution and for chains associated into micelles. This might be explained by the fact that the access for the base to the reactive sites (ester junctions) is hindered by the polymer chains which are organized into micelles. On the other hand, light does not have to diffuse towards the reactive sites through the solvent and is thus not hindered by the arrangement of the polymer chains. This illustrates once more the utility of using light as a stimulus compared to a chemical stimulus.

Table 6.2: Photo- and chemical cleavage of PEO_{113}-$h\nu$-PS_{176} in solution and in a selective solvent.

Entry	Solvent	State	NaOH	$h\nu$	t (h)
1	DMF	fully solubilized	50 equiv.	/	3.00
2	$MeOH/H_2O$	micelle	1000 equiv.	/	72.00[a]
3	CH_2Cl_2	fully solubilized	/	300 nm	0.25
4	$MeOH/H_2O$	micelle	/	300 nm	0.25[a]

[a] Time needed to reach the same level of turbidity.

6.3 Photocleavage of diblock copolymers bearing photocleavable side groups

The general reaction for the photocleavage of PNBA-*b*-PS diblocks is presented in Figure 6.10. The reaction unmasks the carboxylic acid functions yielding a PS-*b*-PAA diblock copolymer while liberating *o*-nitrobenzylaldehyde. The photocleavage was firstly investigated on a $PNBMA_{109}$ homopolymer synthesized by a typical ATRP procedure as described in Chapter 5 (M_n = 24,100 g/mol, PDI=1.24).

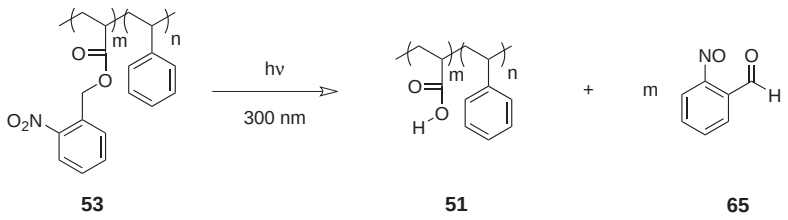

Figure 6.10: Photocleavage of PNBA-*b*-PS.

The homopolymer was dissolved in CH_2Cl_2 (0.026 g/L) and then irradiated at 300 nm during 25 minutes. The reaction was followed by UV-visible spectroscopy and the results are presented in Figure 6.11(a). The UV-visible spectrum of the homo-$PNBMA_{109}$ displays a band at a λ_{max} of 260 nm. This hypsochromic shift in comparison with the first family (λ_{max}=309 nm) is due to the *o*-nitrobenzyl aromatics which are not substituted. Indeed, without any substituants, the λ_{max} of *o*-nitrobenzyl compounds is equal to about 260 nm and the addition of donor substituents on the aromatic ring can increase the λ_{max} up to about 370 nm [12]. During the irradiation of the homopolymer, absorbance bands corresponding to the formed *o*-nitrosobenzaldehyde (238, 280-400 nm) appeared progressively (Figure 6.11(a)). Moreover, the formation of a white precipitate corresponding to insoluble homo-PAA, evidenced the occurrence of the photocleavage. Finally, the efficiency of the photocleavage was estimated to about 80 % by ^{1}H NMR of the irradiated mixture performed in d^6-DMSO, by comparing the signal of the remaining benzylic -CH_2- of the *o*-nitrobenzyl groups with the signals of the whole aromatic protons (*o*-nitrobenzyl + *o*-nitrosobenzaldehyde).

The photocleavage of the P(NBA-*co*-AA)-*b*-PS block copolymers was investigated using the P(NBA-*co*-AA)$_{74}$-*b*-PS$_{581}$ (Table 5.10, Entry 18) and with P(NBA-*co*-AA) $_{31}$-*b*-PS$_{168}$ (Table 5.10, Entry 9) samples. The photocleavage of P(NBA-*co*-AA)$_{74}$-*b*-PS$_{581}$ was followed by UV-visible spectroscopy and is presented in Figure 6.11(b). As for homo-PNBMA, a decrease in the intensity of the band at 260 nm and the appearance of new bands between 280 and 400 nm, corresponding to *o*-nitrosobenzaldehyde, have been observed. However, the band of the starting polymer at 260 nm is not only corresponding to the signal of the nitro groups, but it also contains a contribution coming from the PS absorption.

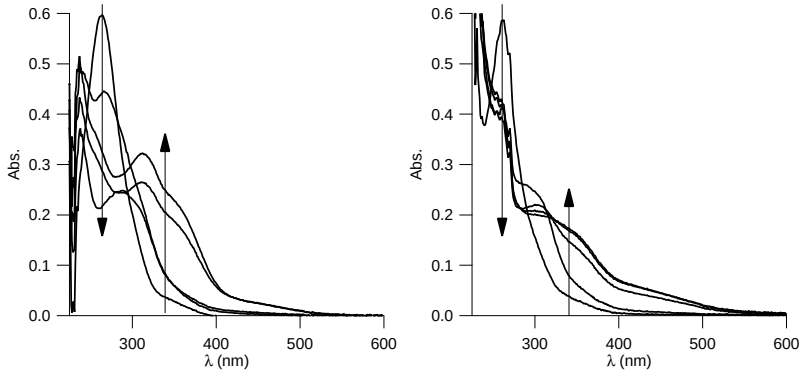

(a) (b)

Figure 6.11: Photocleavage of homo-PNBMA$_{109}$ (a) and P(NBA-*co*-AA)$_{74}$-*b*-PS$_{581}$ (b) in solution (CH_2Cl_2) at $\lambda = 300$ nm: evolution of UV-visible absorption spectra of the solutions as a function of time (t(min)= 0, 5, 10, 15, 20, 25).

As insoluble PAA is formed during the irradiation process, the accordingly generated PAA-*b*-PS block copolymer can self-assemble into micellar objects as depicted in Figure 6.12. For this experiment, P(NBA-*co*-PAA)$_{31}$-*b*-PS$_{168}$ was dissolved in $CHCl_3$ (0.5 g/L) and then irradiated at 300 nm with an intensity of 38.5 mW/cm^2.

The formation of micellar objects during irradiation was followed by

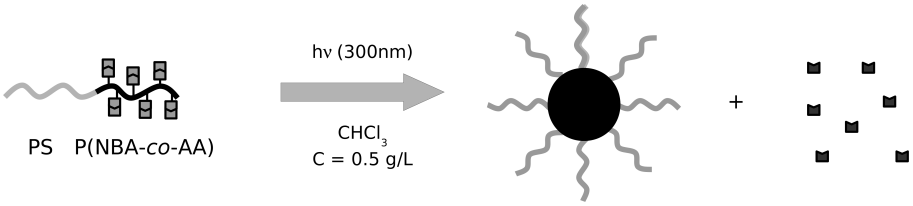

Figure 6.12: Light-induced micellization of P(NBA-*co*-PAA)$_{31}$-*b*-PS$_{168}$ in $CHCl_3$.

DLS by Olivier Bertand. Figure 6.13(a) and Figure 6.13(b) present, respectively, the intensity autocorrelation curves and the Contin size distributions for the solution before (0 min) and after 30, 60, 240 and 850 minutes irradiation time. The intensity autocorrelation curves developped continuously with time until reaching a constant shape, indicating the progressive formation of objects in solution. The Contin size distributions show the coexistence of two populations during the irradiation: one corresponding to the micellar objects with a size of about 100 nm and another one corresponding to the unimers in solution (size $\sim$ 3-5 nm). A decrease of the unimer signal is observed with time and the irradiation was kept until this unimer peak has completely disappeared (850 min). The hydrodynamic radius of the micellar objects after 850 min irradiation time is equal to 100 nm. A polydispersity index of 0.116 is observed, indicating a quite narrow size distribution of the formed objects.

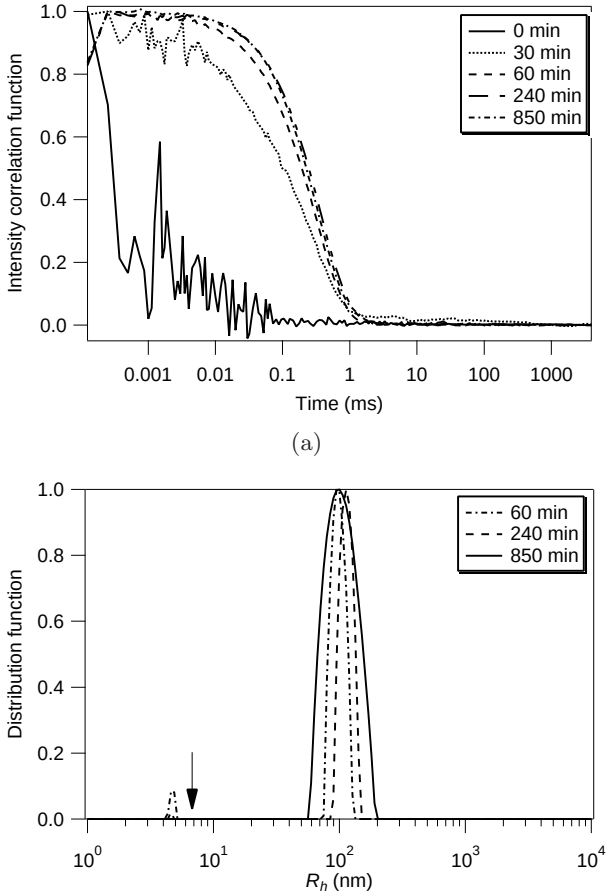

Figure 6.13: Irradiation of P(NBA-*co*-AA)$_{31}$-*b*-PS$_{168}$ in solution: normallized intensity autocorrelation function (above) and Contin size analysis (below).

6.4 Conclusions

The photocleavage of block copolymers from the first and the second family, synthesized in Chapters 4 and 5, was demonstrated in solution. Linear diblocks were firstly cleaved upon UV irradiation at 350 and 300 nm. These block copolymers proved to be also sensitive to chemical cleavage through the hydrolysis of their ester function present between the blocks. It was also shown that micelles of PEO-$h\nu$-PS in a methanol/water mixture could be disrupted upon UV irradiation and under basic hydrolysis, the latter being hindered by the organization of the polymer chains in micellar structures. This further demonstrates the advantage of using light as stimulus.

Concerning the second family, the photocleavage of the *o*-nitrobenzyl side groups was estimated to about 80 % on homo-PNBMA. This yield was obtained for an isolated experiment and might be improved by optimizing the conditions by increasing the irradiation time for instance. Finally, light-induced micellization during the irradiation of P(NBA-*co*-AA)$_{31}$-*b*-PS$_{168}$ was demonstrated by DLS, leading to well-defined micellar object with an hydrodynamic radius of 100 nm.

Experimental part

Materials and Instrumentation. Proton nuclear magnetic resonance (^{1}H NMR) spectra were recorded on a 500 MHz (Bruker Avance II). Molar masses and polydispersity indices of the polymers were measured on a Waters GPC system equipped with a Waters 510 pump and a 410 differential refractometer (40 ℃; eluent: DMF or DMF + NH_4PF_6 (2.5 mM); flow rate of 0.5 mL/min) and on an Aligent GPC auto sampler system equipped with an Aligent 1100/1200 pump and an Aligent differential refractometer (40 ℃; eluent: DMF; flow rate of 1 mL/min). The GPCs were equiped with PSS GRAM columns (Beads 10 μ; porosity of column 1: 1000 Å; porosity of column 2: 100 Å. The calibrations were performed using polystyrene standards. UV-vis spectra were recorded on a Varian spectrophotometer (Cary, 50 Conc). The 300 and 350 nm UV lamps were Rayonet photochemical reactor lamps. Irradiations were performed with 3 lamps with the samples situated a 3 cm of the lamps (the intensity of the UV lamps at that distance was equal to 38.5 mW/cm^2 and to 4.58 mW/cm^2 for the lamps emitting at 300 and 350 nm, respectively. Irradiation intensities have been measured with a radiometer RM12 from Dr. Gröbel UV-electronik GmbH equiped with UVA (315-400 nm) and UVB (280-315 nm) sensors.

Dynamic light scattering (DLS) measurements were performed on a Malvern CGS-3 apparatus equipped with a He-Ne laser with a wavelength of emission at 632.8 nm. The temperature was controlled at 25 *tccentigrade*. The experimental autocorrelation function, $g(t)$, is commonly expressed in the form of a cumulant expansion (eq 6.1):

$$g(t) = \exp\Big(- \Gamma_1 t + (\frac{\Gamma_2}{2!})t^2 - (\frac{\Gamma_3}{3!})t^3 + \dots \Big) \tag{6.1}$$

where Γ_i is the ith cumulant and $\Gamma_1 = Dq^2$ where D is the translational diffusion coefficient and q is the absolute value of the scattering vector. The polydispersity index (PDI) of the objects was estimated from the ratio Γ_2/Γ_1^2. The diffusion coefficient extrapolated to zero concentration is related to the hydrodynamic radius R_h by the Stokes-Einstein equation (eq 6.2):

$$R_h = \frac{k_b T}{6\pi\eta D} \tag{6.2}$$

where k_b is the Boltzmann constant and η the viscosity of the solvent. The experimental data have been also analyzed by the CONTIN method

which is based on an inverse-Laplace transformation of the data and which gives access to a size distribution histogram for the analyzed micellar solutions.

Section 6.2

Photocleavage of PEO_{113}-$h\nu$-PS_{133} in solution. A quartz cell was filled with a solution of PEO_{113}-$h\nu$-PS_{133} in CH_2Cl_2 (C= 2.0 g/L). The solution was irradiated at 350 nm (intensity = 4.58 mW/cm^2). The photocleavage was followed by UV-visible spectroscopy until no change was observed in the spectrograms (t(min)= 0, 2, 4, 6, 8, 10, 15, 20, 30, 40, 50). After 50 min, the solvent was removed in vacuo and the residue was analyzed by GPC.

Block copolymer: λ_{max} = 309 nm; $Abs_{\lambda_{max}}$ = 0.974; ε = 9276 L.mol^{-1}.cm^{-1}.

Photocleavage of PEO_{113}-$h\nu$-$PtBA_{305}$ in solution. A quartz cell was filled with a solution of PEO_{113}-$h\nu$-$PtBA_{305}$ in CH_2Cl_2 (C= 4.0 g/L). The solution was irradiated at 350 nm (intensity = 4.58 mW/cm^2). The photocleavage was followed by UV-visible spectroscopy until no change was observed in the spectrograms (t(min)= t(min)= 0, 2, 5, 10, 20, 35, 50). After 50 min, the solvent was removed in vacuo and the residue was analyzed in GPC.

Block copolymer: λ_{max} = 309 nm; $Abs_{\lambda_{max}}$ = 0.772; ε = 9360 L.mol^{-1}.cm^{-1}.

Photocleavage of PS_{52}-$h\nu$-$PMMA_{278}$ in solution. A quartz cell was filled with a solution of PS_{52}-$h\nu$-$PMMA_{278}$ in CH_2Cl_2 (C= 2.0 g/L). The solution was irradiated at 350 nm (intensity = 4.58 mW/cm^2). The photocleavage was followed by UV-visible spectroscopy until no change was observed in the spectrograms (t(min)= t(min)= 0, 2, 5, 10, 20, 35, 50). After 50 min., the solvent was removed in vacuo and the residue was analyzed in GPC.

Block copolymer: λ_{max} = 309 nm; $Abs_{\lambda_{max}}$ = 0.569; ε = 9445 L.mol^{-1}.cm^{-1}.

Photocleavage of PEO_{113}-$h\nu$-PS_{176} in solution. A quartz cell was filled with a solution of PEO_{113}-$h\nu$-PS_{176} in CH_2Cl_2 (C= 2.2 g/L). The solution was irradiated at 300 nm (intensity = 38.5 mW/cm^2). The

photocleavage was followed by UV-visible spectroscopy until no change was observed in the spectrograms (t(min)= 0, 1.5, 3, 5, 8, 10, 15, 20). After 20 min., the solvent was removed in vacuo and the residue was analyzed in GPC.

Block copolymer: λ_{max} = 309 nm; $Abs_{\lambda_{max}}$ = 0.862; ε = 9246 $L.mol^{-1}.cm^{-1}$.

Section 6.2.3

Typical chemical cleavage of PEO_{113}-$h\nu$-PS_{176} in solution. To a stirred solution of PEO_{113}-$h\nu$-PS_{176} in DMF (510 μL, 2.2×10^{-4} mmol, 1 equiv.) was added 22 μL of $NaOH_{aq}$ 0.5 M (110×10^{-4} mmol, 50 equiv.). After 3 h, the solvent was removed in vacuo and the residue was analyzed in GPC.

Micellization of PEO_{113}-$h\nu$-PS_{176}. PEO_{113}-$h\nu$-PS_{176} (3.3 mg) was dissolved in DMF. The solution was then dialyzed against a methanol/water mixture (9/1) for 48 hours (replacing the solvent three times) affording 4.23 mL of a micellar solution (0.78 g/L). The solution was diluted to 0.5 g/L and then characterized by DLS. R_h = 20.5 nm, PDI = 0.089.

Photocleavage of micelles of PEO_{113}-$h\nu$-PS_{176}. A quartz cell was filled with a micellar solution of PEO_{113}-$h\nu$-PS_{176} in a methanol/water mixture (9/1) (C = 0.5 g/L). The solution was irradiated at 300 nm (intensity = 38.5 mW/cm^2). After 15 minutes, the solution contained a white precipitate corresponding to the insoluble homo-PS.

Chemical cleavage of micelles of PEO_{113}-$h\nu$-PS_{176}. To a micellar solution of PEO_{113}-$h\nu$-PS_{176} in a methanol/water mixture (9/1) (C = 0.5 g/L, 1 mL, $21.5 \times 10_{-6}$ mmol, 1 equiv.) was added 43 μL of $NaOH_{aq}$ 0.5 M (21.5×10^{-3} mmol, 1000 equiv.). The solution was stirred until displaying the same turbidity than the one exposed to UV irradiation (72 h).

Section 6.3

Photocleavage of homo-$PNBMA_{109}$ in solution. A quartz cell was filled with a solution of homo-$PNBMA_{109}$ in CH_2Cl_2 (C= 0.026 g/L). The solution was irradiated at 300 nm (intensity = 38.5 mW/cm^2). The photocleavage was followed by UV-visible spectroscopy until no

change was observed in the shape of the spectrograms (t(min)= 0, 5, 10, 15, 20, 25). The solution was filtered (0.2 μm-Acrodisc) before each UV measurements due to the formation of a PMAA precipitate during the irradiation. Polymer: λ_{max} = 264 nm; $Abs_{\lambda_{max}}$ = 0.597; ε = 553,373 $L.mol^{-1}.cm^{-1}$.

For ^{1}H NMR: Three quartz cells were filled with a solution of homo-$PNBMA_{109}$ in CH_2Cl_2 (C= 0.026 g/L). The solutions were irradiated at 300 nm (intensity = 38.5 mW/cm^2). After 25 minutes, the solutions were gathered and the solvent was removed in vacuo. ^{1}H NMR (500 MHz, d^6-DMSO): δ (ppm) 12.50 (b, 87H, COOH), 8.50-6.50 (m, 436H, aromatics: *o*-nitrobenzyl + *o*-nitrosobenzaldehyde), 5.20 (s, 43H, H_{Ar}, CH_2-O), 2.20-0.5 (b, 545H, CH_2-, CH_3, backbone).

Photocleavage of P(NBA-*co*-AA)$_{74}$-*b*-PS$_{581}$ in solution. A quartz cell was filled with a solution of P(NBA-*co*-AA)$_{74}$-*b*-PS$_{581}$ in CH_2Cl_2 (C= 0.67 g/L). The solution was irradiated at 300 nm (intensity = 38.5 mW/cm^2). The photocleavage was followed by UV-visible spectroscopy until no change was observed in the shape of the spectrograms (t(min)= 0, 5, 10, 15, 20, 25). The solution was filtered (0.2 μm-Acrodisc) before each UV measurements due to the formation of a PMAA precipitate during the irradiation. Polymer: λ_{max} = 260 nm; $Abs_{\lambda_{max}}$ = 0.585;

Photocleavage of P(NBA-*co*-PAA)$_{31}$-*b*-PS$_{168}$ in solution. A quartz cell was filled with a solution of P(NBA-*co*-PAA)$_{31}$-*b*-PS$_{168}$ in $CHCl_3$ (C= 0.5 g/L). The solution was irradiated at 300 nm (intensity = 38.5 mW/cm^2). The photocleavage was followed by DLS until the Contin size analysis showed the complete disappearence of the peak corresponding to the unimers (3-5 nm). (t(min)= 0, 30, 60, 90, 240, 850).

Bibliography

[1] Pillai, V. *Synthesis* **1980**, 1–26.

[2] Bochet, C. G. *J. Chem. Soc., Perkin Trans. 1* **2002**, 125–142.

[3] Pelliccioli, A. P.; Wirz, J. *Photochem. Photobiol. Sci.* **2002**, *1*, 441–458.

[4] Greene, T. W.; Wuts, P. G. *Protective Groups in Organic Synthesis*, 3rd ed.; John Wiley & Sons, Inc., 1999.

[5] Hoffmann, N. *Chem. Rev.* **2008**, *108*, 1052–1103.

[6] Llobet, A. I.; Alvarez, M.; Albericio, F. *Chem. Rev.* **2009**, *109*, 2455–2504.

[7] Barltrop, J. A.; Plant, P. J.; Schofield, P. *Chem. Commun.* **1966**, 822–823.

[8] Patchornik, A.; Amit, B.; Woodward, R. B. *J. Am. Chem. Soc.* **1970**, *92*, 6333–6335.

[9] Reichmanis, E.; Smith, B. C.; Gooden, R. *J. Polym. Chem. Part A* **1985**, *23*, 1–8.

[10] Zehavi, U.; Patchornik, A. *J. Org. Chem.* **1972**, *32*, 2285–2288.

[11] Zehavi, U.; Amit, B.; Patchornik, A. *J. Org. Chem.* **1972**, *37*, 2281–2284.

[12] Aujard, I.; Benbrahim, C.; Gouget, M.; Ruel, O.; Baudin, J.-B.; Neveu, P.; Jullien, L. *Chem. Eur. J.* **2006**, *12*, 6865–6879.

CHAPTER
SEVEN

THIN FILMS FROM PHOTOCLEAVABLE BLOCK COPOLYMERS

Abstract

This chapter deals with the self-assembly of PEO-hν-PS and P(NBA-co-AA)-b-PS block copolymers in thin films. For both families, a cylindrical morphology has been observed and the conditions of annealing leading to the desired perpendicular orientation of the cylinders are presented. For PEO-hν-PS, the creation of porosity after irradiation and removal of the PEO minor phase was studied. UV-visible and infrared (IR) spectroscopies demonstrated the removal of the PEO phase while the formation of nanopores was evidenced by scanning and transmission microscopies (SEM and TEM). In the case of P(NBA-co-AA)-b-PS block copolymers, only preliminary results towards nanoporous thin films are presented.

7.1 Introduction

Figure 7.1 reminds of the general strategy leading to nanoporous thin films from photocleavable block copolymers. Photocleavable block copolymers are firstly self-assembled into thin films and a subsequent UV irradiation followed by the extraction of the minor phase leads to thin films containing nanopores. Chapters 4 and 5 dealt with the synthesis of these block copolymers and their ability to be cleaved upon UV irradiation has been demonstrated in Chapter 6. The present chapter deals with the self-assembly of the photocleavable block copolymers and the creation of porosity inside them.

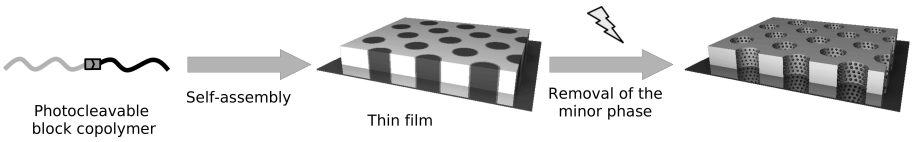

Figure 7.1: Strategy towards nanoporous materials.

Thin films are prepared by spin-coating and further annealing is needed for the obtention of a well-defined morphology. The two first sections discuss the conditions leading to a perpendicular orientation of the cylinders for both of the investigated families (PEO-*hν*-PS and P(NBA-*co*-AA)-*b*-PS). The accordingly obtained thin films were characterized by AFM and the question of knowing if the cylinders span throughout the entire film thickness is also approached. Finally, the last section presents the results about the irradiation of the films and the subsequent extraction of the minor phase leading to nanopores. UV-visible and infrared spectroscopies as well as imaging techniques (TEM and SEM) evidence the formation of such nanopores.

7.2 Thin films from PEO-$h\nu$-PS block copolymers

7.2.1 Spin-coating

Thin films were prepared by spin-coating a solution of block copolymer dissolved in a non-selective solvent. Spin coating consists in depositing some drops of a polymer solution onto the center of a substrate and in subsequently spinning the substrate at high velocity. The spreading of the solution occurs from the center to the edge of the substrate due to the centripetal acceleration. The evaporation of the solvent leaves a thin film of block copolymer on the surface (Figure 7.2).

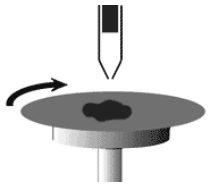

Figure 7.2: Schematic spin-coating process[1].

Thin films of PEO_{113}-$h\nu$-PS_{135} (Table 4.5, Entry 1) and PEO_{113}-$h\nu$-PS_{176} (Table 4.5, Entry 4) were prepared by spin-coating on silicon substrates (1 cm^2) from a benzene (C_6H_6) solution (20 g/L). During the spin-coating process, solvent evaporates causing the phase separation of the block copolymer on the substrate. However, since the evaporation occurs rapidly, the self-assembly process is often incomplete and/or leaves a lot of defects in the accordingly obtained thin film. For instance, atomic force microscopy (AFM) height contrast pictures showing the top view of thin films of PEO_{113}-$h\nu$-PS_{135} and of PEO_{113}-$h\nu$-PS_{176} just after spin-coating are presented in Figures 7.3(a) and 7.3(b), respectively. No significant phase separation can be seen for PEO_{113}-$h\nu$-PS_{135} (Figure 7.3(a)) while an ill-defined organization of randomly orientated cylinders can be distinguished in the case of PEO_{113}-$h\nu$-PS_{176} (Figure 7.3(b)).

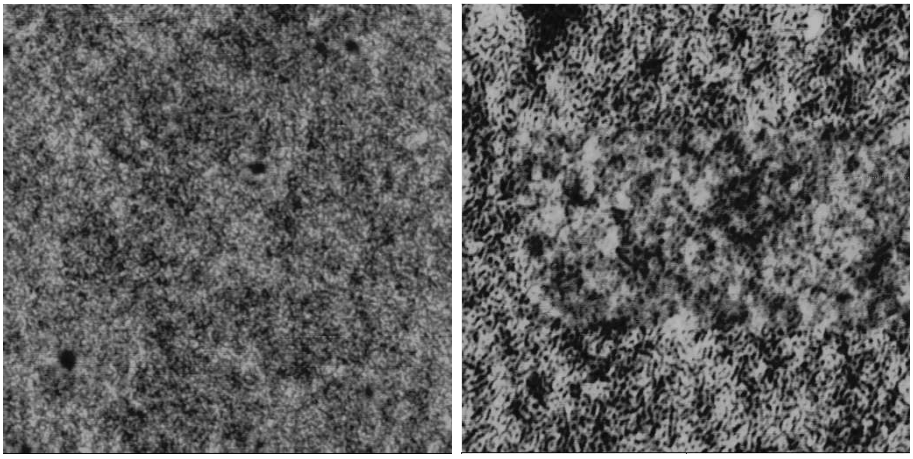

(a) (b)

Figure 7.3: AFM height pictures of thin films of PEO_{113}-$h\nu$-PS_{135} (a) and PEO_{113}-$h\nu$-PS_{176} (b) spin-coated from a C_6H_6 solution (20 g/L).

7.2.2 Solvent annealing

In order to induce and/or improve the self-assembly process, annealings using solvent vapors were employed. The experimental set-up is sketched in Figure 7.4. The samples to be annealed are placed under a glass case with beakers containing solvents. Once the set-up is closed, the solvent vapors fill the glass case causing the swelling of the thin films which are then proned to reorganization as already discussed in Section 1.3.2. The system is kept as hermetic as possible by laying a weight upon the glass case. Beakers with different opening areas were used in order to tune the vapor pressure of solvents in the system. Small (S), medium (M) and large (L) beakers with evaporation area of 4.9 cm^2, 8.6 cm^2, 15.9 cm^2, respectively were used for the experiments.

The annealing conditions were inspired from previous works performed in our laboratory [1, 2] and from the works of Russell, Hawker and coworkers on the annealings of thin films of PEO-*b*-PS and PEO-*b*-PMMA-*b*-PS block copolymers [2–8]. From these studies, it came out that annealings in benzene/water vapors lead to a perpendicular orientation of the PEO cylinders. The presence of humidity plays undoubtedly

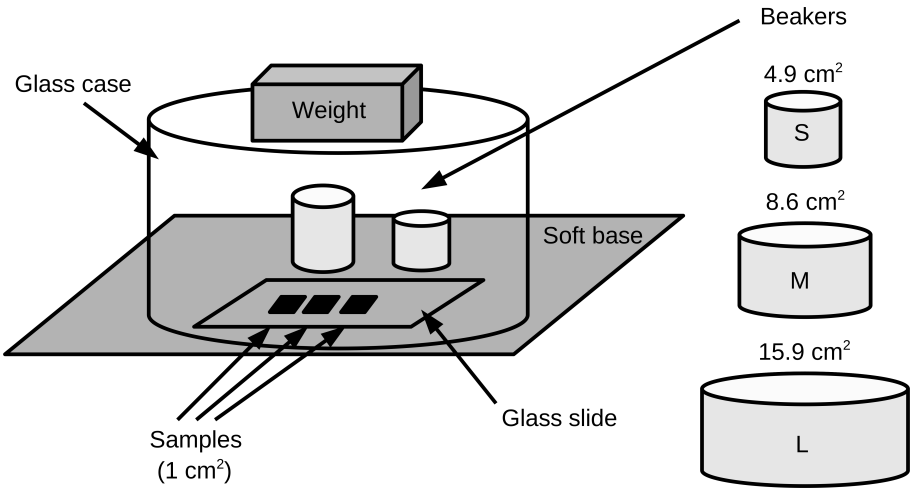

Figure 7.4: Schematic representation of the annealing set-up.

a major role in the control of the orientation and on the long range order of the cylinders. It is thought that the perpendicular orientation process starts with the nucleation of the PEO domains at the surface of the film. This nucleation is induced by the drop of the solvent concentration at the free surface, causing the phase separation of the constituents. Moreover, the nucleation would be enhanced by a preferential swelling of the PEO domain by water [9]. After this primary nucleation, the cylindrical phase separation grows throughout the whole thickness of the thin film following the gradient of solvent concentration (see Section 1.3.2.2).

As water plays a major role, a first set of experiments was carried out on thin films made with PEO_{113}-$h\nu$-PS_{135} by varying the opening area of the water beaker (Table 7.1, Entries 1-3). Figures 7.5(a), 7.5(b) and 7.5(c) present the AFM height images for these experiments after 6 hours of annealing. The three conditions led to nanoscopic cylindrical domains of PEO at the surface of the film. However, a correlation between the opening area of the water beaker and the morphology of the accordingly obtained thin film is noted. Indeed, the optimal condition is found when a medium beaker (M) is used for water (condition MM, Entry 2). In this case, all the cylinders are oriented normal to the substrate. The mean diameter of the cylinders (Ø) is equal to 19 nm with

Table 7.1: Annealing conditions and results for thin films made of PEO_{113}-$h\nu$-PS_{135}.

		Type of beaker[a]			Cylinders	
Entry	Condition	C_6H_6	H_2O	t (h)	$\varnothing^b$ (nm)	λ^c_{C-C} (nm)
1	MS	M	S	6	18 ± 4	29
2	MM	M	M	6	19 ± 4	32
3	ML	M	L	6	26 ± 7	44
4	MM	M	M	15	22 ± 2	35

[a]As defined in figure 7.4.[b]Diameter of the cylinders estimated from the AFM images and the indicated dispersion corresponds to the standard deviation $\sigma_\varnothing$ of the population. [c]Center-to-center interdistance between the neighboring cylinders estimated from the AFM images.

a center-to-center interdistance between neighboring cylinders (λ_{C-C}) of 32 nm (Figure 7.5(b)). When a smaller beaker is used (beaker S, condition MS, Entry 1), a morphology presenting a mixed orientation of perpendicular and parallel cylinders is observed (Figure 7.5(a)). In this case, the mean diameter of the cylinders and the interdistance are equal to 18 nm and 29 nm respectively. Finally, if a larger beaker (L) is used, the PEO cylinders remain perpendicular but begins to swell due to the presence of an excess of water (Figure 7.5(c)). Thereby, a large increase in the size of the cylinders is observed and the diameter Ø displays a value of 26 nm. Increasing the time of annealing in condition MM (15 h, Table 7.1, Entry 4), improved the lateral organization of the cylinders as it can be observed in Figure 7.5(d). Indeed, larger arrays of hexagonally packed cylinders (HEX) can be noticed. The mean diameter (Ø) of the cylinders is equal to 22 nm with a λ_{C-C} of 35 nm. A longer annealing time improves thus the long-range order. Some flower like patches are present on the image. These defects are due to local deformation in the thickness of the film and are not observed on the phase contrast image (not shown here). These results indicate a correlation between the vapor pressure in the system, and the morphology of the film. Indeed, the larger the beaker of water, the bigger the cylinders. The diameters range from 18 nm for the small beaker (S) to 26 nm for the larger one (L). The same behavior is observed for the interdistance (29 nm with beaker S and 44 nm with beaker L).

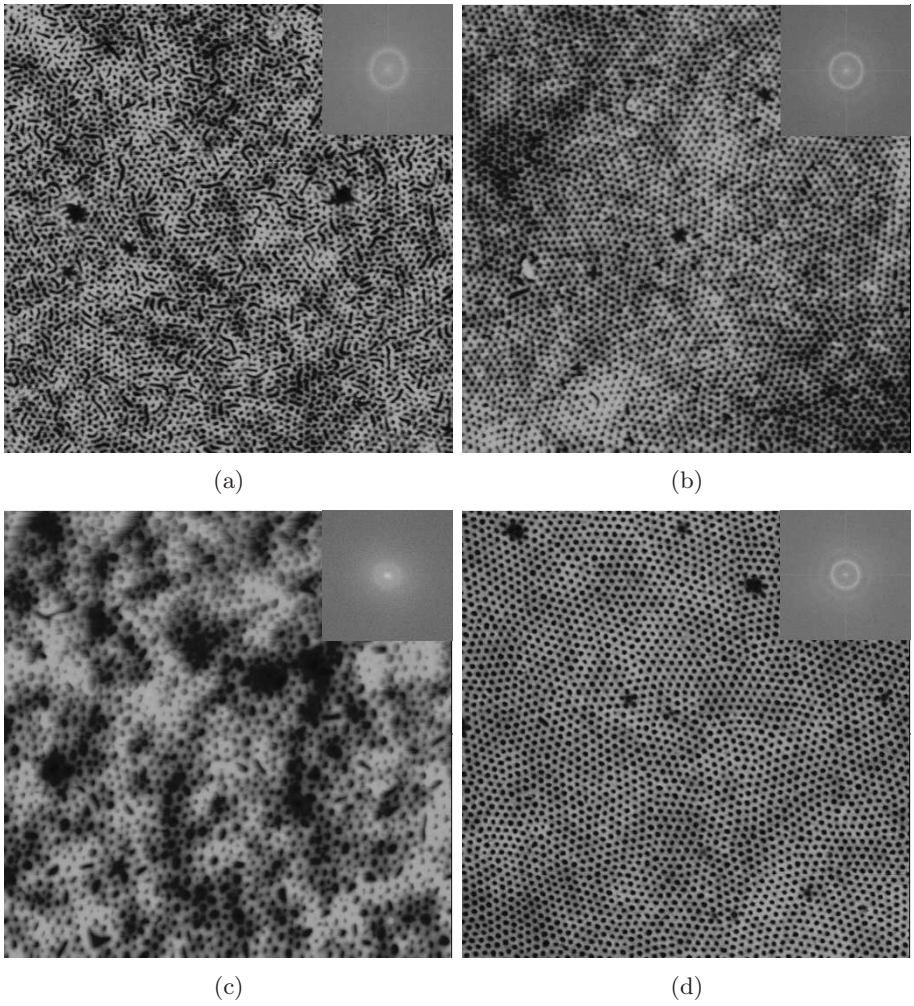

Figure 7.5: AFM height images (2×2 μm) of thin films of PEO_{113}-$h\nu$-PS_{135} spin-coated from a C_6H_6 solution (20 g/L) and annealed in C_6H_6/H_2O vapors in conditions MS (a), MM (b), ML (c) for 6 hours (Table 7.1, Entry 1-3). Conditions MM for 15 hours (d). The insets show the corresponding fast Fourrier transfoms (FFT).

Beside the visual observation of the film, fast Fourrier transforms (FFTs) can be applied to the AFM images giving information about the translational and orientational order of the morphologies (see insets of AFM images) [7, 10, 11]. A ring indicates the presence of a microphase-separated structure but which lacks of a long range order. This is the case for the results of Figure 7.5(a) (Table 7.1, Entry 1). For Figure 7.5(c) (Table 7.1, Entry 3), the circle is very hazy, indicating the absence of order. Nevertheless, in the case of Figure 7.5(b)(Table 7.1, Entry 2) and Figure 7.5(d) (Table 7.1, Entry 4) the circle is clear and additional circles appear around the main one. This additional circles are the premise of a long-range order. When perfect HEX arrangement and long-range order are presents, the FFT is composed of a nice pattern of hexagonally packed dots pattern [7, 10, 11].

The MM conditions were tested with thin films of PEO_{113}-$h\nu$-PS_{176}. After 15 h of annealing time, PEO cylinders oriented normal to the surface ($\varnothing = 24 \pm 4$ nm, $\lambda_{C-C} = 38$ nm) were obtained (Figure 7.6(a)). Increasing the annealing time up to 48 h, improved slightly the long-range order while keeping the diameter ($\varnothing = 24 \pm 2$ nm) and the interdistance ($\lambda_{C-C} = 38$ nm) similar.

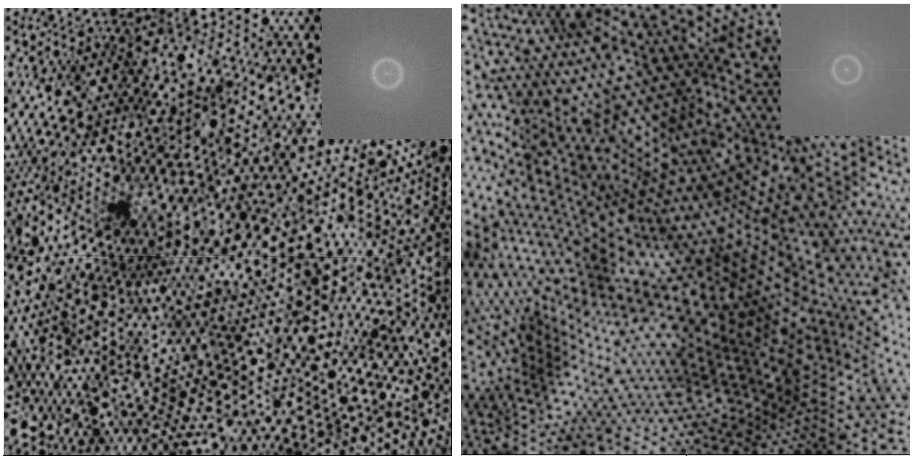

(a) (b)

Figure 7.6: AFM height images (2×2 μm) of thin films of PEO_{113}-$h\nu$-PS_{176} spin-coated from a C_6H_6 solution (20 g/L) and annealed in C_6H_6/H_2O vapors in conditions MM after 15 h (a) and 48 h (b). The insets show the corresponding fast Fourrier transfoms (FFT).

As already mentioned, the perpendicular orientation of the cylinders is thought to start with a nucleation step at the surface of the film followed by the growth of the domains throughout the film [9, 12]. The nucleation is due to the evaporation of the solvent at the free surface. A gradient of solvent concentration is then established throughout the film thickness and its evolution with time dictates the propagation of the orientation of the cylinders and the long-range order. As the drying time influences the evaporation of the solvent and the formation of the gradient, it is thus a critical parameter. Therefore, the rate of evaporation of the solvents after the annealing of the film was investigated. Up to now, the samples were annealed under the glass case in order to be swollen by the solvent vapors. After a time, the glass case was removed and the film is able to dry, causing the phase separation. As the thickness of the films is very small ($\sim$ 130 nm), the drying is nearly instantaneous. In order to slow down the evaporation time, the glass case was kept slightly open after the annealing time by placing some glass slides between the glass case and its base. Once the benzene was totally evaporated, the glass case was completely removed. Figure 7.7 shows the AFM height image

of the top a film of PEO_{113}-$h\nu$-PS_{176} annealed in LM' conditions[2]. The LM' condition was applied during 4 h before evaporating benzene. The benzene solution (2 mL) was completely evaporated within about 2.5 hours. In these conditions, the long-range order was greatly improved as it can be seen on the AFM image and on the corresponding FFT in which a regular dotted pattern replaced the former circle (Figure 7.7). The average diameter of the cylinders is equal to 22 ± 4 nm with an interdistance between the cylinder centers of 39 nm. These conditions are the optimal ones found for a perpendicular orientation of PEO domains for PEO-$h\nu$-PS block copolymers.

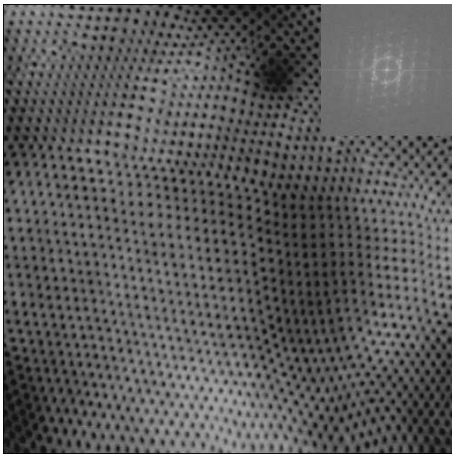

Figure 7.7: AFM height image (2×2 μm) of a thin film of PEO_{113}-$h\nu$-PS_{176} spin-coated from a C_6H_6 solution and annealed in C_6H_6/H_2O vapors (condition LM') during 4 h followed by a slow evaporation of the solvent. The inset shows the FFT of the whole image.

[2]LM' stand for Large beaker for benzene (L), medium beaker for water (M) and slow evaporation of benzene (')

During the annealing experiments, a general trend has been observed concerning the relative humidity present during annealing. Indeed, when only benzene is used, or when the relative humidity in the system is low, a parallel orientation of the cylinders is observed (Figure 7.8(a)) as described by Russell and coworkers [13]. On the contrary, if too much water is present during the annealing, the swelling of the PEO domains leads to the formation of defects in the films (Figure 7.8(b)).

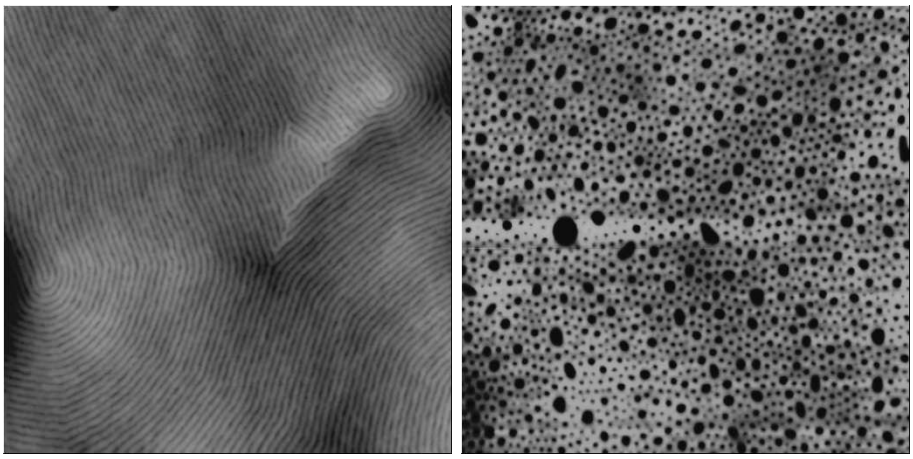

(a) (b)

Figure 7.8: AFM height images (2×2 μm) of thin films of PEO_{113}-$h\nu$-PS_{176} spin-coated from a C_6H_6 solution (20 g/L) and annealed in benzene vapors (a) and benzene/water vapors with a high degree of relative humidity (b).

Finally, beside the opening area of the beakers and the rate of evaporation of benzene, other parameters were tested in order to improve the long-range order. Addition of salt (KI) or of homo-PEO to the block copolymer before thin film preparation were reported [6,7,14] to be efficient and were also tested. In the best cases, similar results than those obtained in the conditions MM (see Figures 7.6(a) and 7.6(b)) were obtained and no significant improvements were observed in comparison with the conditions without any additive.

7.2.3 Do the cylinders span through the whole film?

In the previous Section, the obtention of arrays of perpendicular PEO cylinders has been demonstrated by AFM measurements. However, AFM only gives information about the surface of the films and the question of knowing if the cylinders span throughout the whole film thickness remains open. A first piece of evidence can be given by AFM measurements of the bottom of the film (substrate side). For this experiment, the same thin film of PEO_{113}-$h\nu$-PS_{176} than the one presented in Figure 7.6(a) was prepared on a silicon wafer covered with a 400 nm thick layer of silicon oxide. The sample was then floated on a hydrofluoric acid solution (5 wt.-%) in order to destroy the silicon oxide layer and detach the film from its substrate. The film was then transferred to a water bath. After its flipping and pickup on a new substrate, the flipped film was analyzed by AFM. Figure 7.9 shows the AFM height and phase pictures of the flipped film. Except for few defects, hexagonally packed cylinders which are normal to the substrate are observed, suggesting that the PEO domain orientation propagates throughout the whole film.

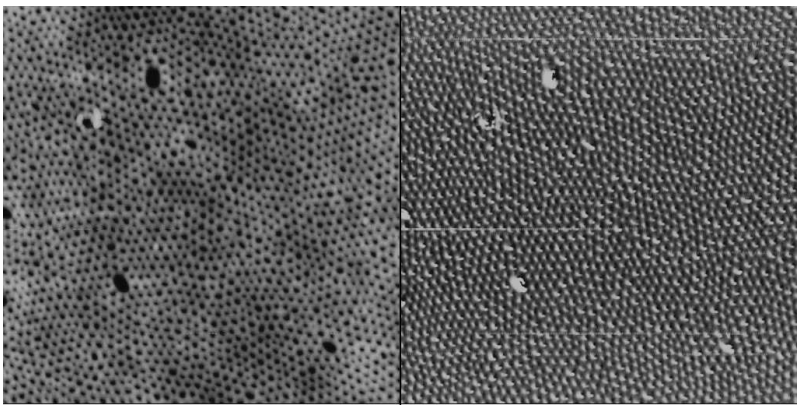

Figure 7.9: AFM height (left) and phase (right) images (2×2 μm) of a flipped thin film of PEO_{113}-$h\nu$-PS_{176} spin coated from a C_6H_6 solution (20 g/L) and annealed in C_6H_6/H_2O vapors (condition MM) during 15 h.

Beside surface measurements, cross-sectional views were obtained with scanning electron microscopy (SEM). The samples were broken

into two pieces exposing their cross-section to analysis. Figures 7.10(a) and 7.10(b) show typical cross-sectional views of a thin film of PEO_{113}-$h\nu$-PS_{176} annealed in condition MM during 15 h. On the pictures, nice HEX arrangement of the cylinders can be visualized at the surface of the films. However, the cross-section does not show the expected perpendicular orientation, but displays an undefined three-dimensional structure. This structure is attributed to the deformation of the film caused by mechanical constraints occurring during the breaking of the sample. Decreasing the thickness of the film to about 30 nm did not avoid this deformation and the undefined structure remains present on all the samples studied.[3]

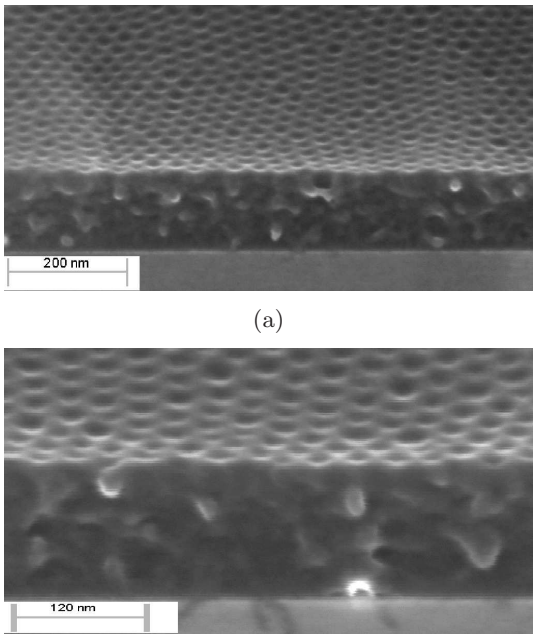

(a)

(b)

Figure 7.10: SEM images of thin films of PEO_{113}-$h\nu$-PS_{176} spin coated from a C_6H_6 solution (20 g/L) and annealed in conditions MM during 15 h (Figure 7.1, Entry 5).

[3]The thicknesses of the films were measured by SEM and are controlled by the concentration in block copolymer of the spin-coated solution (see experimental section).

In order to explore the inside of the films, thin films of $\sim$ 130 nm were etched by oxygen reactive ion etching (O_2 RIE)[4]. The resulting $\sim$ 60 nm thick film was then analyzed by SEM (Figure 7.11). The picture shows an expansion of the diameter of the cylinder (due to the etching) but the picture clearly shows that the perpendicular orientation was kept at least until the middle of the film thickness.

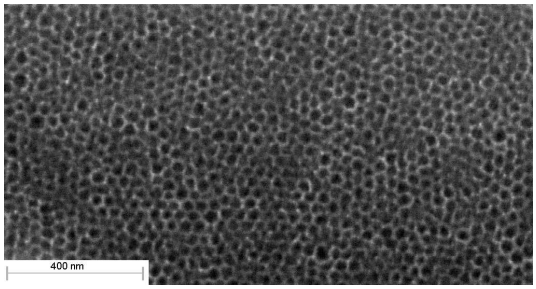

Figure 7.11: SEM image of a thin film exposed to O_2 RIE. The initial thin film was made of PEO_{113}-*hν*-PS_{176} spin-coated from a C_6H_6 solution (20 g/L) and annealed in conditions MM during 15 h. Thicknesses before and after etching are equal to 130 nm and to 60 nm, respectively.

7.3 Thin films from P(NBA-*co*-AA)-*b*-PS block copolymers

7.3.1 Spin-coating and solvent annealings

The self-assembly of P(NBA-*co*-AA)$_{74}$-*b*-PS_{415} and of P(NBA-*co*-AA)$_{74}$-*b*-PS_{581} has been investigated. As for PEO-*b*-PS block copolymers, thin films were prepared by spin-coating from benzene solutions. After spin-coating, AFM images of the films showed no significant phase separation. Therefore, in order to induce the desired self-organization process, solvent annealings were performed. As no data are available in the literature concerning the self-assembly of such block copolymers, different solvents were screened for annealing. Table 7.2 summarizes the conditions and the results of this investigation. The annealings were performed on thin films prepared from a 10 g/L benzene solution. The

[4]The etching was performed by Dr. Alexandru Vlad.

thickness of these films is of about 56 nm. The annealings were performed in slow evaporation mode (') and six solvents or combinations of solvents were tried: benzene (C_6H_6), tetrahydrofuran (THF), dioxane ($C_4H_8O_2$), chloroform ($CHCl_3$), benzene/water (C_6H_6/H_2O) and benzene/nitromethane (C_6H_6/CH_3NO_2).

Table 7.2: Annealing conditions for thin films made of P(NBA-*co*-AA)-*b*-PS block copolymers.

Entry	Annealing solvent	Condition	Cylinder orientation	
			P(NBA-*co*-AA)$_{74}$-*b*-PS$_{415}$	P(NBA-*co*-AA)$_{74}$-*b*-PS$_{581}$
1	C_6H_6	L'	$\perp$	$\perp$
2	THF	L'	$\perp$	//
3	$C_4H_8O_2$	L'	//	$\perp$
4	$CHCl_3$	L'	//	$\perp$
5	C_6H_6/H_2O	LM'	$\perp$	$\perp$
6	C_6H_6/CH_3NO_2	LM'	//	$\perp$

AFM measurements on these films evidenced the existence of a cylindrical morphology for both of the block copolymers. This indicates that the compositions targeted during the synthesis were correct. Moreover, the orientation of the cylinders was found to be either perpendicular or parallel to the surface depending on the solvent used for annealing. In the case of P(NBA-*co*-AA)$_{74}$-*b*-PS$_{415}$, the perpendicular orientation was found only for Entries 1,2 and 5 (Table 7.2), while for P(NBA-*co*-AA)$_{74}$-*b*-PS$_{581}$, the perpendicular orientation was found in each cases except when THF was used (Table 7.2, Entry 2). Even if the block copolymers are the same in terms of chemical structure, the difference in their composition ($r = 0.25$ for P(NBA-*co*-AA)$_{74}$-*b*-PS$_{415}$, $r = 0.18$ for P(NBA-*co*-AA)$_{74}$-*b*-PS$_{581}$) certainly explains the fact that in the same conditions, the orientation of the cylinders is different. Indeed, one possible explanation is that the composition of P(NBA-*co*-AA)$_{74}$-*b*-PS$_{415}$ ($r = 0.25$) is close to the one which gives rise to a lamellar morphology. During the annealing, the swelling of the different phases depends on the type of the solvents used. Thereby, either a cylinder or a lamellar

morphology can be reached if the composition of the block copolymer is close to the border between the composition leading to cylinders and that yielding lamellae.

AFM height images of the two orientations displayed by both of the block copolymers are shown in Figures 7.12(a) and 7.12(c) for P(NBA-*co*-AA)$_{74}$-*b*-PS$_{415}$ and in Figures 7.12(b) and 7.12(d) for P(NBA-*co*-AA)$_{74}$-*b*-PS$_{581}$. The best condition for the perpendicular orientation of P(NBA-*co*-AA)$_{74}$-*b*-PS$_{415}$ is the annealing in THF vapors (cylinders: Ø = 19 ± 4 nm, λ_{C-C} = 39 nm) while for P(NBA-*co*-AA)$_{74}$-*b*-PS$_{581}$ the best condition was the combination benzene/nitromethane (cylinders: Ø = 21 ± 4 nm, λ_{C-C} = 40 nm).

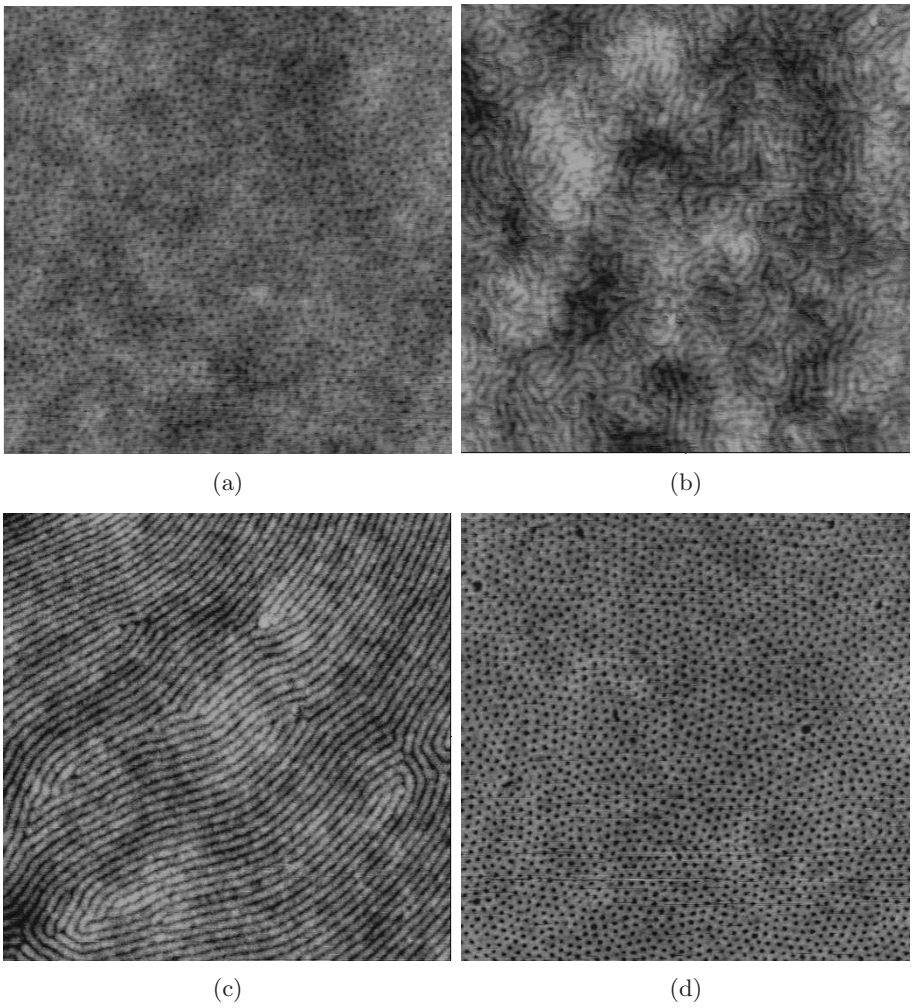

Figure 7.12: AFM height images (2×2 μm) of thin films of P(NBA-*co*-AA)-*b*-PS block copolymers (Thickness: $\sim$ 56 nm). P(NBA-*co*-AA)$_{74}$-*b*-PS$_{415}$ annealed in THF (a) and in C_6H_6/CH_3NO_2 (c). P(NBA-*co*-AA)$_{74}$-*b*-PS$_{581}$ annealed in THF (b) and in C_6H_6/CH_3NO_2 (d).

7.4 Formation of nanoporous thin films

The creation of porosity in thin films made from PEO_{113}-$h\nu$-PS_{176} has been investigated. The formation of the pores was performed in two steps. Firstly, thin films were irradiated with UV light at 300 nm with an intensity of 41,6 mW/cm^2. After irradiation, the films were immersed in a selective solvent for the PEO block in order to extract it. Another operating way was to expose the film to cycles of irradiation and solvent immersion. The thin films employed for this study were films annealed in conditions MM or LM' and showing a perpendicular orientation of the PEO domains similar to those presented in Figures 7.6(a) and 7.7. The removal of the PEO and the subsequent formation of nanopores were evidenced by UV-visible and infrared (IR) spectroscopies as well as by scanning and transmission electron microscopies (SEM and TEM). For thin films made from P(NBA-*co*-AA)-*b*-PS block copolymers, only preliminary results towards the nanoporosity are presented at the end of the section.

7.4.1 UV-visible and IR spectroscopy

The photocleavage of the block copolymers was firstly followed by UV-visible spectroscopy. Figure 7.13(a) presents the evolution of the UV-visible absorption spectra as a function of irradiation time. Even if the intensity at λ_{max} (309 nm) of the *o*-nitrobenzyl junction is relatively low (Abs = 3 $\times 10^{-2}$), the evolution of the spectra with time can be seen. As for the photocleavage in solution, the absorption band corresponding to the nitro group (λ_{max} = 309 nm) decreases with the irradiation time at the expense of that corresponding to the *o*-nitrosobenzyl moiety (λ_{max} = 350 nm). After 10 minutes of irradiation time, no significant change in the absorption spectrum was observed.

The extraction of PEO with a selective solvent (methanol/water mixture) was then investigated with UV-visible and infrared (IR) spectroscopies. Different parameters have been tested such as the time of irradiation and of immersion, as well as the number of irradiation-immersion cycles. Figure 7.13(b) shows the UV-visible spectra of a thin film of PEO-$h\nu$-PS after 2 cycles of 10 minutes of irradiation at 300 nm and 1 hour of immersion in a methanol/water (50/50) mixture (total irradiation time: 20 minutes; total immersion time: 2 hours). The spectra of

the starting film and of a homoPS are also shown for the sake of comparison. The spectrum of the irradiated and immersed film is similar to the one of a homoPS film. This is a first evidenced that PEO has been extracted. Indeed, the fact that PEO chains are end-functionalized by *o*-nitrosobenzaldehyde and that no signal corresponding to the nitroso moieties are observed, demonstrates the successful extraction of the PEO minor phase.

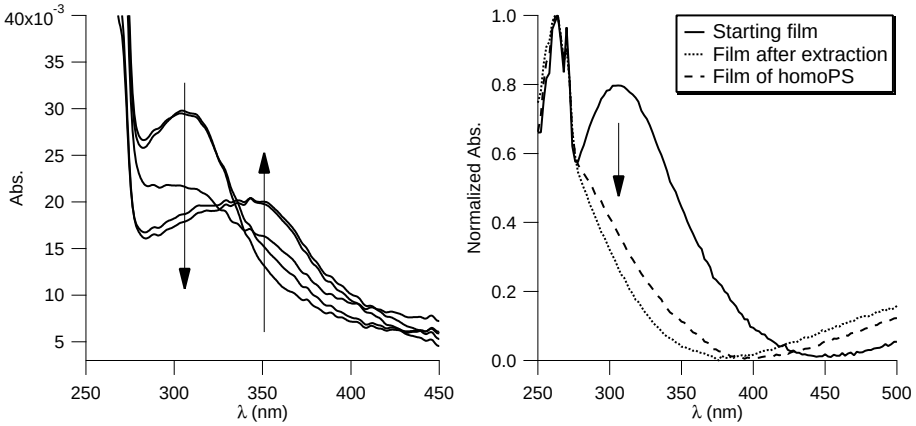

Figure 7.13: Photocleavage of PEO_{113}-$h\nu$-PS_{176} thin films. Evolutions of the UV-visible absorption spectra as a function of the irradiation time: t(min)= 0, 0.5, 2.5, 5.0, 7.5 , 10 (a). UV-visible absorption spectra of a film of homoPS and of films of block copolymers before and after irradiation and extraction (b).

The extraction of PEO was also demonstrated by infrared (IR) measurements. Figure 7.14(a) shows the IR spectra of a thin film made of PEO_{113}-$h\nu$-PS_{176} before and after 13 cycles of 2 minutes irradiation at 300 nm and 90 minutes immersion in a methanol/water (50/50) (total irradiation time: 26 minutes; total immersion time: 19.5 hours). For comparison, Figure 7.14(b) presents the IR spectra of thin films made of homoPEO and homoPS. After extraction, the intensity of the signals corresponding to the PEO block (bands at 2900 cm^{-1} and at 1100 cm^{-1}) decreased significantly, evidencing the extraction of PEO. However, since these signals do not disappear completely, some PEO could

remain inside the film (Figure 7.14(a)). Nevertheless, the remaining signal or, at least a part of it, can be attributed to the absorption of the silicon substrate. This overlay between the PEO signal and the silicon substrate signal at about 1100 cm^{-1} is not negligible due to the small thickness of the block copolymer films compared to the substrate.

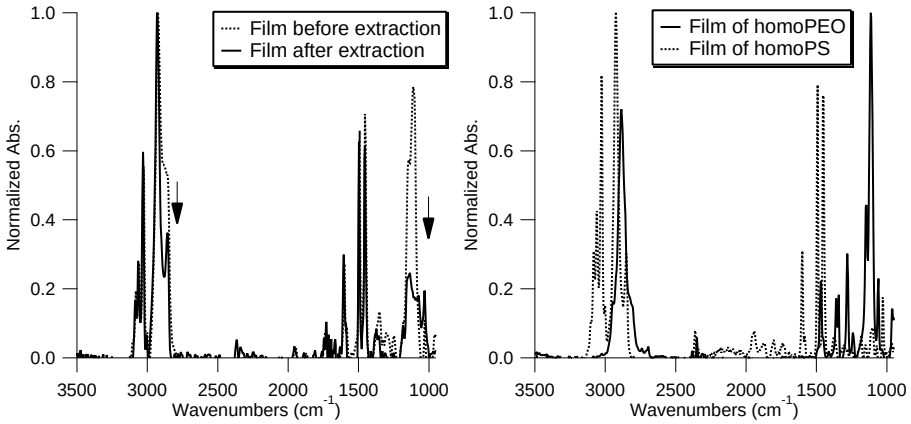

(a) (b)

Figure 7.14: Infrared (IR) measurements on polymer thin films. IR spectra of a PEO_{113}-$h\nu$-PS_{176} thin film before and after irradiation and extraction of the PEO block (a). Superposition of the IR spectra of thin films of homoPEO and homoPS (b).

It is also noteworthy to precise that UV-visible and IR measurements have to be interpreted carefully. Indeed, due to the small thickness of the film, the signal for both methods is quite weak (the thickness limit of detection for both method is around 60-80 nm). Moreover, in the case of IR spectroscopy, the silicon substrate also absorbs at around 1100 cm^{-1} and interfere thus with the PEO signals. The results have to be carefully interpreted and only qualitative interpretations can be obtained. Despite these drawbacks, general trends have been extracted from those results. In order to observe a *good removal*[5] of the PEO, 20 minutes irradiation time in combination with long immersion time (at

[5]A *good removal* is defined here as a removal of at least $\sim 60\%$ of the PEO based on IR measurements (without taking account of the interference with the substrate).

least 6 hours) is at least needed. Finally, several irradiation-immersion cycles did not improve significantly the extraction efficiency. Thereby, the extraction can be performed by a simple irradiation followed by a long immersion time.

7.4.2 Imaging techniques

UV-visible and IR spectroscopies evidenced the possibility of removing PEO from the films. However, these techniques do not give information about the morphology of the film after extraction of the PEO minor phase. In other words, they do not show if empty pores are created. In order to demonstrate the formation of nanopores, SEM and TEM imaging were performed on irradiated and extracted thin films of PEO_{113}-$h\nu$-PS_{176} with a thickness of $\sim$ 30 nm[6]. Figure 7.15 shows the AFM height picture of the starting thin film of PEO_{113}-$h\nu$-PS_{176} (cylinders: $\varnothing = 18 \pm 3$ nm, $\lambda_{C-C} = 30$ nm).

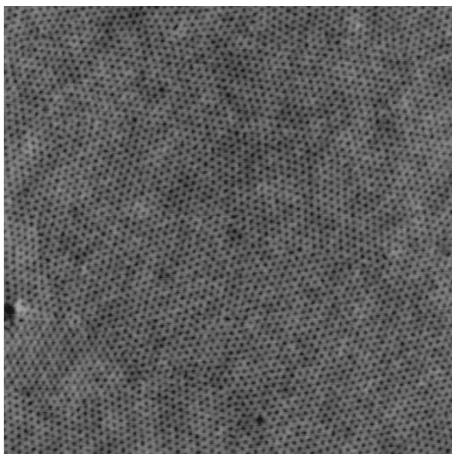

Figure 7.15: AFM height image (2×2 μm) of a thin film of PEO_{113}-$h\nu$-PS_{176} spin coated from a C_6H_6 solution (5 g/L) and annealed in benzene/water vapors during 4 hours in condition LM'.

[6]30 nm thick films were prepared by the spin-coating of 5 g/L solutions.

This thin film was continuously irradiated at 300 nm during 20 minutes and then immersed in a methanol/water (9/1) mixture for 24 hours. The film was then dried and splitted into two parts in order to expose its cross-section. Figures 7.16(a) and 7.16(b) present SEM pictures of the cross-section. The images show the long range ordering of the cylinders (surface of the film). Moreover, several nanopores spanning throughout the whole thickness of the film are visible in the cross-section, evidencing the formation of a nanoporous material made from this photocleavable block copolymer.

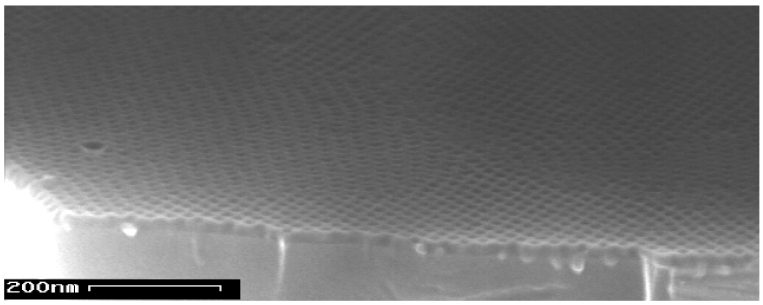

(a)

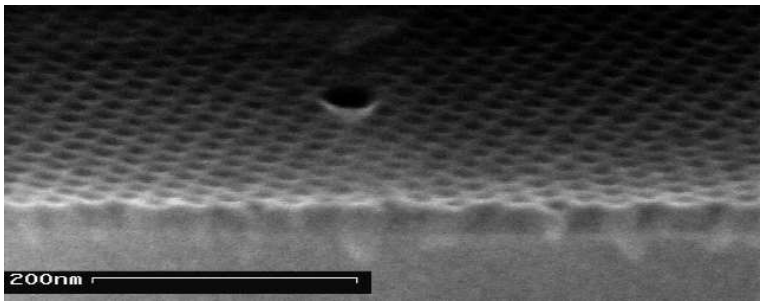

(b)

Figure 7.16: SEM cross-section pictures of thin film of PEO_{113}-$h\nu$-PS_{135} irradiated and washed.

In order to further characterize the films, TEM measurements have been performed. For these experiments, thin films were detached from their substrates, floated on water and picked up on TEM grids. Figures 7.17(a) and 7.17(b) show the TEM pictures of the film before and after extraction, respectively. Except few defects (holes) certainly due to the transfer of the films, the films show arrays of hexagonally packed cylinders. The average diameter of the cylinders is equal to 19.7 nm which is in agreement with the AFM measurements ($\varnothing$ = 19.3 nm). No difference could however been seen before and after extraction except a slight difference in the contrast. In order to improve the contrast, the films were stained with RuO_4 vapors during a long time (75 min) in order to stain also the PEO domains. Figures 7.17(c) and 7.17(d) show the TEM pictures of the stained film before and after extraction, respectively. Before extraction, no contrast is visible indicating a homogenous staining of the film (PS + PEO) (Figure 7.17(c)). On the contrary, for the film after extraction, small white dots are observed, indicationg that only the PS matrix has been stained and that a significant amount of PEO has been extracted.

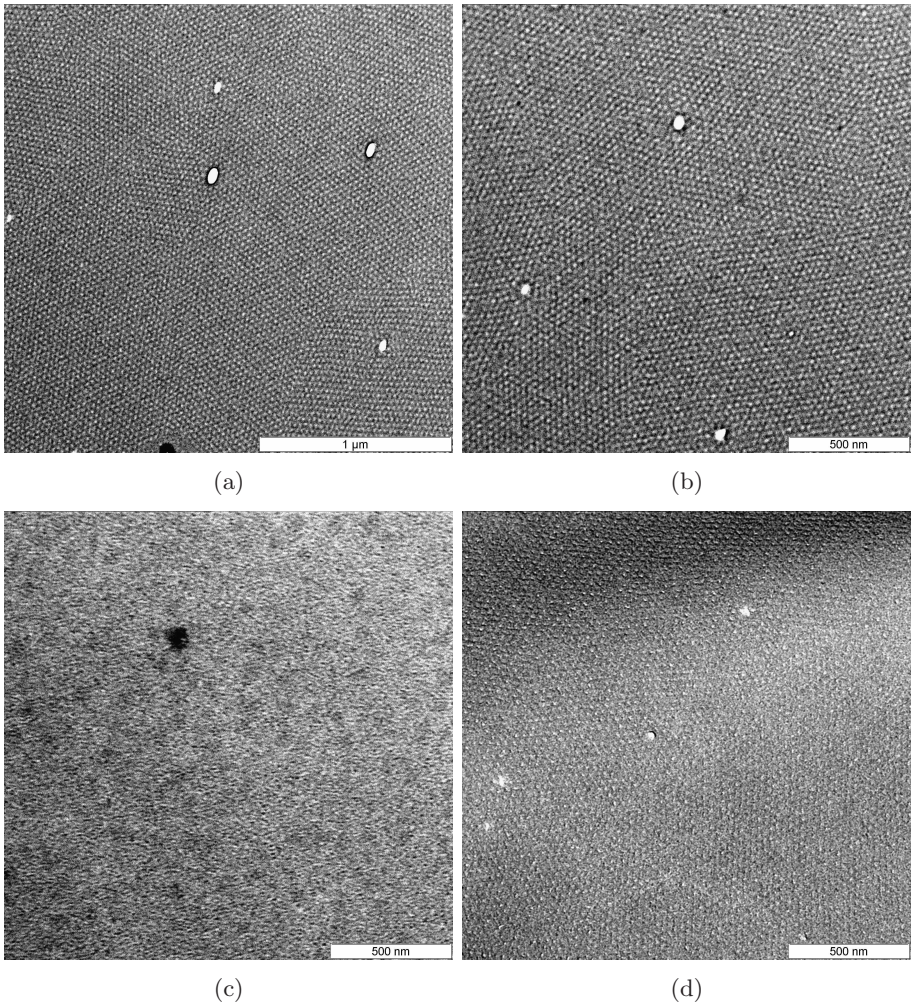

(a) (b)

(c) (d)

Figure 7.17: TEM pictures of thin films of PEO_{113}-$h\nu$-PS_{135} annealed in conditions LM' (thickness: 35 nm): Starting film not stained (a), extracted and not stained (b); starting film and stained with RuO_4 (c); extracted and stained with RuO_4 (d).

7.4.3 Towards nanoporous P(NBA-*co*-AA)$_{74}$-*b*-PS$_{581}$ thin films

Concerning the creation of porosity in the films made from the second family of block copolymers, no complete study has been performed so far. However, preliminary results are presented here for the P(NBA-*co*-AA)$_{74}$-*b*-PS$_{581}$ block copolymer. The photocleavage of the side groups was followed by UV-visible spectroscopy on thin films prepared in the best annealing conditions (Table 7.2, Entry 6). Figure 7.18 shows the evolution of the UV-visible spectra as a function of time. The band corresponding to the nitro groups (λ = 260 nm)) decreased while that of the nitrosobenzaldehyde product appeared progressively (λ = 350 nm).

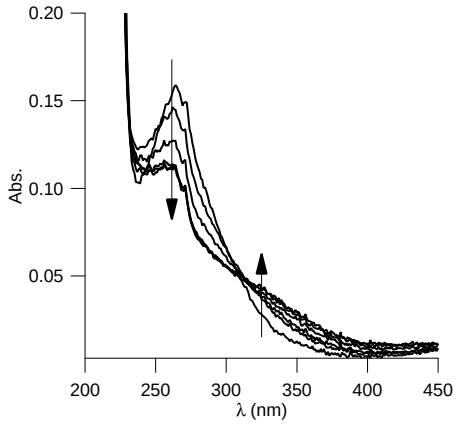

Figure 7.18: Photocleavage of P(NBA-*co*-AA)$_{74}$-*b*-PS$_{581}$ thin films: Evolution of the UV-visible absorption spectra as a function of the irradiation time: t(min)= 0, 2, 4, 6, 8, 9, 10, 12.

Figure 7.19(a) shows the infrared spectrum of a thin film of P(NBA-*co*-AA)$_{74}$-*b*-PS$_{581}$. The band at 1531 cm^{-1} corresponds to the stretching of the nitro group. After 13 cycles of irradiation (300 nm, 2 min) and immersion in nitromethane, a selective solvent for the PNBA block, (30 min) (total = 26 min of irradiation and 390 min of extraction), a decrease in the intensity of this band is observed ($\sim$ 40 %). This result is encouraging for further experiments in which parameters such as the time of irradiation and immersion or the selective solvent have to be

screened.

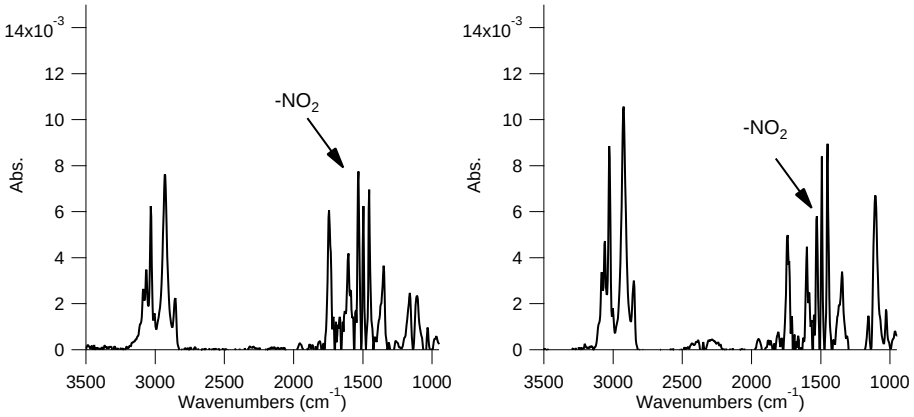

Figure 7.19: Infrared (IR) measurements on polymer thin films of P(NBA-*co*-AA)$_{74}$-*b*-PS$_{581}$ before (a) and after irradiation and extraction (b).

7.5 Conclusions

Thin films of PEO-*hν*-PS and P(NBA-*co*-AA)-*b*-PS block copolymers presenting the desired cylindrical morphology have been successfully obtained by spin-coating and further annealing. After optimization, solvent annealing led to well-ordered hexagonally packed cylinders orientated normal to the substrate. The thickness of the films was controlled by the concentration of the solution to spin-coat. Thicknesses ranging from 30 to 130 nm were obtained while maintaining the desired orientation of the cylinders. For both families of block copolymers, the mean diameter of the cylinder was equal to about 20-22 nm. In the case of PEO-*hν*-PS thin films, AFM measurements of the top and the bottom of the film in addition with the SEM picture of a film etched to the middle of its thickness suggested that the PEO cylinders span throughout the whole film.

After the obtention of the desired morphology, the creation of the

nanopores was approached. The UV irradiation of the film followed by the extraction of the minor phase was discussed. For PEO-$h\nu$-PS the formation of nanopores was evidenced by TEM measurements and SEM views of a cross-section of the films. Concerning the second family, nitromethane is a promising extraction solvent for the released side groups as demonstrated by IR spectroscopy. Further investigations have however to be performed before the obtention of nanopores and their characterization.

Experimental part

Thin film preparation. Silicon and quartz substrates were cleaned by a piranha solution (H_2SO_4 98%/H_2O_2 30% 3/1) during 30 minutes before being rinsed in ultra-pure water. The substrates were then dried with the spin-coater at a velocity of 4000 rpm for 20 s. Filtered solutions (0.2 μm) of polymer in benzene were then spin coated onto these substrates at 2000 rpm during 40 s. The thicknesses of the film were controlled by the concentration of the solution to spin-coat. Figure 7.20 shows the linear dependance of the thickness and the concentration of the solution. The thicknesses were measured by SEM.

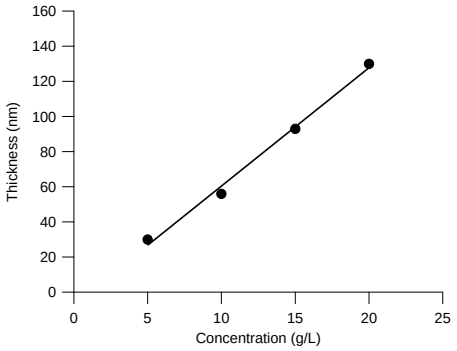

Figure 7.20: Thickness of the films as a function of the concentration of the spin-coated solution.

Typical procedure for annealings (condition MM, Table 7.1, Entry 4). The annealing set-up is described in Figure 7.4. The samples are placed under a glass case with one medium beaker (M) containing benzene (8 mL) and one medium beaker (M) containing water (10 mL). A weight is placed on the glass case in order to keep the system as hermetic as possible. After 15 hours, the glass case is removed leaving the samples to dry.

Typical procedure for annealings in slow evaporation mode (condition LM', Figure 7.7). The annealing set-up is described in Figure 7.4. The samples are placed under a glass case with one large

beaker (L) containing benzene (2 mL) and one medium beaker (M) containing water (2 mL). A weight is placed on the glass case in order to keep the system as hermetic as possible. After 4 hours, a small space is realized by carefully inserting 3 microscopy glass slides between the glass case and the base. The system is put near the extraction of the fume hood and once all the benzene has evaporated ($\sim$ 2.5 h), the glass case is removed.

Typical procedure for the irradiation and extraction (Section 7.4.2) The thin film was put under three Rayonet photochemical reactor UV lamps emitting at 300 nm. The distance to the lamps was of about 3 cm (the intensity of the UV lamps at this distance was equal to 41.6 mW/cm^2). After 20 minutes of irradiation time, the film was immersed in a methanol/water (9/1) mixture for 24 hours. The film was then dried to open air. Irradiation intensities were measured with a radiometer RM12 from Dr. Gröbel UV-electronik GmbH equipped with UVB (280-315 nm) sensors.

AFM measurements. Atomic force microscopy was performed on a Digital Instruments Nanoscope IV scanning force microscope in tapping mode using NCL cantilevers (Si, 48 $N/m, 330kHz$, Nanosenors).

UV-visible measurements. UV-visible spectra were recorded on a Varian spectrophotometer (Cary, 50 Conc). Thin films were prepared on quartz substrates.

FTIR measurements. Fourier transformed infrared absorption spectra were obtained using an Omnic spectrometer (Omnic 7.1) with a resolution of 8 cm^{-1} and 256 scans. The system was purged with dry air during 30 minutes before measurement.

SEM measurements. Scanning electron microscopy (SEM) was performed on a Zeiss Supra 60 VP (IXRF EDX) and on a Zeiss LEO 982 microscopes operating at an acceleration voltage of 15 and 10 kV, respectively. Cross section views were measured with a tilt angle of 15°.

TEM measurements. Transmission electron microscopy (TEM) was performed on a LEO 922 microscope, operating at 200 kV accelerating

voltage in bright field mode. Samples for TEM experiments were prepared by spin-coating the polymer solution onto a silicon substrate with a large silicon oxide top layer (400 nm). The samples were then floated on a HF solution (5 wt.-%). After about 90 seconds, they were transferred on pure water and they were detached from their support, floating on water. Parts of the films were then picked up on TEM grids (pure copper, mesh:300). The grids were then dried in vacuo for 15 hours. For RuO_4 stained samples: the samples were exposed to vapors of a fresh solution of RuO_4 (2 wt.-%) during 75 minutes.

O_2 reactive ion etching. The O_2 reactive ion etching (RIE) was performed with an Electrotech ET340 apparatus with a O_2 flow of 80 sccm (standard cubic centimeter per minute) and a pressure of 15 mTorr. The etching time was equal to 120 s with a power density of 2.5 mW/cm^2.

Estimation of the mean diameter of the cylinders, Ø. The mean diameter of the cylinders (Ø) was estimated with ImageJ 1.44e, an image processing program. The AFM image to process is firstly loaded and binarized as following:

- *Image* → *Type* → *8-bit*
- *Process* → *Binary* → *Make binary*

The scale is set by:

- *Analyse* → *Set scale*

The mean area, $\overline{a}$, of the particles and the standard deviation, σ_a, of the distribution is given by:

- *Analyse* → *Analyse Particles*
- *Analyse* → *Distribution*

The mean diameter is then calculated by using the following equation:

$$Ø = 2\sqrt{\frac{\overline{a}}{\pi}} \tag{7.1}$$

The dispersion on the mean diameter corresponds to the standard deviation of the population $\sigma_Ø$:

$$\sigma_Ø = \frac{Ø\ \sigma_a}{2\ \overline{a}} \tag{7.2}$$

Estimation of the center-to-center interdistance, λ_{C-C}. The interdistance λ_{C-C} was estimated from the 2-D power spectral density (PSD) profile of the images. This profile was obtained with the image processing program Nanoscope 5.12 as following: The AFM image to process is firstly loaded. Then in the menu:

- $Analyse \rightarrow Power\ Spectral\ Density \rightarrow 2D$

Fast Fourrier transforms (FFTs) on AFM pictures. FFTs were performed on the binarized AFM images with ImageJ 1.44e. The AFM image to process is firstly loaded and binarized. The corresponding FFT is then obtained by:

- $Process \rightarrow FFT \rightarrow FFT$

Bibliography

[1] Fustin, C.-A.; Lohmeijer, B. G. G.; Duwez, A.-S.; Jonas, A. M.; Schubert, U. S.; Gohy, J.-F. *Adv. Mater.* **2005**, *17*, 1162–1165.

[2] Fustin, C.-A.; Guillet, P.; Misner, M. J.; Russell, T. P.; Schubert, U. S.; Gohy, J.-F. *J. Polym. Sc. Part A* **2008**, *46*, 4719–4724.

[3] Lin, Z. Q.; Kim, D. H.; Wu, X. D.; Boosahda, L.; Stone, D.; LaRose, L.; Russell, T. P. *Adv. Mater.* **2002**, *14*, 1373–1376.

[4] Kim, S. H.; Misner, M. J.; Xu, T.; Kimura, M.; Russell, T. P. *Adv. Mater.* **2004**, *16*, 226–231.

[5] Bang, J.; Kim, S. H.; Drockenmuller, E.; Misner, M. J.; Russell, T. P.; Hawker, C. J. *J. Am. Chem. Soc.* **2006**, *128*, 7622–7629.

[6] Kim, S.; Misner, M.; Yang, L.; Gang, O.; Ocko, B.; Russell, T. *Macromolecules* **2006**, *39*, 8473–8479.

[7] Zhang, M. F.; Yang, L.; Yurt, S.; Misner, M. J.; Chen, J. T.; Coughlin, E. B.; Venkataraman, D.; Russell, T. P. *Adv. Mater.* **2007**, *19*, 1571–1576.

[8] Bang, J.; Kim, B. J.; Stein, G. E.; Russell, T. P.; Li, X.; Wang, J.; Kramer, E. J.; Hawker, C. J. *Macromolecules* **2007**, *40*, 7019–7025.

[9] Bang, J.; Jeong, U.; Ryu, D. Y.; Russell, T. P.; Hawker, C. J. *Adv. Mater.* **2009**, *21*, 4769–4792.

[10] Tang, C.; Bang, J.; Stein, G. E.; Fredrickson, D. H.; Hawker, C. J.; Kramer, E. J.; Sprung, M.; Wang, J. *Macromolecules* **2008**, *41*, 4328–4339.

[11] Kim, S.; Briber, R. M.; Karim, A.; Jones, R. L.; Kim, H.-C. *Macromolecules* **2007**, *40*, 4102–4105.

[12] Phillip, W. A.; Hillmyer, M. A.; Cussler, E. L. *Macromolecules* **2010**, DOI: 10.1021/ma1012946.

[13] Kim, S. H.; Misner, M. J.; Russell, T. P. *Adv. Mat.* **2008**, *20*, 4851–4856.

[14] Kim, S. H.; Misner, M. J.; Russell, T. P. *Adv. Mater.* **2004**, *16*, 2119–2123.

CHAPTER

EIGHT

CONCLUSIONS AND PERSPECTIVES

This work was devoted to the formation of nanoporous thin films made from photocleavable block copolymers. Self-assembly of block copolymers into well-ordered nanostructures has been firstly introduced in Chapter one. For self-assembly in thin films, the cylindrical morphology with the cylinders oriented perpendicular to the surface is one of the most interesting for applications such as membrane filtration and templating. Indeed with a block copolymer approach, the nanoporosity can be easily obtained by removing the minor phase.

Very recently, light-sensitive block copolymers have been attracting much attention as it was shown in Chapter two. That chapter provided an overview of the different photo-responsive moieties that have been incorporated so far in block copolymers. Moreover, the related applications such as holographic materials or light tunable micelles were also discussed.

Block copolymers containing photocleavable moieties can be used for the creation of nanopores as described in Chapter three. In this approach, light is used as stimulus in order to cleave the link between the blocks or the link between one block and its side groups. Once the components are cleaved, a simple rinsing with a selective solvent of the polymer composing the minor phase generates the nanoporosity. The advantages of this strategy are the use of mild and non destructive conditions, in addition with a control of the chemical functions inside the pores.

The attention was firstly focused on the synthesis of two families of photocleavable block copolymers. The first one was composed of block copolymers in which the two blocks are separated by a photocleavable *o*-nitrobenzyl ester junction. The challenge was to introduce this junction quantitatively. A simultaneous one-pot reaction combining a CuAAC-click reaction coupled with ATRP polymerization proved to be an efficient and versatile approach (Chapter Four). Concerning the second family, the strategy involving a direct polymerization of monomers containing *o*-nitrobenzyl revealed to be possible but tedious because of the difficult tuning of the polymerization conditions (Chapter five). The reason of such difficulties originates in side reactions due to nitroaromatic compounds. In this context an easier and more controlled way based on the grafting of *o*-nitrobenzyl derivatives on PAA-*b*-PS block copolymers was developed, and well-defined P(NBA-*co*-AA)-*b*-PS block copolymers were synthetized by this method. However, even if high grafting efficiencies were obtained, the functionalization of carboxylic acid groups is not quantitative and depends greatly on the composition of the block copolymer. The degrees of functionalization which have been reached are probably enough for the targeted creation of free volume in thin films. However, if it were not the case, two alternative strategies might be considered. Firstly, the grafting of bulkier photocleavable moieties such as substituted *o*-nitrobenzyl could be considered. In this case, as the moieties are bigger, the generated free volume would be also more important. On the other hand, increasing the degree of functionalization may also be an alternative as more photocleavable moieties would be present on the chain. A quantitative functionalization can be reached by a direct polymerization of photocleavable monomers. However, monomers based on other types of photocleavable moieties such as pyvaloyl or methoxyphenacyl should be considered in order to avoid the problems of polymerization encountered with the monomers containing nitroaromatics.

Once the block copolymers were synthesized, their photocleavage has been studied in solution (Chapter six). UV irradiations at a wavelength of 300 nm proved to be efficient for the cleavage of the block copolymers of both families. It was also demonstrated that *o*-nitrobenzyl esters can be cleaved chemically in basic medium. Moreover, the advantage of using a light-sensitive strategy versus a traditional chemical approach was

demonstrated with micelles made from a PEO-$h\nu$-PS block copolymer. Indeed, it was shown that the rate of the cleavage reaction was much slower in case of the chemical cleavage performed on micelles. This was attributed to the limited accessibility of the ester groups in the micelles towards the chemical cleaving agents. In sharp contrast, light could reach easily the ester groups to be cleaved in case of the photochemical cleavage. Concerning the second family, micellar objects were obtained in solution by the photocleavage of the side groups of the block copolymers. This behavior is explained by a change in the hydrophilic balance of the block copolymer. Indeed, the formation of hydrophilic poly(acrylic acid) triggered the self-assembly of the block copolymer in solution. Such objects should be further characterized by imaging techniques in order to determine their morphology.

Finally, the self-assembly of the photocleavable block copolymers into thin films and the subsequent creation of nanoporosity was investigated (Chapter seven). Thin films were prepared by spin-coating diluted solutions of block copolymers onto silicon substrates. After suitable solvent annealing, both families, *i.e.*, PEO-$h\nu$-PS and P(NBA-*co*-AA)-*b*-PS block copolymers, led to well-ordered morphologies with cylinders oriented perpendicular to the substrate. The formation of nanopores was demonstrated with thin films made from PEO-$h\nu$-PS block copolymers. Indeed, after UV irradiation and the selective removal of the PEO phase, nanopores were obtained. Further studies could be carried out in order to demonstrate the presence of the carboxylic acid functions inside the pore. A proof of concept could be firstly performed with fluorescent molecular probes such as pyrenyl diazomethane (Figure 8.1). The strategy would consist in immersing a nanoporous film in a solution containing the dye. The diazomethane functions will react with the carboxylic acids in order to form ester bonds. Fluorometry will be then used to check the grafting of the dyes (after elimination of the non-coupled molecules by rinsing). Afterwards, experiments investigating the dual filtration, based on the size and on the affinity, could be performed as described in chapter three. Virus filtration could be coupled with a selective protein filtration. For example, desthiobiotin ethylenediamine (DSB-X^{TM}) (Figure 8.1) could be grafted inside the pore via an amidation reaction. Like biotin, desthiobiotin can selectively bind avidin and streptavidin. In that way, the filtration process would involve the isolation of a non-binding protein from a mixture of that protein mixed

with a virus and avidin. The virus and the non-binding protein could be the same as those used in the example described in section 1.3.2.3 (Rhinovirus and BSA, respectively).

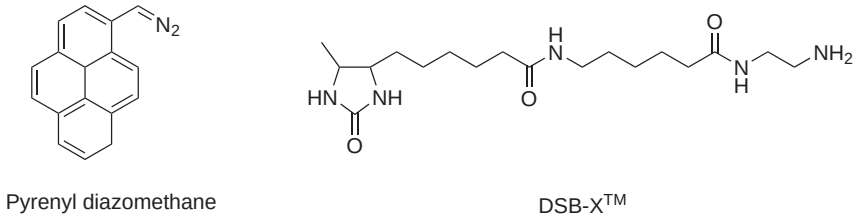

Pyrenyl diazomethane DSB-X™

Figure 8.1: Molecules to bind to the carboxylic function covering the pores of the nanoporous thin films.

Beside the use of nanoporous thin films for filtration, they could also be used as templates for the formation of inorganic nanodots. Indeed, the nanopores could be filled with a metal either by metal deposition or by electroless plating. After removal of the polymer matrix by its simple dissolution in a good solvent, arrays of metallic nanodots would be obtained. Additionally, as mentioned in Chapter Three, creating porosity only in selected regions of the films could be possible by the use of lithographic masks. Demonstrating the possibility to easily achieve some patterns of arrays of metallic nanodots would evidence the possibility of playing on two levels of structuration with photocleavable block copolymers. Indeed, the first level being nanoscopic, due to the self-assembly behavior of the block copolymer, and the second being mesoscopic and controlled by the use of lithographic masks.

Concerning thin films of P(NBA-*co*-AA)-*b*-PS block copolymers, the removal of the side groups should be improved and the porosity, demonstrated. In this case, the photoremoval of the side groups will lead to the creation of a free volume in an entangled network made of PAA chains. An interesting perspective would be to demonstrate the possibility to control the permeability of the nanoporous thin films. Indeed, it should be possible to open or close the pores by the swelling of the polymer brushes located inside the pores. This could be controlled by the nature of the solvent and/or the pH used insofar as the latter is a non-solvent

of the PS matrix. Finally the degree of permeation could also be tuned by the amount of removed photocleavable side groups. This could be controlled by time and/or the intensity of irradiation.

Another interesting field of applications for nanoporous thin films is their use as chemosensors. Indeed it would be possible to attach chemosensors inside the pore and use them for detection. For example fluorescent metal-binding sensor could be grafted inside the pores. The advantage of the nanoporous film would be the huge concentration of functions coming from the pore area coupled with the high pore density. This would be especially true for the second family, where the second block offers a higher concentration for the reactive functions.

To conclude, it would be also interesting to further investigate and develop the self-assembly of both families in solution. Indeed, the formation of nanocages and their applications as encapsulation agents and nanoreactors could be considered. For the first family, the general strategy would consist in firstly forming micelles from those block copolymers (Figure 8.2). UV irradiation would then be used to cleave the junctions between the cores and the coronas of the micelles. The cores could be removed with a selective solvent leaving the nanocages empty. In order to avoid the total destruction of the objects, the corona of the micelles should be previously cross-linked. The degree of permeation could be tuned by the percentage of cross-linking and/or the nature of the solvent. Such systems could be achieved from diblock or triblock copolymers such as PS-$h\nu$-PAA or PS-$h\nu$-PDMAEMA-*b*-POEGMA (PDMAEMA = poly(dimethylaminoethylene methacrylate); POEGMA = poly(oligoethyleneglycol methacrylate)). For the second family, the encapsulation of molecules could be directly triggered by the formation of micelles upon irradiation (Figure 8.3). This could be demonstrated by the encapusation of a fluorescent dye into micelles made from irradiated P(NBA-*co*-AA)-*b*-PS block copolymers.

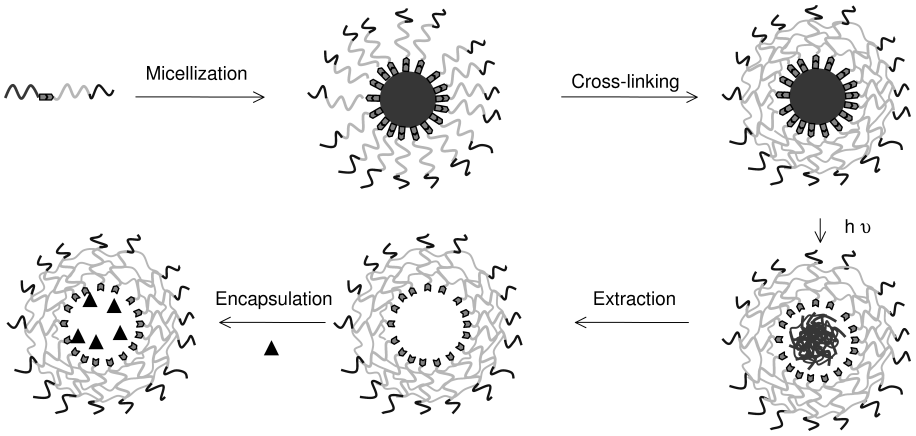

Figure 8.2: General strategy toward nanocages made from photocleavable block copolymers.

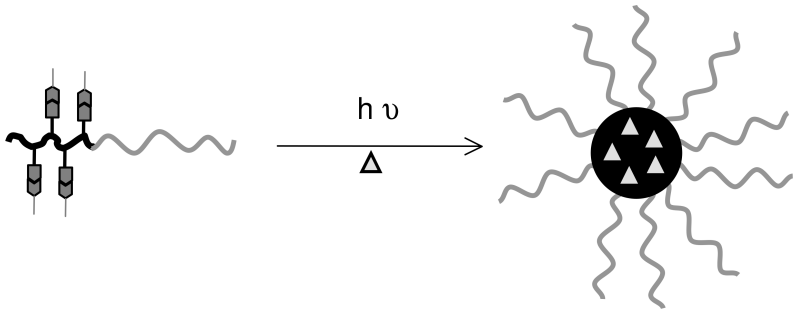

Figure 8.3: Simultaneous micelle formation and molecules encaplusation triggered by light.